Strontium and nickel substituted lanthanum cobaltite as cathode in Solid Oxide Fuel Cells

Hjalmarsson, Per

Publication date:
2008

Document Version
Publisher's PDF, also known as Version of record

Fuel Cells and Solid State Chemistry Department
Risø National Laboratory for Sustainable Energy
Technical University of Denmark

PhD thesis - Strontium and nickel substituted lanthanum cobaltite as cathode in Solid Oxide Fuel Cells

Per Hjalmarsson

Roskilde, August 2008

Abstract

The objective of this thesis was to investigate oxide materials that show promising materials properties for SOFC cathode applications. An initial literature survey found that strontium and nickel substituted lanthanum cobaltite, $(La_{1-x}Sr_x)_sCo_{1-y}Ni_yO_{3-\delta}$, to be an interesting materials system and the thesis will firstly review the literature with respect its to materials and kinetic properties.

Secondly, it reports on thermodynamic and structural properties measured on a selected number of compositions within $(La_{1-x}Sr_x)_{0.99}Co_{1-y}Ni_yO_{3-\delta}$. This includes the crystal-, defect- and electronic structure as well as how these properties relates to the electronic conductivity and the thermal and chemical expansion behaviour. Conductivity measurements showed that strontium substitution increases the metallic like character due to the p-type doping and that partial substitution of nickel in $(La_{1-x}Sr_x)_sCoO_{3-\delta}$ increases the mobility of the p-type charge carriers. A dual electronic conductivity mechanism was proposed in which *intrinsic charge* of intermediate and high spin cobalt is argued to follow a small polaron conduction and where the conductivity of the *extrinsic charge* (due to strontium substitution) is shown to be metallic-like. Lattice expansion coefficients are shown to increase to first and second order degrees with respect to both T and oxygen substoichiometry. Substitution of Co with Ni was reported to decrease both expansion coefficients.

Thirdly, it reports on electrochemical and oxygen transport properties measured on a selected number of compositions. It was shown that $(La_{1-x}Sr_x)_sCo_{1-y}Ni_yO_{3-\delta}$ has a very high electro-catalytic activity towards oxygen reduction/oxide ion oxidation. This activity increases strongly with strontium content. The results could not demonstrate any improvements in oxygen transport properties and the electrochemical activity. The uncertainties are substantial, however, due to the activity of porous $(La_{1-x}Sr_x)_sCo_{1-y}Ni_yO_{3-\delta}$ electrodes being very susceptible to changes in manufacturing parameters such as sintering temperature. It is further reported that the electro-catalytic activity and the short term degradation is dependent on storage time and conditions.

Outline of Chapters

Chapter 1 gives a short introduction to fuel cells including the electrochemical principles and the conventional and state-of-the-art materials of Solid Oxide Fuel Cells (SOFC). It also presents the motivation and objectives of the thesis.

Chapter 2 gives the theoretical background to the thesis including a literature survey of both thermodynamic and kinetic/transport properties of strontium and nickel substituted lanthanum cobaltite.

Chapter 3 evaluates two synthesis methods and gives introductory results on powder characterisation. The single phases region of $(La_{1-x}Sr_x)_sCo_{1-y}Ni_yO_{3-\delta}$ is characterised and the compositions studied throughout this in thesis are motivated. It finally introduces some interesting phenomena found during the work of this thesis, which will be discussed in detail in the following chapters.

Chapter 4 determines the effect on structural and electrochemical properties when SrO on A-site in $(La_{0.6}Sr_{0.4})_{0.99}CoO_{3-\delta}$ is substituted with equal amounts of NiO on B-site. Parts of this chapter was presented orally and as a conference proceeding [1] at the conference: Materials Science and Technology (MS&T), 2006, Cincinnati, Ohio. The results have been published in Solid State Ionic. [2]

Chapter 5 presents the defect structure of a selected number of compositions within $(La_{1-x}Sr_x)_sCo_{1-y}Ni_yO_{3-\delta}$. It reports further on the conductive and expansive properties as function of temperature and oxygen stoichiometry. The results have been published in Journal of Solid State Chmeistry, 2010. Parts of this chapter was presented at the conference: 33nd International Conference & Exposition on Advanced Ceramics and Composites, Jan 2009, Daytona Beach, Florida.

Chapter 6 presents the electrochemical properties of a selected number of compositions within $(La_{1-x}Sr_x)_sCo_{1-y}Ni_yO_{3-\delta}$ when used as porous oxygen electrodes. Parts of this chapter was presented orally and in the conference proceeding [3] at the conference: SSI-16, 2007, Shanghai. The results have been published in Solid State Ionics.

Chapter 7 presents oxygen transport properties of porous and dense $(La_{0.8}Sr_{0.2})_{0.99}Co_{0.8}Ni_{0.2}O_{3-\delta}$ using two different methods, the electrical conductivity relaxation and AC impedance spectroscopy techniques. The results have been published in Solid State Ionics.

Chapter 8 summarises the thesis with a general discussion on the results presented throughout the report. It stresses the most important conclusions in the context of SOFC and finally comments on how the research of this topic could be continued.

Acknowledgement

This PhD-project was carried out within the framework of the consortium "Design of functional nanomaterials", which have dealt with the development of rational design strategies to make new functional nanostructures. This work was supported by the Danish Research Agency, the programme committee for nanoscience and technology, biotechnology and information technology (NABIIT), grant no. 2106-05-0033. The work has been supervised by Prof. *Claus H. Christensen*, Centre for sustainable and green chemistry, DTU. The scientific work has been supervised by Research prof. *Mogens Mogensen* at Risø National Laboratory for sustainable energy.

I would like to thank the following people:

Mogens Mogensen for giving me the opportunity to work in this exciting field of research. I am deeply grateful for your efforts and support and for always having a moment for discussions despite that you often actually don't. You have been a constant source of infinite knowledge and of contagious inspiration, energy and enthusiasm.

Martin Søgaard for patiently helping me with numerous experimental and theoretical matters throughout the whole thesis period.

My friend and "office-mate", *Peter Blennow*, for persuading me to apply for this PhD project and for all the scientific discussions and personal "chit chats", which have made the workdays and the total commuting time of almost 2000 hours so much more enjoyable. Over these three years, I think we have spent more time with each other than a married couple do and I can now, with absolute certainty, say that you would become a great wife...:)

All other colleagues at the Fuel Cells and Solid State Chemistry Department for providing an excellent research environment, both on a professional and personal level. Special thanks goes to *Nikolaos Bonanos* for teaching of electrical impedance spectroscopy, *Finn Willy Poulsen* for help with X-ray diffraction measurements and *Anke Hagen* for help with XANES-measurements at HASYLAB, Hamburg. I am looking forward to continuous collaborations with you all.

Peter B, Johan H and *Mats L* for putting up with me two hours a day, 10 hours a week, 45 hours a month and almost 500 hours a year on the roads back and forth to work.

Finally, I want to thank all my *Friends* and my Family, *Marianne, Lars, Anna* and *Lisa*, for always being there for me and for making my life such a wonderful and joyful experience. I love you all.

Contents

Chapter 1

Introduction

1.1 Introduction to fuel cells

Development of new energy technologies have become increasingly important in times when our knowledge and awareness of the global warming and its detrimental climatological, ecological and sociological effects are growing fast. This has caused a push for sustainable energy technologies and laid ground for the concept of the *hydrogen society* in which the energy produced from sustainable sources is stored in the form of hydrogen. A key feature of such an energy system is an efficient converter that transforms the chemical energy into the electrical energy needed in our modern society. This is exactly what a fuel cell does. Moreover, a fuel cell can also be operated in the reverse mode, as an electrolyzer, to split water into oxygen and hydrogen using electricity from e.g. a windmill. Several types of fuel cells exist today, all operating on the same principle. The cell is based on an electronically insulating, gas tight electrolyte that only carries charge in the form of ions. Two electrodes on each sides of the electrolyte accommodate the reduction of oxygen (the cathode) and the oxidation of fuel (anode) respectively. For the full reaction to be completed, the electrons produced at the fuel electrode are transported through an external circuit, over which the electrical power is gained. The principle is illustrated for a Solid Oxide Fuel Cell (SOFC) in Figure 1.1.

Table 1.1: List of the the most important characteristics of the five most common types of fuel cells, the alkaline FC, the polymer electrolyte membrane FC, phosphoric acid FC, molten carbonate FC and solid oxide FC.

Fuel Cell	AFC	PEMFC	PAFC	MCFC	SOFC
Charge carrier	OH^{-1}	H^+	H^+	CO_3^{2-}	O^{2-}
Electrolyte	KOH	Polymer	H_3PO_4	Li_2CO_3 + K_2CO_3	Zr_2 + Y_2O_3
$T_{\text{oper.}}$ [°C]	100	80	200	650	650-850
Fuels	Pure H_2	Pure H_2	CO free H_2	H_2, CO, CH_4	H_2, CO, CH_4, NH_3

The different types of fuel cells are characterised by the material of the electrolyte. This in turn determines the operating temperature, electrode materials and possible fuels. The most common types of fuel cells are listed in Table 1.1.

The high operating temperature used in SOFCs and molten carbonate fuel cells (MCFC) is of course a practical disadvantage. It also lowers the maximum theoretical efficiency. On the other hand high temperature cells have a number of other beneficial properties relative to the low temperature cells including:

- Higher electrical efficiency, ∼60%, compared to ∼40% for low temperature cells.
- Low cost electrode materials can be used instead of expensive noble metals such as platinum.
- A large variety of fuels can be used including natural gas, biogas, CO, methanol and ammonia all of which are poisoning the low temperature cells.
- Produces "high quality" heat which can be utilized efficiently in CPH-units (combined heat and power).

Major drawbacks with MCFC are the corrosion and creep problems caused by its electrolyte, whereas the electrolyte in the SOFC is very stable in comparison.

The fuel cell is driven by the reactions taken place at each of the electrodes. In case of hydrogen as fuel in a SOFC, the oxidation at the anode proceeds according to Reaction 1.1.

$$H_2 + O^{2-} \leftrightarrows H_2O + 2e^- \tag{1.1}$$

oxygen is reduced at the cathode according to Reaction 1.2:

$$\frac{1}{2}O_2 + 2e^- \leftrightarrows O^{2-} \tag{1.2}$$

and the overall balanced reaction is thus:

$$\frac{1}{2}O_2 + H_2 \leftrightarrows H_2O \tag{1.3}$$

The reactions are driven thermodynamically by the difference in chemical potential between the reactants and products of Reaction 1.3, whereas the diffusion of oxide ions through

the cell is driven by the the difference in oxygen partial pressure between the two side of cells. The difference in chemical potential can be converted into an electric potential or electromotive force by the Nernst equation, which in the case of hydrogen as fuel can be written:

$$E = E^0 - \frac{RT}{nF} ln \left(\frac{P_{\mathrm{H_2O}}}{P_{\mathrm{O_2}}^{1/2} P_{\mathrm{H_2}}} \right) \tag{1.4}$$

where E^0 is standard cell potential (1.23 V for H_2 as fuel), R is the gas constant, F is the Faraday constant, n is the number of electrons involved and T is the temperature. Equation 1.4 implies that the theoretical voltage that can be gained decreases with increasing temperature. The cells are on the other hand more efficient at higher T due to thermally activated reactions as well as higher oxide ion conductivities, which decreases the polarisation losses of the cell. The electrical loss can be divided into activation, ohmic and concentration polarisation according to Figure 1.2. The activation polarization is associated with the reactions at the electrodes and occurs at already small perturbations from open circuit voltage (OCV). The ohmic loss arise from the resistivity of the electrolyte and current collecting components and increases linearly with current load accordingly. At sufficiently high current densities, i.e. high fuel utilization, gas diffusion will start contributing to the total loss of voltage. With this picture in mind it is obvious that a number of aspects must be improved in order to increase the efficiency including better electro-catalysts (activation), better electronic and ionic conducting materials (ohmic) and better flow designs (gas transport). An improved microstructure has the potential of decreasing all kinds of losses and is thus also of great importance. The resistance arising from the electrode reactions and mass transport is often referred to as the polarisation resistance, R_{P}, whereas the the resistance arising from resistive contributions from the electrolyte and current collecting components is referred to as the serial resistance, R_{S}. For further information on technological aspects and thermodynamic principles of fuel cells see the handbook of fuel cells. [4]

1.2 The solid oxide fuel cell

This chapter will briefly discuss different components and materials aspects of an Solid Oxide Fuel Cell (SOFC). For further insight into the SOFC technology and its components the reader is referred to these review articles, [5] and [6] and references therein. Other components such as interconnects and sealings are also of great importance for the operation of an SOFC but are out of the scope of this thesis.

The solid oxide fuel cell (SOFC) is produced from oxide materials, which become active for transportation of oxide ions and electro-catalysis at high temperatures. Figure 1.1 shows

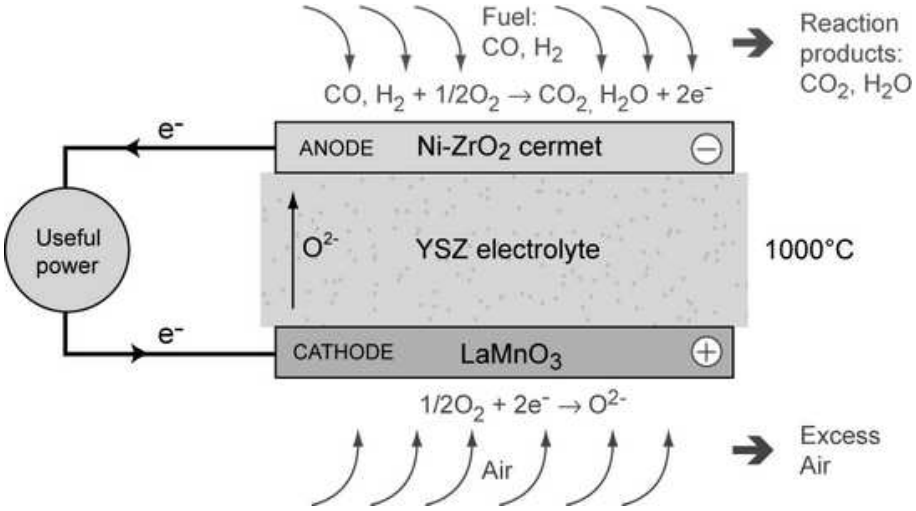

Figure 1.1: Illustration of the principle of an Solid Oxide Fuel Cell (SOFC) as well as the conventional materials used in the different components. Oxygen is reduced at the cathode to form O^{2-}. The oxide ions are transported through the electrolyte driven by the difference in oxygen potential over the cell. The fuel (here H_2 and CO) is oxidised at the anode and reacts with O^{2-} to form water or carbon dioxide. For the redox processes to be completed the electrons must be transported back to the cathode. As the electrolyte is electronically insulating the transport of electrons occurs via an external circuit, over which the electrical power is gained.

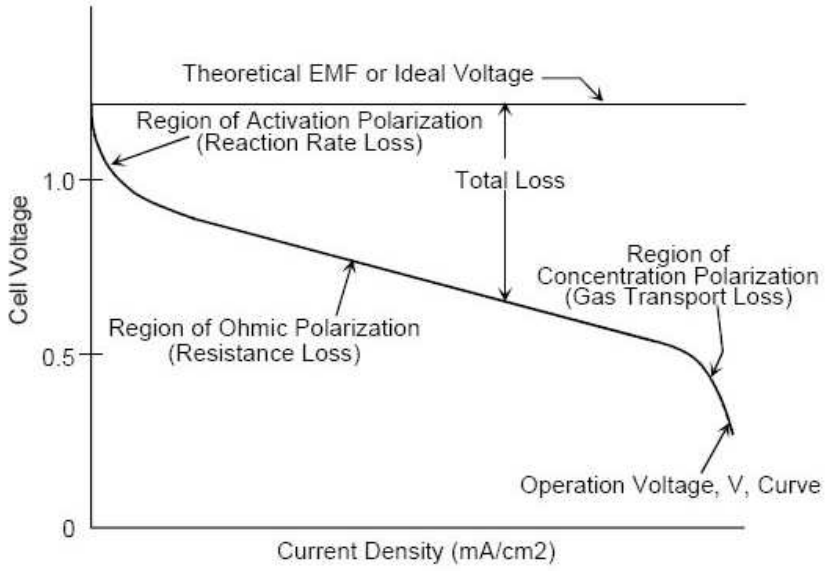

Figure 1.2: Cell voltage as function of current density of a fuel cell. The regions where the different losses are dominating are also marked. Close to open circuit voltage the resistance is mainly associated with the electrode reactions. At higher current densities ohmic losses becomes significant and at even higher current densities (and thus high fuel utilizations) gas transport starts contributing to the total voltage drop of the cell.

the choices of material of a conventional SOFC as well the reactions taking place at each of the electrodes.

1.2.1 Electrolyte materials

The conventional electrolyte is made of Yttria (Y_2O_3) Stabilised Zirconia (ZrO_2), abbreviated YSZ (typically 8 or 10 % Y_2O_3). YSZ is an electronically insulating oxide both in oxidizing and reducing atmospheres. It incorporates lattice defects in the form of missing oxide ions, so called oxygen vacancies. The oxygen vacancies allocate diffusion of oxide ions through the electrolyte which give rise to a relatively high oxide ion conductivity. The ionic conductivity can be improved by a factor of up to 10 by partial substitution of scandium. This material is unfortunately a relatively expensive metal. Gadolinium doped Ceria (CGO) is an alternative oxide ionic conductor, which is well studied within the field of SOFC. It has an substantially higher ionic conductivity than YSZ but shows also an electronic conductivity in reducing atmospheres (H_2) at operating temperatures, which gives rise to leak currents. In state-of-the-art cells CGO does however fill an important purpose as a barrier layer between the YSZ-electrolyte and the cathode to prevent reactions between these two components. Materials aspects of different electrolyte materials are summarised in [**?**].

1.2.2 Anode materials

The conventional anode is a cermet (ceramic-metallic composite) of metallic nickel and YSZ, where nickel provides the electronic conductivity and the catalytic activity, while YSZ provides the oxide ion conductivity. The anode is also required to have a porosity of 20-40 % to allow for mass transport of fuel to the reaction sites. The reaction is believed to take place at the so called three phase boundary (TPB), where the Ni- and YSZ phases meet the gas phase. In recent years research has also focused on finding new materials that is less susceptible to anode problems such as redox stability, degradation and poisoning. However it has been difficult to find a materials system with an equally high catalytic activity. The current status on anode materials for SOFC has been reviewed in [7].

1.2.3 The Cathode

The high temperature and oxidizing atmosphere limit the choice of cathode materials to oxides and the most popular materials belong to the family of perovskite-type oxides. This is due to the fact that a particularly broad spectrum of physical and chemical properties

can be obtained by carefully choosing the constituting metal ions. In technological cathodes the perovskite is mixed with an electrolyte material to form a composite in order to increase the oxide ion conductivity. The cathode also requires a porous microstructure to allow for mass transport of oxygen. The conventional cathode is the LSM/YSY composite where the strontium substituted lanthanum manganite, $La_{1-x}Sr_xMnO_3$, (LSM), provides the electronic conduction and the catalytic activity while the YSZ phase allocate the transport of oxide ions away from the reaction site. The reactions are believed to occur at the TPB.

1.2.3.1 Requirements

As an SOFC is to be operated at high temperatures, for long periods of time and should be able to withstand repeated thermal cyclings, a number of requirements are therefore must be met for a SOFC. For the cathode these include:

- High catalytic activity towards oxygen reduction.
- High electronic conductivity.
- High ionic conductivity.
- A thermal expansion coefficient (TEC) comparable to that of other SOFC-components.
- Low reactivity towards other materials used in the SOFC.
- High thermal stability.

Other requirements are optimised microstructure, low cost materials and mechanical strength.

1.2.3.2 State-of-the-Art materials

The LSM/YSZ cathode has proved to be reliable, durable and technologically compatible with other components in SOFCs. It is also sufficiently efficient at temperatures above ≈850 °C. However to make SOFC economically viable it is of great importance to lower the operating temperature to allow for cheaper interconnect materials as well as reduce the degradation problems. This has caused a push for new materials that are efficient, i.e. show low polarisation resistance, R_P, at low temperatures. Among the more promising candidate materials is LSC ($La_{1-x}Sr_xCoO_3$), which belongs to a category of oxides known as mixed ionic and electronic conductors (MIECs). This material has been shown to possess high electro-catalytic activity towards oxygen reduction.[8], [9], [10], [11] The electro-catalytic properties are promising and also maintained at low T due to an apparently low activation

energy of R_P. One reason for the high activity is its high mixed conducting properties which extends the reaction zone beyond the TPB and thus activates a larger fraction of the available surface area. However, this material has other problems, such as a high TEC, high reactivity towards YSZ and thermal instability. In order to avoid a TEC-mismatch with the rest of the cell cobalt has partially been substituted with iron into $(La_{0.6}Sr_{0.4})_sCo_{0.2}Fe_{0.8}O_{3-\delta}$ [12]. $(La_{0.6}Sr_{0.4})_sCo_{0.2}Fe_{0.8}O_{3-\delta}$ is generally considered the material of choice for the next generation of low temperature SOFCs. Even better cathode performance, i.e. low R_P, has been shown for the perovskite BSCF ($(Ba_{0.5}Sr_{0.5})_sCo_{0.8}Fe_{0.2}O_{3-\delta}$) but this material has been shown to be rather instable. [13]

1.3 Project motivation

As previously mentioned, there are many requirements on the SOFC-cathode that must be fulfilled for a commercialization of the technology to be viable. So far no material has emerged fulfilling all requirements and extensive research is ongoing in order to find such a material. Moreover, there is still very little fundamental knowledge on the physical and electrochemical processes taking place inside the oxygen electrode and the discrepancies in the literature are many. It is therefore of great importance to pursue the research on SOFC cathodes.

$La_{1-x}Sr_xCoO_3$ has been shown to be highly active towards oxygen reduction and partial substitution of cobalt with iron has been shown to improve at least one crucial property. What would happen if cobalt instead was partially substituted with nickel? Teraoka et. al. have argued that partial substitution on the B-site in $La_{1-x}Sr_xCoO_3$ always increases the catalytic activity.[8], [14] Partial substitution of cobalt with nickel has been shown to increase both electronic [15], [16] and ionic conductivity [17], [18], [19] as well as to decrease the thermal expansion coefficient. [20], [21] Huang *et al* [22] have studied the $(La_{1-x}Sr_x)_sCo_{1-y}Ni_yO_{3-\delta}$-system and measured a reduced polarization resistance when substituting 20% Sr on A-site with equal amounts of Ni on B-site in the high performing composition $La_{0.6}Sr_{0.4}CoO_3$. Despite these encouraging results when it comes to beneficial properties for SOFC applications, there is still very little published on the materials system $(La_{1-x}Sr_x)_sCo_{1-y}Ni_yO_{3-\delta}$. This PhD project has therefore focused on understanding the thermodynamic as well as the electrochemical properties of this materials system.

1.4 Objectives

The objectives of this project have been to:

- Gain fundamental knowledge on the thermodynamics of $(La_{1-x}Sr_x)_{0.99}Co_{1-y}Ni_yO_{3-\delta}$ including crystal and defect structure, electronic conductivity and lattice expansion.

- Gain fundamental knowledge on electrochemical behaviour of $(La_{1-x}Sr_x)_{0.99}Co_{1-y}Ni_yO_{3-\delta}$ when used as porous SOFC cathode, including electrode reaction behaviour and transport of oxygen across the gas-solid interface and trough the bulk.

- Develop a technologically relevant SOFC cathode that better meet the necessary requirements. We have specifically focused on developing a cathode that shows high electro-catalytic activity at low T.

Chapter 2

Theory

2.1 Thermodynamic properties

Essentially all properties that potentially makes $(La_{1-x}Sr_x)_sCo_{1-y}Ni_yO_{3-\delta}$ useful as component material in solid oxide fuel cells can be related to thermodynamics. The free energy as function of temperature and oxygen partial pressure, P_{O_2}, will determine not only phases and their crystal structures but also the electronic configuration, lattice defects and surface morphology/chemistry, all of which will have influence on the applicability of the material when used as a SOFC-cathode. In order to explain properties and trends thereof as well as develop new and better materials it is of fundamental importance to study and describe these structures as thoroughly as possible. Numerous reports exists revealing the thermodynamics of $LaCoO_3$. Also $(La_{1-x}Sr_x)_sCoO_{3-\delta}$ has received substantial attention when it comes to its intrinsic structural properties. However, for the doubly doped system, $(La_{1-x}Sr_x)_sCo_{1-y}Ni_yO_{3-\delta}$, little is known. This chapter recapitulate parts of the current knowledge of $LaCoO_3$ and $(La_{1-x}Sr_x)_sCo_{1-y}Ni_yO_{3-\delta}$ with respect thermodynamics. Focus will be laid on the structural characterizations of crystal, electronic, defect and surface properties. The idea of this thesis is partly to increase the thermodynamic knowledge of $(La_{1-x}Sr_x)_sCo_{1-y}Ni_yO_{3-\delta}$.

2.1.1 Introduction

Perovskite-type oxides have the general formula $ABO_{3-\delta}$ where A is typically a lanthanide or an alkali earth metal ion and B is a transition metal ion, positioned in the octahedral hole within the oxygen sublattice. δ is the oxygen nonstoichiometry factor reflecting lattice defects in the form of missing oxygen ions, so called oxygen vacancies. If this structure is to be formed depends mainly on two parameters, size and valency of the metal ions. Electro neutrality must always prevail which means that the total positive charge on the two metal ions must equal that of the oxygen ions. They can be combined as $A^{3+}B^{3+}O_3^{2-}$ (e.q.

$LaCoO_3$), $A^{2+}B^{4+}O_3^{2-}$ (e.q. $SrTiO_3$) or $A^{5+}B^{1+}O_3^{2-}$ (e.g. $NbLiO_3$). Electro neutrality can also be fulfilled by oxygen vacancy compensation if the net positive charge of the metal ions is less than 6. The ability of the perovskite to allocate such vacancies has strong influence on both thermodynamic and kinetic properties and is of great importance when these materials are considered for use in technological applications. The geometric criteria is that the A-site ion should have a Shannon radii close that of O^{2-} while the B-site ion should be small enough to fit into the the octahedral hole but still large enough to form bonds with the oxygen ions. This criteria is expressed as the Goldsmith tolerance factor, G_t, (see Equation 2.1). This tolerance factor must be between 0.8-1 for a perovskite structure to form. The ideal cubic structure is crystallized when this factor is close to one while differently distorted structure are formed when the factor is below one (and thus the B-site ion is "too big" for the octahedral hole). [23]

$$G_\mathrm{t} = \frac{r_A + r_O}{\sqrt{2}(r_B + r_O)} \tag{2.1}$$

There are many reports on the thermodynamics of pure and partially substituted $LaCoO_3$. Petrov *et. al.* have reviewed some of them in [24], which also covers thermodynamic studies on $(La_{1-x}Sr_x)_sCo_{1-y}Ni_yO_{3-\delta}$. The phase diagram of nominal $LaCoO_3$ as function of temperature and oxygen partial pressure is shown in Figure 2.1, which shows a decreasing P_{O_2}-range in which $LaCoO_3$ is stabile when increasing T. The reason is the reduction of cobalt taking place at increasing temperatures and decreasing oxygen partial pressures. This can to some extent be compensated by the formation of oxygen vacancies but will ultimately result in a decomposition into $La_4Co_3O_{10}$ and CoO. The thermodynamic stability range is narrow compared to parental oxides such as the manganite (eg. $LaMnO_{3-\delta}$).

Figures 2.1 plots further the phase diagram of $(La_{1-x}Sr_x)_sCoO_{3-\delta}$ at 1100 °C. It shows that the stability range decreases with increasing substitution of strontium on A-site. Sr-substitution introduces an extra positive charge on either the cobalt ions (oxidation) or on the oxide ion (which is effectuated as an vacancy). With cobalt being partially oxidised, the perovskite will have a higher potential to undergo a reduction process at higher T or lower P_{O_2}, thus the thermodynamic stability decreases with increasing Sr-content.

Figure 2.2 shows the crystal structures of $(La_{1-x}Sr_x)_sCo_{1-y}Ni_yO_{3-\delta}$ at 1100 °C in air. It concludes that only small levels of either nickel substitution in $(La_{1-x}Sr_x)_sCoO_{3-\delta}$ are possible if the single phase perovskite structure is to be maintained. $LaNiO_3$ has earlier been shown thermally instable above 825 °C [25]. This indicates that at lower temperatures higher substitutional level of nickel is possible. Still the narrow stability range restricts the compositions possible to research. This is associated redox behaviour of Ni^{3+}, which has an even large tendency to undergo reduction at high T or low P_{O_2} than Co^{3+}.

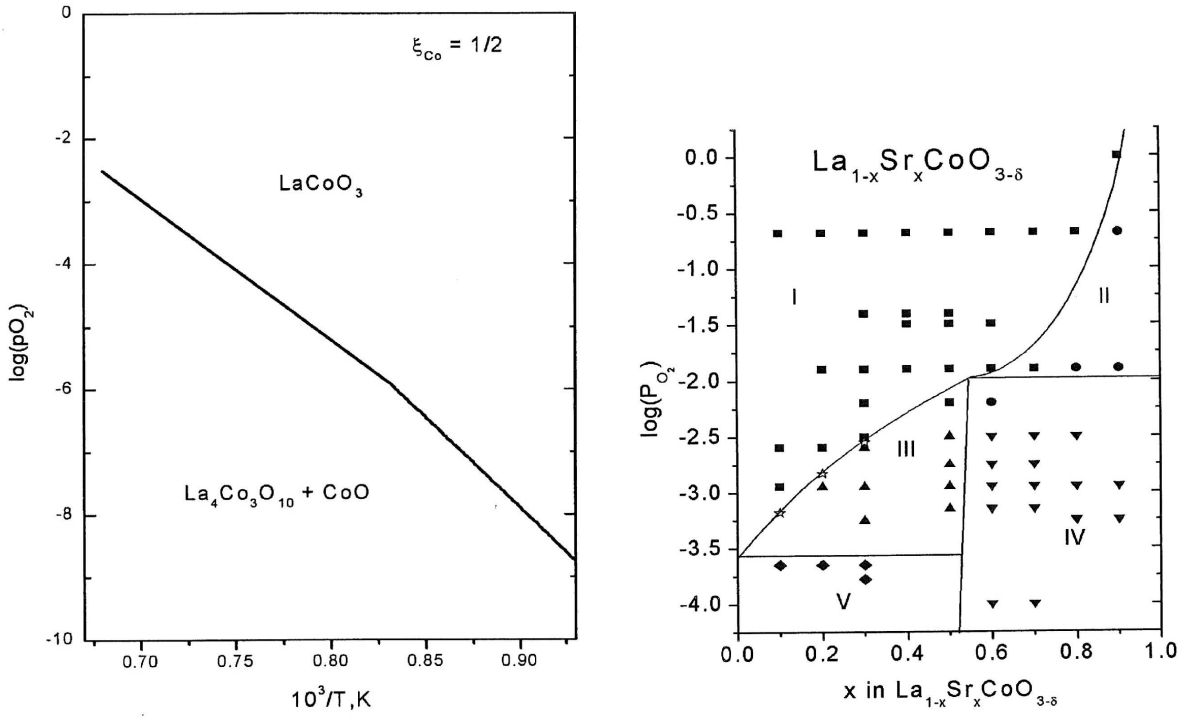

Figure 2.1: Left: Phase diagram of $LaCoO_3$ as function of temperature and P_{O_2}. **Right:** Phase diagram $(La_{1-x}Sr_x)_sCoO_{3-\delta}$ as function of P_{O_2} and x at 1100 °C in air. Region I represent the perovskite phase.

2.1.2 Crystal structure

Figure 2.3 shows the unit cell of the ideal cubic structure of perovskites-type oxides. The cell is face centered cubic (FCC) with the oxygen ions positioned on each face of the unit cell. The A-site ions are found at each of the eight corners and the smaller B-site ion within the center of the cell.

Perovskites are structured as closed cubic packed (CCP) (illustrated to the right of Figure 2.3) arrays of oxygen ions where every forth oxygen has been replaced by the A ion and where the smaller B ions occupy every forth octahedral site to form BO_6-octahedra, which are interlinked to form a 3-D network. The crystal constitutes of a 3-layered structure of the type ABCABC..., where repetitive FCC unit cells are found in the [111] direction and where the interplane distance is 1.633 $r_{O^{2-}}$.

A number of different distortions exist (eg tetragonal, orthorhombic, monoclinic) as a result of a mismatch between the radius of the B-site and the octahedral hole. One common distorted structure is the rhombohedral unit cell, which can be described as the two [100]-planes being shifted diagonally with respect to each other so that the rhombohedral angle, $\alpha < 90$ °C. The rhombohedral unit cell and hexagonal unit cell essentially describe the same crystal structure and the only difference is the definition of the lattice parameters. The structure is described in Figure 2.4 for $(La_{1-x}Sr_x)_sCoO_{3-\delta}$, where lattice parameters and atomic positions are designated. The rhombohedral unit cell will still arrange itself

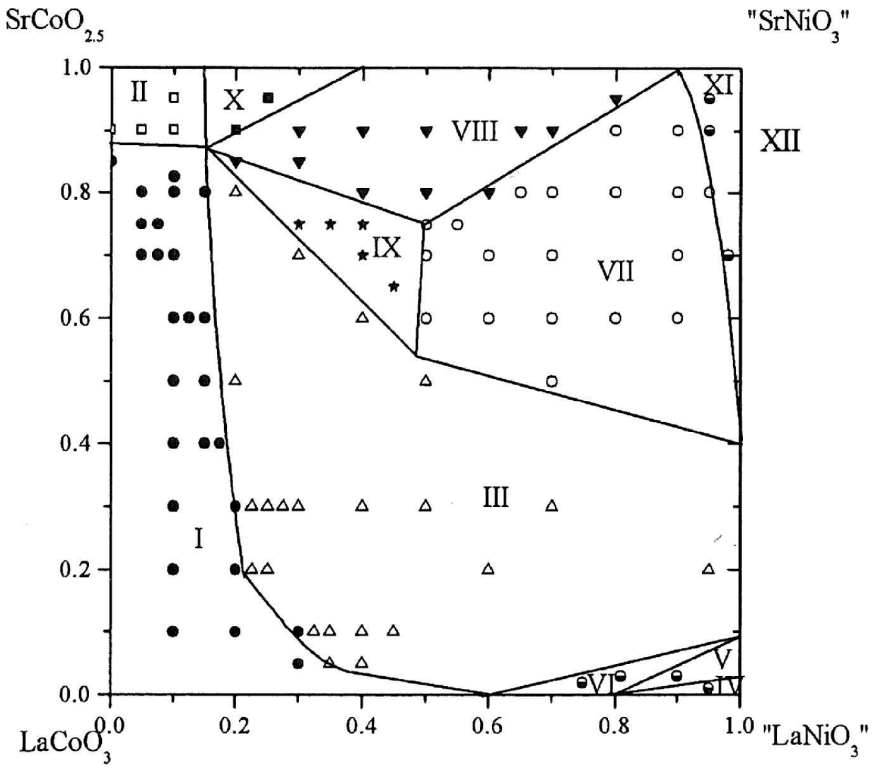

Figure 2.2: Psuedo Phase diagram of $(La_{1-x}Sr_x)_sCo_{1-y}Ni_yO_{3-\delta}$ as function of x and y at 1100 °C in air. Region I represent the perovskite phase. [26], [27]

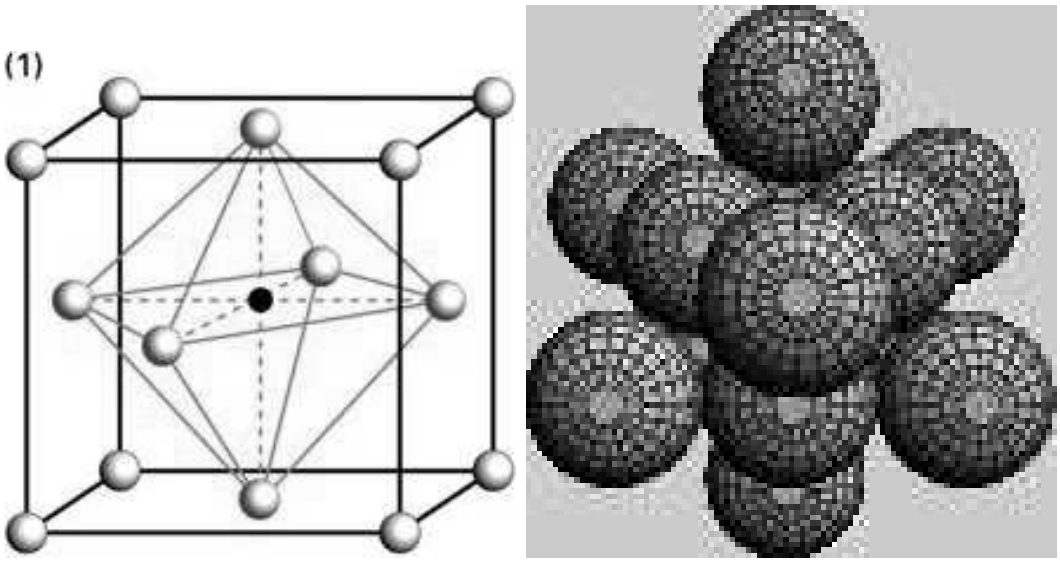

Figure 2.3: **Left:** The face center cubic (FCC) unit cell of the ideal perovskite structure. In the case of $LaCoO_3$, Co is situated in the center while O is placed on each of the six faces and La on each corner. **Right:** The CCP structure is formed by arranging the FCC unit cells in the repeating 3-layer assembly in the perpendicular direction (pointing towards you), where every the O and La ions are positioned in the triangular "hole" of the succeeding and preceding layers. Co is positioned in the octahedral hole.

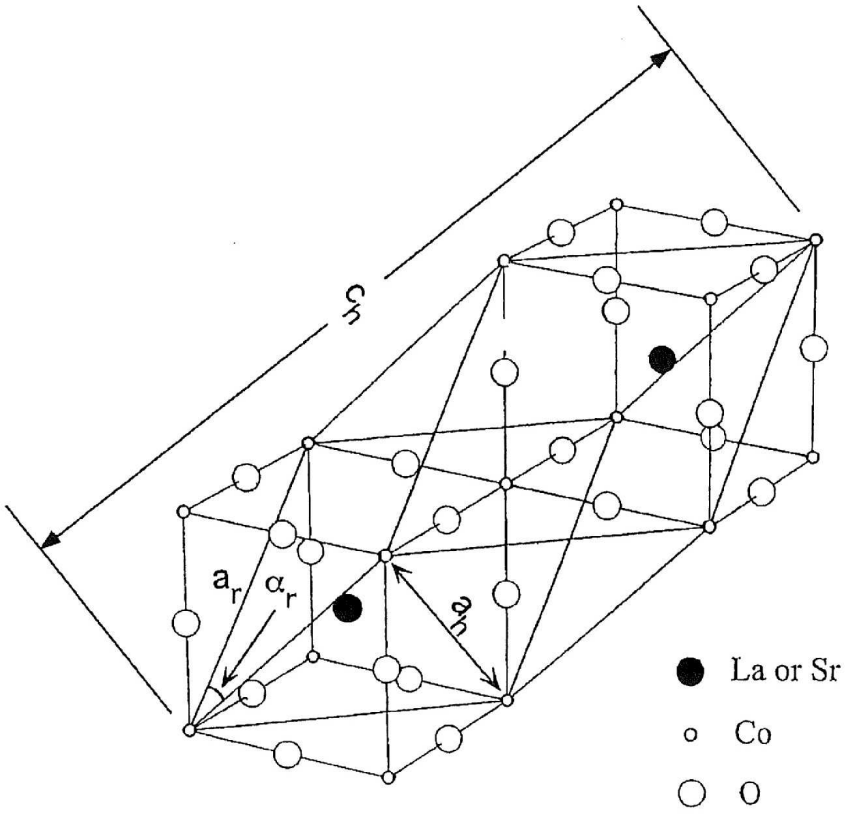

Figure 2.4: The rhombohedral structure of a perovskite where the rhombohedral unit cell parameters, α and a, are marked as well as the positions of the oxygen- and metal ions. The hexagonal lattice parameters, a_h and c_h, are also marked in the figure.

according to the cubic closed packed.

$LaCoO_3$ is known to have a rhombohedral structure with space group $R\overline{3}c$. Thornton et. al. [28] have measured the lattice parameters, bond lengths and angles accurately using neutron diffraction and found that $LaCoO_3$ maintains the $R\overline{3}c$ symmetry over the temperature region, 4-1248 K. Recently Maris *et. al.* [29] have shown neutron diffraction data suggesting a lowering of the symmetry of $R\overline{3}c$ to its monoclinic subgroup *I2/a* which means that the Co-O distance is three-fold degenerated. This structure was also supported using EXFAS measurements [30]. The origin of this structure could perhaps explained the Jahn-Teller distortion that has been observed in several studies [30], [31], [32]. This removes the degeneracy of the $e_\alpha e_\beta$ orbitals that are filled in the intermediate and high spin states of Co^{3+}. A subsequent chapter will look into this aspect in more detail.

The crystal symmetry of $LaCoO_3$ changes with increasing temperature from rhombohedral to cubic structure and the transition has been reported to occur at 1337 °C. [33] Replacing La with Sr in $(La_{1-x}Sr_x)_sCoO_{3-\delta}$ gradually changes the crystal structure from the rhombohedral, $R\overline{3}c$, to cubic structure, *Pm3m*, which is fully reached at room temperature for x=0.55.[34]. Mastin *et. al.*[35] argued this transition to occur at x=0.65 instead and showed

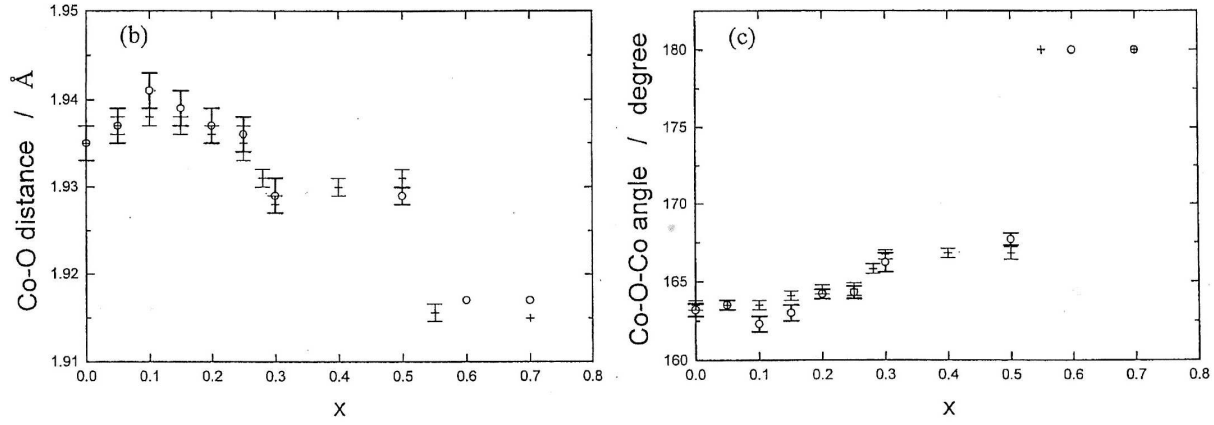

Figure 2.5: Co-O distances and Co-O-Co angles as function of x in $(La_{1-x}Sr_x)_sCoO_{3-\delta}$.

further that the transition temperature, T_c at which the crystal transforms from rhombohedral to cubic symmetry increase linearly with decreasing x.

Bond lengths in $(La_{1-x}Sr_x)_sCoO_{3-\delta}$ have also been measured by Mineshige *et. al.* [34], who observed abrupt changes in Co-O distance and the Co-O-Co angle at the rhombohedral to cubic transitions (x=0.55) but also at $x\approx0.25$, the same strontium level at which an insulator to metal transition occur (see Figure 2.5).

The crystal structure has been described as rhombohedral which transforms gradually with temperature towards a cubic phase [36]. This was later claimed by Huang et. al [37] to be an effect of entropy. However as the Goldsmidt tolerance factor for $LaNiO_{3-\delta}$ is close to 1, the rhombohedral structure has also been explained by a small oxygen substoichiometric crystal while the fully stoichiometric $LaNiO_3$ is in fact cubic.[38] Robert et. al. [39] have used neutron diffraction to show that substituting 20% Co with Nickel in $LaCoO_3$ maintains the the rhombohedral space group. It also showed that no transition occurs up to 700 K. Substituting 50 % or more Co with Ni in $LaCoO_3$ have also been shown to maintain the rhombohedral structure with lattice parameters decreasing with cobalt content [40], [41], [42]. Echigoya *et. al..* [43] have on the other hand found a phase transition from rhombohedral to orthorhombic with increasing nickel content, with a phase transition close to the composition $LaCo_{0.4}Ni_{0.6}O_{3-\delta}$. Huang et. al. [22] have studied the material system $(La_{1-x}Sr_x)_sCo_{1-y}Ni_yO_{3-\delta}$ and found that the rhombohedral angle α increases with nickel substitution and decreases with strontium substitution.

2.1.2.1 Lattice expansion

An important technological aspect is the lattice expansion as a too large expansion mismatch between component materials in SOFC can induce mechanical stresses and eventually mechanical rupture of the entire cell. Chen *et. al..* [44] have carried out the most thorough and accurate investigation of this property of $(La_{1-x}Sr_x)_sCoO_{3-\delta}$ by measuring thermal

and chemical expansion as function of P_{O_2} and temperature. The expansion coefficients were calculated by fitting data to a second-order multi-variable Taylor expansion around T and x_v, where $x_v = \delta/3$. The thermal expansion coefficient (TEC), calculated below 400 °C, was found to be almost independent on Sr doping (16-18 $\times$ 10^{-3}) for 0.2<Sr<0.7. Chemical expansion was shown to be dependent on oxygen vacancies irrespective of Sr content or temperature but was instead found to be related to the electron occupancy number (thus oxidation state of transition metal). They unsuccessfully tried to relate the chemical expansion coefficient to the ionic radius of the transition metal. A different theory was instead proposed, where the increase in bond length next to a vacancy is compensated by a reduced average bond length, which in turn induces a stress in the lattice. At higher vacancy concentrations the alioradiant cations may begin to cooperate spatially in an ordered way that reduces the stress and allows for the measured stoichiometric volume increase.

B-site substitution of nickel in $LaCoO_3$ has been reported to reduce the TEC of the end-member $LaCoO_3$ from $21 \cdot 10^{-6}$ to $11.9 \cdot 10^{-6}$ when doping $LaCoO_3$ with 60% nickel [15] while Echigoya *et. al.* [43] measured the TEC to 16-17$\cdot 10^{-6}$ for the compositions with 40-60 % Nickel.

2.1.3 Surface structure

As the electro-catalytic oxygen redox reaction take place at the surface of the electrode it is of importance to know the structure and chemistry of this surface. Unfortunately little is known of the surface structure of nominal and substituted $LaCoO_3$, especially at operating conditions. Only a few studies on surface structures have been published, most of them being based on computational modelling. Computational studies have calculated the energies of the three basic Miller indices [100], [110] and [111] of both relaxed and unrelaxed surface of $LaCoO_3$. The calculations hav eals obeen made for different terminations planes. [45], [46], [47] All studies point towards the same order of stability: [110]-(O) > [100]-(OLa) > [100]-(OCoO) > [111]-(LaOOO) > [111]-Co > [110]-(LaOCo), where the elements in the brackets are the constituting metal ions in the terminating plane. The order is for the relaxed surfaces, which have substantially lower energies compared to the unrelaxed ones. These studies have furthermore calculated the surface energies of $(La_{1-x}Sr_x)_sCoO_{3-\delta}$ with oxygen vacancies compensating strontium doping to maintain electro neutrality. The result showed that vacancies are energetically favored at the surface. Additionally, the vacancies are generally coupled to the positive defect (Sr^{2+} or Co^{2+}), which thus also tend to segregate to the surface. If the vacancy is associated with Sr^{2+} [110]-(O) is still the preferred surface structure followed by [111]-(LaOOO) where as if the vacancy is associated with Co^{2+} the preferred surface morphology is instead [100]-(OCoO) followed by [110]-(O). These structure are illustrated in Figure 2.6, which also schematically shows two fundamentally different catalytic mechanisms (supraficial and intraficial) of a perovskite oxide as described by Voorhaeve *et. al.* [48]

In the suprafacial mechanism, the surface provide an electronic structure and configura-

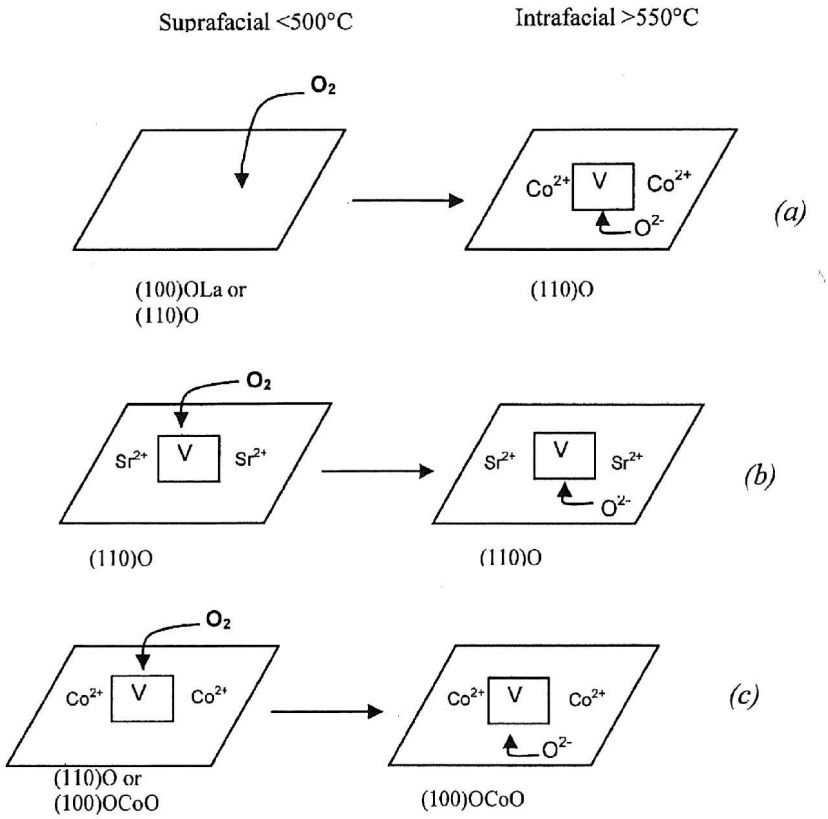

Figure 2.6: Illustration of the intrafacial and suprafacial reaction mechanisms occurring at differently terminated surface calculated in [47].

tion (atomic orbitals) that lowers the energy of transition states (see general textbooks in heterogeneous catalysis for further information). This allows for the reaction to proceed at an increased rate without a cyclic replenishment of the surface atoms. The intrafacial mechanism, in contrast, involves the incorporation of atomic oxygen into and the removal of oxygen ions from the lattice. This process is endothermic and thus requires high temperatures, however, it has also been shown to occur at much higher rates [49] as compared to suprafacial reactions, provided high enough temperatures. The degree to which the redox reactions occur with one of the two mechanisms depends on the temperature but also, as will be discussed in more detail in Chapter 2.2, on the defect structure of the electro catalyst. It is the intrafacial reaction that is of interest in for an cathode as oxygen is to be consumed under SOFC operation.

Segregation of strontium to the surface of $(La_{1-x}Sr_x)_sCoO_{3-\delta}$, annealed in oxygen at 800 °C, has also been measured experimentally using X-ray Photon Spectroscopy (XPS) [50], [51]. Fullarton and coworkers [52] have studied the related compound $Sm_{1-x}Sr_xCoO_{3-\delta}$ using Low Energy Ion Scattering (LEIS) and concluded an enrichment of strontium at the surface. They could also note a depletion of oxygen upon of strontium doping, which indicates an increase in oxygen vacancies associated with strontium ions, in agreement with modelling results. Teraoka et. al. [51] used XPS to argue that the surface of $(La_{1-x}Sr_x)_sCoO_{3-\delta}$ was enriched with A-site ions and especially with strontium, indicating its larger tendency to segregate to the surface. It showed further that the excess of strontium as compared to bulk stoichiometry decreased with increasing calcination temperature, explained as a result of Sr sublimation. This finding was also correlated with a decrease in catalytic activity with respect to oxygen reduction. Baumann et. al. [53] have measured an improved electro-catalytic performance by two orders of magnitude in $(La_{0.6}Sr_{0.4})_sCo_{0.2}Fe_{0.8}O_{3-\delta}$ micro-electrodes after 1V cathodic polarization for a few minutes. This was again correlated with an increased fraction of strontium at the surface measured by XPS.

2.1.4 Electronic structure

The applicability of an SOFC electrode depends also on the electronic properties of the material. $LaCoO_3$ is known to undergo spin transitions as function of temperature with subsequent changes in structural, electronic and magnetic properties as a result [54], [55], [56]. Senaris and Goodenough have published a thorough study on the electronic structure as function of x and T in $LaCoO_3$ and $(La_{1-x}Sr_x)_sCoO_{3-\delta}$. [57], [58] They argue that bulk cobalt are all low spin Co(III) between 0-35 K as the crystal field splitting energy is large enough to overcome orbital interactions (which disobeys Hund's rule). It undergoes a transition to reach a dynamic ordered semiconducting state consisting of 50% high spin Co^{3+} ($t_\alpha^3 t_\beta^1 e_\alpha^2$) and 50% low spin cobalt Co(III) ($t_\alpha^3 t_\beta^3$) prevailing over the region 110-350K. Recent studies have shown strong support that this transition is in fact from low spin to intermediate spin (IS) Co(iii) ($t_\alpha^3 t_\beta^2 e_\alpha^1$), which is stabilized by a Jahn-Teller distortion to remove the $e_{\alpha,\beta}$ degeneracy. [59], [60], [31], [61], [62]. The ordered array of intervening localised Co^{3+} and Co(III)/Co(iii) are thought to be stabilised by a periodic displacement of the oxygen ions, where low spin cobalt forms $(CoO_6)^{9-}$-clusters. Korotin *et. al.* [63] have instead

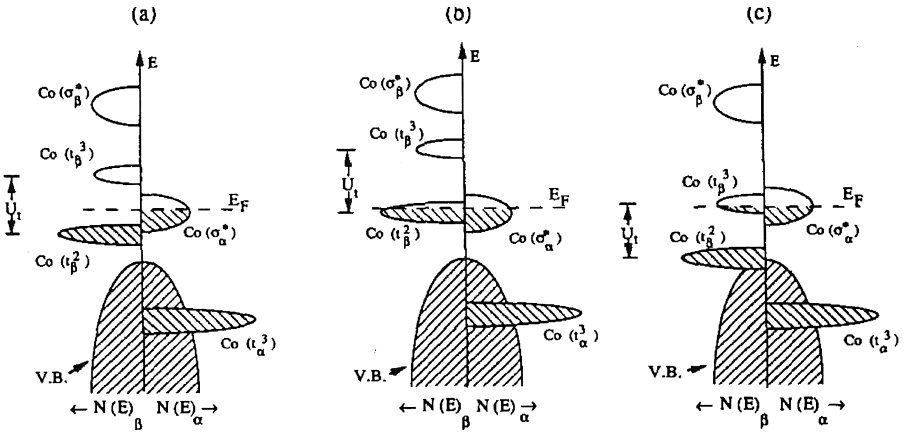

Figure 2.7: Band structure of $LaCoO_{3-\delta}$ where (b) and (c) represent illustrations of itinerant conduction bands set op by overlapping O-2s and Co-3d orbitals.[58]

suggested this ordering to be stabilized by the large hybridization of between O-2p and Co-e_g.

Conduction occurs through an excitation from the cluster π^*-orbital to an empty t_β state on Co^{3+}, where it is trapped to form a Co^{2+}. This band gap is small and the mobile hole migrates as thermally activated polarons, giving rise to a p-type semi-conduction. A second transition from 350-650 K, transform all low spin Co(III) into intermediate spin Co(iii) ($t^3_\alpha t^2_\beta e^1_\alpha$). Due to translational symmetry, e_α, of both Co(iii) and Co^{3+} electrons split into two itinerant orbitals by overlapping with the O-2p orbitals, where the upper band is positioned across the fermi level, which induces metallic conduction (illustrated in Figure 2.7). It must be stressed that the nature of spin transitions in $LaCoO_3$ is not yet fully understood and that the debate is ongoing. Zhuang *et. al.* [64] have argued that transitions only occurs to the HS-state but recent studies using XAS [59], neutron diffraction [60], infrared spectroscopy [31], magnetic susceptibility [32] local density approximation (LDA+U) calculations [63] have shown support for the transitions occurring to the intermediate spin state and that the electronic structure in cobalt is dominated by the Co(iii) at intermediate to high temperatures. Others [65], [66] stress the importance of taking all three state into account when modelling and explaining properties related to electronic structure in $LaCoO_3$

Doping $LaCoO_3$ with SrO into $La_xSr_{1-x}CoO_3$ introduces holes on low spin Co(IV), which dramatically changes the transport properties. Senaris and Goodenough [58] distinguish two region with different electronic properties (see Figure 2.8). Below the percolation threshold, x $\approx$ 0.2, (x $\approx$ 0.1 according to Caciuffo [67]) low spin, covalent Co(IV)O_3 are trapped at Sr^{2+} and form clusters with six surrounding high spin Co^{3+}. These are concentrated into "hole rich" regions, which are isolated in a "hole poor", insulating LaCo(III)O_3-like matrix. This long-range magnetic ordering was further supported by neutron diffraction and EXAFS measurements but the Co-ion is argued to be stabilized at intermediate spin state, which increases with strontium content.[68], [67], [69]. Potze et. al. have also argued for a stabilized intermediate spin state in $SrCoO_3$ using atomic multiplet calculations.[61] In the

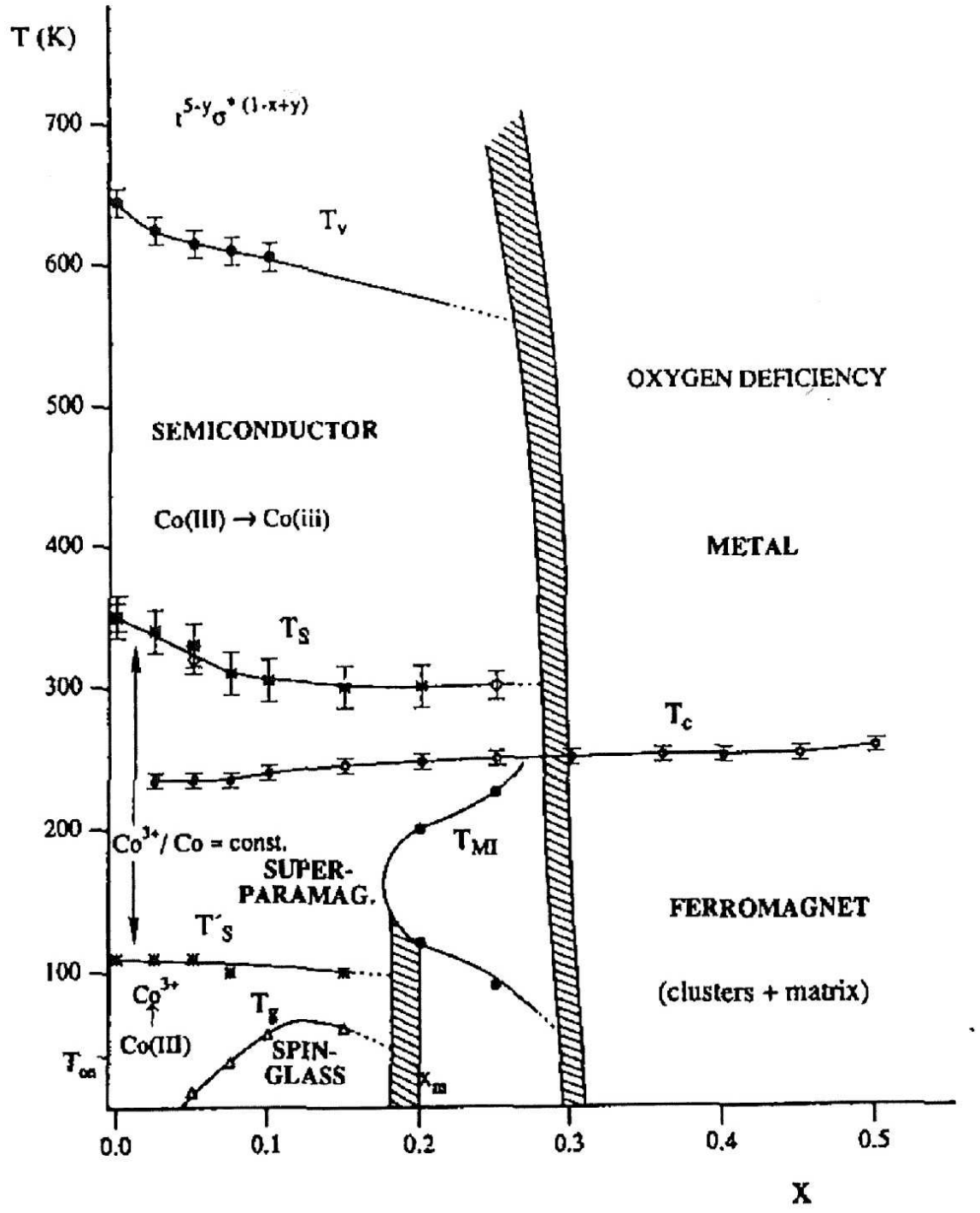

Figure 2.8: A "pseudo phase diagram" of spin states in $(La_{1-x}Sr_x)_sCoO_{3-\delta}$ as function of temperature and x.[58]

temperature interval (110-350K for $LaCoO_3$) where a semiconducting array of intervening Co(III)/Co^{3+} is established the cluster move by inter exchange of two t_β and two e_α between neighboring ions. Caciuffo et. al. [67] have explained this as a stabilisation of intermediate Co(iii) t_5e_1 by the low spin Co(IV)t_5e_0, where the e-electrons are delocalised within the "hole-rich" clusters. In fact a recent study have suggested that this transition progress to the intermediate spin state Co(iii). [70] This was also supported by Basker and Adler [71] who also showed that localised electronic states still exist up to about 700 °C

Above a critical temperature (650K for $LaCoO_3$) both Co(III) and Co^{3+} transform into Co(iii) allowing e-orbital interaction along the arrays resulting in itinerant electron orbitals (σ^*). A metallic-like state is reached with an increased electronic conductivity due to an increase in charge carrier concentration. Furthermore, the transition temperatures are lowered with x due to an enhanced covalent overlap between O-$2p_\sigma$ and Co-e. Above the percolation threshold metallic conduction is established at all temperatures. Two oppositely competing mechanisms above room temperature exist where spin-disorder scattering reduces conductivity and transformation into Co(iii) increases it. At higher temperatures, Co^{IV} is reduced and an average electronic configuration can be expressed as $t_2^{5-y}\sigma^{*(1-x-y+2\delta)}$, where y=Co^{3+}.

$LaNiO_3$ is claimed to be in a low spin Ni(III) state ($t_\alpha^3 t_\beta^3 e_\alpha$) with an overlap between O-2p and Ni-3d orbitals that transform the e_α orbital into a narrow itinerant conduction band σ^*, rendering $LaNiO_3$ metallic character. [72] Nickel substitution in $LaCo_xNi_{1-x}O_3$ appears to suppress the Co(III) $\rightarrow$ Co^{3+} transition which for x=0.7 does not initiate until above 300 °C. [16] The electronic conductivity is mainly carried by the narrow itinerant conduction band of the Ni-arrays. Only below the percolation threshold, $x \gtrsim 0.7$, does $LaCoO_3$ start dominating conductive properties.

Zaanen, Sawatzky and Allen [73] have developed a model (ZSA-model) to outline the band gap structure of transition metal compounds such as $(La_{1-x}Sr_x)_sCoO_{3-\delta}$ and to explain the electronic structure and properties. The theory is illustrated in Figure 2.9 and predicts two types of insulators depending on if the charge transfer band gap is between metal 3d bands (Mott-Hubbard insulator) or between O-2s and Metal-3d (charge tranfer insulator). The oxide will become metallic if any these band gaps is smaller than the bandwidth, W. A few studies [54], [74] have shown that $LaCoO_3$ is charge transfer insulator, which becomes metallic at higher temperatures or when La is partially substituted with Sr as $(La_{1-x}Sr_x)_sCoO_{3-\delta}$. This occurs by filling states within the band gap (Δ), which in turn broaden the band to overlap with the Co-3d band, forming a conduction band. Torrance *et. al.* [75] have also used this theory to explain why $LaNiO_3$ has metallic character at room temperature. The importance of these band structures and the occurrence of a conduction band in $(La_{1-x}Sr_x)_sCoO_{3-\delta}$ will be dealt with further in Chapter 2.2.

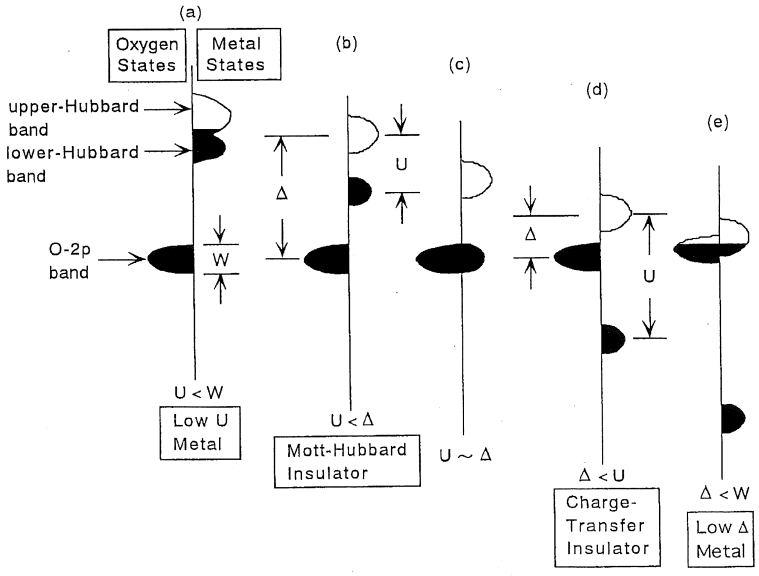

Figure 2.9: The ZSA model describing the two different kinds on oxide insulator, Mott-Hubbard insulator and Charge-Transfer insulator.[73]

2.1.5 Defect structure

Crystal defects are lattice irregularities where an ion has either been replaced by a different kind (extrinsic substitution), is missing completely (Schottky defect) or squeezed into an interstitial position (Frenkler defect). The Kröger-Vink defect notation has been developed in order to describe defect reaction and equilibria more easily. Each reactant or product is written in the form A_B^C, where A is the ionic specie (V in case of a vacancy), B is the position of the defect (the ion it has replaced, if any) and C is the the effective charge ($\bullet$=positive and $\prime$=negative). An oxygen vacancy is thus written $V_O^{\bullet\bullet}$.

Defect reactions and equilibria are generally under two conservation requirements. The structural requirement of a perovskite implies that the ratio $(O+V_O^{\bullet\bullet})/(A+B)$ always equals 3. This means that e.g. an extrinsic substitution of an A-site inevitably results in the removal of another A-site ion or by the addition of one B-site ion and 3 oxygen ion. This requirement does not hold for Frenkler defect but these defect are on the other hand very scarce in perovskites.[23] The second conservation requirement is the charge neutrality. Based on these criteria the general defect reaction can be written as:

$$\sum_i \nu_i A_i = 0 \tag{2.2}$$

where ν_j is stoichiometric coefficient of the$j$th reaction component, A. These reactions will at each condition (P_{O_2} and T) strive to reach thermodynamic equilibrium, expressed as:

$$\sum_i \mu_i A_i = 0 \tag{2.3}$$

where μ_j is chemical potential of the jth reaction component, A. These Equations holds also for defects and thus defining a defect model is essentially the work of defining thermodynamic expressions for the chemical potential of each reaction specie and solving these equations. The defect properties of perovskites are often explained by the use of different dilute point defect models where the defects are assumed to be non-interacting.

Mizusaki *et. al.* [76] have studied the defect structure of $(La_{1-x}Sr_x)_sCoO_{3-\delta}$ using thermograviometry. They have concluded that $(La_{1-x}Sr_x)_sCoO_{3-\delta}$ is fully stoichiometric (ie δ=0) at room temperature for $x \leq 0.3$ and substitution of strontium is instead compensated electronically by oxidation of cobalt. At higher temperatures or lower oxygen partial pressures cobalt is reduced to a lower valency which creates oxygen vacancies according Equation 2.4 (as a result of the electro-neutrality principle).

$$2Co_{Co}^{\cdot} + O_O^X \rightarrow 0.5O_2(g) + V_O^{\bullet\bullet} + 2Co_{Co}^X \tag{2.4}$$

Several different models exist which aim at describing this reaction. Petrov *et. al.*. [77], [24] have developed the most extensive point defect model for, which also integrates "defect cluster" and was argued to hold also for non-dilute systems, where x>0.01, (see Equation 2.5). The authors assume $[Sr_{La}^{\cdot}(unassociated)]$ is independent on temperature and that the right term in the bracket is much larger than one.

$$[Sr_{La}^{\cdot}(unassociated)] = [Co_{Co}^{\bullet}]\left(1 + 2K_{V_0}\frac{[Co_{Co}^{\bullet}][O_O^X]}{[Co_{Co}^X]^2}P_{O_2}^{-0.5}\right) \tag{2.5}$$

Point defect models assume non-interacting localized defects. This is not likely a valid assumption for the apparent metallic like perovskite-type oxides , $(La_{1-x}Sr_x)_sCoO_{3-\delta}$, as discussed in the previous chapter. Substantial evidence exists for a partially filled conduction band in $(La_{1-x}Sr_x)_sCoO_{3-\delta}$ (thus delocalized electronic defects) and point defect models have therefore received criticisms. Lankhorst and coworker [78], [79], [80] have instead developed a model referred to as *the itinerant electron model* to describe oxygen defects in $(La_{1-x}Sr_x)_sCoO_{3-\delta}$ and related compounds. It is based on the oxidation reaction (see Reaction 2.6) and the equilibrium condition (see Equation 2.7). It couples further the electrochemical potential of oxygen with the density of state at the fermi level, i.e. the electrochemical potential of electron in the conduction band.

$$O_2^{gas} + 2V_O^{\bullet\bullet} \rightleftarrows 2O_O^X \tag{2.6}$$

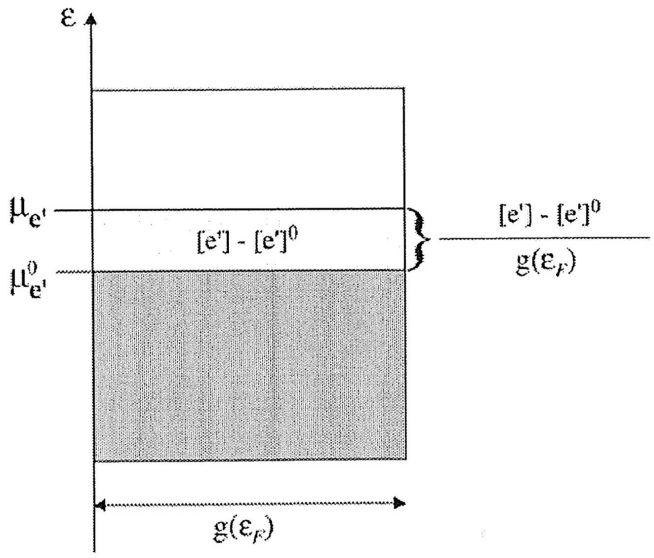

Figure 2.10: The gas rigid band model, where a change in chemical potential is effectuated by a shift in the fermi energy, whereas the entropy is fixed.

$$\mu_{O_2}^{gas} + 2(\mu_{V_0^{\bullet\bullet}} - \mu_{O_O^X}) + 4\mu_{e'} = 0 \tag{2.7}$$

The model assumes a (i) conduction band to which electrons are donated upon reduction, (ii) that there is no electrostatic interactions between oxygen vacancies (ideally diluted) and (iii) that electron entropy is negligible. The last assumption is referred to as the gas rigid band model [81] and can be sketched as shown in Figure 2.10. This allows for the normal logarithmic expression of the chemical potential of lattice oxygen and vacancies described in Equation 5.2.

$$\mu_k = \mu_k^0 + RTln[K] \tag{2.8}$$

K is the mole fraction of lattice oxygen and oxygen vacancies ($V_O^{\bullet\bullet}$). The electron occupancy number,i.e. the fraction of electrons in the conduction band can be approximated by assuming no thermal excitation above the Fermi level as expressed in Equation 2.9 (no Fermi-Dirac distribution).

$$[e'] \approx \int_{\epsilon=\epsilon_B}^{\epsilon=\epsilon_T} g(\epsilon)f(\epsilon)d\epsilon \approx \int_{\epsilon=\epsilon_B}^{\epsilon=\epsilon_F} g(\epsilon)d\epsilon \tag{2.9}$$

ϵ_B, ϵ_T and ϵ_F are the energies at the bottom top and fermi level respectively. g(ϵ) and f(ϵ) are the density of states and Fermi-Dirac distribution. The chemical potential of the electrons

(which is the same as the Fermi level) can be approximated by Taylor expansion of Equation 2.9 leading to Equation 2.10.

$$\mu([e']) = \epsilon([e']) = ([e']^0) + \frac{([e'] - [e']^0)}{g(\epsilon_F)} \tag{2.10}$$

where $[e']^0$ is the electron occupation at δ=0 and x=0. Recognizing the electro-neutrality principle ($([e'] - [e']^0) = 2\delta$) and inserting Equations 2.10 and 5.2 into 2.7 results in the following equilibrium condition.

$$\mu_{O_2}^{gas} = \mu_{O_2}^{oxide} = E_{oxide} - TS_{oxide} + 2RTln\left(\frac{[O_O^X]exp\left(\frac{-4[V_O^{\bullet\bullet}]}{RTg(\epsilon_F)}\right)}{[V_O^{\bullet\bullet}]}\right)$$

where E_{oxide} and S_{oxide} are energy and entropy associated with filling two vacancies with an oxygen molecule from vacuum and simultaneously adding four electrons at the fermi level. The energy and entropy of oxygen incorporation can be identified as.

$$\epsilon_{O_2}^{ox} = E_{oxide} - \frac{8[V_O^{\bullet\bullet}]}{g(\epsilon_F)} \tag{2.11}$$

$$s_{O_2}^{ox} = S_{oxide} + 2Rln\left(\frac{[O_O^X]}{[V_O^{\bullet\bullet}]}\right) \tag{2.12}$$

Noteworthy is that neither $\epsilon_{O_2}^{ox}$ nor $s_{O_2}^{ox}$ is dependent on temperature. Other defect models exists [24], [82] but the itinerant electron model has received the greatest acceptance and is often used in theoretic models relating thermodynamics and kinetics. [83]

An important phenomena associated with oxygen vacancies is super-structured micro-domains, which have been reported to form at high strontium levels (x>0.5 in $(La_{1-x}Sr_x)_sCoO_{3-\delta}$) [84], [85] but possibly also at low P_{O_2} or high T. Van Doorn et. al. [86] have studied these feature in more detail using transition electron microscopy (TEM), selected area electron diffraction (SAED) and parallel electron energy loss spectroscopy (PEELS). They found that oxygen vacancies in micro-domains of $La_{0.3}Sr_{0.7}CoO_{3-\delta}$ are ordered along the [001] planes resulting in an average cobalt valency of $Co^{+2.7}$, where as the normal domains are fully stoichiometric ($\delta = 0$ and $Co^{+3.7}$). Oxygen vacancy ordering was also found for $(La_{0.6}Sr_{0.4})CoO_{3-\delta}$ below a smooth transition around 790-840 °C [87]. The authors measured a steadily decreasing ionic conductivity with time (2 orders of magnitude over about 400 hours) at 750 °C after annealing at 1160 °C, an effect they attributed to this transition. Also others have reported detrimental effects on ionic conductivity as a result of vacancy ordering [8].

2.2 Kinetic and oxygen transport properties

$LaCoO_3$ was early recognized as a catalytic material for oxygen reduction in high temperature ceramic devices such as solid oxide fuel cells (SOFC), membranes, sensors etc [88]. The technologically more relevant compound $(La_{1-x}Sr_x)_sCoO_{3-\delta}$ has improved its catalytic properties, partly by an increased electronic conductivity due to the p-type doping. More importantly is, however, the increased concentration of oxygen vacancies at the surface and in the bulk, which are believed to accommodate both active site for catalysis and transport of oxygen ions towards the electrolyte interface. Due to these beneficial properties $(La_{1-x}Sr_x)_sCoO_{3-\delta}$ and related mixed ionic and electronic conducting perovskites show promising results when used as SOFC cathodes. MIECs have therefore been studied extensively over the last decades (see ref [89] and references therein) in order to clarify the mechanism of the oxygen reduction reaction as well as to find a material that better meets the criteria of a SOFC cathode. Despite all the effort, no consensus have been reach as to how this reaction proceeds and which of the numerous elementary reaction(s) are rate limiting.[90], [91], [92], [83], [93] This chapter will briefly discuss the key processes occurring in a MIEC as well as the overall reaction mechanism when such a material is employed as cathode in a solid oxide fuel cell. Special focus will be laid on the lanthanum cobaltite based perovskites. The oxygen reduction reaction has been discussed in numerous paper over the years and many of these papers were reviewed thoroughly in [89] to which to reader is referred for detailed discussions.

2.2.1 Introduction

The overall reaction path occurring within an mixed conducting cathode of a solid oxide fuel cells has been the subject of an ongoing debate for more than 20 years. Takeda and coworkers [94] were one of the first to study oxygen reduction in different mixed conducting oxides. They found an improved performance of $(La_{1-x}Sr_x)_sCoO_{3-\delta}$ as compared to the related perovskites such as LSM ($(La_{1-x}Sr_x)_sMnO_{3-\delta}$). They also outlined the different possible reaction paths in a mixed conducting cathode (see Figure 2.11) which since then have been the basis for the mechanistic discussions of oxygen reduction on MIECs.

In cathodes where the electronic and ionic conductivities are restricted to two separate phases (such as in the conventional LSM/YSZ electrode) the oxygen reduction reaction is believed to occur in the vicinity if the so called three phase boundary (TPB), where they both meet the gas phase. [95] In single phase mixed ionic and electronically conducting (MIEC) cathodes oxygen reduction can in principle take place anywhere on the surface, extending the available catalytic area well beyond the TPB. This has been shown by Baumann *et. al.*. [96], [97] who have measure the impedance on geometrically well defined micro-electrodes produced with lithography techniques. The result showed that whereas the electrode resistance scaled with the diameter of the $(La_{1-x}Sr_x)_sMnO_{3-\delta}$ electrode, the same trends could not be observed for the mixed conducting $(La_{0.6}Sr_{0.4})_sCo_{0.2}Fe_{0.8}O_{3-\delta}$

electrode. this electrode showed instead a large capacitance, which could only be explained by oxygen stoichiometric change within the bulk. This in turn strongly indicated that a larger fraction of the surface was involved in the oxygen surface exchange. The extended reaction zone depends on a number of factors which have been modelled and discussed in a number of papers [98], [99], [100], [101]. The overall reaction can in principle be divided in two different categories, transport of charge (electronic conduction, ionic conduction and charge transfer from electrode to electrolyte) and the chemical reaction itself (often referred to as the oxygen surface exchange).

A number of papers have reported that the surface exchange rate is in general limiting the overall reaction in an mixed conducting SOFC cathode. Kawada et. al. [102] measured the surface exchange rate, k_{ex}, by O_{18}-isotope exchange/SIMS experiment as function of T and P_{O_2} in $(La_{0.6}Sr_{0.4})CoO_{3-\delta}$. Activation energies and P_{O_2}-dependencies compared well to those of k_{ex} when extracted mathematically from measured electrode impedance on dense $(La_{0.6}Sr_{0.4})_{0.99}CoO_{3-\delta}$. The literature is in fact full of data showing the electrode resistance increases with decreasing P_{O_2}. This value would have been positive if the electrode had been dependent on oxygen ion diffusion as the oxygen vacancies increase with decreasing P_{O_2}.

In the conventional LSM/YSZ electrode the resistance is often attributed to a charge transfer process where oxygen ions are transported across the electrode/electrolyte interface.[95] However, measured capacitances of mixed ionic electronic conducting electrodes are often orders of magnitude higher ($1 - 10^{-3}$ Fcm^{-2}) than what is expected if the charge transfer reaction was rate limiting the process ($\approx 10^{-6}$ F cm^{-2}). This indicates that charge transfer processes are not likely the rate limiting process of resistance of a MIEC electrode.

On the other hand, electrochemical impedance spectroscopy often shows several features, usually interpreted as overlapping semicircles originating from different electrochemical processes. Thus under a DC-limit more than one process can contribute to the overall electrode resistance. It can therefore be misleading to assume that the complex scheme of reactions and processes occurring within the cathode of a solid oxide fuel cell is only limited by one step (i.e. the bottleneck principle is too simple). Many workers find a high frequency response (often rather small but still existing) when measuring the impedance of mixed conductors as SOFC-electrode, a response which they attribute to a charge transfer between the electrode and the electrolyte.[96], [103]. The major impedance response occurring at lower frequencies have, as already mentioned, often been attributed to the surface exchange. However a few authors [104], [98], [105] have stressed a coupling of the surface reaction with a transport process (eg bulk or surface diffusion). This coupling of an electrochemical and a chemical process have been shown to lead to an impedance expression referred to as Gerischer impedance, which resembles a finite diffusion impedance (see Appendix). It is often difficult to distinguish a Gerischer-type impedance from the ordinary semicircular impedance of an RQ-circuit. Also other more complicated equivalent circuits model have been derived for the impedance response of mixed ionic and electronic conductors, in which the bulk path is argued to play a dominant role.[106], [107]

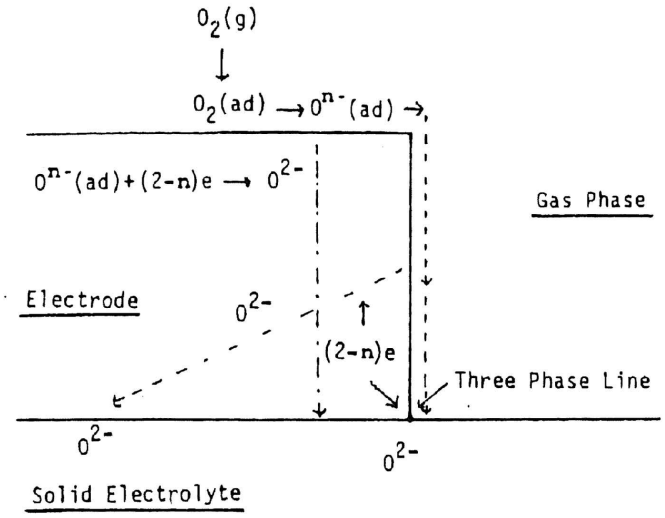

Figure 2.11: Overall reaction model in a porous mixed conducting SOFC cathode. [94]

2.2.2 Charge transport

2.2.2.1 Electronic conductivity

The electronic conductivity of $(La_{1-x}Sr_x)_sCoO_{3-\delta}$ is very high for being an oxide. It is generally not considered rate limiting the overall reaction, however, fundamental understanding of the conductive behavior of a material is still of great importance when it is to be used in an electrode. The electronic conductivity of $(La_{1-x}Sr_x)_sCoO_{3-\delta}$ is closely related to the electronic structure, outlined in the previous chapter. At lower temperature strontium substitution will be electronically compensated by electron holes (oxidation of cobalt) which gives rise to a *p*-type conductivity. At increasing temperature cobalt is reduced, which decreases the hole concentration at the same time as the oxygen vacancy concentration increases. On the other hand spin transitions from low spin (LS) to a higher spin (IS or HS) will increase the itinerant conduction band. Phonon scattering and crystallographic phase changes will contribute further to make up a rather complicated temperature dependence.

Mizusaki *et. al.* [108] and Petrov *et. al.* [109] have studied the electronic conductivity of $(La_{1-x}Sr_x)_sCoO_{3-\delta}$ as function of T, P_{O_2}, x using 4 point dc measurements. The studies showed a small polaron conduction behaviour for x < 0.3 with a decreasing temperature at which the conductivity reaches its maximum. Mizusaki found further that σ is dependent on rhombohedral angle as well as the oxygen nonstoichiometric parameter, δ, but surprisingly independent on x when δ=[Sr]/2 ,i.e. no *extrinsic* charge carriers. Mineshige *et. al.* [110] have measured the electronic conductivity as function of P_{O_2} and T and showed a metal-

insulator transition at x=0.25 at room temperature. Measurements of the conductivity in $La_{0.7}Sr_{0.3}CoO_3$ after different annealing conditions (temperature and cooling rate) found this transition to increase if the oxygen vacancies are retained upon an increased cooling rate. They also showed that this transition can occur in samples with x>0.3 if the P_{O_2} is low (below 10^{-3}). Both studies found that $(La_{1-x}Sr_x)_sCoO_{3-\delta}$ is p-type conductor as the conductivity decreased with P_{O_2}. Sitte *et. al.* [111] have measured the electronic conductivity in $(La_{0.6}Sr_{0.4})CoO_{3-\delta}$ and $(La_{0.4}Sr_{0.6})CoO_{3-\delta}$ at different T and P_{O_2}, from which they calculated isostoichiometric activation energies at different δ, a parameter which was shown to increase with δ and was close to typical small polaron activation energies. [22] Søgaard *et. al.* have derived the hole mobility in $(La_{0.6}Sr_{0.4})CoO_{3-\delta}$ and found it to be inversely proportional to T if fitted to the Equation 2.13. This indicate that the conductivity of $(La_{0.6}Sr_{0.4})CoO_{3-\delta}$ has metallic character, in accordance with studies of its electronic structure (see earlier chapter).

$$\sigma = C_1(C_2 - \delta)\frac{\mu_0}{T} \tag{2.13}$$

Huang et. al. [22] have measured the electronic conductivity of a selected number of compositions within the system $(La_{1-x}Sr_x)_sCo_{1-y}Ni_yO_{3-\delta}$. It showed a 50% increase in conductivity when doubling the nickel content from 10 to 20 % in $(La_{1-x}Sr_x)Co_{0.9}Ni_{0.1}O_{3-\delta}$; x<0.3. The data was fitted to the small polaron conduction (see Equation 4.3) below T=600 °C and from the their different activation energies, the author concluded that trapping of hole at Sr^{2+} affects the conduction behaviour. Also the charge disproportionation between cobalt and nickel (see Equation 2.15) were assumed important as the redox potentials of the respective redox couple Co^{IV}/Co^{iii} and Ni^{III}/Ni^{2+} are close.

$$\sigma(T) = pe\mu_{\mathrm{p}} \sim \frac{A}{T}exp\left(\frac{-E_A}{kT}\right) \tag{2.14}$$

$$Co^{iii} + ni^{III} \rightleftarrows Co^{IV} + Ni^{2+} \tag{2.15}$$

Seebeck measurements on $La_{0.99}Co_{0.6}Ni_{0.4}O_{3-\delta}$ and $La_{0.99}Co_{0.4}Ni_{0.6}O_{3-\delta}$ showed that conduction are of p-type along the cobalt arrays while it is of n-type along the nickel arrays. The motion enthalpy was also found larger along the cobalt arrays, which indicate a lower mobility as compared to the nickel. This in agreement with the wider itinerant conduction band in $LaNiO_3$ as compared to $LaCoO_3$ as discussed in the previous chapter. On the other hand both Echigoya et. al.[43] and Hrovat et. al. [15] measured the highest electronic conductivity in $La_sCo_{1-x}Ni_xO_{3-\delta}$ for x=0.4-0.6 at all temperatures.

Decreasing the oxygen partial pressure will increase vacancies, associated with the ionic conductivity, at the expense of the hole concentration, associatied with the electronic conductivity, thus these bulk transport properties are intimately correlated. This phenomena has been modelled electrochemically by Jamnik and Maier [106], [107], who have derived a

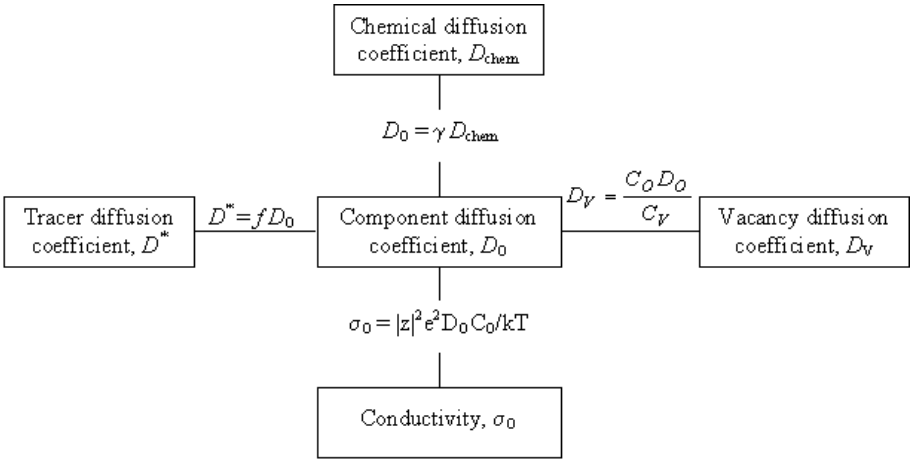

Figure 2.12: Schematic illustration of the different diffusion coefficients and how they relate to the ionic conductivity.

"chemical capacitance" to couple the transport resistance of the two species, e^- and $V_O^{\bullet\bullet}$. This capacitance is proportional to the bulk volume and much higher than the electrochemical capacitance occurring at interfaces, a fact that is helpful also in mechanistic analysis [112].

2.2.2.2 Ionic conductivity

The ionic conductivity is generally much lower than the electronic in a MIEC (often by an factor of at least 1000) and can under certain conditions limit the rate of the overall reaction in a solid oxide cathode. The conduction is believed to occur via diffusion of oxygen vacancies under a chemical or electrical gradient. The equations for the transport of oxygen ions are outlined in [113] to which the reader is directed for further details. A large number of studies have tried to measure the diffusion coefficient as function of T, x and P_{O_2} in $(La_{1-x}Sr_x)_sCoO_{3-\delta}$. The diffusion coefficients are generally measured using either relaxation techniques (see [114]), which gives a chemical diffusion coefficient, D_{chem} or by the O^{16}/O^{18}-isotope exchange/SIMS which results in a tracer diffusion coefficient, $D^\star$. These are correlated to the vacancy diffusion coefficient and the ionic conductivity as illustrated in Figure 2.12.

f is the form factor determined by Ishihara to be about 0.65-0.69 for a number of related perovskites.[115] γ is the thermodynamic enhancement factor, which in the case of oxygen ions is defined as:

$$\gamma = \frac{1}{2}\frac{\partial ln P_{O_2}}{ln C_O} \tag{2.16}$$

Preis *et. al.* [116] measured the diffusion coefficient by relaxation measurements and found that D_{chem} was independent on P_{O_2}, explained as a counterbalanced result of vacancy formation and defect ordering. This is in agreement with results from Kawada *et. al.* [102] and van Doorn *et. al.* [117] who used isotopeexchange/SIMS and Wang *et. al.* [118] who used relaxation measurements to study this process. It disagrees however with a study Sitte *et. al.* [111] which measured an increase in D with P_{O_2} for the composition $(La_{0.4}Sr_{0.6})CoO_{3-\delta}$. The ionic conductivity have also been measured more directly by the use of flux measurements and by the use of the Wagner Equation. Chen *et. al.* [119] measured ionic conductivity through a dense membrane of $La_{0.3}Sr_{0.7}CoO_3$ and concluded that it is independent on P_{O_2} in agreement with above discussions. Wang *et. al.* [118] argue that the relaxation is faster at higher final partial pressures and that the absolute value of D_{chem} is dependent on whether it is subjected to oxidation or reduction.

The results in literature show sometimes relatively large discrepancies, which could be due to different techniques employed or differently treated samples. For instance Carter *et. al.* [120] measured the E_A of $D^\star$ for $La_{0.8}Sr_{0.2}CoO_3$ to 60.5 kJmol^{-1} using SIMS/Isotope exchange whereas De Souza et. al. [121] measured E_A of the same compound and with the same technique to 214 $\pm$ 6 kJmol^{-1}. There is further a trend that the activation energy decreases with strontium content. Wang measured the activation energy (E_A for D_{chem} to 133 kJmol^{-1} for $La_{0.5}Sr_{0.5}CoO_3$ in air, in agreement with $D^\star$ measured by De Souza et. al.[121] (136 $\pm$ 2 kJmol^{-1}). Ishigaki *et. al.*. have measured E_A of the tracer diffusion coefficient in $La_{0.9}Sr_{0.1}CoO_3$ [122] 270$\pm$ 38 while Routbort et. al. [123] measured E_A to 232 $\pm$ 8 kJmol^{-1} in $La_{0.9}Sr_{0.1}CoO_3$ used the same technique. The activation energy consists of the enthalpy of migration and enthalpy of association (defect formations). Calculations based on non-stoichiometry data by Ishigaki and coworkers suggested the enthalpy of vacancy formation to be dominant for compositions with low Strontium content ie $La_{0.9}Sr_{0.1}CoO_3$ and $LaCoO_3$ but also that this enthalpy will decrease with increasing Sr-content. This could in such case partly explain the observed trend.

2.2.2.3 Solid state charge transfer

The transfer of oxygen ions from the electrode to the electrolyte can be of significance to the overall reaction rate if (a) the region at which this process occur is small (such as the TPB in the LSM/YSZ electrode) or if (b) electronically insulation impurities or reaction products hinder the transfer across the interface. This charge transfer process is generally not believed to be rate limiting in $(La_{1-x}Sr_x)_sCoO_{3-\delta}$ electrodes as the mixed conductivity expands the transfer region to a much larger fraction of the electrode/electrolyte interface. It was early found, however, that $(La_{1-x}Sr_x)_sCoO_{3-\delta}$ reacts with YSZ to form Sr_2ZrO_2 and $La_2Zr_2O_7$ which have very poor conductivity [124], [125], [126]. These reactions have prohibit $(La_{1-x}Sr_x)_sCoO_{3-\delta}$ to be used directly on YSZ and enforced CGO barrier layers to be used in between the cathode the the YSZ electrolyte. No reactions between these phases have so far been reported at reasonable processing and operating conditions. Skinner

[127] has on the other hand stressed the importance of taking into account reaction between $(La_{1-x}Sr_x)_sCoO_{3-\delta}$ and additives and inevitable impurities in the CGO phase.

2.2.3 Oxygen reduction

The most complex and least understood process in the overall SOFC-cathode mechanism is the oxygen reduction reaction. This process is often referred to as the surface exchange of oxygen, perhaps because we still don't know which of the many elementary reactions is rate limiting the overall reaction and in which order they occur. The surface exchange reaction is generally believed to consist of the following sub reactions (not elementary): O_2-adsorption (2.17), O_2-dissociation (2.18), incorporation of oxygen species into the the oxide lattice (2.19) and the reduction of either diatomic or mono-atomic oxygen species (2.18-2.19).

$$O_2(g) + ne^- \rightarrow O_{2,ads}^{n-} \tag{2.17}$$

$$O_{2,ads}^{n-} + me^- \rightarrow 2O_{ads}^{(n+m)-} \tag{2.18}$$

$$O_{ads}^{(n+m)-} + (2-n-m)e^- + V_O^{\cdot\cdot} \rightarrow O_O^X \tag{2.19}$$

The reduction reaction is generally considered to proceed simultaneously with the other reactions to form arbitrarily charged surface species e.g. $O_{2,ads}^{n-}$, O_{ads}^{n-} or O_O^{n-}, depending on which reaction is the rate-limiting step. De Souza et. al. found a remarkable linear relationship between the effective surface exchange coefficient and the oxygen diffusion coefficient measured over large range of mixed conducting materials, temperatures and P_{O_2}s. Merkle et. al. [92], [128] have argued the incorporation step to be rate limiting based on this correlation. As these processes are of Arrhenius-type there is also a linear relation between their respective activation energies, where the activation energy of vacancy diffusion is strongly related to enthalpy of vacancy formation. Based on these recognitions, the authors conclude that oxygen vacancies must take part in the rate limiting step and that this could only be interpreted as that the incorporation process is the rate limiting step. This ionization is further argued to occur simultaneously as the surface oxygen specie is fully oxidized.

Such a reaction mechanism with a simultaneous incorporation/oxidation reaction (see Equation 2.19) as rate limiting step was early proposed by van Takeda *et. al.*. [94] for $(La_{1-x}Sr_x)_sCoO_{3-\delta}$ and later supported by van Doorn et. al. [117] on $La_{0.3}Sr_{0.7}CoO_3$ who combined the P_{O_2} dependance of the oxygen adsorption (which is 0.5) and oxygen vacancies formation (measured by Mizusaki to 0.07 [76]) to find a total P_{O_2} dependance of 0.43 for incorporation reaction, which agreed reasonably well with their measured value of 0.41. Wang et. al. measured the same P_{O_2}-dependance to 0.40±0.05 and 0.44±0.04 for $La_{0.5}Sr_{0.5}CoO_3$ at 620-650 °C but only 0.30±0.02 for 700 °C and stressed the difficulty in extracting mechanistic information from such simple discussions. Yang et. al. found the same P_{O_2} dependance on oriented [100] surface of $La_{0.5}Sr_{0.5}CoO_3$ to be 0.31 at 750 °C using EIS. The discrepancies found in literature could arise from differently treated samples but also from different mechanism occurring under different conditions.

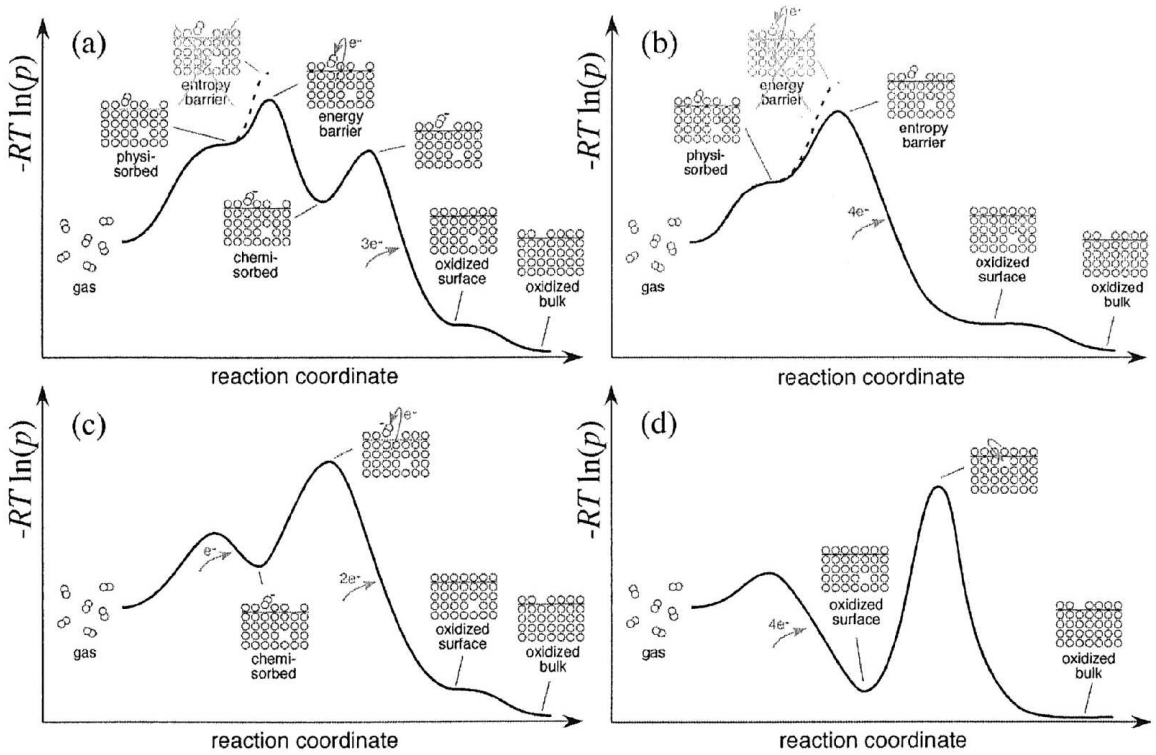

Figure 2.13: Reaction mechanism for incorporation of gaseous oxygen into the lattice of a mixed conducting oxide with four different steps being rat-limiting. Increasing -RTln(p) reflects a less probably configuration. (a) chemisorption-limited: the rate-limiting steps is adsorption and the reaction follows a typical energy barrier with as superoxide O_2^- as transition state. (b) Dissociative-adsorption-limited: the rate-limit step is the dissociation of physisorbed O_2 where the barrier is solely entropic as it requiring two adjacent surface oxygen vacancies (low probability). (c) Dissociation-limited: the rate-limiting steps is the dissociation of the chemisorbed superoxide, which involves a energy barrier when the second oxygen reacts to form a bond. (d) incorporation-limited: exchange of vacancies between the bulk and the surface is rate-limiting while O_2 (g) equilibrates fast with the surface. [83]

Adler et. al. have thoroughly modelled oxygen exchange kinetics on mixed conducting surfaces [83] at non-equilibrium conditions by the use of the *itinerant electron model* and by the construction of neutral building units, which have well defined chemical potential, independent of electronic states. Driving forces for the reactions 2.17, 2.18, 2.19 are identified from which rate expression are derived for each of these reactions being rate-limiting (while the others are quasi-equilibrated). Four different scenarios are considered as shown in Figure 2.13 namely chemisorption-limited (a), Dissociative-adsorption-limited (b), Dissociation-limited (c) and incorporation-limited (d). Comparing the theoretical rate expression of these four limiting cases with experimental data from van der Haar et. al. [129] over a vide range of T, P_{O_2} and x in $(La_{1-x}Sr_x)_sCoO_{3-\delta}$ revealed that the mechanism limited by dissociative adsorption (b) was clearly most consistent with measured data. The authors argue that the adsorption occurs only at two adjacent surface oxygen vacancies and thus that the observation that surface vacancies play a crucial catalytic role does not ultimately imply incorporation step as rate limiting. This topic is still an open question.

Chapter 3

Synthesis and powder characterization of $(La_{1-x}Sr_x)_{0.99}Co_{1-y}Ni_yO_{3-\delta}$

3.1 Abstract

This is an introductory result chapter that includes a crystallographic analysis of 22 compositions within the materials system $(La_{1-x}Sr_x)_{0.99}Co_{1-y}Ni_yO_{3-\delta}$. It also evaluates two synthesis routes in terms of powder characterization and performance when these powders are utilized as porous SOFC-cathodes. It presents further interesting electrode behaviour, which will discussed in more detail in subsequent chapters. We have found an approximate total substitutional level of 40-50 % NiO and/or SrO using the Glycine-Nitrate and still maintaining a single phase perovskite type oxide. The microstructure, ie particle size and specific surface area, of the the different powders with compositions; $(La_{1-x}Sr_x)_{0.99}Co_{0.6+x}Ni_{0.4-x}O_{3-\delta}$ $< x < 0.4$; were fairly similar despite the different crystallite size and structure. The chapter lays the ground for further investigations of thermodynamic and electrochemical properties of $(La_{1-x}Sr_x)_sCo_{1-y}Ni_yO_{3-\delta}$.

3.2 Introduction

Perovskite type oxides is a well established family of ceramic materials used in a wide range of applications including, sensors, catalysts and superconductors.[23] Several synthesis methods have been developed to produce ceramic compounds.[130], [131], [132], [133], [134], [135] We will in this chapter study two fundamentally different synthesis routes, one explosive, water-based method and one dry, low temperature method. The Glycine Nitrate Combustion (GNC) synthesis [130] is a rapid high temperature process (a combustion temperature of above 1000 °C) that produces relatively small particles. Metal nitrate are mixed the required stoichiometric ratio into water based solution to which glycine is added as a fuel. The

drawback of GNC is the required calcination step due to carbon residuals formed as a consequence of incomplete combustion of glycine. The High Energy Ball Milling (HEBM) is a room temperature technique in which precursor oxides are milled to form the perovskite structure. Hard and fast rotating stainless steel balls provide high local pressure at the point of impact. This delivers enough energy to the material being milled for a reaction to take place.[136], [137] This means that it does not require any subsequent heat treatment.
Gavrilova et al.[138], [26], [27] have investigated the perovskite homogeneity range in the $(La_{1-x}Sr_x)_sCo_{1-y}Ni_yO_{3-\delta}$ materials system. These studies demonstrated a rather narrow single phase region for the perovskite type oxide. The study used the solid state method where the precursor oxides were repetitively pressed, sintered at 1100 °C and grind. The oxide samples were quenched from 1100 °C.
This chapter aims at finding a suitable synthesis route as well as the single phase region of powder samples of $(La_{1-x}Sr_x)_sCo_{1-y}Ni_yO_{3-\delta}$ produced using the GNC process without repetitive high temperature heat treatments. It investigates further powder characteristics of the selected acquired samples.

3.3 Experimental

Powders of 22 different compositions within the perovskite system $(La_{1-x}Sr_x)_{0.99}Co_{0.6+x}Ni_{0.4-x}O_{3-\delta}$ were synthesized using the glycine-nitrate combustion route, described in detail in [130]. As a nominally stoichiometric A/B ratio of 1 is practically impossible to synthesize, traces of secondary oxide phases are inevitable. We have for that reason deliberately chosen an A/B-ratio of 0.99 in order to know which types of secondary phase to expect. Metal nitrates of($La(NO_3)_3{\cdot}6H_2O$, $Sr(NO_3)_2$, $Co(NO_3)_2{\cdot}6H_2O$ and $Ni(NO_3)_2{\cdot}6H_2O$) were disolved in deionized water and mixed with glycine to give a glycine to nitrate molar ratio of 0.548. The obtained solution was first stirred and heated to approximately 200 °C in order to evaporate water and to form a gel. The gel was heated further to approximately 300 °C where it self-ignited and initiated a vigorous exothermic reaction, which produced fine black powders. The powder was successively ball-milled for 24 hours. All compositions found in Figure 3.1 have been calcined at 1250 °C with a slow cooling rate of 20 °Ch^{-1}. 7 compositions (see Table 3.1) were consecutively heat treated in air at 350 °C, 650 °C, 950°C and 1250 °C for 12 hours with a ramp rate of 20 °Ch^{-1}. Five compositions were isostatically pressed into pellets at 325 MPa for 30 seconds and sintered at 1250 °C for 12 h with a ramp rate of 100 °Ch^{-1}. The sintering was repeated once with a cooling rate of 20 °Ch^{-1}.

The composition $(La_{0.8}Sr_{0.2})_{0.99}Co_{0.8}Ni_{0.2}O_{3-\delta}$ was also synthesized using the High Energy Ball Milling (HEBM) technique were motion force provides the energy required for the reaction to take place. This allows the perovskite structure to form without calcination at elevated temperatures. Prior to mixing, La_2O_3 was heated to 500 °C in order to dry possible traces of $LaOH_3$ into pure lanthanum oxides. La_2O_3, NiO, Co_2O_3 and $Sr(NO_3)_2$ were mixed in a stoichiometric ratio corresponding to $(La_{0.8}Sr_{0.2})_{0.99}Co_{0.8}Ni_{0.2}O_{3-\delta}$. The mixture was placed in a the milling equipment (Fritsch Pulverisette 4 varioplanetary)

comprising a 250 ml tungsten carbide vial and 9 Ø20 mm tungsten carbide balls of 58 g each. A counterweight of similar mass and dimensions as the vial was used to keep the ball mill balanced during operation. The main plate rotational speed was set to 400 rpm, while the vial had a rotation of 640 rpm in the opposite direction. The milling was interrupted every hour for 30 min in order to keep the temperature low. Total reaction time was 36 hours.

The specific surface area (SSA) was measured using BET-analysis (nitrogen adsorption/desoprtion measurements) in an Gemini 2360 V2.01. All samples were degassed at 300 °C for 24 hours before the BET analysis. SSA was calculated between 0.05-0.21 of relative N_2-pressures (p/p_0) of the adsorption isotherm. A STOE Theta-Theta diffractometer (40kV, 30 mA) with Cu K_α -radiation was used for powder x-ray diffraction (XRD) measurements. Powder samples were scanned with 2Θ ranging from 20-60° with 0.05° incremental steps.

Symmetric cells of the two differently synthesized powders of $(La_{0.8}Sr_{0.2})_{0.99}Co_{0.8}Ni_{0.2}O_{3-\delta}$ were fabricated using a 200 μm dense $Ce_{1.9}Gd_{0.1}O_{1.95}$ (CGO10) tape as electrolyte. A slurry with approximately 11 g perovskite powder, 15 g ethanol and 1 g PVP was mixed and ball-milled for about 24 hours. The particle size distribution was measured after ball-milling with an LS13320 laser diffraction particle size analyzer. The slurry was sprayed onto both sides of the electrolyte and sintered at 950 °C for 2 h. The spraying and sintering procedures were repeated twice in order to fabricate a symmetric cell with approx. 25 μm thick electrodes. The cells were cut to dimensions of 4.0×4.0 mm^2 and painted with platinum paste to serve as current collectors. Four identical cells were measured with Electrochemical Impedance Spectroscopy (EIS) under open circuit voltage from 1Mhz - 0.01 Hz with a Solartron-1260 frequency response analyzer at temperatures from 600-900 °C with an amplitude of 75 mV. A Zeiss Supra 35 Scanning Electron Microscope (SEM) was used to study the microstructure of the powders and the symmetric cells.

3.4 Results

3.4.1 Powder characterisation

Figure 3.1 shows a pseudo phase diagram of 22 different compositions within the $(La_{1-x}Sr_x)_sCo_{1-y}Ni_yO_{3-\delta}$ materials system, qualitatively assessed using powder X-ray diffraction (XRD) in air at room temperature. The XRD was performed on dry powder after calcination and 24 hours of ball-milling. A more detailed analysis of the lattice parameter as function of compositions and temperature will be given in a subsequent chapter for a selected number of perovskites. In this chapter we will only investigate the compositions that will be single phased after the calcining the GNC-powder at 1250 °C with a cooling rate of 20 $°Ch^{-1}$. The results showed an increasing difficulty to synthesize a single-phased perovskite with increasing levels of strontium when 15 % Co has been replaced with Ni (i.e.

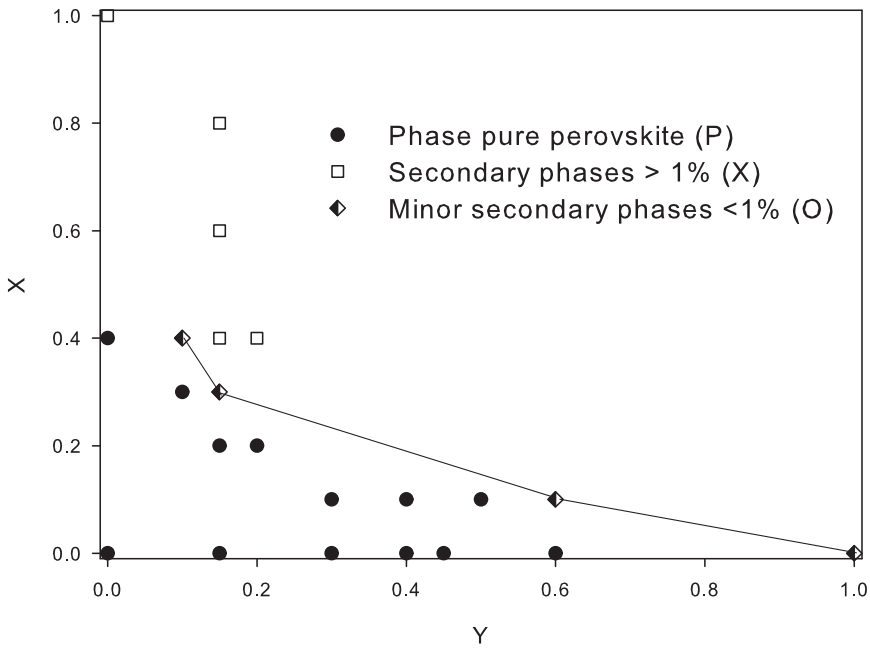

Figure 3.1: Room temperature *pseudo* phase diagram of $(La_{1-x}Sr_x)_{0.99}Co_{1-y}Ni_yO_{3-\delta}$ measured in air. The symbols represent a semi quantitative assessment of the levels of secondary phases. Representative XRD-diffractograms for the different notations are found in Figure 3.2.

increasing x in $((La_{1-x}Sr_x)_{0.99}Co_{0.85}Ni_{0.15}O_{3-\delta})$. Figure 3.1 indicated an upper limit of 40 % Sr substitution when 15 % nickel is present on the B-site. Conversely, the nickel substitution seems to be limited to 50 % when 10 % Sr is present on the A-site. Figure 3.2 shows three XRD diffractograms of $(La_{0.8}Sr_{0.2})_{0.99}Co_{0.8}Ni_{0.2}O_{3-\delta}$, $(La_{0.6}Sr_{0.4})_{0.99}Co_{0.8}Ni_{0.2}O_{3-\delta}$ and $(La_{0.9}Sr_{0.1})_{0.99}Co_{0.4}Ni_{0.6}O_{3-\delta}$, which represent compositions considered single phased, containing minor secondary phases (<1%) and containing major secondary phases (>1%) respectively. Generally only small amounts of secondary phases were present when substituting with large amounts of nickel and keeping the strontium level low or at zero. These compositions consisted exclusively of K_2NiF_4-type oxides and CoO and/or NiO. The levels of secondary phases increased dramatically with x in $(La_{1-x}Sr_x)_{0.99}Co_{0.85}Ni_{0.15}O_{3-\delta}$.

The phase purity of some selected compositions after calcination at four different temperatures was also assessed semi-quantitatively by observing the possible existence of secondary phase peaks and their relative intensity (see Table 3.1). XRD-analysis after calcination at the lowest temperature, 350 °C, showed evidence of large amounts of different carbon residuals in all compositions. This temperature did not appear to be sufficiently high for full combustion of carbonaceous materials. The non-perovskite peaks corresponded mainly to strontium carbonates, $Sr(CO_3)$. For some compositions e.g. $SrCoO_{3-\delta}$, these carbonates were retained also after heat treatment at 1250 °C. Only calcination temperatures at and

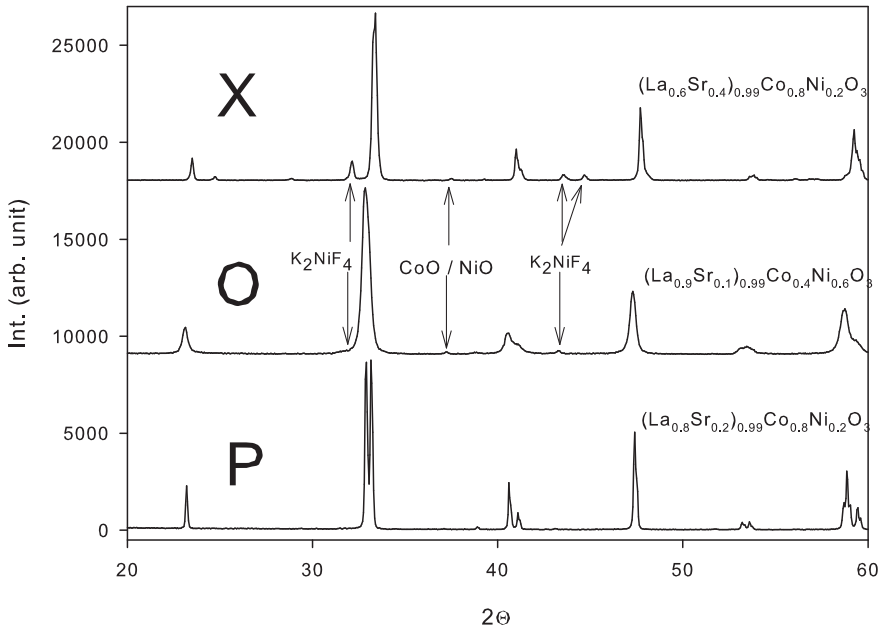

Figure 3.2: X-ray diffractogram of three compositions representing the notation of levels of secondary phases in Figure 3.1. X is considered ta have $> 1\%$ secondary phases, O is considered ta have minor secondary phases $< 1\%$ and P considered to be phase pure.

above 650 °C are reported in Table 3.1. Calcination at 650 °C acquired pure oxides, however, traces of secondary oxide phases were seen in the XRD of all compositions. These oxides appeared to be of the type $La_{2-x}Sr_xCo_{1-x}Co_{1-y}Ni_yO_4$ and $Co_{1-y}Ni_yO$. For compositions without strontium a temperature of 950 °C was sufficient to acquire a single phase perovskite. However, when containing strontium these secondary phases were retained also after calcination at 950 °C and only disappeared completely in the XRD diffractogram after heat treatment at 1250 °C. In $(La_{1-x}Sr_x)_{0.99}Co_{0.85}Ni_{0.15}O_{3-\delta}$ with $x \geq 0.4$, traces of secondary phases were present even after calcination at 1250 °C. The amount of secondary phases increased dramatically with increasing Sr-content.

Table 3.2 lists a semi-quantitative assessment of possible secondary phases in dense sintered samples, which have been cooled from 1250 °C with two different rates. XRD-analysis indicated rather large differences, where a rapid cooling rate (100 $°Ch^{-1}$) resulted in significant amounts of secondary phases while the samples cooled at a slower rate (20 $°Ch^{-1}$) appeared single phased in XRD.

Figure 3.3 shows SEM images of the powder microstructure of the compositions $La_{0.99}Co_{0.6}Ni_{0.4}O_{3-\delta}$ and $(La_{0.6}Sr_{0.4})_{0.99}CoO_{3-\delta}$. The particles of both composition appeared to have diameters of approximately 200-500 nm. However the particles of $(La_{0.6}Sr_{0.4})_{0.99}CoO_{3-\delta}$ appeared to consist of smaller crystallites which had sintered or

Table 3.1: Semi quantitative assessment of possible peaks from secondary phases seen in XRD of the $(La_{1-x}Sr_x)_{0.99}Co_{1-y}Ni_yO_{3-\delta}$-system at three different temperatures. P = Pure perovskite structure. Numbers refers to intensity of the main peak of K_2NiF_4-type (at $\sim 2\Theta$) phase relative to the [110] perovskite peak (at $\sim 33\ 2\Theta$).

X	0	0	0	0	0.1	0.2	0.4
Y	0	0.15	0.3	0.45	0.3	0.15	0.15
650 °C	1	1	2	4	5	4	20
950 °C	P	P	P	P	1	1	5
1250 °C	P	P	P	P	P	P	4

Table 3.2: Semi quantitative assessment of possible secondary phases in dense, sintered samples which have been subsequently heat treated at 1250 °C for 12 h twice with different cooling rates. Notations are the same as in Table 3.1

X	0	0.1	0.2	0.3	0.4
100 °C h^{-1}	2	3	4	2	1
20 °C h^{-1}	P	P	P	P	P

almost melted into the larger particles. The crystallites of $La_{0.99}Co_{0.6}Ni_{0.4}O_{3-\delta}$ appeared to be larger than those of $(La_{0.6}Sr_{0.4})_{0.99}CoO_{3-\delta}$ and seemed to have sintered less. Powder SEM analysis of $(La_{1-x}Sr_x)_{0.99}Co_{0.6+x}Ni_{0.4-x}O_{3-\delta}$, $0 \geq x \geq 0.4$, showed that the tendency with a decreased crystallite size and an increased sintering increased gradually with increasing x in $(La_{1-x}Sr_x)_{0.99}Co_{0.6+x}Ni_{0.4-x}O_{3-\delta}$. A third feature is the clear facets of the crystallite surface seen explicitly in Figure 3.3a. The degree of faceted surface structures seemed to decrease as x increased in $(La_{1-x}Sr_x)_{0.99}Co_{0.6+x}Ni_{0.4-x}O_{3-\delta}$.

$$d_{\text{avg}} \approx \frac{\kappa \cdot \lambda}{\beta \cdot cos(\theta)} \tag{3.1}$$

d_{avg} is the average particle size, κ is the shape factor (normally κ=0.9), λ is the wavelength of the X-ray radiation (here λ=0.154 nm), β is the peak width at the half peak maximum and θ is the Bragg's angle.

Table 3.3 shows calculated and measured data on crystallite size, particle size, and specific surface area. The crystallite size, calculated from XRD-data using the Scherrer formula (see Equation 3.1), decreased with a factor of 4 when x increased from 0 to 0.2 in $(La_{1-x}Sr_x)_{0.99}Co_{0.6+x}Ni_{0.4-x}O_{3-\delta}$. This trend agreed fairly well with the results from the powder SEM analysis (see Figure 3.3), where the crystallite size was substantially larger for $La_{0.99}Co_{0.6}Ni_{0.4}O_{3-\delta}$ than and $(La_{0.6}Sr_{0.4})_{0.99}CoO_{3-\delta}$. However, the absolute values stand in contrast to the SEM analysis of $La_{0.99}Co_{0.6}Ni_{0.4}O_{3-\delta}$, in which the crystallites seemed to be about 3-5 times larger. The mean particle size was measured after the powders had been mixed into an ethanol based solution and ball-milled for another 24 hours. The particle

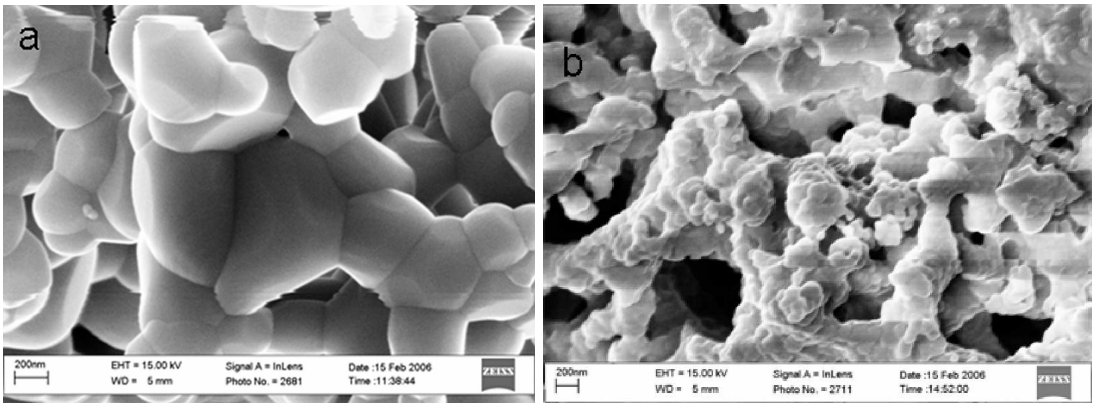

Figure 3.3: SEM images of powder samples of $La_{0.99}Co_{0.6}Ni_{0.4}O_{3-\delta}$ (a) $(La_{0.6}Sr_{0.4})_{0.99}CoO_{3-\delta}$ (b) acquired with $V_{acc.} = 15$ kV. Note the large crystallite size and the faceted surface of $La_{0.99}Co_{0.6}Ni_{0.4}O_{3-\delta}$.

Table 3.3: Mean crystallite diameter (calculated using the Scherrer formula se Equation 3.1), specific surface area (SSA) measured with BET, and particle size distribution measured with laser particle size analyzer of five compositions, $(La_{1-x}Sr_x)_{0.99}Co_{0.6+x}Ni_{0.4-x}O_{3-\delta}$, $0 \geq x \geq 0.4$.

X	0	0.1	0.2	0.3	0.4
crystallite diameter [nm]	84	54	22	28	33
SSA [m^2g^{-1}]	0.43	0.46	0.43	0.33	0.29
particle diameter d_{mean} [nm]	360	340	350	340	360

size was measured to approximately 350±10 nm for all compositions. The specific surface area (SSA) of the dry powders after calcination at 1250 °C was found to be approximately 0.3-0.5 m^2 g^{-1}. The SSA did not vary significantly between the compositions.

3.4.2 Evaluation of synthesis methods

Powders of $(La_{0.8}Sr_{0.2})_{0.99}Co_{0.8}Ni_{0.2}O_{3-\delta}$ have been synthesised using both the Glycine Nitrate (GNC) and the High Energy Ball Milling technique (HEBM), also referred to as reactive grinding. Symmetric cells with porous electrodes of $(La_{0.8}Sr_{0.2})_{0.99}Co_{0.8}Ni_{0.2}O_{3-\delta}$ were fabricated using both the GNC- and HEBM-synthesised powders (see the experimental section). The crystal structure of the porous electrodes were studied using XRD (see Figure 3.4). The XRD diffractograms showed that the perovskite made from HEBM was completely free from secondary phases while the electrode made from powder produced with the GNC-process revealed small amounts of secondary phases (less than 1%). The size of the crystallites were calculated from width of the [110] perovskite peak using the Scherrer formula (see Equation 3.1). Approximately the same crystallite diameter of 22 nm was found for the two material irrespective of the fact that they had been produced with fundamentally different techniques

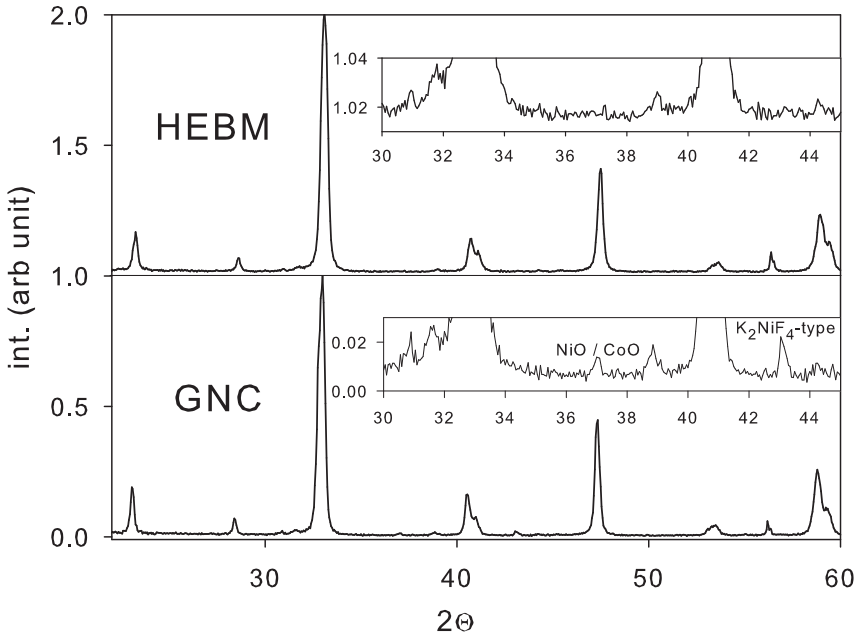

Figure 3.4: X-Ray Diffractogram of two different electrodes of $(La_{0.8}Sr_{0.2})_{0.99}Co_{0.8}Ni_{0.2}O_{3-\delta}$. HEBM and GNC referred to the synthesis method of the powder. The inset figures show enlargements of the intensity close to baseline in order to more clearly show the small amounts of secondary phases seen in the "GNC"-electrode. The small reflection at 39 2Θ is the [113] perovskite peak and not a secondary phase.

and had experienced different heat treatments. The particle size distribution was measured after the powders were mixed into the slurry suspensions used in the spraying of the electrodes. These slurries had been ball-milled for 24 hours prior to these measurements. The particle size distributions are shown in Figure 3.5. The HEBM-particles had a broader size distribution and an average particle size that was approximately twice as high as compared to the GNC-particles (∼350 nm for GNC-particles compared to ∼735 nm for HEBM-particles). Furthermore, the HEBM-particles seemed to have a bimodal distribution were the second peak resulted in a mean diameter of about 2-3 μm (see Figure 3.5).

Figure 3.6 shows the electrode microstructure of the HEBM- and GNC-electrodes. It appeared as if the HEBM-electrode comprise agglomerated particles, which were not found in the GNC-electrode. This is consistent with the analysis of the particle size distribution of the suspended powders.

The symmetric cells with electrodes made of GNC-powder and HEBM-powder were analysed with electrical impedance spectroscopy (EIS) after the cells had been stored at room temperature (at ambient conditions) for different periods of time. The results are shown in Figure 3.7 where the logarithm of the polarization resistance, R_P, is plotted as function of the reciprocal temperature. Storing the cells appeared to have a surprisingly enhancing effect on the electrode performance. This phenomena will be discussed in more detail in

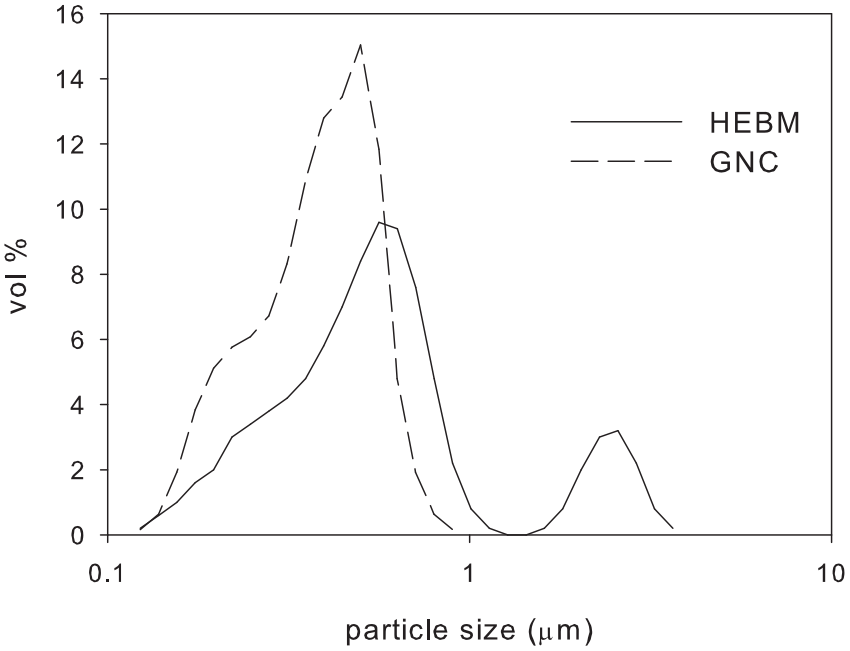

Figure 3.5: Particle size distribution of two suspensions with $(La_{0.8}Sr_{0.2})_{0.99}Co_{0.8}Ni_{0.2}O_{3-\delta}$ particles produced using the HEBM- and GNC-synthesis.

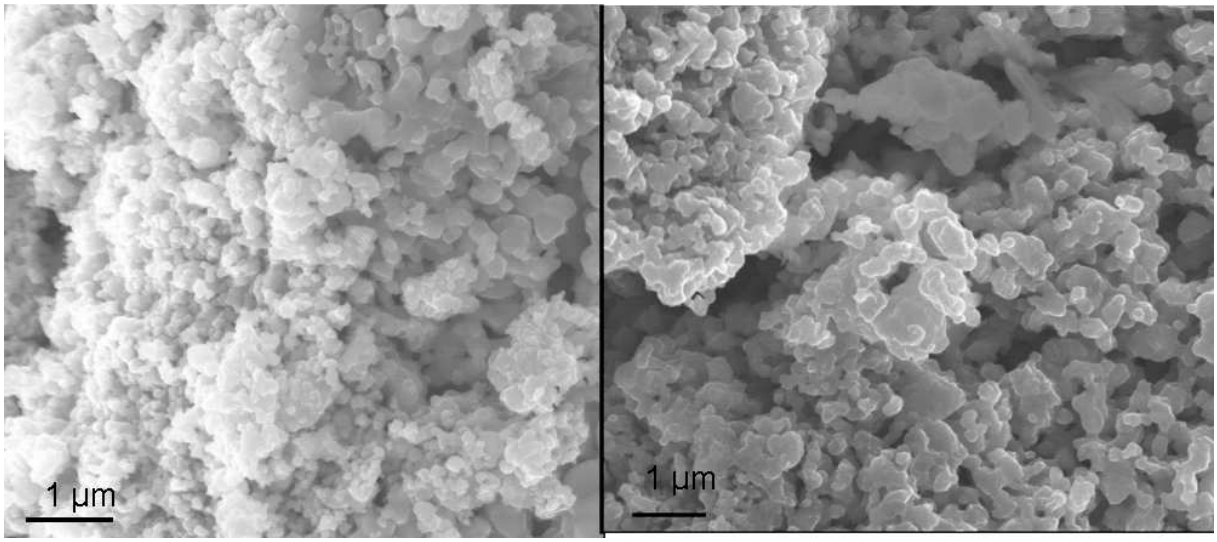

Figure 3.6: SEM-images of two porous electrodes consisting of powders of $(La_{0.8}Sr_{0.2})_{0.99}Co_{0.8}Ni_{0.2}O_{3-\delta}$, which have been produced with two different synthesis techniques, high energy ball milling (HEBM)(left) and glycine nitrate combustion (GNC)(right).

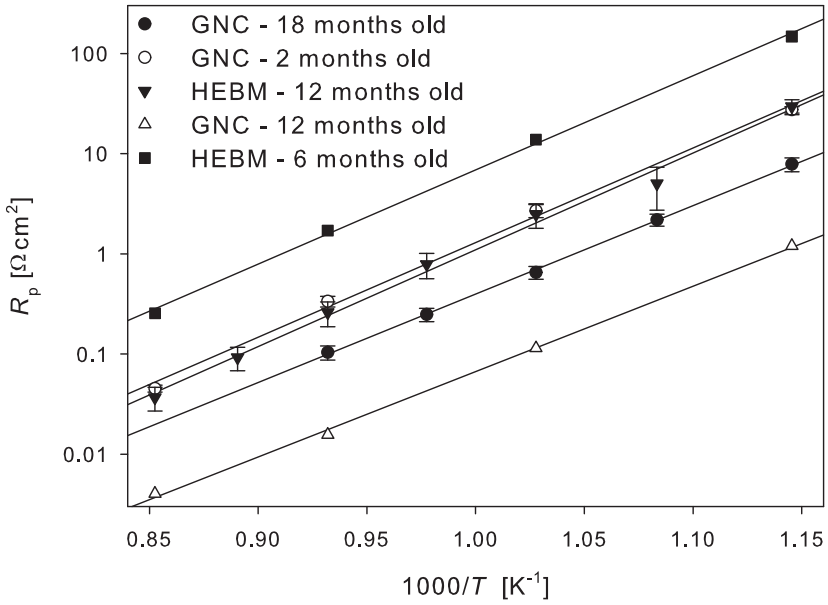

Figure 3.7: Arrhenius plots of the polarisation resistance, R_P, at open circuit voltage and ambient air of two electrodes fabricated from powders produced using two different synthesis routes, GNC and HEBM. The performance of the electrodes was measured after storing the symmetric cells at room temperature (at ambient conditions) for different periods of time.

Chapter 6. Irrespective of this effect, the results showed that the electrode with powder produced using the GNC process had a better performance compared to the cells produced with the HEBM-technique. The activation energy of R_P was found to be 1.65-1.85 eV for both electrodes. The P_{O_2} dependence of of R_P of the two electrodes was also measured at 750 °C as shown in Figure 3.8. Both electrodes had been stored for 12 months. The results showed very similar behaviour where $R_P \propto P_{O_2}^{-0.2}$.

The polarization resistance of both electrodes was furthermore measured as function of time at 850 °C in order to determine degradation rates, measured as the increase in the total resistance per day. Figure 3.9 shows the increase in R_P of the two different symmetric cells measured simultaneously during the same experiment. In this experiment, the "GNC-cells" had been stored for 12 months whereas the "HEBM-cells" had been stored for 6 months. The degradation rate was found higher for the HEBM-electrodes, which also were found to have a higher initial R_P in accordance with Figure 3.7. The figure to the right shows the degradation relative to initial performance. Interestingly, the degradation rates are different when calculated in absolute values as Ωh^{-1} but are fairly similar when calculated relative to the initial resistance. The degradation rates are surprisingly high for both electrodes and the resistance is approximately doubled over 100 hours.

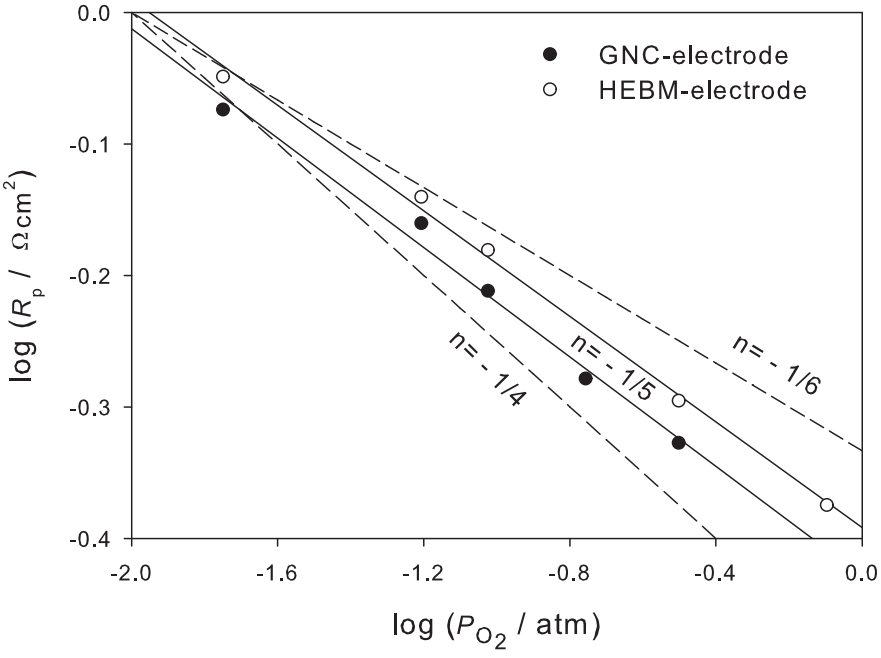

Figure 3.8: P_{O_2} dependence of R_P at open circuit voltage and 750 °C for the two electrodes presented in Figure 3.7. $R_P \propto P_{O_2}^n$. The GNC-cells had been stored for 14 months and the HEBM-cells had been stored for 7 months.

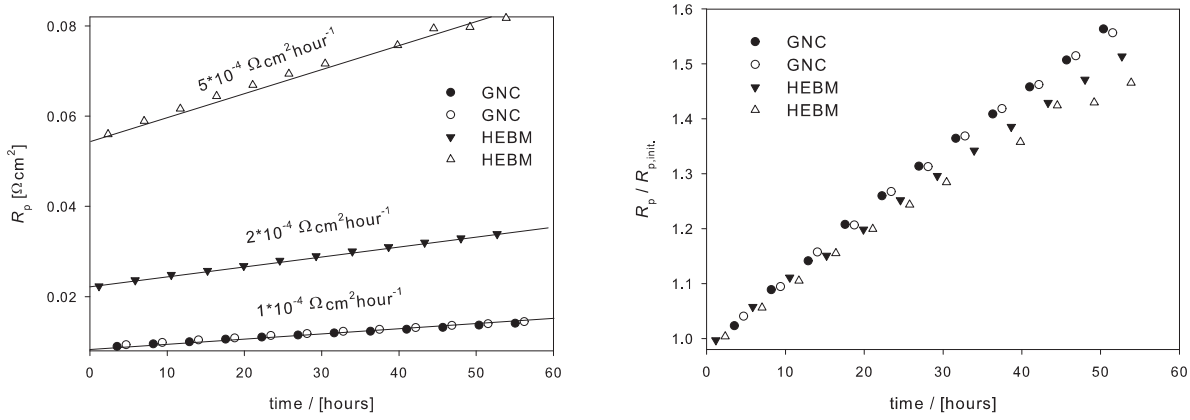

Figure 3.9: **Left:** Increase in polarization resistance with time at 850 °C for symmetric cells with $(La_{0.8}Sr_{0.2})_{0.99}Co_{0.8}Ni_{0.2}O_{3-\delta}$ as porous electrodes. The powder had been synthesized using either the HEBM- or the GNC-methods. The HEBM-electrodes had been stored for 6 months whereas the GNC-electrodes had been stored for 12 months. **Right:** Degradation of R_P relative to the initial $R_{P,init}$ of the symmetric cells presented in the figure to the left.

3.5 Discussion

Analysis of the XRD difractograms of the compositions containing secondary phases and correlation of peak positions and intensities with known phases in crystallographic databases strongly suggested that the secondary phases consisted of K_2NiF_4-type oxides and NiO and/or CoO phases. $Co_{1-x}Ni_xO$ will inevitably be found in all samples due to the stoichiometric A/B ratio of 0.99. With K_2NiF_4-type oxides present, equal amounts of $Co_{1-x}Ni_xO$ will additionally be found as a stoichiometric necessity. However, due to the low intensity of these peaks it is difficult to conclude which type of composition these secondary phases have. Furthermore, both $(La_{1-x}Sr_x)_2Co_{1-x}Ni_xO_4$ and $Co_{1-x}Ni_xO$ appear approximately at the same position in the diffractogram, irrespective of x. Therefore is XRD not a suitable technique to determine the exact composition of the detected secondary phases. The secondary phases could possibly result from an incomplete reaction due to e.g. inhomogeneities during synthesis. Repetitive pressing, sintering and grinding could possibly have completed the reactions and transformed these secondary phases into the perovskite type oxide. However, the aim of this study was to find the compositions which could be synthesised into a single phased powder using the GNC-process without additional pressing and heat treatment processes. The composition and reactions of the secondary phases will be discussed in more detail in Chapter 4.

It appears from Table 3.1 that high temperatures, at least above 950 °C, are necessary when firing strontium containing compositions in order to remove the strontium carbonates formed during synthesis. High temperature also appeared necessary in order to form the perovskite from the two secondary phases, $(La_{1-x}Sr_x)_2Co_{1-x}Ni_xO_4$ and $Co_{1-x}Ni_xO$. Nickel rich and strontium poor perovskites tend to form after heat treatment at 950 °C. On the other hand, Table 3.2 indicated that secondary phases are formed at higher calcination temperatures, ie 1250 °C, which are retained if the cooling is too rapid (100 °Ch^{-1}). This is in agreement with Hofer et. al. [25] who measured the decomposition of $LaNiO_3$ into $La_4Ni_3O_{10}$ and NiO between 825-1200 °C and further into La_2NiO_4 and NiO at even higher temperatures. The reduction of nickel is due to the low thermal stability of $LaNiO_3$ at elevated temperatures.[139], [9]

Calculation of the mean crystallite size of $(La_{1-x}Sr_x)_{0.99}Co_{0.6+x}Ni_{0.4-x}O_{3-\delta}$; $0 \geq x \geq 0.4$, using the Scherrer formula, revealed sizes of about 20-85 nm, whereas measurements of the particle size distributions using laser diffraction resulted in an average particle size of 350 ±10 nm for all compositions. The disagreement between crystallite and particle size calculated from XRD data (see Table 3.3) is likely due that the crystallites have sintered into larger particles. This can also be seen in the micrographs of the particles of $(La_{0.6}Sr_{0.4})_{0.99}CoO_{3-\delta}$ in Figure 3.3, where the sample appeared to consist of smaller crystals that had sintered together and formed a continuous network. The microstructure of $La_{0.99}Co_{0.6}Ni_{0.4}O_{3-\delta}$, as seen in SEM, was rather different from $(La_{0.6}Sr_{0.4})_{0.99}CoO_{3-\delta}$ as the particles appeared to be larger and consist of single crystals with faceted surfaces. In the SEM images, the crystallites of $La_{0.99}Co_{0.6}Ni_{0.4}O_{3-\delta}$ appeared to be larger than those of $(La_{0.6}Sr_{0.4})_{0.99}CoO_{3-\delta}$. This trend was also found when calculating the crystal size based on

XRD peak widths, however, there is still an unresolved disagreement between the crystal size of $La_{0.99}Co_{0.6}Ni_{0.4}O_{3-\delta}$ calculated from XRD data (2Θ∼85 nm) and SEM-analysis (2Θ∼350 nm).

The specific surface area measured with BET after synthesis was rather low, 0.3-0.5 m^2g^{-1}, considering that the particles were in nanometer size (see Table 3.3). Estimating the surface area by assuming non-interacting spherical particles with a diameter of 350 nm results in a surface area of approximately 3 m^2g^{-1}. Furthermore, particles that have non-spherical shapes, as is the case with the particles seen in Figure 3.3, have a larger surface to volume ratio, which implies that the expected surface area should be even larger. This area is on the other hand an overestimate as SEM-analysis showed clear particle interaction, however, this can only partly explain the large discrepancy of about one order of magnitude. It must also be stressed that the BET-analysis was performed on the powder prior to mixing it into the ball-milling suspension whereas the particle size distribution was measured after this treatment. A second reason for the disagreement between particle size and surface area could thus be the presence of agglomerates after synthesis, which have been grounded and disintegrated into smaller particles when ball-milled the suspension. The symmetric cells with sintered porous electrodes were unfortunately too small to perform BET-analysis on, and therefore, this hypothesis could not be tested afterwards. However, there was some consistency when comparing the particle size and the specific surface area of the five compositions listed in Table 3.3. The variations between the different samples were relatively small even though both XRD and SEM showed rather large differences crystallite sizes. This suggests that the microstructure of these materials is fairly similar, despite the different crystal characteristics. However the surface structure can nevertheless be quite different between the compositions.

Figure 3.7 showed a relatively large difference in performance between the two different electrodes. The electrode fabricated from GNC-synthesised powder showed lower polarisation resistance, R_P, as compared to the electrode with powder produced with the HEBM-technique. More surprising was the result that R_P changed rather dramatically by storing the cells at room temperature (at ambient conditions). This effect and the general electrochemical response of porous electrodes of $(La_{1-x}Sr_x)_{0.99}Co_{1-y}Ni_yO_{3-\delta}$ will be discussed in depth in Chapter 6. Here it is sufficient to notice that the activation energy of R_P for the two cells was relatively similar as is their respective P_{O_2}-dependence (see Figures 3.7 and 3.8). This indicates that the variation in performance is not related to different reaction mechanisms. No further mechanistic discussion will be given here as this is far to complicated to discuss based on just a few measurements on non-ideal porous system.

Analysis of the particle size distribution (PSD) after ball-milling revealed that the HEBM-particles had twice as large mean particle diameter as compared to the particles synthesized using the GNC-process. Moreover, PSD-analysis of the suspended HEBM-powder showed evidence of agglomerates in the size of 2-3 μm. The difference in performance could possibly be explained as a micro structural effect where the HEBM-electrodes have a smaller active

surface area. Unfortunately, we have not been able to measure the surface area of the electrodes as their total surface area was too small. Figure 3.4 showed that the GNC-electrodes had small amounts of secondary phases whereas the HEBM-electrode appeared to be phase pure within the detection limit of XRD. The fact that the GNC-electrodes still showed a better electrochemical performance indicated that any secondary phases of the types $(La_{1-x}Sr_x)_2Co_{1-x}Ni_xO_4$ and $Co_{1-x}Ni_xO$, do not have any dramatic detrimental effects on the electrochemical performance.

The degradation measurements (see Figure 3.9) showed that there was no major difference in the degradation rate measured as R_P relative to the initial resistance, between the two symmetric cells. This indicated that the degradation is associated with an intrinsic effect of the material $(La_{0.8}Sr_{0.2})_{0.99}Co_{0.8}Ni_{0.2}O_{3-\delta}$ rather than a microstructural phenomena. The degradation of porous electrodes of $(La_{1-x}Sr_x)_{0.99}Co_{1-y}Ni_yO_{3-\delta}$ will be discussed in more detail in Chapter 6.

3.6 Conclusions

It is only possible to substitute relatively small levels of NiO and SrO into $LaCoO_3$ without obtaining a multi phase system when the samples are produced by the GNC synthesis. With high levels of strontium it appeared that calcination temperatures above 950 °C was required. With high levels of nickel substitution moderate calcination temperatures seemed favorable whereas too high temperatures resulted in the formation of secondary phases when the cooling rate was too rapid (100 °Ch^{-1}). A relatively slow cooling rate of 20 °C h^{-1} appeared to be favourable when heat treating nickel containing compositions to high temperatures. The microstructure, ie particle size and specific surface area, of the the different powders with compositions; $(La_{1-x}Sr_x)_{0.99}Co_{0.6+x}Ni_{0.4-x}O_{3-\delta}$ $0 \geq x \geq 0.4$; were fairly similar despite a clear difference in crystallite size and structure between the compositions. For practical SOFC temperatures, ie below 950 °C the total substitutional level appeared to be approximately 40-50%, irrespective of whether the dopant was NiO or SrO. In the following chapter we have therefore studied compositions with a total dopant level of 40% and where we instead have varied the dopant element, NiO or SrO.

The synthesis method appeared to have an impact on the microstructure where the Glycine Nitrate Combustion (GNC) route showed better microstructural properties, i.e. smaller particles and less agglomerates, as compared to powder produced using the High Energy Ball Milling (HEBM). The GNC synthesis is furthermore a rapid and convenient process, whereas the HEBM is very time- and energy-consuming as producing 30 g perovskite powder required about 150 kWh of energy. The electrode produced from GNC-powder showed also a better performance when used a porous electrode. The electrochemical behaviour with respect to T, P_{O_2} and time was found to be very similar between the two electrodes. We have therefore decided to utilize the GNC technique when producing materials for subsequent studies on materials properties and electrochemical performance of $(La_{1-x}Sr_x)_{0.99}Co_{1-y}Ni_yO_{3-\delta}$.

Chapter 4

Structural properties and electrochemical performance of $(La_{1-x}Sr_x)_{0.99}Co_{0.6+x}Ni_{0.4-x}O_{3-\delta}$

4.1 Abstract

This study presents structural and defect properties as function of doping, temperature and pO_2 in $(La_{1-x}Sr_x)_{0.99}Co_{0.6+x}Ni_{0.4-x}O_{3-\delta}$ (x = 0; 0.1; 0.2; 0.3; 0.4). Thermogravimetric analysis showed a linear increase in δ with both T and x in the high temperature regime. The onset temperature of reduction was seen to increase with x which was confirmed with dilatometry and XANES. XANES measurements further indicated that reduction was exclusively associated with cobalt. A transition from polaronic to itinerant electronic conduction was measured with increasing x ranging from 2000-3500 Scm^{-1} in the intermediate SOFC temperature range of 500-800 °C. The polarisation resistance when used as porous SOFC cathodes was measured to decrease with x. The activation energy of about 1.8 eV for all electrodes but $(La_{0.6}Sr_{0.4})_{0.99}CoO_{3-\delta}$, for which it was about 1 eV.

4.2 Introduction

The perovskite $LaCoO_3$ was early recognized as a candidate material in SOFC-cathodes [88] and the aliovalently substituted $La_{1-x}Sr_xCoO_3$ has shown promising electrochemical activity towards the oxygen reduction reaction [112], [140], [141]. The main reason $(La_{0.6}Sr_{0.4})_{0.99}CoO_{3-\delta}$ is believed to be its high mixed ionic and electronic conductivity at high temperatures, which is a property that makes its interesting for use also in other high temperature ceramic devices such as membranes and sensors. The ionic conductivity arises from the creation of oxygen vacancies upon reduction of Co(IV) to Co(III) at high temper-

atures. Also B-site doping with various transition metals have been investigated extensively and the composition $(La_{0.6}Sr_{0.4})_sCo_{0.2}Fe_{0.8}O_{3-\delta}$ is often referred to as a functional "state of the art" cathode due to its suitable thermal expansion coefficient (TEC). [15], [43] Nickel-doping has also been studied in several papers. This substitution has shown to increase both electronic [15], [16] and ionic conductivity [17], [18], [19] as well as decrease the thermal expansion coefficient. [20], [21] Huang *et al* [22] have studied the $(La_{1-x}Sr_x)_sCo_{1-y}Ni_yO_{3-\delta}$-system and measured a reduced polarization resistance when substituting 20% Sr on A-site with equal amounts of Ni on B-site in the high performing composition $La_{0.6}Sr_{0.4}CoO_3$.

We have studied the compositions $(La_{1-x}Sr_x)_{0.99}Co_{0.6+x}Ni_{0.4-x}O_{3-\delta}$ (x=0-0.4) were the total dopant concentration in the nominal perovskite $LaCoO_3$ was kept at a constant level of 40 % but where A-site dopant SrO in $(La_{0.6}Sr_{0.4})_{0.99}CoO_{3-\delta}$ has been replaced with the B-site dopant NiO. The idea was to study whether Ni(II) can be stabilized, fully or partially, in the perovskite structure and, as a consequence of electro-neutrality, maintain the concentration of oxygen vacancies. Aksenova *et al.* [138] have thoroughly investigated crystal phases of $(La_{1-x}Sr_x)_sCo_{1-y}Ni_yO_{3-\delta}$ at high temperatures and shown that all these compositions would be possible to synthesize single phased. We will here report on how the crystal- and defect properties changes with x, T, P_{O_2} and discuss our results in the light of theory reported in the literature and as applied electrode materials in solid oxide fuel cells.

4.3 Experimental

Powder of $(La_{1-x}Sr_x)_{0.99}Co_{0.6+x}Ni_{0.4-x}O_{3-\delta}$ (x = 0; 0.1; 0.2; 0.3; 0.4) was synthesised using the glycine-nitrate combustion route.[130] As an exactly stoichiometric A/B ratio of 1 is practically impossible to synthesise, traces of either transition metal- or alkali earth metal oxides is inevitable. For that reason we have deliberately chosen an A/B-ratio of 0.99 in order to know which type of secondary phases to expect. The stoichiometric accuracy is such that we can assume the composition to be A-site substoichiometric. The powder which had d50-values of 350-500 nm were calcined at 1250 °C for 12h. The powder was first pressed uniaxially into bars, isostactically pressed at 325 MPa for 30 seconds and sintered again at 1250 °C for 12 h. The bars were finally cut to dimensions of 4×4×18 mm. A STOE Theta-Theta diffractometer (40kV, 30 mA) with Cu K_α -radiation was used for high temperature X-ray diffraction measurements to 1000 °C. Powder samples were scanned with 2Θ ranging from 20-60° with 0.05° incremental steps. Dilatometry was measured on sintered bars with a NETZSCH DIL 402C with the temperature scanned to 1300 °C with 2 °Cmin^{-1} in airflow of 50 mlmin^{-1}. A Zeiss Supra 35 electron microscope was used to study the microstructure and possible secondary phases not detectable with XRD. Sintered samples were polished beforehand with a 0.5 μm SiC cloth.
Powder samples were analysed thermograviometrically with a NETZSCH STA 409C/CD to estimate oxygen non-stoichiometry as a function of temperature. 300 mg of powder sample was heated and cooled in 50 ml/min airflow to 1300 °C with a heating rate of 10 °Cmin^{-1}. Cooling rate was set to 1°Cmin^{-1} down to 600 °C followed by a rapid cooling of 10 °Cmin^{-1} to room temperature. XANES measurements were performed at DESY (Deutsches Elektronen Synchrotron) at beam line E4. The synchrotron radiation (4.5 GeV)

was monochromatized by two Si(111) crystals. Spectra of the sample and the respective metal foil as reference were measured simultaneously in transmission mode. The sample chamber was evacuated to 10^{-6} mbar. High temperature measurements were done in air at atmospheric pressure. About 3 mg of powder sample was mixed with 50 mg cellulose in a mortar, subsequently pressed into wafers with a diameter of about 11 mm, and placed in the sample holder. High temperature samples were prepared by mixing about 3 mg of powder sample with 50 mg of alumina oxide. XANES spectra were taken in the energy range from 44 eV below the edge energy of the metal to 266 eV above the edge. The obtained raw data were calibrated using the spectrum of the metal foil (edge energy: first inflection point), background corrected by two linear polynomials in the pre-edge and after the main edge region, and normalized to an edge jump of one at ≈100 eV above the edge.
The conductivity was measured with a standard 4 point probe DC-technique. Sintered bars were painted and wired with platinum at both ends and fired at 1100 °C prior measurements. The resistance was measured with a Keithley 2700 multimeter. Voltage probes were separated 6.8 mm apart and measurements were performed at temperatures ranging from 50 °C to 1000 °C at P_{O_2}=0.209 and from $\log(P_{O_2})$ ranging from 0 to -2.5 at 1000 °C.

Symmetric cells with porous perovskite electrodes were produced using a 200 μm dense $Ce_{1.9}Gd_{0.1}O_{1.95}$ (CGO10) tape as electrolyte. A cathode slurry of about 11 g perovskite powder, 15 g ethanol and 1 g PVP was mixed and ball-milled over night. The slurry was sprayed onto both sides of the electrolyte and sintered at 950 °C for 2 h. The spraying and sintering procedure was repeated in order to fabricate a symmetric cell with approx. 25 μm thick electrodes. The cells were cut to dimensions of 4.0 by 4.0 mm and painted with platinum paste to serve as current collectors. Four identical cells were measured with Electrochemical Impedance Spectroscopy (EIS) under open circuit voltage with a Solartron-1260 frequency response analyzer at temperatures from 600-900 °C with an amplitude of 50 mV.

4.4 Results

4.4.1 Crystal structure

X-ray powder diffraction on $(La_{1-x}Sr_x)_{0.99}Co_{0.6+x}Ni_{0.4-x}O_{3-\delta}$ showed that all five composition were single phased at room temperature within the detection limit (see Figure 4.1). The unit cells were determined to be rhombohedral (spacegroup $R\overline{3}c$). However, the degree of peak splitting is observed to decrease with increasing x, indicating that the crystal structure becomes closer to a cubic phase. This has also been reported for the $(La_{1-x}Sr_x)_sCoO_{3-\delta}$-system where a fully cubic structure was found for $(La_{0.45}Sr_{0.55})_{0.99}CoO_{3-\delta}$. [34] The lattice parameter, a, rhombohedral angle, α, theoretical density, ρ_{theo}, are listed in table 4.1. The theoretical density was further compared with densities measured geometrically on sintered bars in order to obtain their porosities.

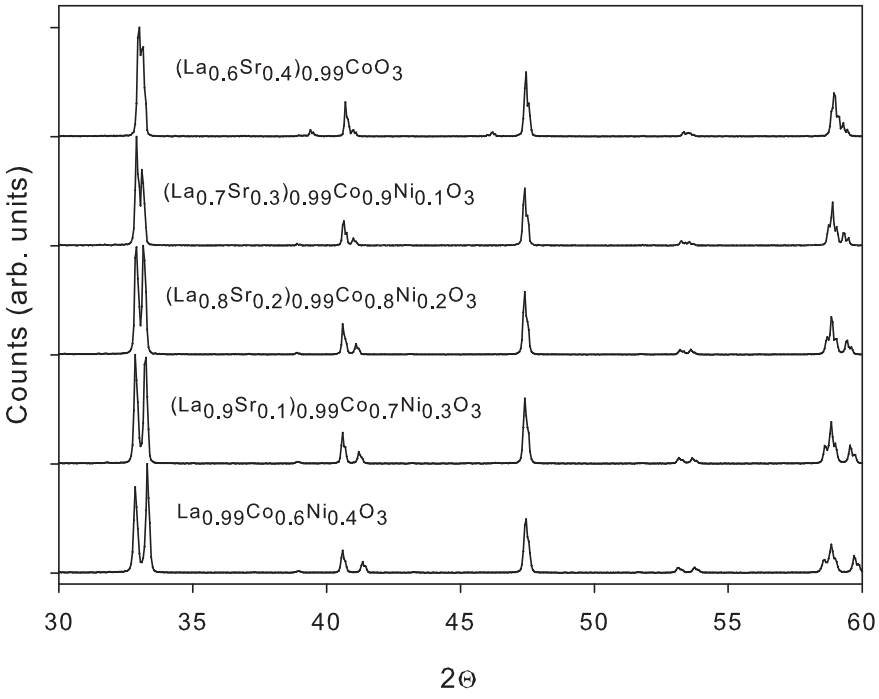

Figure 4.1: Powder XRD-diffractgram of $(La_{1-x}Sr_x)_{0.99}Co_{0.6+x}Ni_{0.4-x}O_{3-\delta}$ at room temperature. Note the shift from rhombohedral to psuedocubic with increasing strontium/nickel ratio.

Table 4.1: Crystal related properties of $(La_{1-x}Sr_x)_{0.99}Co_{0.6+x}Ni_{0.4-x}O_{3-\delta}$. a is the lattice parameters. α is the rhombohedral angle. $T_{trans.}$ is the transition temperature where the crystal is estimated to be fully cubic. TEC_{XRD} and TEC_{dil} are the calculated thermal expansion coefficient based on volume expansion measured with from HTXRD and dilatometry from RT to the onset temperature of thermal reduction determined with thermograviometry. G_{t} is the Goldsmidt tolerance factor, ρ_{theo} and ρ_{geo} are calculated (from lattice parameters) and geometrically measured densities. ϵ is the calculated relative density

X	0.0	0.1	0.2	0.3	0.4
a [$\mathring{A}$]	5.3903	5.3953	5.3992	5.4017	5.406
α [°]	60.87	60.72	60.56	60.42	60.34
$T_{\mathrm{trans.}}$ [°C]	1525±35	1140±10	980±30	810±10	475±25 [142]
$TEC_{\mathrm{XRD}} \cdot 10^{-6}$ [°C^{-1}]	17.6±0.2	16.7±0.2	17.4±0.2	12.8±0.2	17.3 [142]
$TEC_{\mathrm{dil}} \cdot 10^{-6}$ [°C^{-1}]	17.4±0.1	16.7±0.1	16.5±0.1	16.1±0.1	16.3±0.2
G_{t}	0.990	0.992	0.994	0.996	0.997
ρ_{theo} [gcm^{-3}]	7.19	7.08	6.94	6.80	6.63
ϵ ($\rho_{\mathrm{geo}}/\rho_{\mathrm{theo}}$)	0.91	0.95	0.97	0.95	0.95

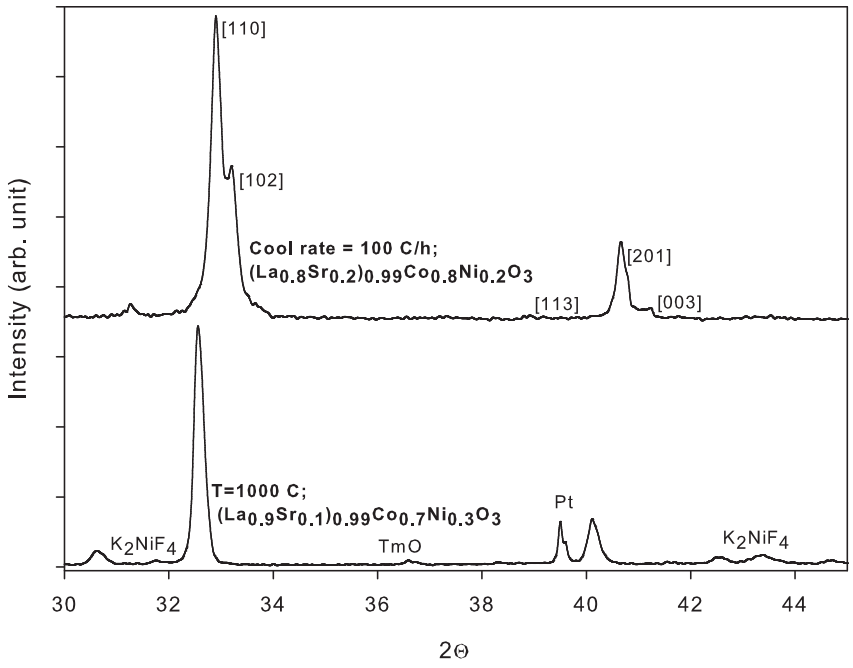

Figure 4.2: XRD diffractogram of sintered $(La_{0.8}Sr_{0.2})_{0.99}Co_{0.8}Ni_{0.2}O_{3-\delta}$ at room temperature and $(La_{0.9}Sr_{0.1})_{0.99}Co_{0.7}Ni_{0.3}O_{3-\delta}$ at 1000 °C. Peaks from secondary phases of K_2NiF_4-type appear at angles just below the main perovskite peak.

From XRD it was found that a slow cooling rate of less than 20 °C/h was required when calcining at T=1250 °C in order to obtain single phase perovskites. Strontium rich compositions (x=0.4; 0.3) showed evidence of strontium carbonates when calcined at lower temperatures while a rapid cooling resulted in CoO- and/or NiO-phases as well as K_2NiF_4-type phases for the nickel and strontium containing compositions (x=0.1-0.3). These phases also tend to form, preferably in the doubly doped compositions, at temperatures above 1000 °C and is possibly retained under rapid cooling due to slow cation diffusion (see Figure 4.2).

High Temperature X-ray diffraction (HTXRD) revealed a transition from rhombohedral to cubic structure with increasing temperature for all five compositions. Figure 4.3 shows the XRD patterns at different temperatures for the composition $La_{0.99}Co_{0.6}Ni_{0.4}O_{3-\delta}$. The rhombohedral angle was calculated for all temperature and the transition where the cubic cell is fully reached ($\alpha = 60°$) was estimated by linear extrapolation. These temperatures are listed in Table 4.1. Figure 4.4 shows the decrease of the rhombohedral angle as well as the lattice volume expansion with temperature for the perovskite $La_{0.99}Co_{0.6}Ni_{0.4}O_{3-\delta}$. Thermal expansion coefficients (TEC), calculated from high temperature x-ray diffraction, are listed in Table 4.1.

TEC was also calculated by differentiating the expansion measured in dilatometry as function of temperature. These data are reported in Figure 4.5 and reveals relatively stable

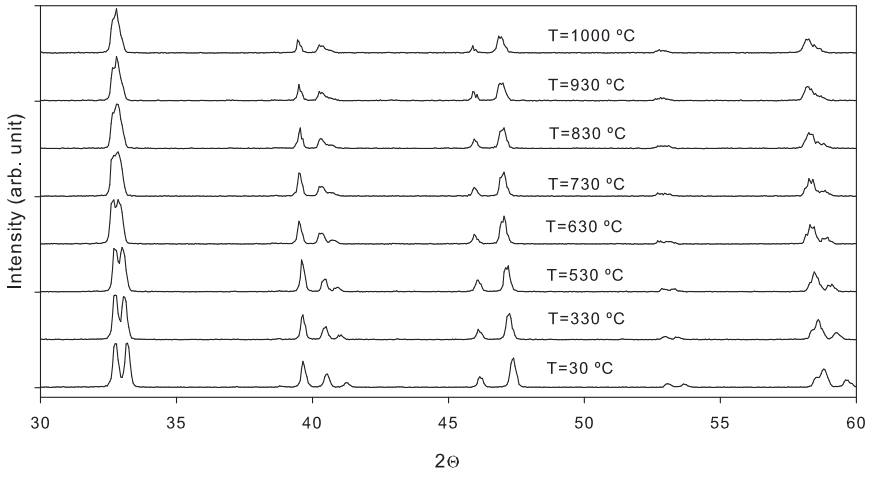

Figure 4.3: High temperature XRD diffractogram of powder $La_{0.99}Co_{0.6}Ni_{0.4}O_{3-\delta}$. A transition from a rhombohedral towards a cubic phase is seen as function of increasing temperature.

values of TEC at low temperatures. These data are also in reasonable agreement with what was measured with HTXRD. Furthermore, there was a sudden drop in the expansion coefficient for the compositions $(La_{0.6}Sr_{0.4})_{0.99}CoO_{3-\delta}$ at approximately 750 °C, which could possibly be due to a phase transition. Figure 4.6 reveals that this drop occurs at around 920 °C during heating. This drop was seen at the same temperature in a repeated measurements on $(La_{0.6}Sr_{0.4})_{0.99}CoO_{3-\delta}$ but in none of the repeated measurements of the nickel containing compositions. The high temperature hysteresis seen in figure 4.6 was also found for the other compositions and is likely due to sintering as it would only affect expansion during heating.

At a certain onset temperature, TEC is seen to increase dramatically. The onset temperature is further observed to decrease with increasing x from about 1000 °C for $La_{0.99}Co_{0.6}Ni_{0.4}O_{3-\delta}$ to about 400 °C for $(La_{0.6}Sr_{0.4})_{0.99}CoO_{3-\delta}$. As will be shown later this expansion behavior correlates very well with measured thermal reduction behaviors of the perovskites. It is worth to note that the dense sintered bars are not necessarily in chemical equilibrium with surrounding atmosphere due to slow oxygen transport and the chemical expansion might be larger for powder samples. Though induced by increasing temperature, this expansion behavior is mainly believed to result from chemical changes within the material and is therefore referred to as the stoichiometric expansion coefficient (SEC). [44] A more thorough investigation of this property in these materials will be reported in Chapter 5.

Scanning electron microscopy (SEM) was employed in order to determine possible traces of secondary phases not detectable in XRD. Figure 4.7 illustrates several grains of darker contrast in the composition $(La_{0.9}Sr_{0.1})_{0.99}Co_{0.7}Ni_{0.3}O_{3-\delta}$, reflecting a chemical contrast compared to the bulk composition. This is a result of a composition consisting of lighter elements. Energy Dispersive Spectroscopy (EDS) mapping showed that the small grain inclusions con-

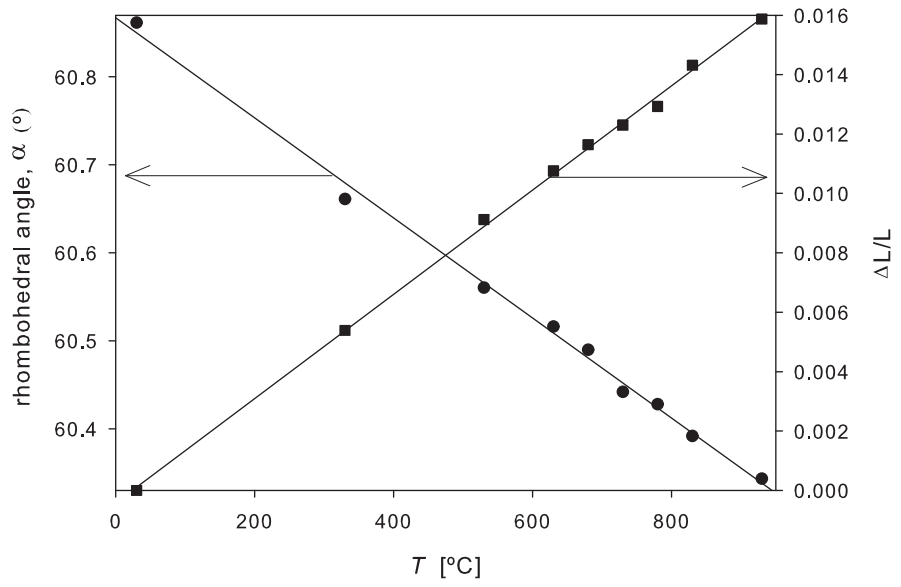

Figure 4.4: Measured volume expansion and rhombohedral angle, α, as function of temperature in powder $La_{0.99}Co_{0.6}Ni_{0.4}O_{3-\delta}$, from which TEC and T_{trans} was calculated.

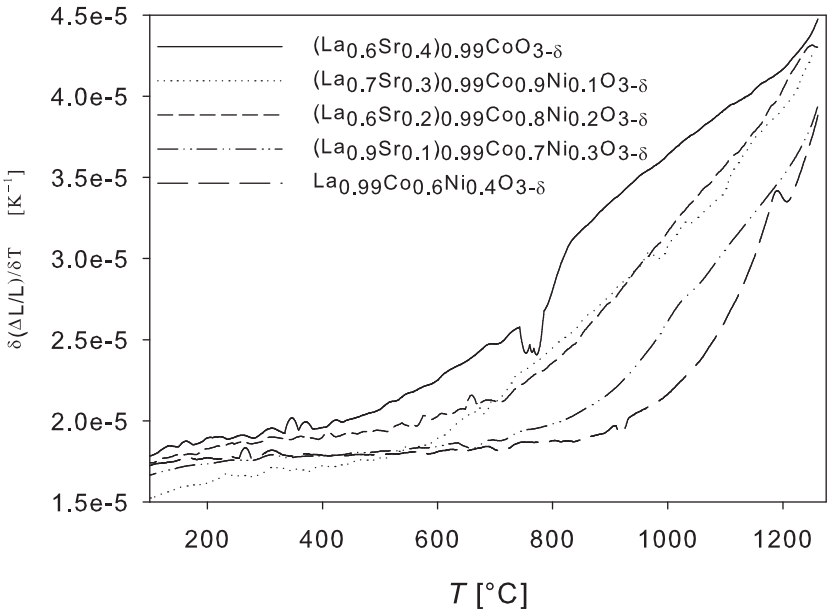

Figure 4.5: Thermal Expansion Coefficient (TEC) versus temperature for $(La_{1-x}Sr_x)_{0.99}Co_{0.6+x}Ni_{0.4-x}O_{3-\delta}$ measured using a dilatometer. Expansion increases at higher temperatures as a result to thermal reduction of cobalt. This increase occurs at low temperature for the strontium rich compositions due the presences of Co(IV).

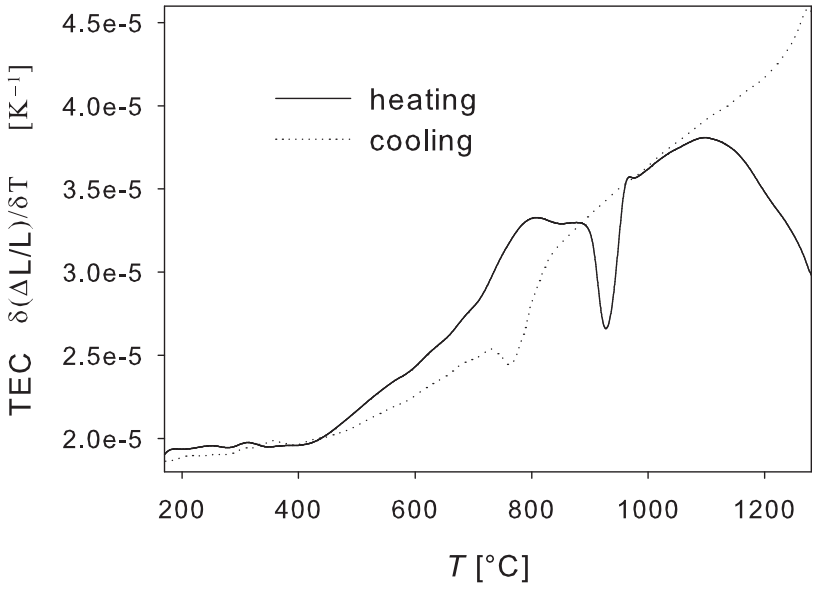

Figure 4.6: Thermal Expansion Coefficient (TEC) versus temperature for $(La_{0.6}Sr_{0.4})_{0.99}CoO_{3-\delta}$ during heating and cooling measured using a dilatometer. The features at intermediate temperatures arise from reduction/oxidation of cobalt oxide impurities. Hysterisis at the highest temperatures is attributed to sintering.

sisted exclusively of NiO. Indications of small traces of secondary phases are also present in the other investigated compositions. This is likely a result of the nominal A-site substoichiometry in these materials. No grains of pure cobalt oxides could be found in the nickel containing samples.

4.4.2 Defect structure

TGA analysis of powder samples was conducted in order to study oxygen nonstoichiometry as function of temperature. The materials are close to single phase according to XRD. Thus, it is is a fair approximation to assume that weight loss is entirely due to loss of lattice oxygen (and thus creation of vacancies) and not due to phase transitions. We assumed further fully stoichiometric perovskites at room temperature ($\delta = 0$) based on study by Mizusaki et. al. [76] on oxygen stoichiometry in $(La_{1-x}Sr_x)_sCoO_{3-\delta}$. Søgaard et. al. [142] measured δ to 0.014 $\pm$0.02 at room temperature for $(La_{0.6}Sr_{0.4})_{0.99}CoO_{3-\delta}$ which indicate a slight oxygen substoichiometry but also that δ=0 lies within experimental errors. Figure 4.8 illustrate this coefficient as function of temperature for the five samples and shows that the onset temperature of weight loss decreases linearly with decreasing x. It is further shown that the increase of δ with temperature, $\frac{\Delta\delta}{\Delta T}$, is constant and independent on x once the samples start losing oxygen. Comparing the onset temperatures with what was measured with dilatometry reveals a reasonably good agreement. The fact that the expansion coefficient continues to

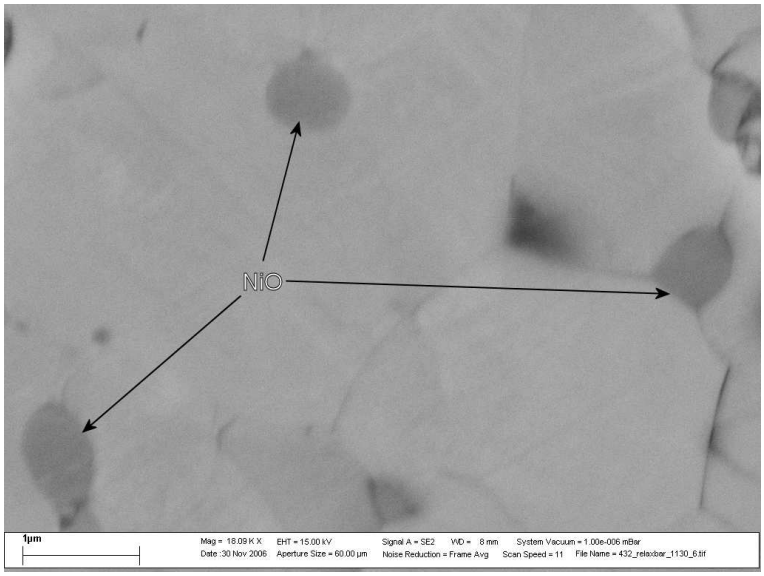

Figure 4.7: Scanning electron micrograph of sintered and polished $(La_{0.9}Sr_{0.1})_{0.99}Co_{0.7}Ni_{0.3}O_{3-\delta}$. Grains of darker contrast reflect oxides composed of lighter elements. EDS mapping have shown strong indication that these grains consist of NiO. Grains were found throughout the sample but not necessarily in the same concentration as shown in this figure.

increase above the temperature at which $\frac{\Delta\delta}{\Delta T}$ is constant indicates that the stoichiometric expansion coefficient is not constant but depends on a second order term involving δ and/or T. This will be discussed in detail in Chapter 5. A third distinguishable feature, which comes as a result of the two previous observations, is that δ increases almost linearly with strontium content in the high temperature region. These findings support that the dramatic increase in expansion is intimately coupled to the thermal reduction.

X-ray absorption near edge structure (XANES) was employed to study changes in oxidation state of cobalt and nickel separately with T and x in $(La_{1-x}Sr_x)_{0.99}Co_{0.6+x}Ni_{0.4-x}O_{3-\delta}$. The absorption edge energy reflects a transition of core s-electrons to unfilled d-orbitals of the transition metal and is thus strongly dependent on its oxidation state but also on coordination with surrounding ions. A shift towards lower energies corresponds to a lower oxidation state of the studied atomic specie and a value of the oxidation state can, in theory, be obtained by fitting the measured spectra with a linear combination of reference spectra of known oxidation states. This requires reference spectra of structures with well known oxidation states as well as identical coordination symmetry and closely related chemical surrounding as the studied structure. This proved to be too difficult to find and our XANES results were therefore only analyzed qualitatively in order to obtain trends relative to doping and temperature. However, as XANES is element specific, it allow us to study reduction/oxidation behavior on nickel and cobalt independently.

Figure 4.9 depict room temperature XANES measurements on the compositions $(La_{1-x}Sr_x)_{0.99}Co_{0.6+x}Ni_{0.4-x}O_{3-\delta}$ x=0 - 0.4. The Co-XANES spectrum of

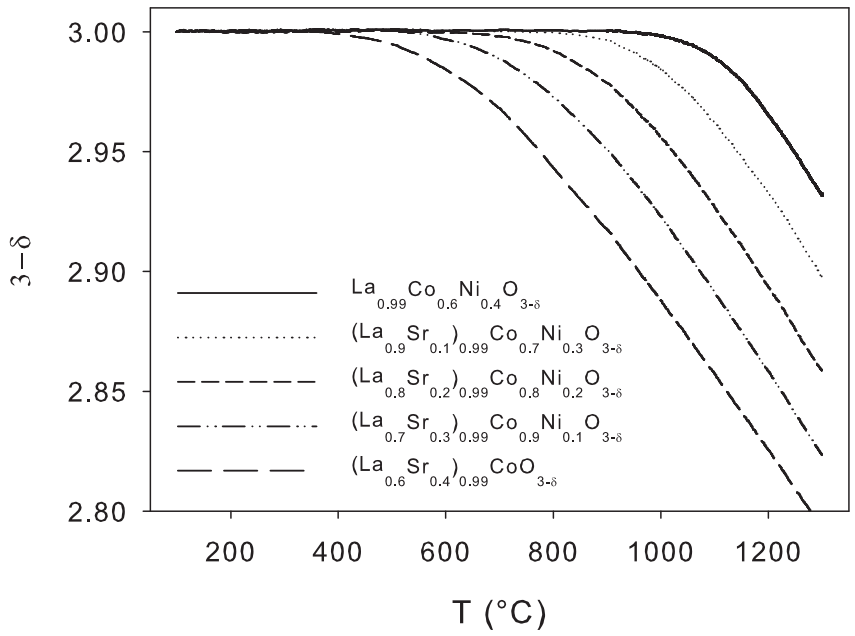

Figure 4.8: Thermograviometry of samples with compositions $(La_{1-x}Sr_x)_{0.99}Co_{0.6+x}Ni_{0.4-x}O_{3-\delta}$ x=0-0.4 as a function of temperature

$La_{0.99}Co_{0.6}Ni_{0.4}O_{3-\delta}$ is almost superimposed onto the reference spectrum of $LaCoO_3$ indicating that the valency of cobalt ions in $LaCoO_3$ is not changed upon substitution of nickel. When introducing strontium into the perovskite we see a clear shift of the cobalt edge towards higher energies, which is consistent with an oxidation process. This finding stands in contrast to what was reported by Grice et al. [143], who did not measure such a shift and therefore claimed these perovskties to be substoichiometric at room temperature. The Ni-XANES spectra are lying close to each other indicating that nickel ions do not change their valency when introducing strontium. This suggests that cobalt is the sole donator of electrons when strontium is substituted into $LaCoO_3$. Expressing the Co-XANES spectra of $(La_{1-x}Sr_x)_{0.99}Co_{0.6+x}Ni_{0.4-x}O_{3-\delta}$ x=0.1-0.3 as a linear combination of the spectras of $La_{0.99}Co_{0.6}Ni_{0.4}O_{3-\delta}$ and $(La_{0.6}Sr_{0.4})_{0.99}CoO_{3-\delta}$ allows us to estimate the trend in oxidation on cobalt as a result of strontium substitution. Figure 4.10 illustrates the shift in oxidation state of the cobalt ions and shows that, within the measurement uncertainty, the extent of reduction on the cobalt ions increases linearly with increasing concentration of strontium.

High temperature XANES measurements were performed in order to study the reduction of cobalt and nickel independently as function of temperature. Figures 4.11 and 4.12 show the high temperature spectra of the compositions $(La_{0.6}Sr_{0.4})_{0.99}CoO_{3-\delta}$ and $(La_{0.7}Sr_{0.3})_{0.99}Co_{0.9}Ni_{0.1}O_{3-\delta}$ respectively. A small shift of the absorption edge towards lower energies is observed for the cobalt ions in the composition $(La_{0.6}Sr_{0.4})_{0.99}CoO_{3-\delta}$ already below 400 °C, where thermograviometry indicated that no reduction processes would take

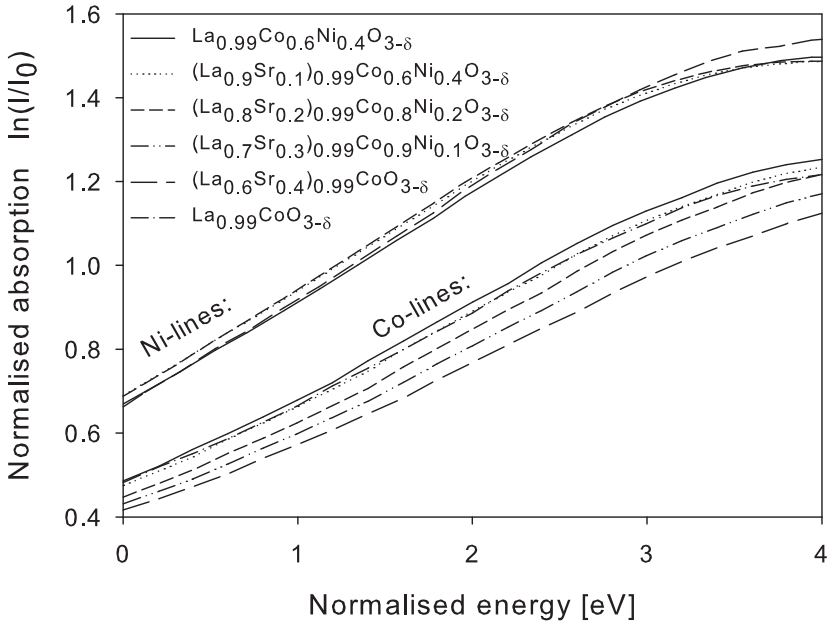

Figure 4.9: XANES edge energies of cobalt and nickel ions in powder samples of $(La_{1-x}Sr_x)_{0.99}Co_{0.6+x}Ni_{0.4-x}O_{3-\delta}$ and reference sample $La_{0.99}CoO_3$ at room temperature and in vacuum.

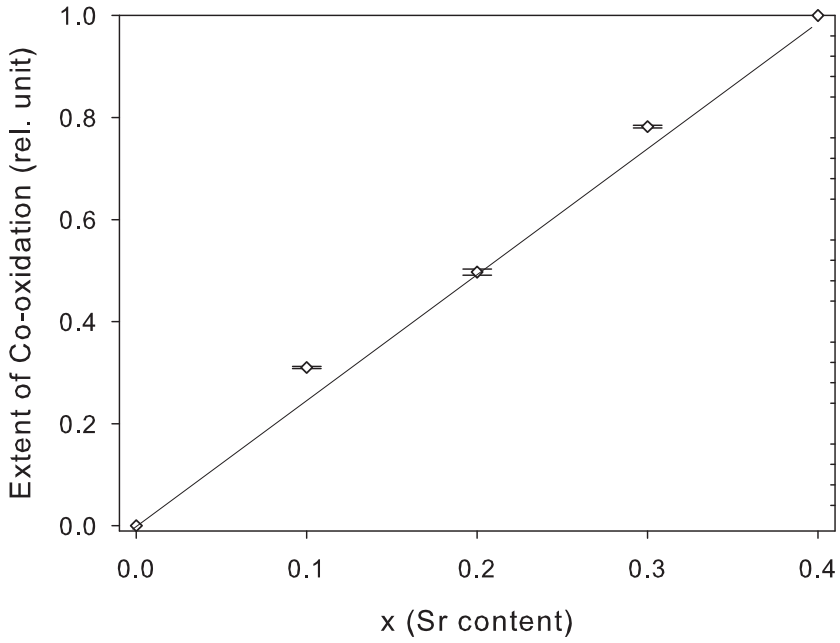

Figure 4.10: Relative oxidation of cobalt as function of strontium doping at room temperature and vacuum.

place. These small shifts could in fact indicate that cobalt is, to a small extent, reduced even at these low temperature. As oxygen diffusion is very slow at these temperature, this weight change might not be detectable unless equilibrated under very slow cooling rates. Figure 4.12 shows a relatively pronounced shift towards lower energies for the highest temperature (860 °C). A corresponding shift was not observed for the nickel ions, which indicates that the large thermal reduction seen in the thermograviometric measurements is concentrated on the cobalt ions. These edge energy shifts at higher temperatures are even more pronounced in XANES measurements on $(La_{0.6}Sr_{0.4})_{0.99}CoO_{3-\delta}$ as seen in figure 4.11 and the linear combination technique was used to determine the reduction trend in $(La_{0.6}Sr_{0.4})_{0.99}CoO_{3-\delta}$ relative to the maximum reduction (being the $(La_{0.6}Sr_{0.4})_{0.99}CoO_{3-\delta}$-spectra at the highest measured temperature, 875 °C). These reduction trends are seen in Figure 4.13 together with measured thermograviometry data (see figure 4.8), which appears to correlate relatively well.

4.4.3 Conductivity

Figure 4.14 shows the measured electrical conductivity for all five compositions in atmospheric air from room temperature to 1000 °C. As the transference number for these materials is close to one, the total electric conductivity is approximately equal to the electronic conductivity. The materials exhibit high conductivities and all compositions except $La_{0.99}Co_{0.6}Ni_{0.4}O_{3-\delta}$ showed metallic-like temperature dependences ie decreasing with temperature. The conductivity of all samples appears to converge towards approximately 1200

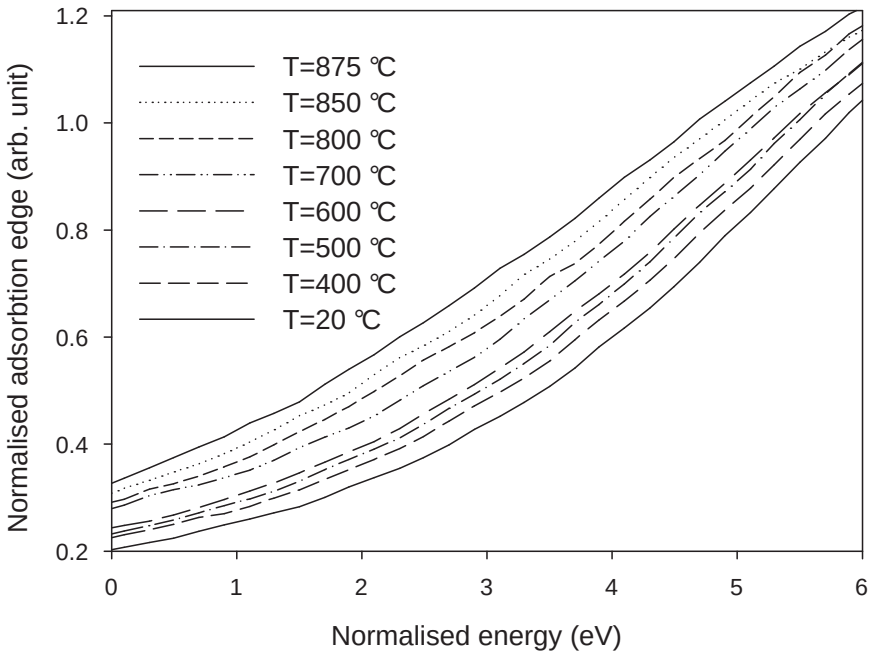

Figure 4.11: XANES edge energies of cobalt ions in $(La_{0.6}Sr_{0.4})_{0.99}CoO_{3-\delta}$ measured in air at the indicated temperatures. An exponentially increasing shift is seen with increasing temperature

.

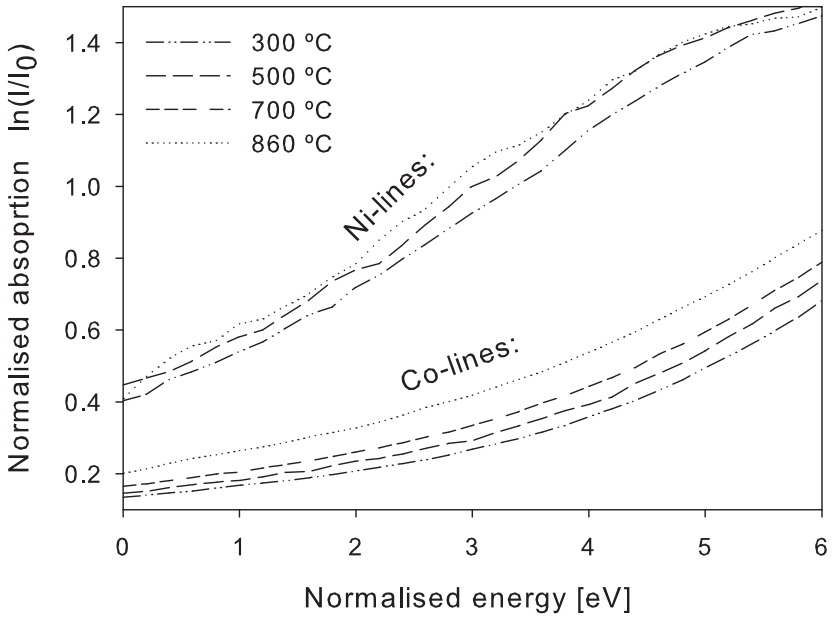

Figure 4.12: XANES edge energies of cobalt and nickel ions for $(La_{0.7}Sr_{0.3})_{0.99}Co_{0.9}Ni_{0.1}O_{3-\delta}$. A relatively large shift is seen for the highest temperature of the cobalt line.

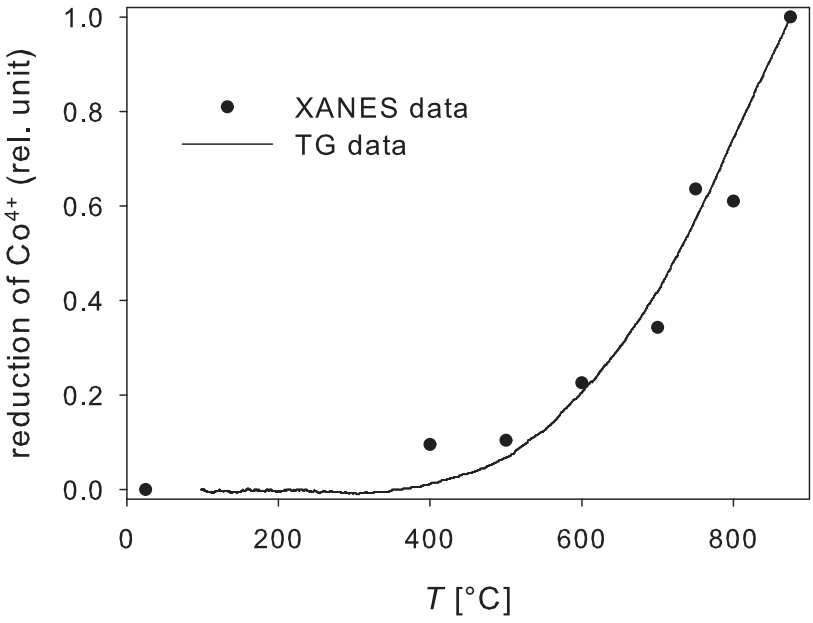

Figure 4.13: Relative extent of cobalt reduction in $(La_{0.6}Sr_{0.4})_{0.99}CoO_{3-\delta}$ as function of temperature in ambient air. Calculation was based on linear combination analysis of XANES spectra at highest (875 °C) and lowest (20 °C) temperature. Normalized data from thermograviomery added for comparison.

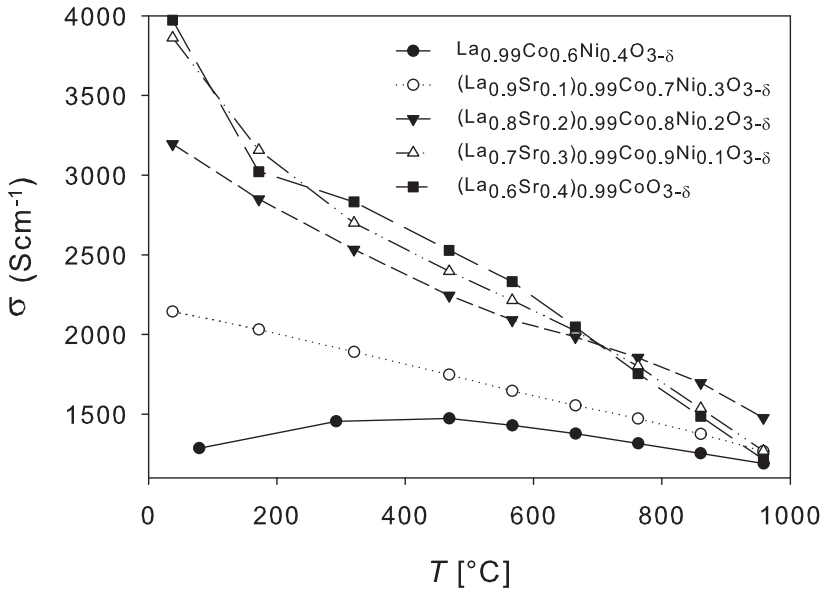

Figure 4.14: Total conductivity, σ, of samples with compositions $(La_{1-x}Sr_x)_{0.99}Co_{0.6+x}Ni_{0.4-x}O_{3-\delta}$ x=0-0.4 as a function of temperature

Scm^{-1} at $T \approx 1000$ °C except $(La_{0.8}Sr_{0.2})_{0.99}Co_{0.8}Ni_{0.2}O_{3-\delta}$ which measured about 300 Scm^{-1} higher. At lower temperature a large difference in conductivity between the five samples is observed, where the conductivity increases with about 1000 Scm^{-1} for $x \leq 0.2$, while it is approximately on the same magnitude across the entire temperature range for $x \geq 0.2$.

The electrical conductivity was further measured as function of P_{O_2} at 1000 °C and was seen to decrease with decreasing P_{O_2}. This indicates a p-type conductivity (see Figure 4.15). The conductivity for the composition $(La_{0.8}Sr_{0.2})_{0.99}Co_{0.8}Ni_{0.2}O_{3-\delta}$ showed a similar P_{O_2} dependence as compared to $(La_{0.7}Sr_{0.3})_{0.99}Co_{0.9}Ni_{0.1}O_{3-\delta}$ and $(La_{0.6}Sr_{0.4})_{0.99}CoO_{3-\delta}$ but measured about 300 Scm^{-1} higher conductivity than the other two. This is further in agreement with figure 4.14. The P_{O_2} dependence of the conductivity for strontium rich compositions is consistent with a decrease in p-type charge carriers upon reduction of cobalt according to reaction 4.1. $(La_{0.9}Sr_{0.1})_{0.99}Co_{0.7}Ni_{0.3}O_{3-\delta}$ and $La_{0.99}Co_{0.6}Ni_{0.4}O_{3-\delta}$ showed a weaker P_{O_2} dependence and, consequently, a higher conductivity at low P_{O_2}. This suggests that these compositions are relatively inert to changes in P_{O_2} within the experimental conditions. This is also consistent with the picture that these compositions have less Co(IV) (holes) that can be reduced at low P_{O_2}s.

$$2Co_{Co}^{\cdot} + O_O^X \rightarrow \frac{1}{2}O_2(g) + V_O^{\bullet\bullet} + 2Co_{Co}^X \tag{4.1}$$

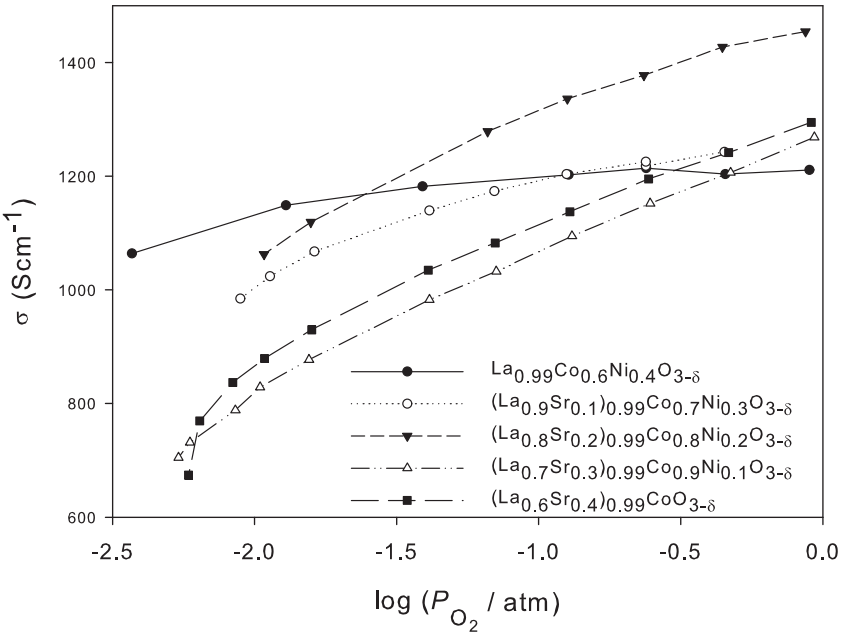

Figure 4.15: electrical conductivity as function of P_{O_2} at 1000 °C

4.4.4 Electro-catalytic activity

The polarization resistance was measured on 4 identical symmetric cells with perovskite powders as porous electrodes. The electrochemical impedance spectra will be analyzed in Chapter 6 whereas only the activation energies for the total polarization resistances are given here. Figure 4.16 plots the Arrhenius behavior of the area specific polarization resistance from 600-900 °C. Evidently $(La_{0.6}Sr_{0.4})_{0.99}CoO_{3-\delta}$ has a much lower activation energy and thus it seems as this cathode is under limitation of different physical processes. Furthermore these cathodes show large differences in polarization resistance, especially at lower temperatures due to the low activation energy of $(La_{0.6}Sr_{0.4})_{0.99}CoO_{3-\delta}$.

4.5 Discussion

The change from rhombohedral to cubic structure with increasing x can possibly be explained by a gradual change in the tolerance factor towards unity. The G_t found in table 4.1 have been calculated assuming stoichiometric perovskites, where all Nickel are found as low spin Ni(III), strontium substitution is compensated with low spin Co(IV) and the remaining trivalent cobalt are found as 50% low spin and 50% high spin according to literature. [58] G_t of $La_{0.99}Co_{0.6}Ni_{0.4}O_{3-\delta}$ increases from about 0.98 to 1.00 when all cobalt have transformed from low spin to high spin in the composition and could thus explain the smooth rhombohedral

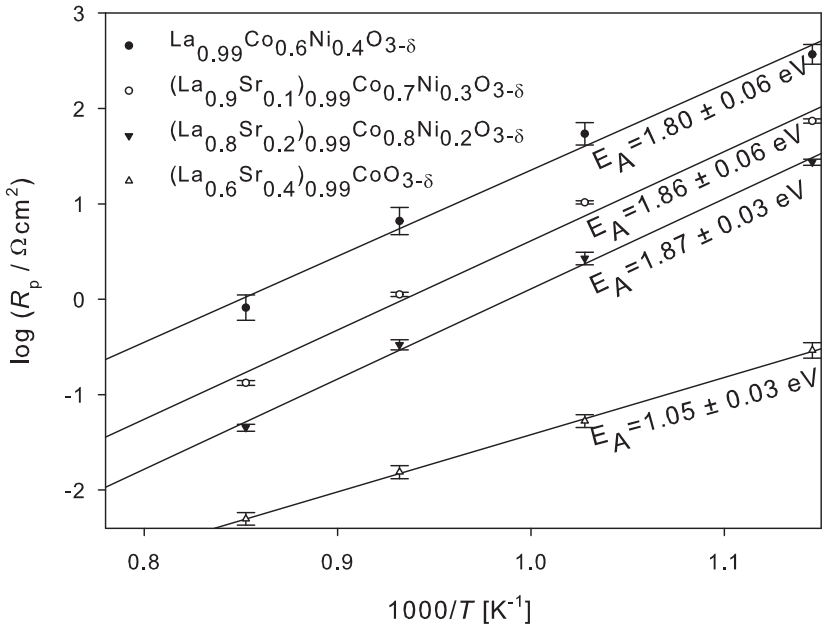

Figure 4.16: Arrhenius plots of polarization resistance of symmetric cells in ambient air with $(La_{1-x}Sr_x)_{0.99}Co_{0.6+x}Ni_{0.4-x}O_{3-\delta}$ as electrodes and CGO10 as electrolyte

to cubic transition with temperature.

Heating the nickel rich compositions to temperatures above 1000 °C appears to result in secondary phases (see Figure 4.2). Our XANES data suggests that nickel does not change valency upon substitution of strontium and is found as Ni(III) in this perovskite structure at room temperature. The decomposition of $LaNiO_3$ has been measured to start at 825 °C [25] while thermal reduction of $LaNiO_3$ was found to start at about and 575-600 °C [144], [139]. The Goldsmith factor for $LaNi(II)O_{2.5}$ is 0.93, deviating substantially from ideality. Thus it is not thermodynamical favorable to reduce Ni^{3+} to Ni^{2+} inside the perovskite structure. The hypothesis finds support in the crystallographic study on the LSCN-system where the oxide of pure lanthanum and nickel quenched from 1100 °C showed no indication of perovskite formation.[27] Thermal reduction of $LaCoO_3$ has been measured to start at 900 °C [139] or 775 °C [144]. The higher reduction temperature and a more tolerable G_t of $LaCo(II)O_{2.5}$ (0.95) indicate that any secondary phases due to thermal reduction will preferably be NiO. Figure 4.7 reveals secondary phases, which were shown by EDS mapping to consist exclusively of pure nickel oxides, which further supports this hypothesis.

Senaris el. al. [57] have reported a reduction of Co_3O_4 to CoO occurring at 920 °C when found as impurity phase in $LaCoO_3$. This is in agreement with the measured transition seen in figure 4.6 and could point toward small secondary phases below detection limit of XRD. As the A/B ratio is 0.99 there will always be found small amounts of a transition metal oxide in the samples. The fact that the reduction of Co_3O_4 to CoO was only found in the composition

lacking Ni $(La_{0.6}Sr_{0.4})_{0.99}CoO_{3-\delta}$ also indicate that secondary phases will preferably consist of NiO in all samples containing. Figure 4.2 showed also presence of K_2NiF_4-type oxides at higher temperatures or after rapid cooling. This is a result of thermal reduction at higher temperature. Reaction 4.2 comprises our hypothesis of a thermal reduction of nickel at increasing temperatures. This reaction also takes into account the formation of oxygen vacancies as a result of the thermal reduction of also seen above 1000 °C for compositions.

$$\begin{gathered} La_{1-x}Sr_xCo(IV)_xCo(III)_{0.6}Ni_{0.4-x}O_3 \rightarrow \\ (1-z)La_{1-x}Sr_xCo(IV)_{x-2\delta}Co(III)_{0.6+2\delta}Ni(III)_{0.4-x}O_{3-\delta} \\ +zNi(II)O + \tfrac{\delta}{2}O_2(g) + \\ \tfrac{z}{2}(La_{1-x}Sr_x)_2Co(III)_{2x}Co(II)_{1-2x}O_4 \end{gathered} \tag{4.2}$$

This reaction comprise the trends observed within our measured temperature- and P_{O_2}-regime, where z is the unknown degree to which the secondary phases are formed at high temperatures or low P_{O_2}. Not included is the spin transitions, which in known to occur on the cobalt ions in these perovskites [58], thus the number in brackets designates an arbitrary spin state.

Electronic conduction in these perovskite are believed to occur in the conduction band set up by the overlapping O-2s and TM-3p orbitals, which in turn is dependant on unit cell structure of the perovskite [22]. The conductivity of $La_{0.99}Co_{0.6}Ni_{0.4}O_{3-\delta}$ shows a parabolic temperature dependence (see figure 4.14) which points towards an electronic conductivity that follows the small polaron mechanism as described by Equation 4.3. Figure 4.17 plots log (σT) vs 1/T and depicts a good agreement to the small polaron mechanism for $La_{0.99}Co_{0.6}Ni_{0.4}O_{3-\delta}$. The conductivities of $(La_{0.9}Sr_{0.1})_{0.99}Co_{0.7}Ni_{0.3}O_{3-\delta}$ and $(La_{0.8}Sr_{0.2})_{0.99}Co_{0.8}Ni_{0.2}O_{3-\delta}$ also fit reasonably well according to this mechanism at lower temperatures but start deviating from linearity at approximately 900 °C and 700 °C respectively. These onset temperatures agrees well with what was measured with thermogravimetry and hence this sudden change is believed to be due to the thermal reduction of cobalt which decreases the charge carrier concentration. The conductivities of $(La_{0.7}Sr_{0.3})_{0.99}Co_{0.9}Ni_{0.1}O_{3-\delta}$ and $(La_{0.6}Sr_{0.4})_{0.99}CoO_{3-\delta}$ did not fit according to this conduction mechanism.

$$\sigma(T) = pe\mu_p = \frac{A}{T}exp\left(\frac{-E_A}{kT}\right) \tag{4.3}$$

Mizusaki *et al.* [108] have argued for a relationship between the electronic conduction and the lattice parameters where a transition from small polaron- to metallic-type conduction occurs when decreasing the rhombohedral angle to around 60.3-60.4°. The small polaron conduction (see Equation 4.3) describes this behaviour with a thermally activated hopping mechanism for the rhombohedral unit cell and a reciprocal temperature dependence

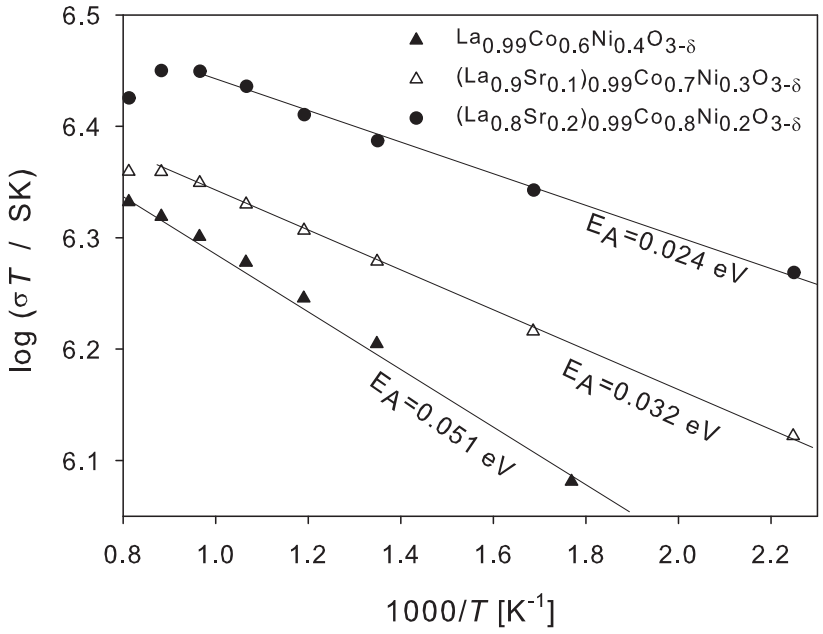

Figure 4.17: Fitting of conductivities to the small polaron conduction mechanism.

at temperatures where the unit cell is cubic or close to cubic. This might be true for $(La_{1-x}Sr_x)_sCoO_{3-\delta}$ $0< x <0.5$. However substitution of nickel appears to alter this picture. The small polaron behaviour is clearly seen for $La_{0.99}Co_{0.6}Ni_{0.4}O_{3-\delta}$ in Figure 4.14 but the transition seems to occur at about 325 °C, where the rhombohedral angle is 60.7. Comparing the electronic conductivity of $(La_{1-x}Sr_x)_{0.99}Co_{0.6+x}Ni_{0.4-x}O_{3-\delta}$ x = 0.1 - 0.3 to that of the purely cobalt containing compositions $La_{1-x}Sr_xCoO_3$ x = 0.1 - 0.3 measured by Mizusaki *et al* [108] reveals that introducing nickel into the perovskite will increase the metallic character. In fact, $LaNiO_3$ has been determined metallic at room temperature [145], [54], [146] while $LaCoO_3$ is a room temperature insulator and undergoes a semiconductor-metallic transition first at about 750 °C [147]. The room temperature conductivity of $La_{0.99}Co_{0.6}Ni_{0.4}O_{3-\delta}$ was also measured to about 1200 Scm^{-1}, which clearly shows the effect nickel doping has on conductive properties when substituted into $LaCoO_3$. This could be due to differences in crystal structure between the two perovskites where $LaCoO_3$ is rhombohedral while $LaNiO_3$ is believed to be cubic. However, $(La_{0.9}Sr_{0.1})_{0.99}Co_{0.7}Ni_{0.3}O_{3-\delta}$ showed metallic conductivity at room temperature despite a pronounced rhombohedral structure.

The main parameter determining the electronic conductivity is probably instead the electronic structure. Octahedral Ni in $LaNiO_3$ has the low spin configuration, $t_{2g}^6e_g^1$, at room temperature while the corresponding configuration for cobalt is t_{2g}^6. Nickel will thus have one electron occupying one of the e-orbitals, which is geometrically directed towards the oxygen ions while the electrons on the cobalt ions will exclusively be found in t-orbitals

with orientations towards lanthanum ions. The transition from low spin Co(III), t_{2g}^6, to intermediate spin Co(iii) $t_{2g}^5 e_g^1$ or high spin Co^{3+} $t_{2g}^4 e_g^2$, measured in numerous studies will excite electrons to the e-orbitals and thereby increasing its overlap to form a conduction band. [56], [55], [59], [60], [31], [61], [62] The band gap between the low spin state, t_{2g}^6 and high spin state, $t_{2g}^4 e_g^2$ is only 0.05 eV [16] thus thermal energy is sufficient to excite electrons and transform the σ-orbital into an itinerant conduction band explaining the semiconducting behaviour at low T. Accordingly, the electronic conductivity is mainly dependant on crystal field splitting of d-orbitals and the transitions of electrons in between the energetically distinguished states, which is in turn dependant on x and T [57], [58]. This however does not rule out a correlation between the crystal geometry and conductivity. In fact Mineshige et. al.[34] found that the metal-insulator transition in $(La_{1-x}Sr_x)_sCoO_{3-\delta}$ $0< x <0.7$ always occurred when the Co-O-Co angle was $\approx 165°$, independently of x, T or P_{O_2}. Whether this correlation is direct or indirect is not yet clear but was argued by the authors using the ZSA-theory [73] to be a secondary effect of an increased band overlap between O-2s and Co-3d orbitals with increasing x and/or T.

At room temperature strontium doped lanthanum cobaltites are effectively p-type conducting materials as the oxidation of Co(III) to Co(IV) introduces acceptor levels in the charge carrying Co-arrays. Above a percolation threshold, x> 0.25, [58], [110] strontium doping introduces metallic or semi-metallic properties. As seen in Figure 4.14 the conductivities decrease with temperature. This is an effect not only related to spin-disorder scattering but is further a result of thermal reduction of Co(IV), which successively decreases the extent of acceptor levels in the crystal. This is counterbalanced by the transitions to intermediate or high spin cobalt which increases the width of the itinerant conduction band. The conductivity of all compositions was measured to range from 1000 to 4000 Scm^{-1} across the compositional and temperature range and were close to what as reported by Huang et. al. [21] for the $(La_{0.8}Sr_{0.2})_{0.99}Co_{0.8}Ni_{0.2}O_{3-\delta}$ and $(La_{0.7}Sr_{0.3})_{0.99}Co_{0.9}Ni_{0.1}O_{3-\delta}$ but substantially higher than for $La_{0.99}Co_{0.6}Ni_{0.4}O_{3-\delta}$. Small-polaron activation energies for the compositions $(La_{1-x}Sr_x)_sCo_{1-y}Ni_yO_{3-\delta}$ x=0-0.2 are further about 30-40 % lower than what was reported in the aforementioned study (see figure 4.17).

Figure 4.15 plots the conductivities as function of P_{O_2} at 1000 °C and show an increasing dependence on P_{O_2} up to x=0.2. Above this approximate percolation threshold the conductivities appears to have a similar P_{O_2} dependence though the absolute values differs with $(La_{0.8}Sr_{0.2})_{0.99}Co_{0.8}Ni_{0.2}O_{3-\delta}$ being the best conductor. This could be due to that both nickel and strontium levels have reach an approximate percolation threshold giving rise to several conductive pathways. The conductivities decrease with P_{O_2} which confirms a p-type conduction as decreasing P_{O_2} will decrease the number of holes according to equation 4.1. It seems that, for $x \geq 0.2$, electronic conductivities as function of both temperature and P_{O_2} resembles each other and that the higher charge carrier concentration in $(La_{0.6}Sr_{0.4})_{0.99}CoO_{3-\delta}$ as a result of electro neutrality $[Sr_{Sr}^X] = p + 2[V_O^X]$ is compensated in the nickel containing compositions by the increased conduction band introduced by orbital overlap between Ni-3p,σ and O-2p. This is in accordance with a study by Mineshige et. al. [34] who measured insulator-metal transition at x=0.25 in $(La_{1-x}Sr_x)_sCoO_{3-\delta}$ with a sudden subsequent change in the Co-O distance and Co-O-Co angle. They explained this transition according to the

theory developed by Zaanen, Sawatzky and Allen [73] with a closing of the charge transfer band gap in $LaCoO_3$ by a band formation of acceptor states introduced by strontium substitution. In the case of increasing x in $(La_{1-x}Sr_x)_sCo_{1-y}Ni_yO_{3-\delta}$, where nickel is present on B-site, a narrow itinerant electron band exists at room temperature for x=0 and this transition seems instead to be of the type small polaron to metal.

Another effect of the electronic structure changing from low to high spin cobalt is the lattice expansion as a function of temperature, which is substantially higher than other perovsite type oxides used in SOFC components. Thermal expansion coefficient (TEC) is about $22{\cdot}10^{-6}$ K^{-1} for $LaCoO_3$ and $10{\cdot}10^{-6}$ K^{-1} for $LaNiO_3$ [22]. Our measured TEC for $La_{0.99}Co_{0.6}Ni_{0.4}O_{3-\delta}$ can be expressed as a linear combination of the TEC of these end member perovskites, suggesting that nickel doping does not influence the electronic configuration of cobalt dramatically. This stand in contrast to Rao *et al.*[16] who claim that the low spin to high spin transition is suppressed by nickel doping. TEC does not seem to increase towards that of $LaCoO_3$ when increasing x in $(La_{1-x}Sr_x)_sCo_{1-y}Ni_yO_{3-\delta}$ but instead remains relatively unchanged. This could partly be explained by suppression of spin transitions but is more likely due to a reduced concentration of trivalent cobalt ions that potentially can undergo such a transition. As seen in equation 4.2 the number of trivalent cobalt that can undergo spin transition is independent on x and only moderately dependent on T. The onset temperature of the increase in expansion at higher temperature are closely related to our results from thermograviometric analysis and is attributed to a reduction expansion. The extra electron when cobalt is reduced expands its Shannon radius from 0.53 $\mathring{A}$ (HS) to 0.61 $\mathring{A}$ (HS) in 6-fold coordination, which explains the higher TEC for $LaCoO_{3-\delta}$

Figure 4.8 illustrates oxygen vacancy formation in the samples $(La_{1-x}Sr_x)_{0.99}Co_{0.6+x}Ni_{0.4-x}O_{3-\delta}$ (x = 0-0.4) as function of temperature. The measurements show that δ increase linearly with both strontium doping and temperature in the high temperature regime and that the onset temperture of thermal reduction decreases with x. The effect of thermal reduction is seen also when measuring lattice expansion as function of temperature, which for strontium rich compositions takes off at higher temperatures. (see Figure 4.5). The generally accepted idea is that strontium oxide doping oxidises trivalent to tetravalent cobalt near room temperature and that Co(IV) is reduced back to Co(III) at increasing temperatures. This was further supported by XANES measurements (see figure 4.9 and 4.10) which showed linear shifts in oxidation state of cobalt from $LaCo(III)O_3$ to higher valency upon introduction of strontium. Moreover high temperatures XANES indicated that the reduction is exclusively associated with cobalt. Contradictory to these findings is the study by Grice *et. al.* [143], who employed XANES measurements to argue that both cobalt and nickel remain in trivalent oxidation state upon introduction of strontium at room temperature and that oxygen vacancies instead fully compensate the oxidation.

Figure 4.8 also shows that $La_{0.99}Co_{0.6}Ni_{0.4}O_{3-\delta}$ desorbs oxygen first at temperatures above 1000 °C. This is somewhat surprising as the thermal reduction temperature for both end member $LaCoO_3$ and $LaNiO_3$ have been reported to 900 °C and 600 °C respectively. [139] Teraoka et. al. [9] measured the same temperatures to 777 °C for ($LaCoO_3$) and 577

°C for ($LaNiO_3$) but also noted a major decrease in oxygen desorption corresponding to reduction of trivalent transition metal in the sample $La_{0.6}Sr_{0.4}Co_{0.8}Ni_{0.2}O_3$ compared to $La_{0.6}4Sr_{0.4}CoO_3$.[10] These result and our thermograviometric measurements point toward a stabilizing effect Ni and Co have on each other in strontium an nickel doped lanthanum cobaltite.

Electrochemical impedance spectroscopy showed that the polarization resistance decrease dramatically with increasing strontium content (x). The analysis of these spectra will be reported in greater detail in a Chapter 6 and we here limit ourselves to note a correlation between substantially different oxygen vacancy concentrations and polarization resistances in the temperature regime measured. These results are also in contrast to what was report by Huang *et. al.* who measured a lower resistance for $(La_{0.8}Sr_{0.2})_{0.99}Co_{0.8}Ni_{0.2}O_{3-\delta}$ as compared to $(La_xSr_{1-x})_{0.99}CoO_{3-\delta}$. The activation energies are approximately the same for $x \leq 0.2$ while its was substantially lower for $(La_{0.6}Sr_{0.4})_{0.99}CoO_{3-\delta}$. This indicate that the cells with $(La_{1-x}Sr_x)_{0.99}Co_{0.6+x}Ni_{0.4-x}O_{3-\delta}$ x=0-0.2 are under limitation of another electrochemical process as compared to $(La_{0.6}Sr_{0.4})_{0.99}CoO_{3-\delta}$. As seen in figure 4.8, $(La_{0.6}Sr_{0.4})_{0.99}CoO_{3-\delta}$ has a substantial concentration of vacancies at the temperatures where our electrochemical measurements were performed while the other compositions show no or very few vacancies at the same temperature. This could possibly indicate that the reaction mechanism of $(La_{0.6}Sr_{0.4})_{0.99}CoO_{3-\delta}$ involves bulk and/or surface vacancies whereas the mechanism of other electrodes follows a different path.

4.6 Conclusions

We have investigated the materials system $(La_{1-x}Sr_x)_sCo_{1-y}Ni_yO_{3-\delta}$ by experimental studies of the compositions $(La_{1-x}Sr_x)_{0.99}Co_{0.6+x}Ni_{0.4-x}O_{3-\delta}$ $0<x<0.4$ with the aim of finding a suitable electrode material for SOFC as well as studying whether Ni(II) can be stabilised within this perovskite. The nonstoichiometric coefficient, δ increases linearly with T and x in the high temperature region, which has been ascribed as an effect of reduction of Co(IV). These data showed further that Ni(III) was retained to about 1000 °C. Above this temperature HTXRD showed evidence of impurity phases, which were indicated by SEM-analysis to consist of NiO. XANES measurements have shown that cobalt is exclusively oxidized upon strontium substitution at room temperature and is reduced back to a lower valency upon heating. We have found that a transition from small polaron to itinerant conduction occurs with increasing x in $(La_{1-x}Sr_x)_{0.99}Co_{0.6+x}Ni_{0.4-x}O_{3-\delta}$. The conductivity was measured from 1000-4000 Scm^{-1} across the entire temperature and compositional range. Thermal expansion coefficient measured with both HTXRD and dilatometry showed good agreement. Dilatomery data also showed a large expansion increase at higher temperature which could be correlated with thermal reduction of Co(IV), measured both with thermograviometry and XANES. The polarization resistance decreased with x, which could perhaps be a result of an increase in δ, necessary for establishing ionic conduction through the perovskite and catalytically active sites at the surface. i-v measurements showed an equally good performance in anodic and cathodic direction as well as a potential to enhance the electro-catalytic activity by polarization.

Chapter 5

Defect structure, electronic conductivity and expansion properties of $(La_{1-x}Sr_x)_sCo_{1-y}Ni_yO_{3-\delta}$

5.1 Abstract

This study reports on oxygen nonstoichiometry, electronic conductivity and lattice expansion of three compositions as function of T and P_{O_2} in the $(La_{1-x}Sr_x)_sCo_{1-y}Ni_yO_{3-\delta}$(x=0.1,y=0.4; x=0.1,y=0.3; x=0.2,y=0.2) materials system. The nonstoichiometry data were successfully fitted using the *itinerant electron model* which indicates the existence of delocalized electronic states. This was also reflected in the high electronic conductivities, above 1000 S cm^{-1}, measured for all three compositions. The electronic conductivity was shown to decrease linearly with the oxygen nonstoichiometry parameter, δ, supporting that the conductivity is dependent on p-type charge carriers. Comparing calculated p-type mobilities with data reported in literature on $La_{1-x}Sr_xCoO_3$ indicated that Ni-substitution into $(La_{1-x}Sr_x)_sCoO_{3-\delta}$ increases the p-type mobility. The electronic conductivity was also found to be dependent on *intrinsic* charge related to spin excitations and Ni substitution rather than the p-type charge. A conductivity mechanism is hypothesized including a metallic like conductivity of the p-type charge and a small polaron conductivity of the *intrinsic* charge. Lattice expansion as function of T and δ was successfully described using first and second order thermal and chemical expansion coefficients. Substituting 10 % Co with Ni in $(La_{0.6}Sr_{0.4})_{0.99}CoO_{3-\delta}$ was found to decrease the apparent thermal expansion with about 25 %.

5.2 Introduction

Sr substituted $LaCoO_3$ has attracted broad attention due to interesting properties, such as electronic spin transitions, metallic like conductivity and its the ability to host vacancies in the oxygen sublattice. [108], [76], [148], [34], [110], [142], [149], [24], [109], [80], [77], [45]. The Sr^{2+} oxidizes the Co^{3+} ion partially which in turn introduces delocalized electronic states. The electronic structure in $(La_{1-x}Sr_x)_sCoO_{3-\delta}$ is also dependent on electronic spin on the Co^3, which influences both magnetic, conductive and expansion properties. Additionally, partial substitution of Co with Ni on B-site introduces further change in the electronic structure of the perovskite.[16], [150]

The degree of the Co oxidation is not fixed but a function of T and P_{O_2} and is related to oxygen vacancy formation via the electro neutrality principle. Also the degree spin transition on the Co^{3+} ion is a function of T and P_{O_2} and this allows us to study the electronic and defect structure in more detail. The electronic structure and the oxygen vacancies have been correlated in various defect models. [24], [80], [151] The *itinerant electron model* developed by Lankhorst and coworkers is the one receiving the broadest acceptance and appears to describe the defect chemistry of $(La_{1-x}Sr_x)_sCoO_{3-\delta}$ and related compounds well.[79]

A number of papers have measured and analyzed the electronic conductivity (σ) of these materials with respect to T, P_{O_2}, δ and lattice parameters in an attempt to describe the conduction mechanisms but no clear consensus has emerged so far. Literature indicate instead that several materials properties might affect the electronic conductivity of $(La_{1-x}Sr_x)_sCoO_{3-\delta}$ as σ has been correlated with both Sr substitution levels, oxygen nonstoichiometry and bond angles. [108], [142], [152]

Expansion of the lattice is not only dependent on the temperature dependency of its atomic vibrations but also on its the electronic and defect structure. Reduction of the Co^{4+} to Co^{3+} at increasing temperatures or decreasing P_{O_2} expands its Shannon radii and thus also the lattice. Additionally, the spin transitions have been argued to add an extra dimension to the lattice expansion as transitions from electronic low spin to intermediate or high spin states increase the Shannon radii of the Co ions.[32] The strain of $(La_{1-x}Sr_x)_sCoO_{3-\delta}$ as function of T, P_{O_2} and x has been reported in several studies in which the total *apparent* thermal expansion is often separated into a thermal and chemical expansion contribution. [142], [153], [154], [44], [155] The chemical expansion coefficient is related to the oxygen nonstoichiometry, which in turn is associated with the Co^{4+}/Co^{3+} ratio through the electro neutrality principle .[156]

Partial substitution of Co with Ni in $(La_{1-x}Sr_x)_sCoO_{3-\delta}$ has earlier been shown to increase electronic conductivity [22], [15] and decrease lattice expansion[21], properties which are of technological interest for instance in solid oxide fuel cells (SOFCs). We have studied the electronic and expansion properties of the compositions $(La_{0.8}Sr_{0.2})_{0.99}Co_{0.8}Ni_{0.2}O_{3-\delta}$, $(La_{0.7}Sr_{0.3})_{0.99}Co_{0.9}Ni_{0.1}O_{3-\delta}$ and $(La_{0.6}Sr_{0.4})_{0.99}Co_{0.9}Ni_{0.1}O_{3-\delta}$ in more detail in an attempt to clarify the effect of Ni substitution in $(La_{1-x}Sr_x)_sCoO_{3-\delta}$. We have also studied the concentration oxygen vacancies (δ) in these compositions as function of T and P_{O_2} in order

to test whether their defect structure can be described by the *itinerant electron model*. [79] The results are discussed with respect to results in recent literature.

5.3 Experimental

Powder and dense sintered bars of $(La_{0.6}Sr_{0.4})_{0.99}CoO_{3-\delta}$ (LSC40), $(La_{0.7}Sr_{0.3})_{0.99}Co_{0.9}Ni_{0.1}O_{3-\delta}$ (LSCN3010), $(La_{0.6}Sr_{0.4})_{0.99}Co_{0.9}Ni_{0.1}O_{3-\delta}$ (LSCN4010) and $(La_{0.8}Sr_{0.2})_{0.99}Co_{0.8}Ni_{0.2}O_{3-\delta}$ (LSCN2020) were fabricated as described in [2]. The abbreviated notations in brackets will be used throughout the paper. An exact stoichiometric A/B ratio of one is practically impossible to synthesize as it is impossible to weigh the starting compounds in such an exact manner. We have for this reason deliberately chosen an A/B-ratio of 0.99 in order to know which type of secondary phases to expect. The stoichiometric accuracy is such that we can assume the composition to be A-site substoichiometric. Bars used for electronic conductivity measurements were cut to dimensions of approximately 2×2×25 mm^3 whereas bars used in the dilatometry measurements were of the dimensions 4×4×20 mm^3. Geometrically measured densities of the sintered samples were above 95 % of theoretical density calculated from XRD data. Powder samples were analyzed thermograviometrically with a NETZSCH STA 409C/CD in order to estimate oxygen non-stoichiometry as a function of temperature. 300 mg of powder sample was heated and cooled in 50 ml min^{-1} airflow to 1300 °C with a heating rate of 10 °C min^{-1}. Cooling rate was set to 1°C min^{-1} down to 600 °C followed by a rapid cooling of 10 °C min^{-1} to room temperature. Data was taken from the cooling ramp of the measurement (oxidation). A differential NETZSCH TG 439 was used to measure oxygen nonstoichiometry as function of P_{O_2} at 4-5 different temperatures in the range 600-1000 °C. About 40 mg of powder was used in the experiments. Powder samples equilibrated within less than one minute as seen in Figure 5.3. The weight of the sample was measured for 2 hours after each change in P_{O_2} to assure that the stoichiometric change was fully equilibrated. In some cases long term transients were observed. Data from these transients (T, P_{O_2}) were not used in the fitting of measured stoichiometry changes to theoretical defect chemistry models. Data from oxidative (increasing) steps in P_{O_2} were used in the defect chemistry analysis.

Expansion measurements were carried out on sintered bars with a NETZSCH DIL 402C. The temperature was scanned from room temperature to 1300 °C with 2 ml min^{-1} and in airflow of 50 ml min^{-1}. Data were taken from the cooling ramp of the measurement (oxidation). Expansion measurements as function of P_{O_2} were carried out at 700-1000 °C from $P_{O_2} \approx$ 0.21-0.005 atm. The samples relaxed for 2-4 hours after each step change in P_{O_2} to assure that equilibrium had been reached. Equilibrated expansion data were taken from the oxidative (increasing) P_{O_2}-steps. Figure 5.3 shows the results of a typical expansion measurement.

The electrical conductivity was measured with a 4 point probe DC-technique. Sintered bars were wired with platinum threads and painted with platinum paste at both ends. The resistance was measured with a Keithley 2700 multimeter. Voltage probes were separated 0.5 cm apart and measurements were performed at temperatures ranging from 700-1000 °C

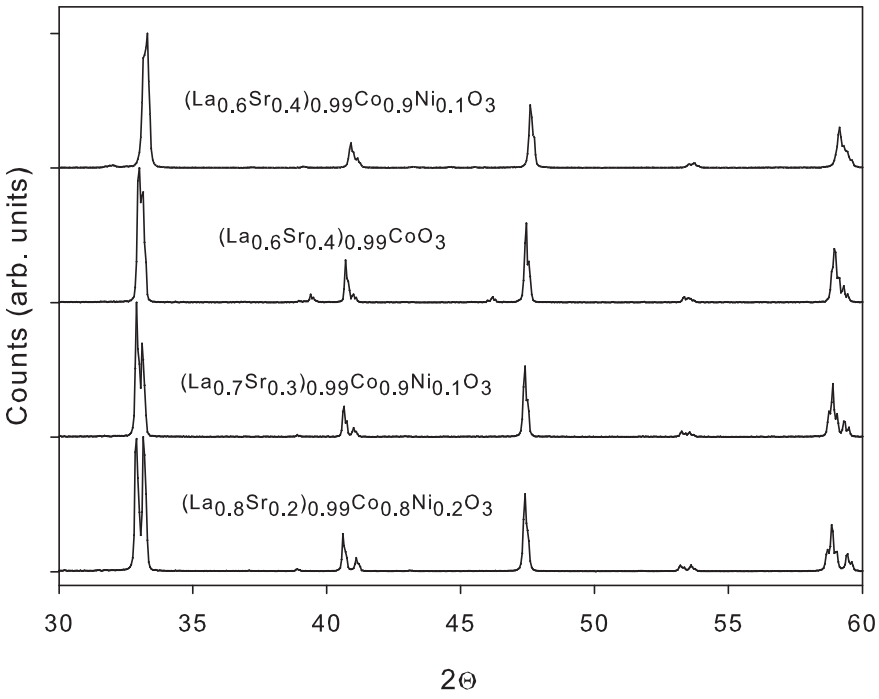

Figure 5.1: Powder X-ray diffraction pattern of the studied compositions.

and P_{O_2} from 0.21-0.001 atm. In all experiments the P_{O_2} was controlled by mixing of N_2 and O_2.

Equilibrium was considered reached in all experiments if the relative change was less than about one percentage within 30 min. The measurement under this specific condition has not been reported in this paper if equilibrium was not reached.

5.4 Results

5.4.1 Electronic and defect structure

Thermograviometric (TG) analysis as function of both temperature and P_{O_2} was conducted on powder samples in order to study the oxygen nonstoichiometry parameter, δ. This parameter corresponds the fraction of missing oxide ions per perovskite formula unit. Figure 5.4 plots changes in δ for LSC40, LSCN4010, LSCN3010 and LSCN2020 as function of temperature. The onset temperature of lattice oxygen loss is seen to increased with decreasing Sr content. This has been discussed in more detail for $(La_{1-x}Sr_x)_sCo_{1-y}Ni_yO_{3-\delta}$ in a previous study to which the reader is referred for further details.[2] Comparing LSC40 and LSCN4010

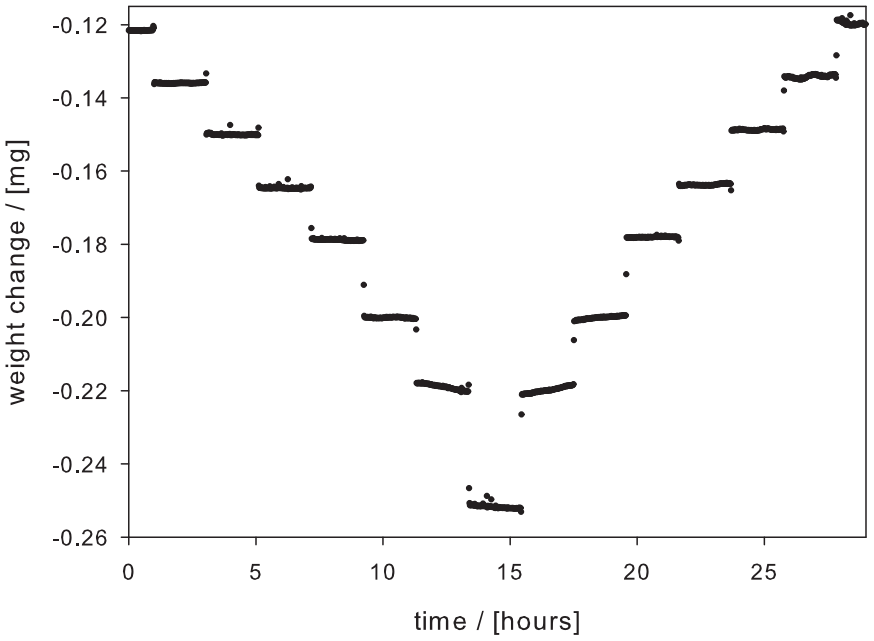

Figure 5.2: Weight equilibration upon sudden changes in oxygen partial pressure at 750 °C for LSCN4010. $\Delta(\log P_{O_2})$ is approximately 0.15.

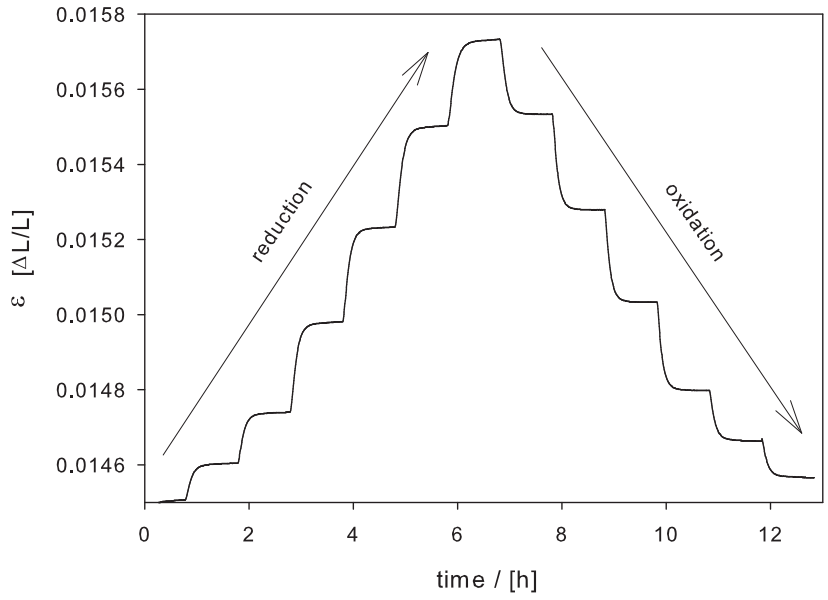

Figure 5.3: Expansion equilibrations upon changes in P_{O_2} at 800 °C for LSCN4010. $\Delta(\log P_{O_2}$.

allows us to study the effect of Ni substitution on B-site in LSC40. Both compositions were shown to have approximately the same the onset temperature of oxygen loss. However, a different behavior is observed above the onset temperature where δ increases more strongly with T for LSCN4010 as compared to LSC40. Above 800 °C the increase in δ is approximately linear with respect to temperature with coefficients of 4.3 $\cdot 10^{-4}$ K^{-1}) for LSCN4010 and 3.1 $\cdot 10^{-4}$ K^{-1} for LSC40. Included in Figure 5.4 is also the predicted δ calculated using the *itinerant electron model* as describe further below. The results show good agreement between calculated oxygen nonstoichiometry and measured data for LSCN2020 and reasonable agreements for LSCN4010 and LSCN3010.

The *itinerant electron model* [80] is today the most widely used defect model for mixed ionic and electronic conductors (MIECs) such as $(La_{1-x}Sr_x)_sCoO_{3-\delta}$. This particular materials shows high electronic, "metallic-like" conductivity, which is indicative of substantial levels of delocalized electronic charge. In this model electrons from the oxidation of oxide ions are transferred into a conduction band which raises the Fermi level. This means that the positive charge introduced by Sr substitution in $(La_{1-x}Sr_x)_sCo_{1-y}Ni_yO_{3-\delta}$ is not associated with the Co ion but is free to move as a delocalized charge carrier. It means further that the entropy of the electrons and defect-defect interactions can be neglected. The relationship between the oxygen nonstoichiometry in an oxide and the chemical potential of oxygen is expressed in Equation 5.1.

$$\mu_{O_2} = \Delta E_{ox} - \frac{4(2[V_O^{\bullet\bullet}] - [Sr'_{La}])}{g(E_F)} - T\Delta S_{ox} - 2RTln\left(\frac{[V_O^{\bullet\bullet}]}{(3 - [V_O^{\bullet\bullet}])}\right) \tag{5.1}$$

ΔE_{ox} and ΔS_{ox} are the energy and entropy associated with filling two vacancies with an oxygen molecule from vacuum and simultaneously adding four electrons at the fermi level. $g(E_F)$ is the density of states at the Fermi level, which is the number of states available for occupation at this specific energy level. $[V_O^{\bullet\bullet}]$ is the concentration of oxygen vacancies and related to the oxygen nonstoichiometry parameter as δ= 3$[V_O^{\bullet\bullet}]$. μ_{O_2} is a function of T and P_{O_2} calculated using the empirical expression according to Equations 5.2-5.3.[157]

$$\mu_{O_2}^{gas} = \mu_{O_2}^{0,gas} + RT\ln(P_{O_2}) \tag{5.2}$$

$$\mu_{O_2}^{0,gas} = RT\left(n_1 + \frac{n_2}{T} + n_3\ln(T) + n_4\ln\left(1 - e^{\frac{-n_5}{T}}\right)\right) \tag{5.3}$$

where T and P_{O_2} are found in K and in atm. n_1 = -1.225, n_2 = -1045 K, n_3 = -3.5, n_4 = 1.013, n_5 = 2242 K.[157]

The change in oxygen nonstoichiometry was measured isothermally as function of P_{O_2} at various temperatures between 600-1000 °C for the compositions LSCN2020, LSCN3010 and LSCN4010. These data are reported in Figures 5.5 to 5.7, where the solid lines represent the best linear least square fit to the *itinerant electron model*. Our experimental data shows

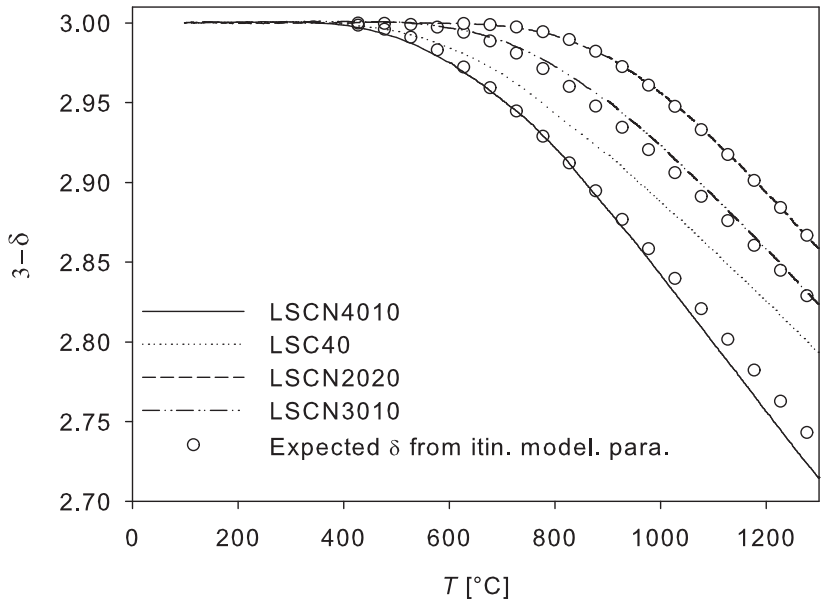

Figure 5.4: 3-δ as function of temperature for LSCN4010, LSC40, LSCN3010 and LSCN2020. Rings denote predicted oxygen nonstoichiometry calculated for the three Ni containing samples using the *itinerant electron model*. Substituting 10 % Co with Ni in LSC40 increases the linear trend with which oxygen vacancies are formed upon heating whereas increasing [Sr] in LSCN3010 to 40 % lowers the onset temperature of lattice oxygen loss.

reasonably good agreement to the model. The parameters ΔE_{ox}, ΔS_{ox} and $g(\varepsilon_F)$ are reported in Table 5.1 together with data for LSC40 reported in [142] and $La_{0.8}Sr_{0.2}CoO_{3-\delta}$ [80]. Table 5.1 also shows the sum of square deviations, χ_δ which is defined as $(\Sigma(logP_{O_2,measured(i)} - log_{O_2,calculated(i)})^2)/(N-3)$, where N is the total number of measurements (N=32-50) and $P_{O_2,measured(i)}$ is the measured P_{O_2} of the i'th measurement.

5.4.2 Electronic conductivity

The electrical conductivity of LSCN2020, LSCN3010 and LSCN4010 was measured as function of temperature and P_{O_2}. In the temperature range (100-1000 °C) and P_{O_2} range (0.001-1 atm) the electrical conductivity was 1000-2000 S cm^{-1} for all compositions. The ionic conductivity of these materials is lower than 1 S cm^{-1} [18], and consequently the transference number is approximately unity. Thus the measured electrical conductivity can be approximated as the electronic conductivity of the materials. Substituting SrO into $LaCoO_3$ is effectively a *p*-type doping as positive holes are introduced when Co is oxidized. This explains the substantial increase in the measured electronic conductivity with increasing x in $(La_{1-x}Sr_x)_sCoO_{3-\delta}$.[108]

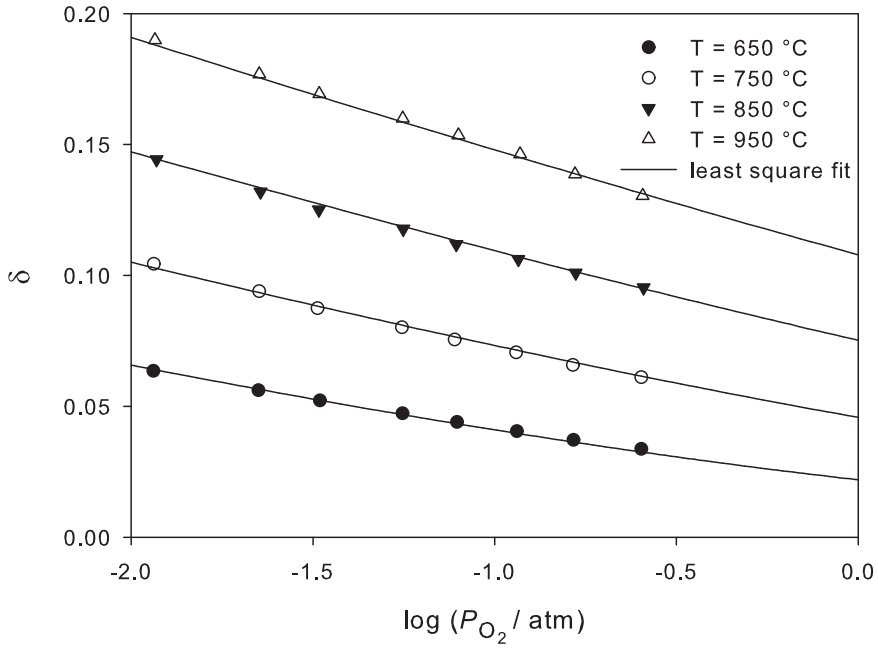

Figure 5.5: δ as function of P_{O_2} for LSCN4010 at various temperatures. Lines represent best fit to the *itinerant electron model* (see Equation 5.1)

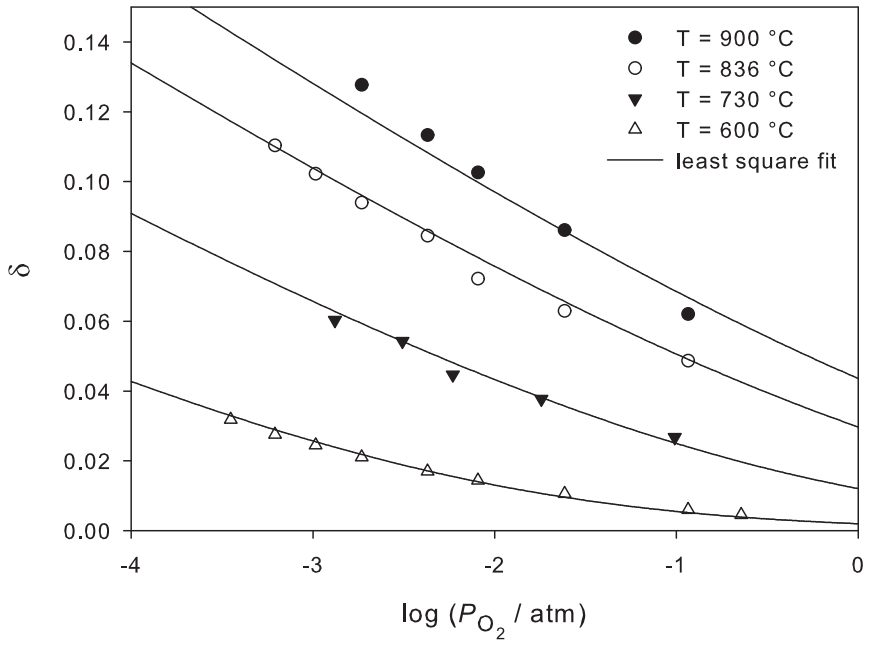

Figure 5.6: δ as function of P_{O_2} for LSCN3010 at various temperatures. Lines represent best fit to the *itinerant electron model* (see Equation 5.1)

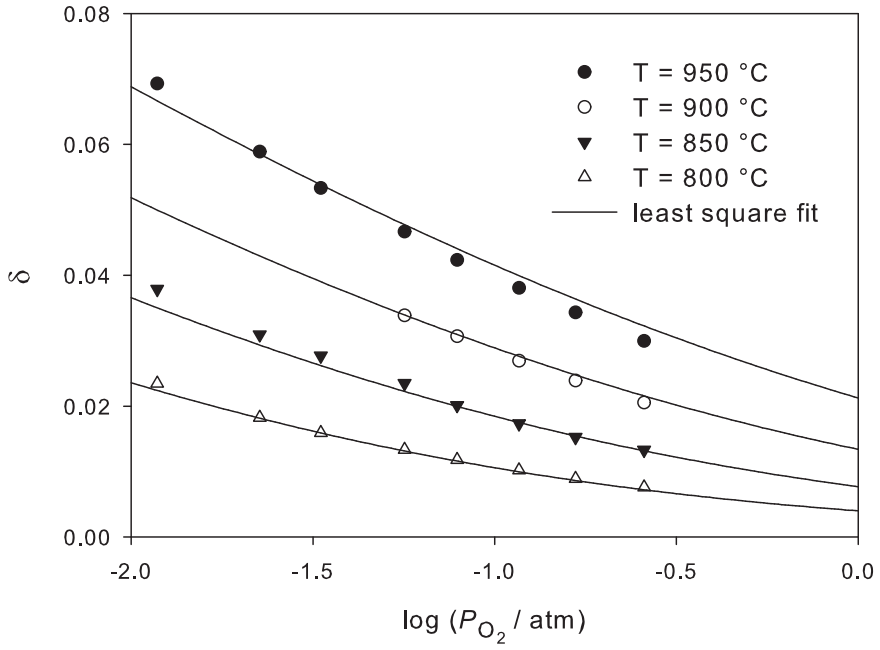

Figure 5.7: δ as function of P_{O_2} for LSCN2020 at various temperatures. Lines represent best fit to the *itinerant electron model*. (see Equation 5.1)

Table 5.1: Least square fitting parameters to the *itinerant electron model* for LSCN2020, LSCN3010, LSCN4010 and LSC40 [142], [80]. ΔE_{ox} and ΔS_{ox} are the enthalpy and entropy of molecular oxygen in the oxide. $g(\varepsilon_F)$ is the density of states at the Fermi level.

	ΔE_{ox} [(kJmol^{-1})]	Δ_{ox} [(Jmol^{-1} K^{-1})]	$g(\varepsilon_F)$ [(kJ^{-1}mol)]	χ_δ
LSCN2020	-320.5	76.4	0.0168	0.0037
LSCN3010	-299.0	88.9	0.0148	0.0149
LSCN4010	-261.3	98.1	0.0192	0.0011
LSC40 [142]	-217.2	141.2	0.0188	
$La_{0.8}Sr_{0.2}CoO_{3-\delta}$ [80]	-334.1	69.5	0.0159	

The oxygen nonstoichiometry was calculated using the *itinerant electron model* and the fitting parameters listed in Table 5.1 for each composition and at each condition (T, P_{O_2}) the conductivity was measured. The conductivity as function of δ is plotted in Figures 5.8 to 5.10 for the three compositions, LSCN2020, LSCN3010 and LSCN4010. At increasing T or decreasing P_{O_2} Co undergoes reduction, which increases δ at the expense of p-type charge carriers, c_p. This occurs as a consequence of the electro-neutrality principle expressed in Reaction 5.4. Consequently, c_p is expected to be a function of T and P_{O_2} and should in theory equal zero at the conditions where $2\delta=[Sr'_{La}]$. Figures 5.8 to 5.10 shows clearly that σ decreases linearly with δ which strongly supports a p-type conductivity in these compositions.

However, the results also show a substantial conductivity at the conditions where c_p is zero, which indicate that the *p*-type conductivity cannot fully describe the conductive behaviour alone. Nominal $LaCoO_3$ is known to conduct charge at high temperatures due to transitions from low to intermediate or high spin state on the Co ions which excites electrons to a narrow itinerant band.[58] $LaNiO_3$ is a reasonable electronic conductor already at room temperature due to one delocalized electron in the d-orbitals of the Ni-ions (the electronic structure, $t_{2g}^6 e_g^1$, is discussed in [36] and [2] to which the reader is referred for further details). It is therefore a fair assumption that there is also an *intrinsic* contribution to the total electronic conductivity, which is independent on *p*-type charge carriers introduced by Sr substitution. This has led us to discriminate between two different contributions to the total conductivity.

1. The *p*-type *conductivity* which is related to the Sr content and the concentration of oxygen vacancies.

2. The *intrinsic* conductivity which is *not* dependent on the degree of Co reduction and Sr content. This conductivity is believe to arise mainly from spin transitions on the Co ions and from the extra electron introduced by the Ni substitution.

$$2Co_{Co}^{\cdot} + O_O^X \rightarrow \frac{1}{2}O_2(g) + V_O^{\bullet\bullet} + 2Co_{Co}^X \tag{5.4}$$

In an attempt to describe our measured electronic conductivities using these two types of conductivity we hypothesized on a simple conductivity mechanism. The mobility of charge carriers in a metal is known to decrease with increasing temperature.[158] $(La_{1-x}Sr_x)_sCoO_{3-\delta}$ is known to have a metallic-like temperature dependence [142] and Ni substitution is known to increase the metallic character further [22], thus all our compositions can be considered metallic-like. As a starting point we have therefore used an approximate "mechanism" expressed in Equation 5.5, which assumes that both the *p*-type and the *intrinsic* conductivity has a "metallic like", reciprocal temperature dependence.

$$\sigma = C\left([Sr'_{La}] - 2\delta\right)\frac{\mu_{ext}}{T} + \left(\frac{\sigma_{int.}}{T} + \sigma_{const.}\right)_{2\delta=[Sr'_{La}]} \tag{5.5}$$

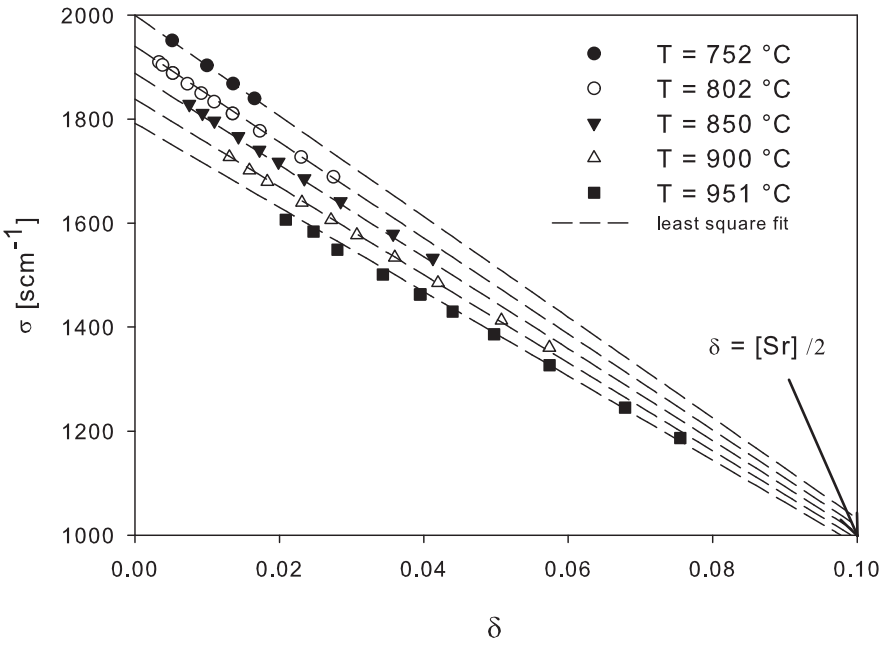

Figure 5.8: Electronic conductivity as function of δ for LSCN2020. Lines represent best fit to Equation 5.5.

$C([Sr'_{La}] - 2\delta)$ is the concentration of charge carriers (c_p). C = $\frac{\rho N_A e}{M}$, where M is the molar mass of the perovskite, ρ is the density, N_A is the Avogadro number and e is the elementary charge. μ_{c_p} is the mobility of the p-type charge carriers, σ_1 and σ_2 are the temperature dependent and temperature independent contributions to the intrinsic conductivity.

The dashed lines in figures 5.9 and 5.10 represent the best linear least square fit to Equation 5.5. The solid lines are linear regressions of the conductivity of the lowest temperature as these data could not be satisfactorily included in the model. The conductivity data for LSCN3010 at 800 °C and LSCN4010 at 700 °C still showed very linear correlation with δ but measured higher p-type mobilities (Approximately 2900 and 2000 cm^2 V^{-1} s^{-1} for LSCN3010 and LSCN4010 respectively). Measured conductivities at all other temperatures could be fitted with good accuracy to Equation 5.5 and the resulting parameters listed in Table 5.2. Table 5.2 also shows the sum of square deviations, χ_σ which is defined as $(\Sigma(\sigma_{measured,(i)} - \sigma_{calculated,(i)})^2)/(N-3)$, where N is the total number of measurements (N=43) and $\sigma_{measured,(i)}$ is the conductivity of the i'th measurement.

As seen in Figure 5.9 the fitted conductivities of LSCN3010 intercepts almost exactly at δ= [Sr]/2 implicating that the intrinsic conductivity of this composition is independent on temperature within this T-range. It should be stressed that the data points are lying relatively close to each other and that the conductivity model includes as many as three fitting parameters. Especially σ_1 and σ_2 are associated with great uncertainty as they are fitted based on only 3 (LSCN3010 and LSCN4010) and 5 (LSCN2020) data points all lying within a narrow temperature range.

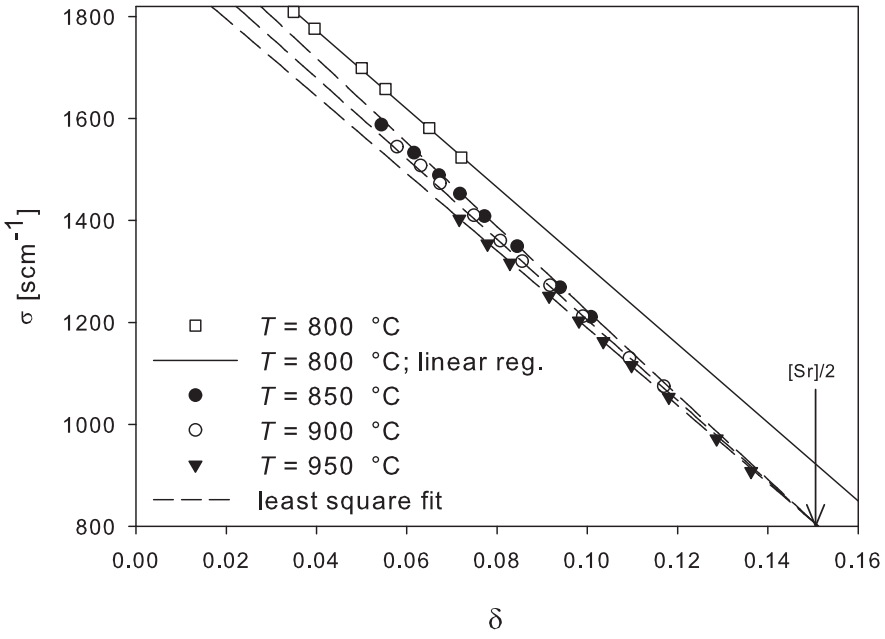

Figure 5.9: Electronic conductivity as function of δ for LSCN3010. Lines represent best fit to Equation 5.5. The lowest temperature could not be fitted to the conductivity model and have instead been regressed linearly to calculated the p-type mobility.

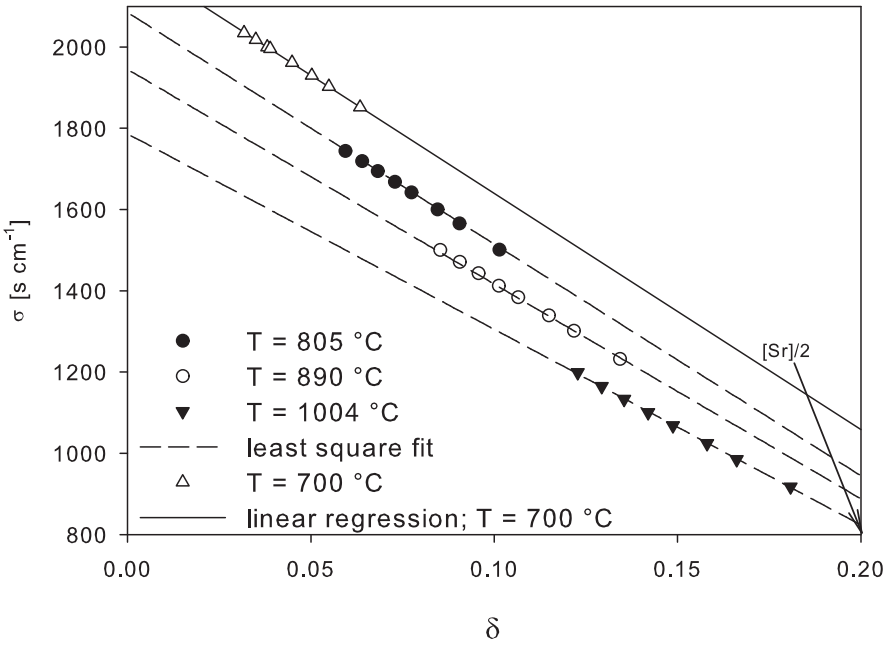

Figure 5.10: Electronic conductivity as function of δ LSCN4010 . Lines represent best fit to Equation 5.5. The lowest temperatures could not be fitted to the conductivity model and have instead been regressed linearly to calculated the p-type mobility.

Table 5.2: Least square fitting parameters to the Equation 5.5 for LSCN2020, LSCN3010, LSCN4010. The extrinsic mobility of LSC40 is included from refs [142] for comparison. C is coulomb.

	C [Ccm^{-3}]	μ_{c_p} [$cm^2V^{-1}s^{-1}K$]	σ_1 [$Scm^{-1}K^{-1}$]	σ_2 [Scm^{-1}]	χ_σ
LSCN2020	2860	1734	$3.15 \cdot 10^5$	724	24
LSCN3010	2844	1630	-	809	22
LSCN4010	2850	1079	$8.37 \cdot 10^5$	168	26
LSC40 [142]	2835	1023	-	-	-

5.4.3 Thermal and chemical expansion

Figure 5.11 plots the apparent thermal expansion coefficient (TEC), calculated by differentiating the strain, ϵ, with respect to temperature. The expansion measurement for LSC40 was reported in an earlier paper [2] in which the sharp drop in TEC at around 800 °C was attributed to the reduction $Co_3O_4 \rightarrow CoO$ of the inevitable traces of secondary Co oxide phases. Two sharp peaks were found in the expansion measurement of LSCN4010. These peaks were not observed in any of the Ni containing compositions in the previous paper nor in the repetitive measurement to only 1100 °C instead of 1300 °C.

Adler et al. [44] have developed a expansion model for nonstoichiometric mixed conducting perovskites such as $(La_{1-x}Sr_x)_sCoO_{3-\delta}$, which takes into account first and second order expansion with respect to both the temperature and oxygen stoichiometry. The expansion model is expressed in Equation 5.6.

$$\epsilon(T,\delta) - \epsilon(T_0,\delta=0) = (\alpha_1 + \alpha_2(T-T_0))(T-T_0) + (\beta_1 + \beta_2\delta)\Delta\delta \tag{5.6}$$

where $\epsilon = \Delta L/L_0$ is the uniaxial strain, α_1 and α_2 are the first and second order thermal expansion coefficients and β_1 and β_2 are the first and second order chemical expansion coefficients.[44]

The lattice expansion of LSCN3010, LSCN4010 and LSC40 was measured as function of P_{O_2} at 700, 800, 900 and 1000 °C. The oxygen nonstoichiometry was calculated using the *itinerant electron model* and the fitting parameters listed in Table 5.1 for at each condition (T, P_{O_2}) at which the expansion was measured. The lattice expansion has been plotted as function of δ in Figures 5.12 to 5.14. The model was applied to our expansion data and the best linear least square fits to Equation 5.6 is shown as the solid lines. The least square fitting parameters are listed as the first and second order thermal and chemical expansion coefficients in Table 5.3. Table 5.3 also shows the sum of square deviations, χ_ϵ which is defined as $(\Sigma(\epsilon_{measured,(i)} - \epsilon_{calculated,(i)})^2)/(N-3)$, where N is the total number of measurements (N=25-28) and $\epsilon_{measured,(i)}$ is the expansion of the i'th measurement.

The lower TEC of LSCN4010 as compared to LSC40 seen in Figure 5.11 is also reflected in

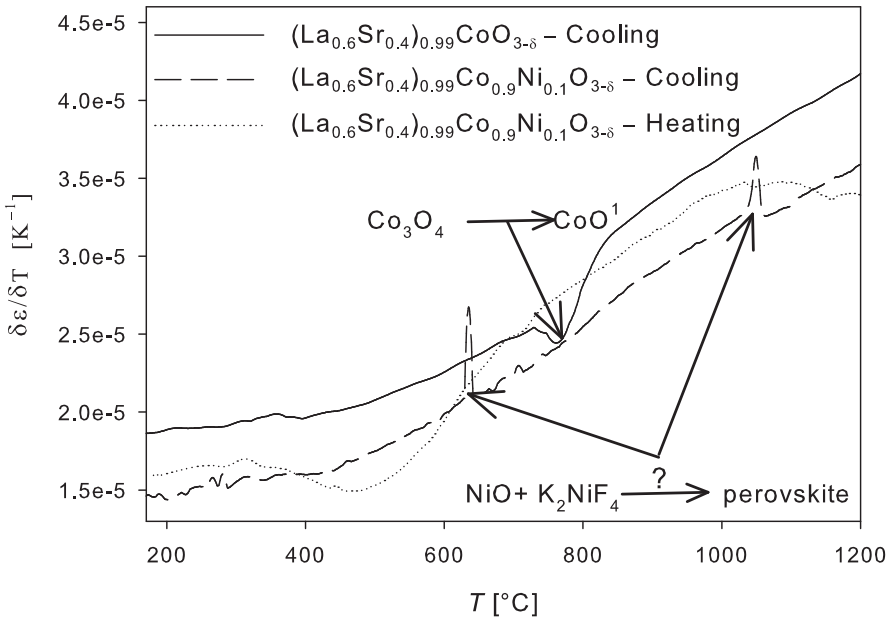

Figure 5.11: The apparent TEC as function of temperature for LSCN4010 and LSC40. Substituting 10 % Co with Ni in LSC40 appears to decrease the TEC substantially. Peaks in the TEC of LSCN4010 are possibly associated with phase transitions of secondary phases.

the expansion coefficients listed in Table 5.3.

5.5 Discussion

5.5.1 Electronic and defect structure

It is evident from Figure 5.4 that substitution of La with Sr increases the concentration of vacancies in the oxygen sublattice above an onset temperature of approximately 500 °C.

Table 5.3: First and second order thermal and chemical expansion coefficients extracted as the best least square fitting parameters to the expansion model expressed in Equation 5.6.[44]

	$\alpha_1 + \alpha_2(T - T_0)$ [K^{-1}]	$\beta_1 + \beta_2\delta$	χ_ϵ
LSCN3010	$14.4 \cdot 10^{-6} + 4.65 \cdot 10^{-9}$(T-$T_0$)	0.0163 + 0.101 δ	$5.0 \cdot 10^{-6}$
LSCN4010	$11.4 \cdot 10^{-6} + 6.54 \cdot 10^{-9}$(T-$T_0$)	0.0197 + 0.0251 δ	$3.0 \cdot 10^{-6}$
LSC40	$15.5 \cdot 10^{-6} + 4.93 \cdot 10^{-9}$(T-$T_0$)	0.0193 + 0.0803 δ	$2.3 \cdot 10^{-6}$
LSC40 [44]	$14.20 \cdot 10^{-6} + 4.84 \cdot 10^{-9}$(T-$T_0$)	0.0183 + 0.270 δ	

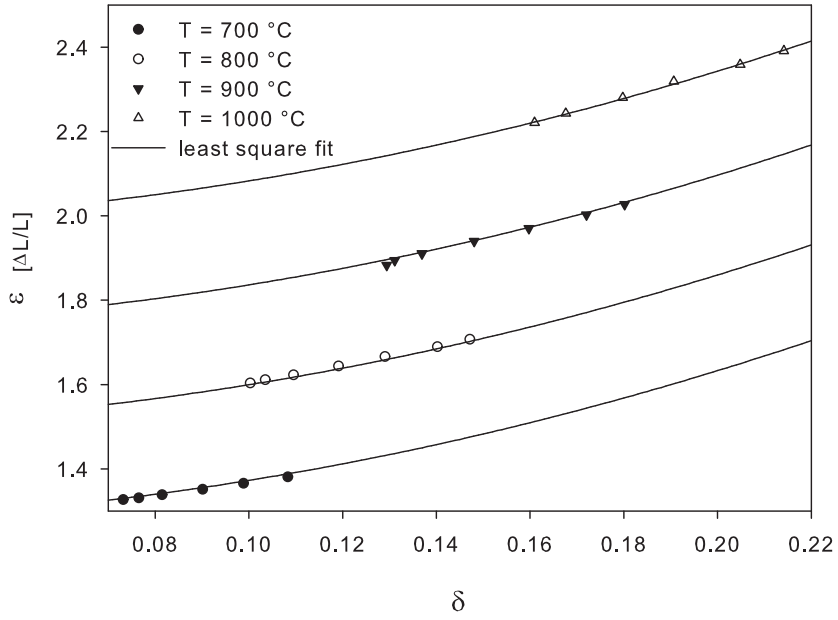

Figure 5.12: Strain as function of δ and T for LSC40. Lines represent best fit to Equation 5.6.

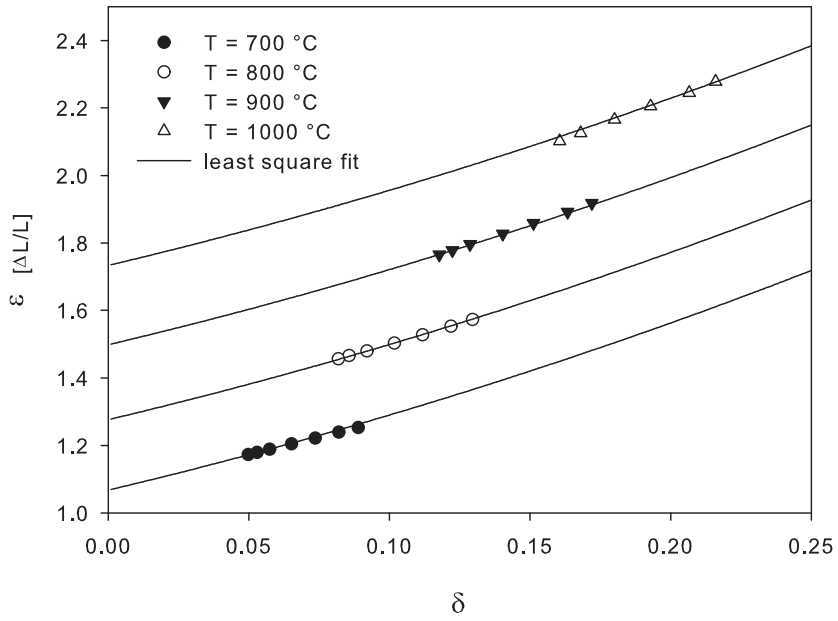

Figure 5.13: Strain as function of δ and T for LSCN4010. Lines represent best fit to Equation 5.6.

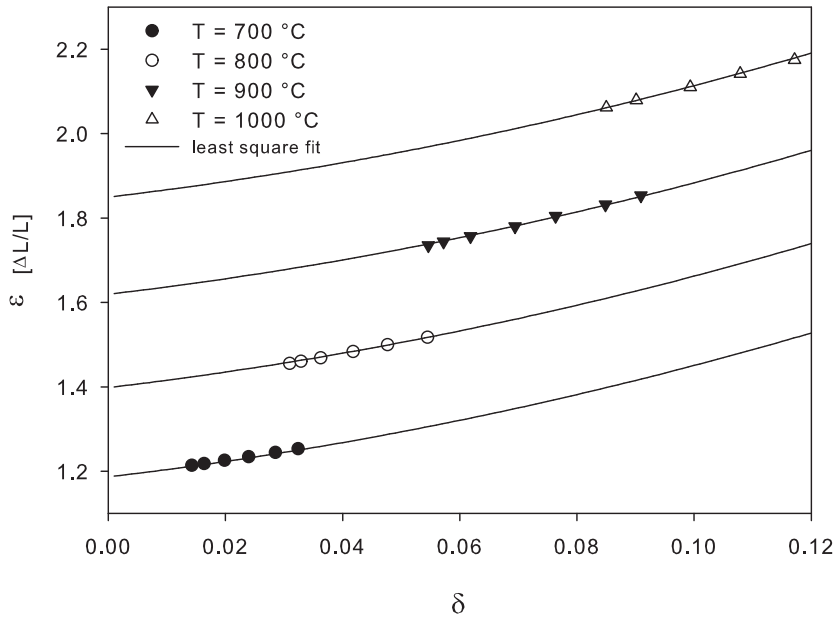

Figure 5.14: Strain as function of δ and T for LSCN3010. Lines represent best fit to Equation 5.6.

The oxygen nonstoichiometry parameter of LSCN4010 is more than twice as large as that of LSCN3010 between 500-800 °C. This can be understood as LSCN4010 having a higher degree Co in its reduced form, Co^{4+}, at room temperature which can undergo thermal reduction upon heating and consequently form oxygen vacancies. This effect is well known and will therefore not be discussed in detail here [76], [2] but it is interesting to note that this trend also holds when Ni is present on the B-site of the perovskite.

Increasing the Ni content appears also to increase the oxygen nonstoichiometry at high T as substituting 10 % Co with Ni in LSC40 increases the linear tendency with which oxygen vacancies are created upon heating. This stand in sharp contrast to results of Teraoka *et. al.*, who have found that substituting 20 % Co with Ni in $(La_{0.6}Sr_{0.4})CoO_{3-\delta}$ decreases the oxygen nonstoichiometry parameter.[10] It's not relevant to ascribe a valency to the Co ion in this configuration as the charge on Co ions are delocalised. Instead it is probably more correct to refer to an average oxidation state, which will be somewhat higher in LSCN4010 than in LSC40 at room temperature. This fact could possibly results in a higher tendency to undergo thermal reduction, in analogy with the above discussed comparison between LSCN3010 and LSCN4010.

The relatively good agreements of the measured nonstoichiometry in LSCN2020, LSCN3010 and LSCN4010 to the *itinerant electron model* indicates that these compositions incorporates delocalises electronic charge. This is also in agreement with the high electronic conductivities measured for these compositions. However, its difficult to make further interpretations of the parameters $g(\varepsilon_F)$, ΔE_{ox} and ΔS_{ox}.

The *itinerant electron model* does not take into account charge disproportionation of the kind $2\mathrm{Co}_{Co}^{x} \rightarrow \mathrm{Co}_{Co}^{\cdot} + \mathrm{Co}_{Co}^{'}$ and thus assumes that the concentration of charge arising as a consequence of such as reaction is negligible compared to the p-type charge introduced by Sr substitution. The reasonably good fit of the stoichiometry data to the model indicate that this holds also in the case when Ni is present on B-site. We have in a previous study presented XANES measurements supporting that the reaction $\mathrm{Co}^{iii} + Ni^{III} \rightarrow \mathrm{Co}^{IV} + \mathrm{Ni}^{2+}$ does not occur to any notable degree.[2] The XANES data in this study showed that Ni remained its valency state irrespective of the degree of Sr or Co in the crystal whereas Co was under strong influence of only [Sr] and not [Ni]. It was also shown support that it is exclusively Co that is reduced at increasing temperatures.

The clear linear correlation between σ and δ, calculated using the *itinerant electron model* indicates that the change in charge concentration as a result of P_{O_2} shifts is only associated with changes in the p-type charge described by the *itinerant electron model*. If charge disproportionation had occurred in $(\mathrm{La}_{1-x}\mathrm{Sr}_x)_s\mathrm{Co}_{1-y}\mathrm{Ni}_y\mathrm{O}_{3-\delta}$ upon P_{O_2} shifts then the concentration of available charge and thus the conductivity would have been higher than predicted by the *itinerant electron model*.

5.5.2 Electronic conductivity

The conductivity as function of oxygen nonstoichiometry was shown to decrease linearly with increasing δ (see Figure 5.8 to 5.10), which indicates that these compositions incorporates p-type charge carriers. It shows further that changes in its concentration as function of P_{O_2} has a much stronger impact on the conductivity as compared to any possible changes in the *intrinsic* charge carrier concentration. The *intrinsic* contribution to the conductivity is however substantial within the measured T-range, being approximately 800-1000 S cm^{-1} for all three compositions. Fitting the conductivity data as function of both T and δ with the model expressed in Equation 5.5 showed good agreement for LSCN2020. Also LSCN3010 and LSCN4010 were found to agree well with the conductivity model at all temperatures but the lowest. The results presented in Table 5.2 indicates that the mobility of the p-type charge carriers μ_{c_p} increases with decreasing Sr content. At 1000 °C the mobility of the p-type charge is about 1.1 to 1.6 $\mathrm{cm}^2\mathrm{V}^{-1}\mathrm{s}^{-1}$ for LSCN4010 and LSCN3010 respectively. This trend is also in agreement with the p-type mobility reported for $(\mathrm{La}_{1-x}\mathrm{Sr}_x)_{0.99}\mathrm{CoO}_{3-\delta}$ by Søgaard *et. al.*. [142] For $(\mathrm{La}_{0.85}\mathrm{Sr}_{0.15})_{0.99}\mathrm{CoO}_{3-\delta}$ the aforementioned study reports mobilities of 1.2-1.4 $\mathrm{cm}^2\mathrm{V}^{-1}\mathrm{s}^{-1}$ in the range from 850-1000 °C. This can be compared with our calculated mobilities of 1.4-1.5 $\mathrm{cm}^2\mathrm{V}^{-1}\mathrm{s}^{-1}$ for LSCN2020 in the same temperature range. Also the p-type mobility of LSCN4010 was found to be about 5 % higher than that of LSC40. These comparisons indicate that Ni substitution in $(\mathrm{La}_{1-x}\mathrm{Sr}_x)_s\mathrm{CoO}_{3-\delta}$ increases the mobility of the p-type charge carriers.

Figure 5.15 shows the *intrinsic* and p-type conductivity as well as the total conductivity from room temperature to 1000 °C, predicted using the results in Table 5.2 together with measured δ as function of temperature (see Figure 5.4). Figure 5.15 also shows the conductivity of the same composition as function of temperature but measured on a different sample

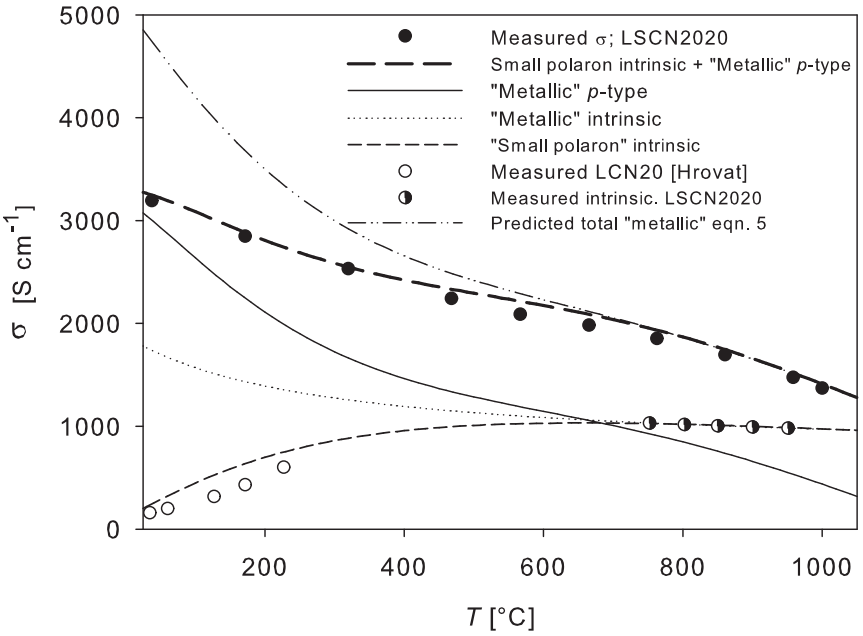

Figure 5.15: Electric conductivity as function of temperature for LSCN2020. Lines represent best fit to Equation 5.5, extrapolated down to room temperature with δ-values taken from Figure 5.4. The fits shows reasonable agreement in temperature trend but deviates substantially in absolute values at low T.

with a different experimental setup. The predicted total conductivity, extrapolated on basis of the mechanism expressed in equation 5.5, was shown to correlate well with the measured data only above 700 °C. At lower temperatures it deviates substantially and overestimates the room temperature conductivity with almost 2000 Scm^{-1} and hence the suggested equation does not seem to satisfactorily describe the conductivity mechanism. The temperature dependence of the p-type conductivity was determined based 43 data points. The delocalized p-type conductivity arises from the fact that the Co ions in LaCoO3 have been partially oxidized upon Sr substitution thus the presence of the p-type charge is not dependent on thermal excitations like for example charge associated with spin transitions. We therefore believe it is fair to assume that the p-type conductivity is of metallic character. A reciprocal temperature dependence has also been suggested previously for $(\mathrm{La}_{1-x}\mathrm{Sr}_x)_s\mathrm{CoO}_{3-\delta}$.[142]

We postulate instead that the discrepancy between measured and predicted conductivity of LSCN2020 is related to the *intrinsic* conductivity mechanism. The predicted *intrinsic* conductivity, i.e. the conductivity at [Sr]=$\delta/2$, at 750-950 °C can be considered accurate within the precision of the experiments. However the reliability when projected to lower T is more questionable. The *intrinsic* conductivity, as defined in this particular paper, is independent on the p-type charge carriers and any change in the *intrinsic* conductivity is instead assumed to be related to spin transitions on the Co ions. This is believed to have substantial effect on the conductivity and this correlation has been discussed in a previous paper for $(\mathrm{La}_{1-x}\mathrm{Sr}_x)_{0.99}\mathrm{Co}_{0.6+x}\mathrm{Ni}_{0.4-x}\mathrm{O}_{3-\delta}$.[2], [76] It can be understood in the light of ligand field theory. When positioned in a octahedral geometry of a crystal, d-orbitals of a transition

metal ion split into 2 e- and 3 t-orbitals, separated by a small band gap. The e-orbitals are oriented towards the p-orbitals of the oxygen ions to form overlap (bonds) that make up the conductive path ways. The overlap comes at the expense of a slightly higher energy than the t-orbitals, in the case of $LaCoO_3$ of approximately 0.05 eV. [159], [58], [57] The thermodynamic consequence is that all 6 d-electrons of the Co^{3+} ion are preferably found in the 3 t-orbitals with no net electron spin. However, the band gap is sufficiently low for thermal energy to excite electrons. The electron will simultaneously change its spin following Hund's rule and transition from low spin Co(III), t_{2g}^6, to intermediate spin Co(iii) $t_{2g}^5 e_g^1$ or high spin Co^{3+} $t_{2g}^4 e_g^2$ occur at elevated temperatures. This increases the degree of the Co3d-O2p overlap that in turn allow charge transport through the crystal. [56], [55], [59], [60], [31], [61], [62] Octahedral Ni in $LaNiO_3$ has the low spin configuration, $t_{2g}^6 e_g^1$ and thus one electron is already found in the conductive e-orbitals. This explains why $LaNiO_3$ shows metallic conductivity at room temperature while $LaCoO_3$ is only a reasonable conductor at much higher temperatures. This property, typical of $LaCoO_3$, gives also rise to interesting expansion properties discussed further below as well as in a previous study on $(La_{1-x}Sr_x)_sCo_{1-y}Ni_yO_{3-\delta}$.

$$\sigma = \frac{A}{T} exp(\frac{-E_A}{kT}) \tag{5.7}$$

The electronic conductivity of $La_sCo_{1-x}Ni_xO_{3-\delta}$ with x <0.4 has been argued by Huang *et. al.* [22] to follow the small polaron conduction as expressed in Equation 5.7. Fitting the *intrinsic* conductivity data of LSCN2020 to this equation yields an activation energy of 0.07 eV. Huang *et. al.* have determined the small polaron activation energy to range from 0.05-0.07 eV for related compositions. [22] An *intrinsic* conductivity predicted on basis of the small polaron conductivity has been included in Figure 5.15 as well as the conductivity of $LaCo_{0.8}Ni_{0.2}O_3$ measured from room temperature to 175 °C by Hrovat el. al. [15] This composition corresponds, in theory, to the LSCN2020 but without p-type charge as there is no Sr^{2+} that have oxidized the Co ions. Hence the *intrinsic* conductivity of LSCN2020 should roughly correspond to that of $LaCo_{0.8}Ni_{0.2}O_3$. As seen in Figure 5.15 the predicted *intrinsic* small polaronic conductivity of LSCN2020 agrees reasonably well with that of $LaCo_{0.8}Ni_{0.2}O_3$. Adding the predicted *intrinsic* small polaron conductivity to the p-type conductivity of LSCN2020 results in a total "predicted" conductivity (plotted as the thick dashed line in Figure 5.15) that agrees well the "true" measured electronic conductivity of LSCN2020. Most interesting is the fact that the "S-shaped" trend with respect to temperature seen in the measured conductivity of LSCN2020 is also predicted by a mechanism including both metallic-like p-type charge carrier and small polarons. The S-shaped trend was also found for all other compositions of $(La_{1-x}Sr_x)_sCo_{1-y}Ni_yO_{3-\delta}$ reported previously.

This could possibly indicate that electronic conduction of LSCN2020 can be described by a dual mechanism where the p-type charge carrier as a result of Sr-substitution follows a metallic-like conductivity and where the *intrinsic* charge carrier from e.g. spin transitions on Co ions follows a small polaron conduction mechanism.

There are uncertainties associated with such a simple explanation to the conductive behavior of $(La_{1-x}Sr_x)_sCo_{1-y}Ni_yO_{3-\delta}$. The data presented covers only a temperature span of roughly RT to 1000 °C. Moreover, both crystal and electronic band structure is often more complicated in oxides as compared to metals. For instance Mineshige *et. al.* [110] have studied the conductivity of $(La_{1-x}Sr_x)_sCoO_{3-\delta}$ and found a metal-insulator transition at a critical Co-O-Co angle of 165 ° irrespective of x, T and P_{O_2}. Figures 5.9 and 5.10 found a slightly higher mobility for LSCN3010 and LSCN4010 at the lowest measured temperature indicating that the p-type mobility might not be independent on temperature over the entire temperature span RT-1000 °C.

5.5.3 Expansion behavior

The measured *apparent* thermal expansion coefficients (TEC) shown in Figure 5.11 for LSCN4010 and LSC40 illustrate that substituting 10 % Co with Ni in LSC40 decreases the TEC across the entire temperature range. The difference is remarkable, about 20-25 %, making LSCN4010 an interesting composition for technological use in SOFC-cathodes as it could possibly reduce the large expansion mismatch between the highly electro-catalytic $(La_{0.6}Sr_{0.4})CoO_{3-\delta}$ and the other components of an SOFC.

Substitution of Co with Ni in $(La_{1-x}Sr_x)_sCo_{1-y}Ni_yO_{3-\delta}$ decreases the thermodynamic stability of the perovskite which could result in partial decomposition of LSCN4010 into secondary phases of the type K_2NiF_4-type and CoO/NiO when reaching temperature as high as 1300 °C. [26], [160], [151] We have previously shown support that secondary phases of transition metal oxides in $(La_{1-x}Sr_x)_sCo_{1-y}Ni_yO_{3-\delta}$ are of NiO. The origin of the sharp peaks in the differential expansion curve of LSCN4010 at 630 and 1050 °C will not be fully explained in this paper. However a possible explanation could be a reaction between the NiO and a K_2NiF_4-type oxide to regain the perovskite structure upon cooling. Such a reaction would involve an uptake of gaseous oxygen expanding the lattice momentarily. The fact that these artifacts were not seen in the repetitive experiment to 1100 °C indicates that this temperature and time (1 h) is not sufficient to adequate amounts of secondary phases.

To describe the thermal expansion behavior of oxides only in terms of a coefficient is somewhat misleading and certainly not sufficient in the case of $(La_{1-x}Sr_x)_sCo_{1-y}Ni_yO_{3-\delta}$. The *apparent* TEC is seen to increase continuously above approximately 500 °C for both LSC40 and LSCN4010, a temperature that correlates well with the onset temperature of oxygen loss seen in Figure 5.4. The increase in the *apparent* TEC at higher temperatures has in previous papers been argued to be related to the thermal reduction of Co(IV) to Co(III) which expands the Shannon radius from 0.53 $\mathring{A}$ for Co^{4+}(VI) (HS) to 0.61 $\mathring{A}$ for Co^{3+}(VI) (HS).[142] This expansion is often referred to as the chemical expansion and relates to the oxygen nonstoichiometry change with the chemical expansion coefficient (CEC). However, also the CEC should not be regarded as a simple coefficient, which the following paragraph attempts to justify.

Figure 5.4, shows clearly that δ increases linearly with T above a certain threshold temper-

ature (expressed in Equation 5.8). In the case of LSC40 and LSCN4010 this temperature is approximately 700 °C. Now if the lattice expansion was found to be dependent on T and δ only to a first order then the *apparent* TEC would be expressed as the sum of two constants, TEC_{500} and TEC_{700}, where the later is valid only above approximately 700 °C. This is expressed in Equations 5.9 to 5.11 where α is the expansion coefficients with respect to temperature, β is the expansion coefficients with respect to δ and γ is the linear coefficient with which δ increases with temperature above 700 °C.

$$\delta = (\gamma \cdot T)_{T \geq 700°C} \tag{5.8}$$

$$\epsilon = \alpha \cdot T + \beta \cdot \delta = \alpha \cdot T + \beta \cdot (\gamma \cdot T)_{T > 700°C} \tag{5.9}$$

$$TEC_{500} = (\frac{\partial \epsilon}{\partial T})_{T \leq 500°C} = \alpha \tag{5.10}$$

$$TEC_{700} = (\frac{\partial \epsilon}{\partial T})_{T \geq 700°C} = \alpha + \beta \cdot \gamma \tag{5.11}$$

This would result in an *apparent* TEC having an s-shaped curve with a constant value of α below 500 °C and another constant value of $\alpha + \beta \cdot \gamma$ above 700 °C. However the *apparent* TEC, shown in Figure 5.11, continues to increase in the high temperature region for both LSC40 and LSCN4010. This suggests that the CEC is not a single order coefficient but depends on δ and/or T to a second order degree. Additionally, the *apparent* TEC of LSC40 appears to increase below 500 °C where δ is approximately zero. This indicates that also the true TEC is dependent on T to a second order degree. This motivated us to characterize the expansion behavior of $(La_{1-x}Sr_x)_sCo_{1-y}Ni_yO_{3-\delta}$ using the mechanism expressed in Equation 5.6. This model was first tested by Adler and coworkers in a study on lattice expansion behavior of $(La_{1-x}Sr_x)_sCoO_{3-\delta}$.[44]

As seen in Figures 5.12 to 5.14 this expansion model was found to fit the measurements on LSC40, LSCN3010 and LSCN4010 well. Comparing LSCN4010 and LSC40 using the results in Table 5.3 shows that substituting 10 % Co with Ni in LSC40 decreases the first order TEC (α_1) substantially. The second order TEC (α_2) is slightly higher for LSCN4010 but calculating the strain up to 850 °C, caused only by heating and not stoichiometric changes ($\epsilon_{\alpha,850C}$), shows that the strain in LSCN4010 is about 15 % lower. This could be explained by the Ni containing composition having less trivalent Co ions which undergoes the electronic spin transition that gives rise to the unusually large *apparent* TEC of these cobaltites. The first order CEC (β_1) of LSC and LSCN4010 was found to be approximately the same, whereas the the second order CEC (β_2) is three times larger for LSC40. This is compensated by the higher δ of LSCN4010 as the strains induced exclusively by the chemical expansion when heated to 850 °C ($\epsilon_{\beta,850C}$) are almost identical.

Comparing α_1 and α_2 of LSCN3010 and LSCN4010 shows that increasing the Sr content will decrease the *true* TEC. The "thermal" strain, ($\epsilon_{\alpha,850C}$), induced when heated to 850 °C is about 8 % lower in LSCN4010. This can again be explained by the lower concentration of trivalent Co ions that can undergo spin transitions upon heating. β_1 appears to increase with Sr substitution whereas β_2 is about 4 times lower. Calculating the $\epsilon_{\beta,850C}$-values of LSCN4010 and LSCN3010 shows a 15 % lower strain for LSCN3010. This is mainly due to the much lower δ of LSCN3010 within this temperature range.

For LSCN4010 the strain induced by α_2 was found to be about 50 % of that induced by α_1 when heated to 850 °C whereas the strain induced by β_2 was about 10 % of that induced by β_1. This indicates further that the second order terms are necessary to fully describe the expansion behavior.

The strain in LSC40 as function of temperatures was calculated from the fitting parameters in Table 5.3 and the oxygen nonstoichiometry shown in Figure 5.4 and compared with the strain measured continuously as function of temperature in air (see Figure 5.11). The result is reported in Figure 5.16 in which we have also include a fit of the strain of $(La_{0.6}Sr_{0.4})CoO_{3-\delta}$ calculated based on expansion coefficients from the study by Chen *et. al.*. [44] The figure shows that the strain calculated from using the coefficients in Table 5.3 agrees reasonably well with the measured strain. The strain calculated from expansion coefficients of [44] overestimated the expansion above 1000 °C if compared to the measured strain of our sample. Comparing the thermal and chemical expansion coefficients from these two studies shows that the β_2 reported by [44] is more than three times higher than ours which results in a much large expansion increase at high δ (ie high T). It is noteworthy that the major contribution to the strain in LSC40 arises from thermal and not chemical expansion.

5.6 Conclusions

We have found that the *itinerant electron model* [80], describes the defect chemistry of LSCN2020, LSCN3010 and LSCN4010 well. This indicates that our investigated compositions are of metallic-like character with delocalized electronic states. This is also reflected in the high electronic conductivities measured. The conductivities were shown to be linearly dependent on the p-type charge carrier concentration. The measured conductivities were suggested to consist of an p-type contribution together with an intrinsic contribution arising from electronic spin transitions and Ni substitution. The p-type conductivity was found to have a metallic-like reciprocal temperature dependence above approximately 800 °C. The thermal behavior and conduction mechanism of intrinsic contribution was hypothesized to be of the small polaron type. This contribution to the conductivity was more difficult to describe and further analysis is needed to fully understand the conductivity of these complicated oxides.

Expansion measurements as function of T and P_{O_2} showed that substituting 10% Co with Ni in LSC40 decreased the *apparent* thermal expansion coefficient with 20-25 % in the entire measured temperature range (25-1300 °C). The expansion behavior could successfully be

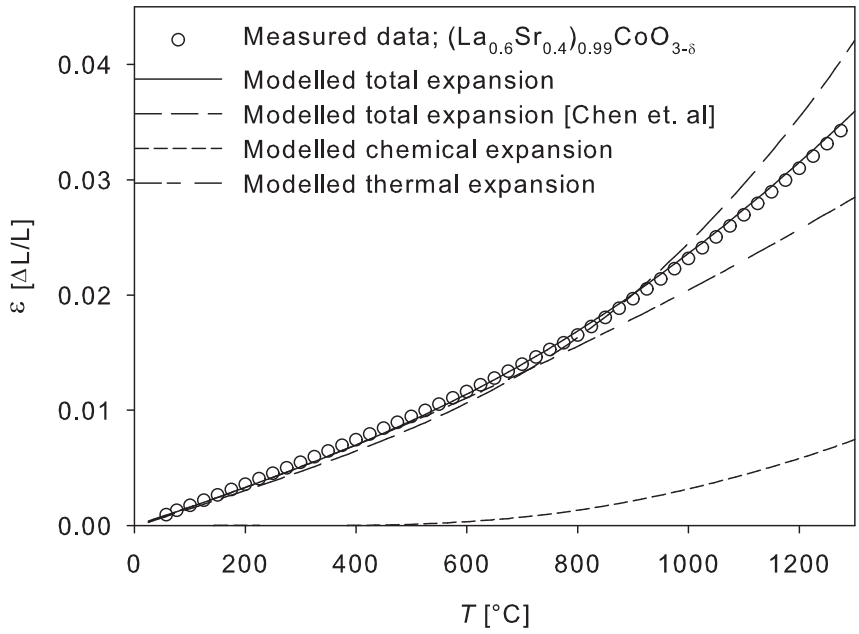

Figure 5.16: Expansion as function of temperature for LSC40 reported in Figure 5.11 where it is differentiated with respect to temperature. Lines represent the predicted expansion according to 5.6, where δ was taken from Figure 5.4 and the expansion coefficients from Table 5.3.

described using a model incorporating first and second order thermal and chemical expansion coefficients. Separating the *apparent* TEC showed that Ni substitution into LSC40 appears to decrease both the thermal and chemical expansion coefficients.

Chapter 6

Electrochemical performance of $(La_{1-x}Sr_x)_sCo_{1-y}Ni_yO_{3-\delta}$ as porous SOFC cathode

6.1 Abstract

This paper shows that storage at room temperature and ambient atmosphere appears to affect the polarization resistance significantly and R_P decreased initially with storage time. This improvement was more pronounced when stored in moisturised air. The performance was, however, also found to decrease when stored for sufficiently long periods. The absolute values of the electrode response of these materials is very difficult to reproduce and the performance appears to be largely dependent on the manufacturing process of the powder or the electrode itself. In spite of this, the electrode behaviours exhibited similar patterns with respect to the dependence on T and P_{O_2}. An increase in polarisation resistance with time at SOFC operating conditions was observed, which was related exclusively to the electrode reaction kinetics and not to oxygen concentration polarisation. It was also found to be higher when measured in moisturised air.

6.2 Introduction

Strontium substituted lanthanum cobaltite $(La_{1-x}Sr_x)_sCoO_{3-\delta}$ (LSC) is a perovskite-type oxide with high electronic and oxide ion conductivity at elevated temperatures and is therefore considered for use in high temperature devices such as ceramic membranes and fuel cells. The mixed conducting property of LSC is believed to account for the low over-potentials measured when used as an solid oxide fuel cell cathode as it expands the catalytically active area of the electrode beyond the triple phase boundary.[125] The mixed

Table 6.1: Calcination temperatures and times for the four Electrode A-D studied in this paper.

Electrode	Composition	$T_{\text{calc.}}$ [°C]	$t_{\text{calc.}}$ [h]	d_{avg} [nm]	a_{surface} [m^2g^{-1}]
A	$(La_{0.6}Sr_{0.4})_{0.99}CoO_{3-\delta}$	1250	12	36	1.1
B	$(La_{0.6}Sr_{0.4})_{0.99}CoO_{3-\delta}$	1150	2	37	0.27
C	$(La_{0.6}Sr_{0.4})_{0.99}Co_{0.9}Ni_{0.1}O_{3-\delta}$	1150	2	35	0.52
D	$(La_{0.8}Sr_{0.2})_{0.99}Co_{0.8}Ni_{0.2}O_{3-\delta}$	1250	12	22	0.87

conductivity has been reported to be increased further by partial substitution of nickel.[15], [16], [17], [18]. Also a more favorable thermal expansion coefficient that matches that of other SOFC components can be achieved by nickel substitution. [20], [21]

However, the use of LSC as a cathode on Yttria Stabilised Zirconia (YSZ) is problematic due to the high thermal and stoichiometric expansion coefficient of LSC (17-20$\times10^{-6}$ K^{-1} and 0.015-0.030 mol $^{-1}$) [44] when compared to that of 8 % Y_2O_3 stabilised ZrO_2 (8YSZ) (10.8$\times10^{-6}$ K^{-1} for 25 - 1000 °C [161]). Also ionic and electronic blocking reaction products ($SrZrO_3$, $La_2Zr_2O_7$ [125]) inhibit the direct use of LSC on YSZ electrolyte at high temperatures. These problems are partially circumvented when going to lower temperatures and to a ceria-based electrolyte/barrier layer. This paper deals with the electrochemical performance and degradation based on data measured on four different electrodes of porous $(La_{1-x}Sr_x)_sCo_{1-y}Ni_yO_{3-\delta}$ that were stored under different conditions. The work is of an exploratory nature as a number of new surprising features were discovered.

6.3 Experimental

Powders of $(La_{0.6}Sr_{0.4})_{0.99}CoO_{3-\delta}$, $(La_{0.6}Sr_{0.4})_{0.99}Co_{0.9}Ni_{0.1}O_{3-\delta}$ and $(La_{0.8}Sr_{0.2})_{0.99}Co_{0.8}Ni_{0.2}O_{3-\delta}$ were synthesized using the glycine-nitrate combustion route. [130] Each composition was used to fabricated one type of porous electrode. These perovskites were used to fabricate four single phase electrodes, denoted A-D, according to Table 6.1. In the table are also listed the different calcination temperatures and times. Note that two batches of $(La_{0.6}Sr_{0.4})_{0.99}CoO_{3-\delta}$ were synthesized using the same synthesis but with different thermal treatments. XRD indicated single phase perovskites as described previously in a previous paper.[2]

Symmetric cells were fabricated according to the following procedure. A cathode slurry of 11 g perovskite powder, 15 g ethanol and 1 g polyvinylpyrrolidone (PVP) was mixed and ball-milled over night. The slurry was sprayed onto both sides of a 200 μm thick tape of $Ce_{0.9}Gd_{0.1}O_{1.95}$ (CGO) and sintered at 950 °C for 2 h. The spraying and sintering procedure was repeated in order to fabricate a symmetric cell with approx. 25 μm thick electrodes.

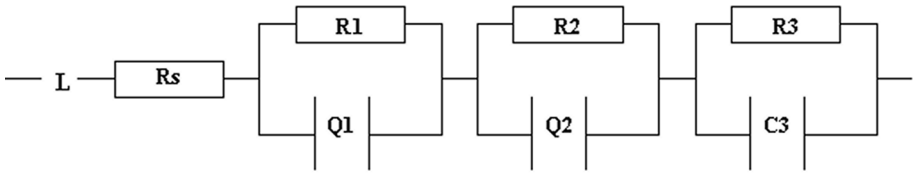

Figure 6.1: Equivalent circuit model used to fit the impedance spectra of porous electrodes of $(La_{1-x}Sr_x)_sCo_{1-y}Ni_yO_{3-\delta}$. *Arc*1 and *Arc*3 could sometimes be excluded depending on conditions and which electrode was modelled.

Electrodes A and D were synthesized and fabricated at a different occasion than Electrode B and C but the procedure was the same. The cells were cut to dimensions of 4.0×4.0 mm^2 and painted with platinum paste immediately before testing. A few cells with Electrode C were also cut to dimensions of 6.0×6.0 mm^2.

Four identical cells were measured with Electrochemical Impedance Spectroscopy (EIS) under open circuit voltage with a Solartron-1260 frequency response analyzer at temperatures from 550-900 °C and oxygen partial pressures (P_{O_2}) from 0.02-1 atm. The cells were also measured after being stored in ambient, dry or highly humidified air for different periods of time. The cells referred to as "dried" have been kept in vacuum for one month and an exsiccator for one month at a constant temperature of 20 °C. The "moisturized" cells have been stored at a constant temperature of 20 °C for two months in a beaker that also contained a small open tray filled with water. The beaker was covered with a plastic film and the air inside was assumed to be saturated with water. The impedance response was further monitored over minimum 3 days in both ambient, dry synthetic air (21% O_2 + 79% N_2) and humidified air. When measured in humidified air, the gas supply was lead through at water bottle prior to entering the experimental setup. Data were treated with a linear least square fit program, ZsimpWin3.21 using an equivalent circuit model of RQ-circuits in series with a resistor and an inductor (see Figure 6.1).

6.4 Electrode performance

6.4.1 Results

All EIS data presented in this paper were fitted to equivalent circuit models consisting of serially coupled $(RQ)^\gamma$ elements. The spectra have been treated with as few $(RQ)^\gamma$ elements as possible. The general model is shown in Figure 6.1. However, depending on conditions and electrode, *Arc*1 and *Arc*3 were in many cases not visible.

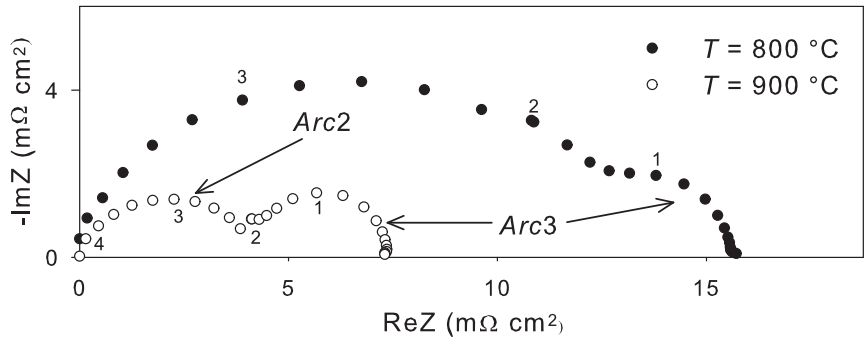

Figure 6.2: Nyqvist plots of the electrode response measured in ambient air and at different temperatures of Electrode A stored for two months. Serial resistance and inductance were subtracted from all spectra to ease comparisons between spectra. Numbers represent log-values of the frequencies.

Figure 6.2 shows Nyqvist plots from EIS measurements at 800-900 °C in ambient air for a symmetric cell with Electrode A and are representative in shape for all impedance spectra of this electrode. The figure clearly depicts the appearance of a low frequency semi circle (summit frequency of approximately 10 Hz) at increasing temperatures. This low frequency response will further on be referred to as $Arc3$, and its resistance and capacitance will be denoted R_3 and C_3. R_3 was found to be about 2-3 mΩcm^2 and relatively independent on T and type of electrode but increased strongly with decreasing P_{O_2}s. The electrode response at higher frequencies will be referred to as $Arc2$, and its resistance and capacitance will be denoted R_2 and C_2. R_2 was found to have a less pronounced P_{O_2} dependence compared to R_3 and proved to be thermally activated. Above 800 °C, the resistance of $Arc2$ was measured to less than 20 mΩcm^2, which allowed $Arc3$ to be distinguished.

Figure 6.3 shows the impedance spectra of a symmetric cell with Electrode C at different P_{O_2}s. These spectra are representative in shape for both Electrode B and C. The low frequency response was found to have very similar P_{O_2} dependence as compared to $Arc2$ of Electrode A. It will for this reason be referred to as $Arc2$ (with the resistance and capacitance denoted R_2 and C_2). The impedance of Electrode C appeared further to consist of a high frequency response which will be referred to as $Arc1$ (with resistance and capacitance denoted R_1 and C_1). $Arc1$ of Electrode B and C were found to be less dependent on changes in temperature and P_{O_2} as compared to $Arc2$. The $Arc3$ seen in the impedance of Electrode A was also found in the impedance of Electrode B and C but was more difficult to resolve, as $Arc2$ of these electrodes was larger.

In order to keep the consistency and the number of fitting parameters as few as possible all γ-values were kept constant over all temperatures and P_{O_2}s. $Arc3$ seen in Figure 6.2 was found to be ideally capacitive and all fits of this response were carried out with γ-value

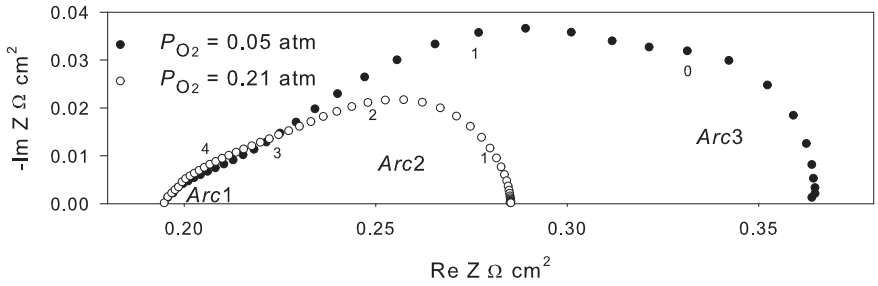

Figure 6.3: Nyqvist plots of the electrode response at 750 °C and different P_{O_2}s measured on Electrode C stored for two months. Numbers represent log-values of the frequencies.

of 1. *Arc*2 was found to be a slightly depressed semi-circle indicating a process with a distributed time constant. All fits were made satisfactorily with a γ-value of 0.75. *Arc*1 found exclusively in the impedance of Electrode B and C (see Figure 6.3) was satisfactorily fitted with a γ value of 0.5.

EIS measurements revealed differences between the Electrodes A-C. The impedance spectra of Electrode A showed a maximum number of two $(RQ)^{\gamma}$-circuit (*Arc*2 and *Arc*3), where *Arc*3 only showed up at high temperatures and/or low P_{O_2}s. The impedance spectra of Electrode B and C were mainly treated as to consist of two separate responses, *Arc*1 and *Arc*2. However *Arc*3 was also visible at high T and low P_{O_2}. *Arc*3 proved to be almost independent on temperature but strongly dependent on oxygen partial pressure. Both *Arc*1 and *Arc*2 proved to be thermally activated and are thus believed to reflect the electrode reaction kinetics.

The serial resistance, R_S, arising mainly from the ionic conductivity of the electrolyte, was routinely compared with the theoretical resistance calculated from the ionic conductivity of CGO10 and the geometry of the symmetric cells in order to verify that no electronic leak currents have influenced the measurements.

It was observed that the polarisation resistance, R_P, of all four electrodes appeared to depend on the time and condition it had been stored at room temperature. Table 6.2 lists the resistance and the activation energy for a number of measurements on electrodes stored for different periods of time and under different conditions. The resistance, R_2, of Electrode A was found to decrease after being stored 14 months in ambient air and at room temperature as compared to a storage of only 2 months in the same conditions. Surprisingly it was found that R_2 increased again after 4 additional months of storage in ambient air.

Electrode D did not fit fully into the above described equivalent circuit model and also

Table 6.2: Tabulated resistances, activation energies and P_{O_2} dependence of the four electrodes. R_P is the sum of R_1 and R_2. The error of E_A is calculated from the standard deviation of the linear regression only.

Electrode	Storage time [months]	Storage cond.	R_X	R_X @ 700 °C [mΩ cm^2]	E_A [eV]	$R_X \propto P_{O_2}^{-n}$ n
A	2	amb. air	R_2	52	1.18 ±0.02	
A	14	amb. air	R_2	26	1.12 ±0.02	n = 0.35-0.42
A	18	amb. air	R_2	51	1.23 ±0.03	
A	14	amb. air	R_3	2	-	n = 0.96-1.09
D	2	amb air	R_P	2690	1.85 ±0.07	
D	12	amb air	R_P	115	1.65 ±0.05	
D	18	amb air	R_P	650	1.70 ±0.02	
B	0.5	amb. air	R_1	96	1.16 ±0.02	
B	0.5	amb. air	R_2	89	1.56 ±0.02	
B	2	dried	R_1	73	1.33 ±0.05	
B	2	dried	R_2	24	1.63 ±0.05	
B	2	moisturized	R_1	40	1.27 ±0.03	
B	2	moisturized	R_2	10	1.4 ±0.1	
B	5	amb. air	R_1	65	1.16 ±0.04	
B	5	amb. air	R_2	14	1.64 ±0.06	
C	0.5	amb. air	R_1	78	1.20 ±0.02	
C	0.5	amb. air	R_2	121	1.53±0.02	
C	5	amb. air	R_1	70	1.13 ±0.01	n ∼ 0
C	5	amb. air	R_2	27	1.62±0.03	n = 0.36-0.38

showed a different temperature and P_{O_2} dependence. In order to avoid confusion we limit ourselves here in presenting the total polarisation of Electrode D. Data of this electrode is presented here as it shares some interesting features with Electrode A-C. The increased performance after 12 months storage was found also for this electrode (with a remarkable increase in performance of a factor of about 20). It also showed an increased resistance when stored for an additional 6 months as did Electrode A.

Also Electrode B and C appear to decrease their resistance when stored at room temperature and in ambient air. Analysis of the impedance data from Electrode C indicated that this decrease in resistance is mainly associated with the $Arc2$ which was reduced from 121 to only 27 mΩcm^2 at 700 °C after 5 months of storage. At 750 °C the initial resistance of R_2 was reduced from 101 to 7 and 138 to 10 mΩcm^2 for Electrode B and C respectively (see Table 6.4). The activation energy does not appear to change significantly by the storage process.

A few cells with Electrode B were kept in dry or highly moisturised conditions for two months in order to test the impact of the atmospheric conditions under which the cells are stored. Post analysis showed that the moisturized cells had decreased the polarisation resistance, R_P, with a factor of about 4 whereas R_P of the cell kept in a dry atmosphere

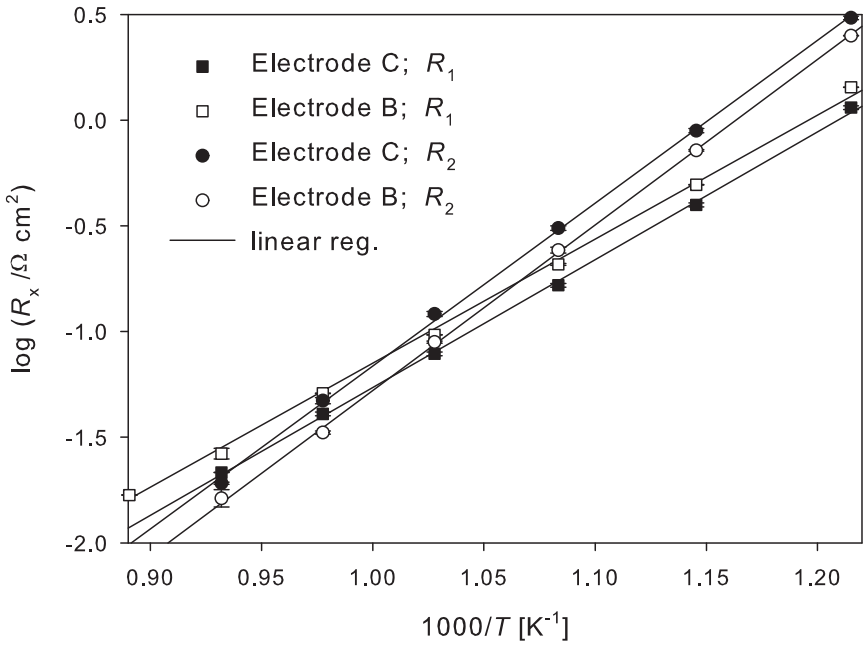

Figure 6.4: Arrhenius plots of R_1 and R_2 of Electrode B and C. The electrodes have been stored for two weeks. Note that there is very little difference between the two electrodes.

decrease with a factor of about 2 (see Table 6.2). The storage treatment appeared again not to change the activation behaviour dramatically. The decrease in resistance was found to be related mainly to R_2.

Figure 6.4 plots the area specific resistance as function of inverse temperature for R_1 and R_2 of Electrode B and C stored for two weeks. The figure shows linear Arrhenius dependence for both electrodes and both $Arc1$ and $Arc2$. Moreover, the difference in both R_1 and R_2 is very small despite that the electrodes are made of two different materials. Table 6.2 together with Figures 6.4 indicate that substituting 10 % cobalt with nickel in $(La_{0.6}Sr_{0.4})_{0.99}CoO_{3-\delta}$ does not change the catalytic properties to any larger extent and that the performance is much more susceptible to changes in processing parameters, storage conditions and heat treatments.

Figure 6.5 shows the P_{O_2} dependance of R_2 and R_3 of Electrode A, where $R_X \propto P_{O_2}^n$. The resistance, R_3, appeared to have a reciprocal P_{O_2} dependence whereas R_2 was found to be dependent on P_{O_2} to the power of -(0.35-0.42) depending on temperature within the range T=550-750 °C and $P_{O_2} \approx$ 1-0.02 atm. Figure 6.6 plots the P_{O_2} dependance of the R_1 and R_2 of Electrode C at 650-850 °C. R_1 appears to be independent on P_{O_2} while R_2 showed a P_{O_2} dependance to the power of -(0.36-0.38). This is close to the measured P_{O_2} dependence on Electrode A. The P_{O_2} dependencies for R_2 and R_3 are listed in Table 6.2. It should be stressed that the P_{O_2} dependence is measured on cells stored for different

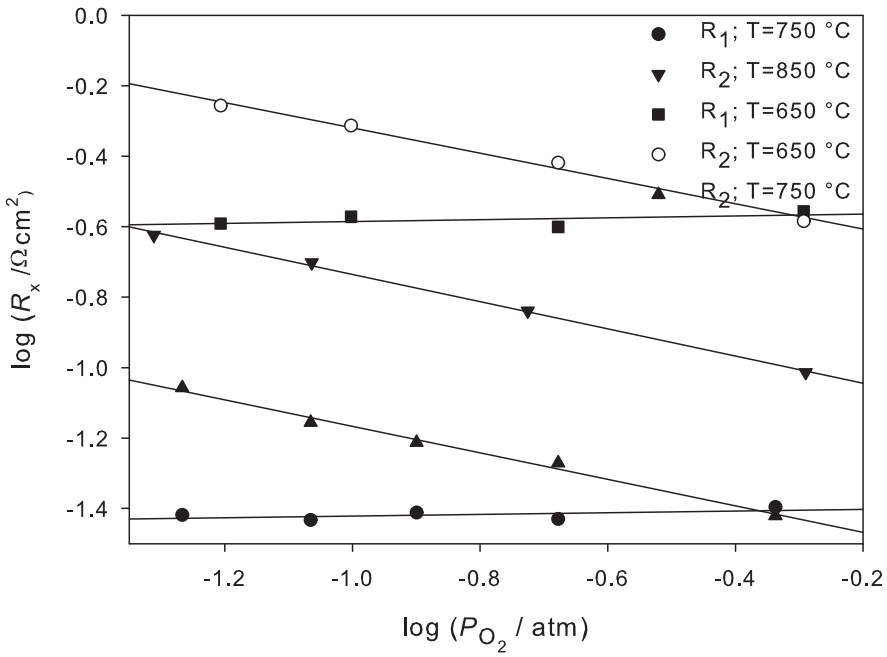

Figure 6.5: Log-log plots showing the P_{O_2}-dependence of R_2 and R_3 of Electrode A stored for 14 months at three different temperatures.

periods of time. The activation energy was however approximately which indicates that no major mechanistic change occur due the storage. Furthermore, the paper does not aim at discussing mechansistic differences between the the different electrodes.

*Arc*3 was perfectly fitted with a γ-value of unity, indicating that the process involved behaves like an ideal capacitor in parallel with a resistor. C_3 was found to be about 5-10 Fcm^{-2} and almost independent on temperature and P_{O_2}. Both *Arc*1 and *Arc*2 were found to be depressed and the capacitances, C_1 and C_2, were calculated using the expression:

$$C = R^{\frac{(1-\gamma)}{\gamma}} \cdot Q^{\frac{1}{\gamma}} \tag{6.1}$$

where R is the resistance, Q is the admittance of the constant phase element (CPE) and γ is the exponent to which the CPE is raised. Figure 6.7 plots the calculated capacitance, C_1 and C_2, of Electrode A-C using Equation 6.1 as function of T and shows fundamentally different thermal behaviour. The capacitance, C_1, of Electrode B and C was found to be approximately 0.5 mFcm^{-2} and appeared rather independent on T. The capacitance, C_2, of both Electrode B and C were measured to about 10-50 mFcm^{-2} and were shown to increase slightly with temperature. The capacitance, C_2, of Electrode A on the other hand appeared to decrease with temperature and followed an apparent Arrhenius relation with a small activation energy of 0.17 ± 0.01 eV. C_2 of Electrode A was calculated to about 10 mFcm^{-2} for T=550-850 °C and P_{O_2}=1-0.02 atm. Figure 6.8 shows the capacitance as function of

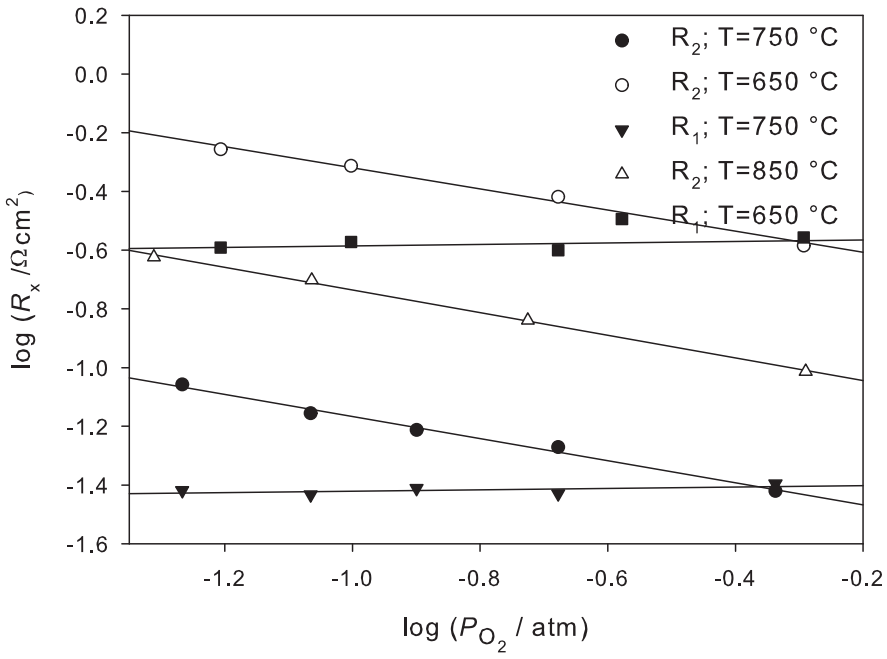

Figure 6.6: Log-log plots showing the P_{O_2}-dependence of the R_1 and R_2 of Electrode C stored for 5 months. R_1 appears independent on P_{O_2} while R_2 shows a dependence with respect to P_{O_2} to the power of -0.37 $\pm$0.01 for the temperature range 650-850 °C.

P_{O_2} for Electrode A and C on a log-log plot. C_2 of Electrode A was found to be dependent on P_{O_2} to the power of about -0.2 whereas C_2 of Electrode C was found to be dependent on P_{O_2} to the power of approximately -1. C_1 of Electrode C appeared to be dependent on P_{O_2} and followed approximately the same P_{O_2}-dependance as C_2 though it did not show a very linear correlation.

Figure 6.9 shows a Scanning Electron Micrographs (SEM) of the electrode/electrolyte interface of Electrode A (top) and Electrode C (bottom). The images indicate that Electrode A is better contacted to the electrolyte as compared to Electrode C. One might also argue that Electrode C contains a higher concentration of distinctive, individual primary particles whereas the particles in Electrode A have sintered together to a higher degree. Electrode C appears further to have a higher degree of porosity. However, one needs to stress that these observations are difficult to quantitatively argue for.

6.4.2 Discussion

Electrochemical analysis of Electrode A-C showed that the impedance spectra of Electrode B and C appear to resemble each other with separate high and low frequency responses ($Arc1$

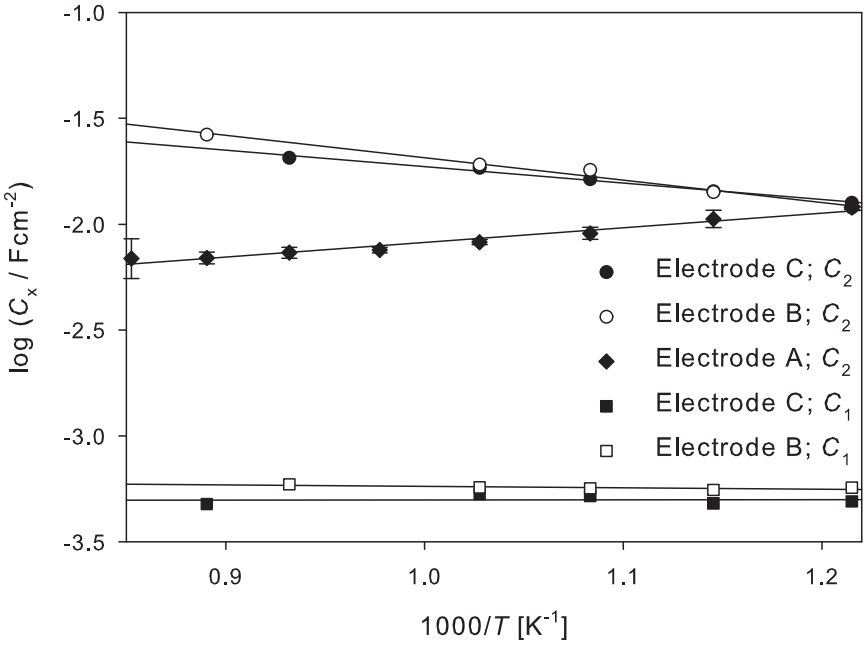

Figure 6.7: Arrhenius plots of C_1 and C_2 of Electrode B and C stored for 2 weeks and the capacitance C_2 of Electrode A stored for 18 months. C_1 of Electrode B and C appears independent on temperature, whereas the C_2 of Electrode B and C show a "reverse" apparent Arrhenius behaviour. C_2 of Electrode A oppositely proved to follow a "true" apparent Arrhenius relation.

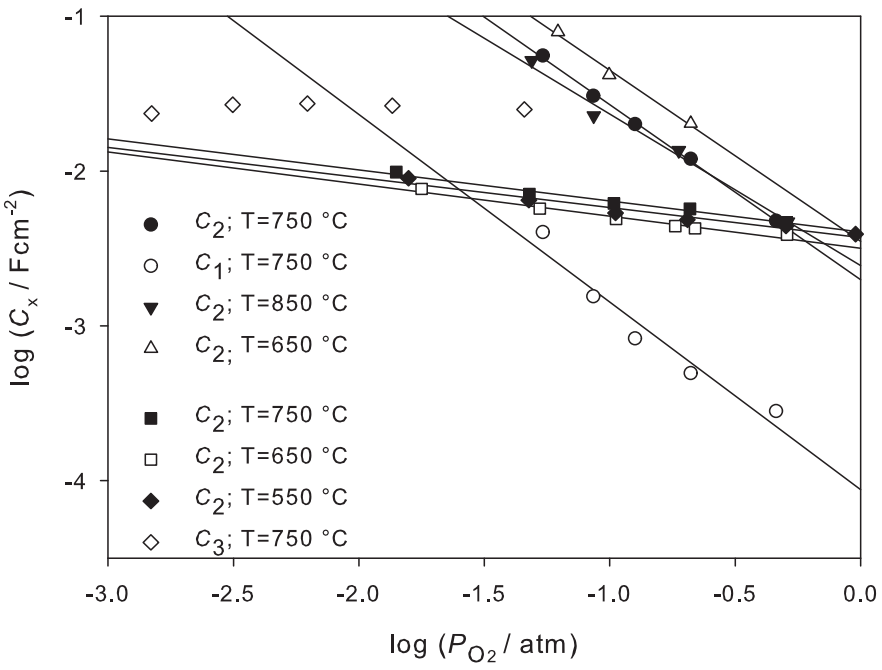

Figure 6.8: Log-log plot showing the P_{O_2}-dependence of C_1 and C_2 of Electrode C stored for 5 months and C_2 of Electrode A stored for 1 months.

and $Arc2$). The resistances, R_1 and R_2 of the two electrodes and their respective activation energies were very similar. Even the capacitance as function of T was approximately the same (see Figures 6.7-6.8). Electrode A and B on the other hand showed quite different electrochemical behaviour despite consisting of the same perovskite composition. Electrode A showed no evidence of the high frequency response, $Arc1$, which was found in the impedance of Electrode B. Also the resistance, R_2, and capacitance, C_2, of $Arc2$ was found to be different both in magnitude and in the way they responded to changes in T. This indicates that the electrochemical response of porous electrodes of $(La_{1-x}Sr_x)_sCo_{1-y}Ni_yO_{3-\delta}$ are more dependent on the heat treatment of the powder and the time and condition the electrodes have been stored in (and perhaps other unknown parameters assumed to change the microstructure and/or the surface chemistry) rather than material changes inflicted by substituting 10 % cobalt with nickel in $(La_{0.6}Sr_{0.4})_{0.99}CoO_{3-\delta}$.

$Arc3$ seen in the low frequency regime of the impedance spectra measured at high temperatures and/or low P_{O_2}s (see Figure 6.2) was nicely described with an RC-element with a rather large capacitance of about 5-10 Fcm^{-2}. The reciprocal P_{O_2} dependence could point towards molecular adsorption as being the rate limiting step of this response, however, no such conclusion has been made in the literature. The fact that it is not a thermally activated process strongly suggest that this process is not part of the electrode reaction kinetics but reflects instead a concentration polarisation (either gas diffusion or gas conversion). [162], [163] This arc is not related to the electrode itself and will not be discussed further on in this paper.

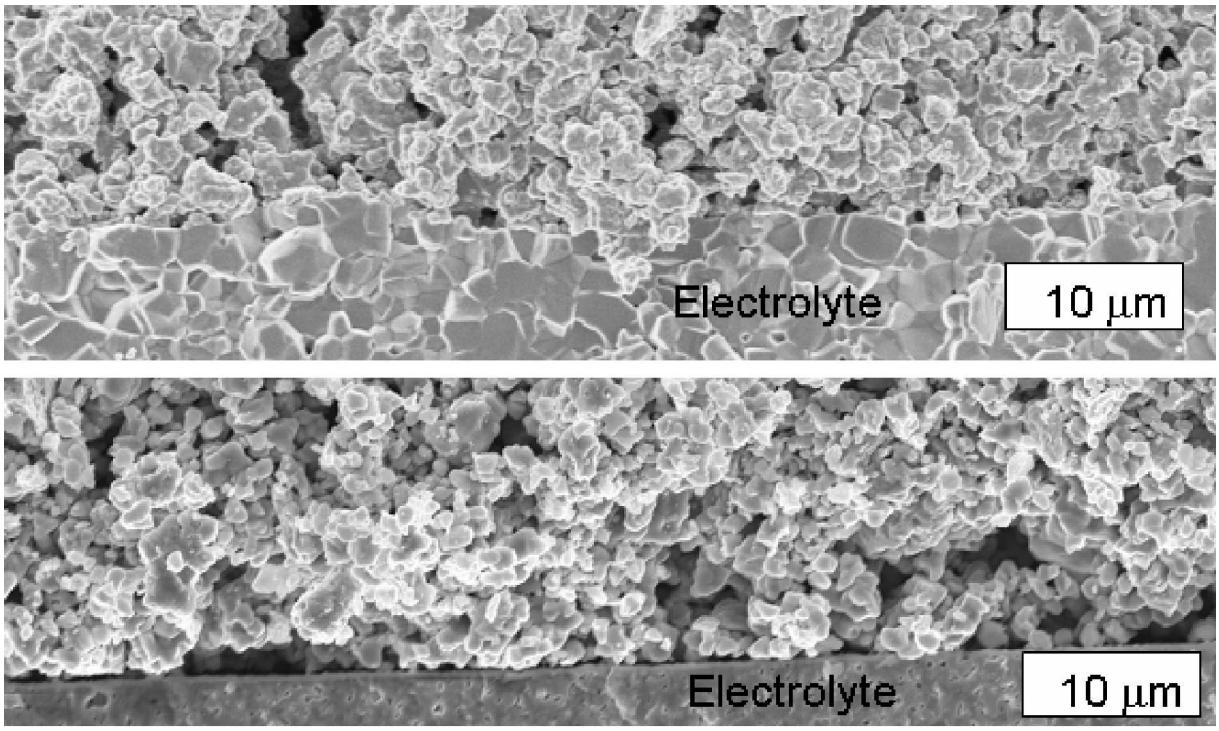

Figure 6.9: Scanning Electron Micrographs (SEM) of the electrode/electrolyte interface of Electrode A (above) and C (below). Both electrodes have been stored in ambient air. Electrode A is 14 months old and Electrode C is 2 months old. The images show the different adhesion between the two electrodes and the electrolyte where Electrode A appears to be better contacted to the electrolyte than Electrode C.

Many earlier studies have attempted to describe the overall reaction mechanism and the rate limiting step(s) of oxygen reduction on mixed ionic electronic conducting (MIEC) electrodes such as $(La_{1-x}Sr_x)_sCoO_{3-\delta}$ and related compositions without coming to a consensus.[98], [99], [100], [101], [95] The reasons why different groups come to different conclusions are several e.g. (1) different measurement conditions e.g. polarization, temperature or atmospheric condition (2) different materials, e.g. different microstructure or levels of impurities/secondary phases and (3) different measurement techniques eg. EIS, relaxation techniques, coulometric titrations etc. On top of this comes the high degree of sensitivity of these kinds of electrodes to fabrication and storage as discussed further below.

Approximately the same P_{O_2} dependence was found for R_2 of Electrode C as compared to R_2 of Electrode A. (see Figures 6.5 and 6.6). This could indicate that the electrochemical response, $Arc2$, in the impedance spectra of Electrode A and C represent a closely related electro-chemical process. However, the activation energy of R_2 is quite different as shown in Table 6.2 where E_A is about 1.1 eV for Electrode A and about 1.5-1.6 eV for Electrode B and C. There are furthermore differences in how the capacitance responds to changes in T or P_{O_2}. This makes it very difficult to draw decisive mechanistic conclusions for porous electrodes of $(La_{0.6}Sr_{0.4})_{0.99}CoO_{3-\delta}$ as a change in processing parameters appear to affect not only the resistance and capacitance of the electrode but also the way it responds to changes in temperature.

Several reports have pointed towards dissociative adsorption as the rate limiting step for mixed conducting SOFC-cathodes, a process that has a theoretical P_{O_2}-dependance according to Equation 6.2 with n= - 0.5 ,[94], [103] [83], [164]. However the n-value is not a true reaction order as changes in P_{O_2} will also affect the electrode potential (vs a reference electrode) as well as the defect structure of the electrode. A decrease in P_{O_2} will increase the concentration of oxygen vacancies, which have been argued to be crucial in rate limiting the oxygen reduction reaction. [83], [128], [92], [19] Thus we would actually expect an apparent 1/R-P_{O_2}-dependence with a n-value different from 0.5. Figures 6.5 and 6.6 show that R_2 of Electrode A is dependent on P_{O_2} to the power of -0.35 to -0.42 and that R_2 of Electrode C is dependent on P_{O_2} to the power of -0.36 to -0.38. The linearity was found to prevail over the entire temperature- and P_{O_2}-region (T = 550-850 °C and P_{O_2} =1-0.02 atm) at which the measurements were conducted. This indicates that no major shift in reaction mechanism occurs within the experimental range.

De Souza *et. al.* found a strong correlation between the oxygen surface exchange coefficient, k_{ex} and the oxygen diffusion coefficient, D_{chem}, irrespective of materials composition, T or P_{O_2}.[165] As oxygen diffusion is dependent on oxygen vacancies this correlation was interpreted as oxygen vacancies playing a major role also in the rate limiting step of the oxygen surface exchange reaction on mixed ionic conducting oxide surfaces. Merkle et al. [92] continued this discussion by correlating the activation energy of the surface exchange reaction with the activation energy of the chemical diffusion coefficient. This correlation was used to argue that the transfer of an arbitrarily charge adsorbed oxygen species, O_{ads}^{-n}

into a surface vacancy is rate limiting the oxygen exchange reaction (ie incorporation limited, see Reaction 6.3). Adler *et. al.* [83] have published a study in which theoretical expressions have been derived for different rate limiting steps of the oxygen exchange reaction. It was found that a reaction mechanism with dissociative adsorption at surface oxygen vacancies as the rate limiting step agreed best with experimentally data published in literature on mixed conducting $(La_{1-x}Sr_x)_sCoO_{3-\delta}$. This is due to the low probability of the unstable physisorbed O_2 to interact with two adjacent surface oxygen vacancies. The physisorbed O_2 is stabilised to a certain degree because of the metallic-like band structure, from which the electronic charge transfer steps (reduction) are believed to occur very fast. Fleig [90], [91] has considered ionic or electronic charge transfer at the gas/MIEC electrode surface as rate limiting the overall reaction when modelling the i-v characteristics of the oxygen exchange reaction. It was found that the i-v and the P_{O_2}-dependence was dramatically different depending on surface coverage, majority oxygen specie (O^-_{ads}, O^{-2}_{ads}, $O^-_{2,ads}$ etc).

Whether or not the oxygen exchange reaction is limited by dissociative adsorption or oxygen incorporation is still a matter of discussion. However, it appears as though both atomic oxygen species and oxygen surface vacancies are taking part in the rate limiting step of the oxygen exchange reaction. A crude way to test if the electrode resistance, R_2, is dependent on the surface exchange reaction is thus by correlating the inverse resistance, $1/R_2$, with the oxygen vacancy concentration, $V_O^{\cdot\cdot}$ and $\sqrt{P_{O_2}}$ according to equations 6.3-6.4.

$$O_2(g) \rightarrow 2O_{ads} \tag{6.2}$$

$$O_{ads} + [V_O^{\cdot\cdot}] + 2e^- \rightarrow O_O^X \tag{6.3}$$

$$\frac{1}{R_2} \propto P_{O_2}^{0.5} \cdot [V_O^{\cdot\cdot}] \tag{6.4}$$

The oxygen vacancy concentration is linearly related to the oxygen nonstoichiometrty parameter, δ, which was calculated using the itinerant electron model (see ref [78]) for each point (T and P_{O_2}) at which R_2 was measured. It is then assumed that δ is linearly correlated with the surface oxygen vacancy concentration. Figure 6.10 plots the relation $R_2 \propto \delta^{-1} \cdot P_{O_2}^{-0.5}$ at 650-750 °C for Electrode A and at 650-850 °C for Electrode C on log-log scales. The figures show linear correlations for both electrodes at all T, which indicates that the resistance, R_2, is associated with the surface exchange reaction. It should be stressed that the experimentally measured range is rather narrow and that this correlation might be pseudo-linear, ie linear on a small scale, but is in fact non-linear on a large scale. Adler *et. al.* [83] argued that the modelled reaction mechanism with dissociative adsorption as rate limiting step holds also when being far from equilibrium. The argument was based on a satisfactorily fitting of the rate to coulometric titration data measured under large chemical potentials. Our data hold for open circuit voltage only and the results might be

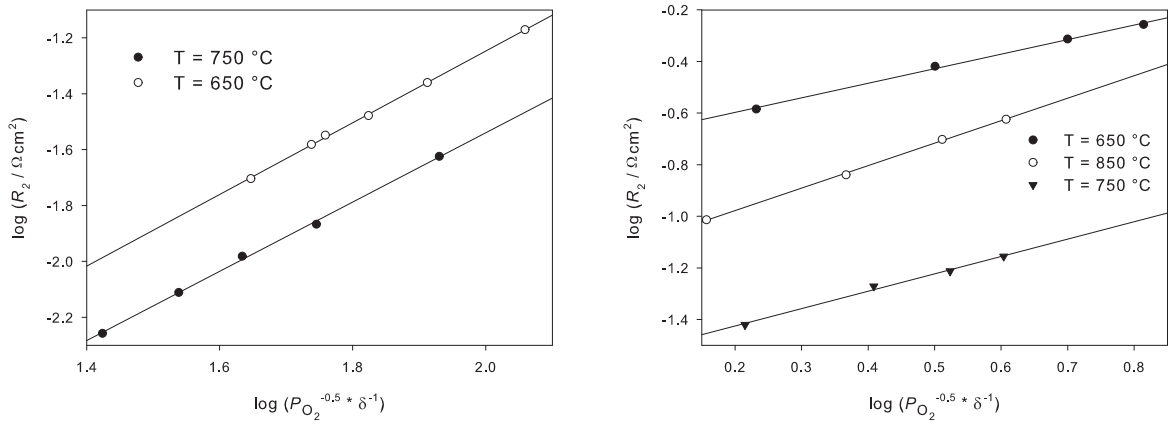

Figure 6.10: Plot of R_2 as function of $\delta^{-1} \cdot P_{O_2}^{-0.5}$ for Electrode A (left) and Electrode C (right).

very different for an electrode under current load or under more extreme conditions (T, P_{O_2}).

R_2 of Electrode A showed activation energies different from those of B and C and C_2 showed different dependence on T and P_{O_2}. There is also a difference in the shape of the impedance spectra of Electrode A and B/C. It appears as though the impedance spectra of Electrode B and C (see Figures 6.3) have shapes that could also be interpreted as a Gerischer impedance or to consist of a Gerischer impedance in series with a small high frequency $(RQ)^\gamma$-circuit instead of two separate $(RQ)^\gamma$-circuits, that we have modelled our data with. The Gerischer impedance arises in systems which are co-limited by more than one process. This has been discussed by Boukamp et. al. for a system with an chemical reaction coupled to a diffusion process. [104] This has also been observed for several different SOFC cathode materials such as platinum [166] and $(La_{1-x}Sr_x)_sMnO_{3-\delta}$ [167] which are not considered mixed conducting. In these cases the diffusion is argued to follow a surface path. Adler *et. al.* [98] have derived a model, referred to as the *ALS-model*, that couples the oxygen surface exchange with oxide ion diffusion into one electrochemical response. This response takes the form of a Gerischer impedance. Thus, if $Arc2$ of the impedance of Electrode B/C is considered as a Gerischer rather than a simple $(RQ)^\gamma$-circuit this could indicate that also oxygen diffusion contribute to $Arc2$. A co-limited reaction means, in this case, that the oxygen surface exchange and oxygen diffusion will not be coupled in series but can instead be pictured as an equivalent circuit with two parallel resistive "rails" representing the diffusion process and the electronic current which are coupled via the RC-circuits, representing the exchange reaction (see Figure 6.11). This concept has been discussed in detail by Jamnik and Maier.[106], [107]

In order to compare the resistive and capacitive contributions to the electrode impedance in a consistent and "simple" way, we have in this paper modelled the EIS data using serially coupled $(RQ)^\gamma$-circuits with constant γ-values. How the *ALS-model* apply to porous electrodes of $(La_{1-x}Sr_x)_sCo_{1-y}Ni_yO_{3-\delta}$ will be discussed in a subsequent paper. We stress however the rationality of such a coupling within a mixed conducting electrode as the

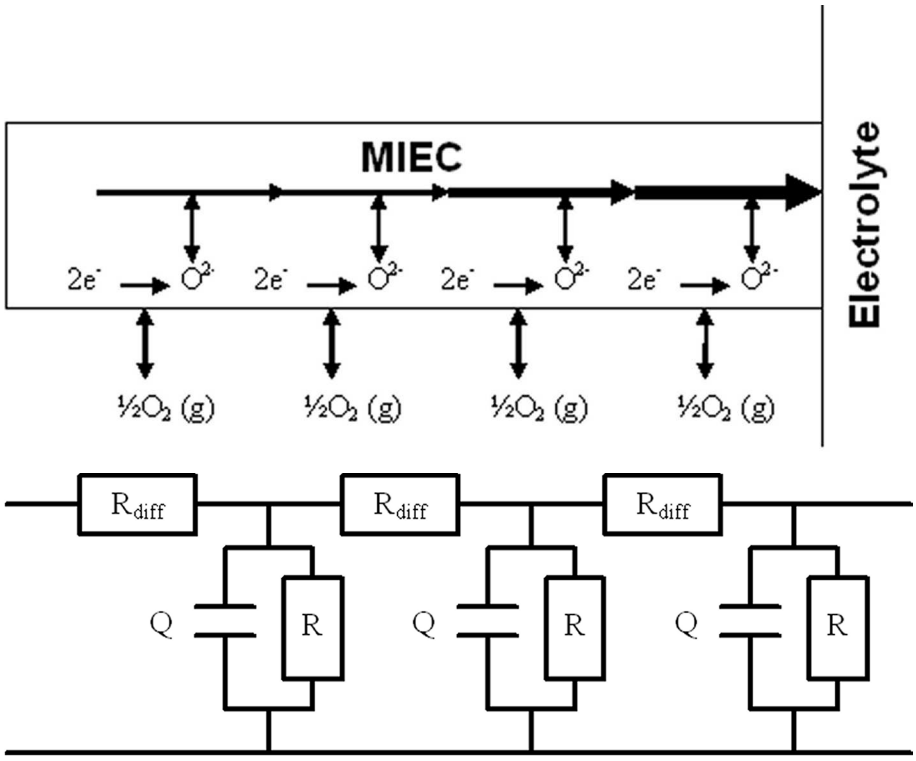

Figure 6.11: Above: Illustration of the overall reaction mechanism where the surface exchange is co-limited to diffusion of oxygen species at the surface or through the bulk of a MIEC. The thick arrows represent oxide ion diffusion **Below:** An equivalent circuit model of the above describe reaction model. The EQC-model, often referred to as a transmission line, has been shown to give rise to a Gerischer impedance in systems where for a diffusion process is coupled to a reaction. [104]

reaction is believed to proceed over a larger fraction of the surface rather than just at the three phase boundary (TPB).

The capacitance, C_2, of Electrodes A-C (see Figure 6.7 and 6.8) is higher by several orders of magnitude than the double layer capacitance of 10^{-5}-10^{-6} Fcm^{-2} typically found for SOFC cathodes limited by charge transfer at the three phase boundary (TPB). [89] This indicates that the reaction is not associated with a charge transfer process but instead the involvement of a larger fraction of the cathode and the presence of a *chemical capacitance* (see ref [106] for definition) that arises as a consequence of a reduction process and formation of bulk oxygen vacancies. Adler has derived a relationship for such a capacitance in porous mixed conducting cathodes (see Equation 6.5) in which the reduction is reflected in the concentration of oxygen vacancies. It depends also on a *utilisation length*, l_δ, describing the depth of the cathode within which the oxygen reduction takes place (see Equation 6.6).

$$C_{\text{chem}} = \frac{2F^2(1-\epsilon)c_{\text{v}}l_\delta}{ART} \tag{6.5}$$

$$l_\delta = \sqrt{D_{\text{v}}/k_{\text{ex}}}. \tag{6.6}$$

where k_{ex} and D_{v} are the surface exchange and vacancy diffusion coefficients respectively. Increasing the surface exchange rate will thus reduce the active thickness while a rapid diffusion while increase the active region.

The calculated capacitance, C_2, of about 10^{-2} Fcm^{-2} indicate that the active region for oxygen reduction extends an unknown distance beyond the TPB. Kawada *et. al.* [168] measured the chemical capacitance of a 1.5 μm thin dense film of $(La_{0.6}Sr_{0.4})CoO_{3-\delta}$ to 0.1-1 Fcm^{-2} in which the bulk was necessarily involved for transport of O^{2-} to the electrode/electrolyte interface. Our calculated capacitance is about one order of magnitude lower which indicate further an active region that is smaller than 1 μm. This is in agreement with the mean particle size of the electrode.

The impedance of Electrode A resembles a RQ-circuit (see Figure 6.2). Adler *et. al.* [112] have shown in his model that the impedance response will have a semicircular shape rather than the characteristic Gerischer curvature in both of the two limiting cases the:

I l_δ approaches the size of the individual particles and the reaction occurs relatively close to the electrode/electolyte interface.

II l_δ approaches the thickness of the cathode and the reaction proceeds throughout the whole electrode.

A linearised expression was derived for the limiting case (II) of the ASL-model where the oxide ion diffusion is so fast that the entire thickness of the electrode is active (see Equation 6.7). This expression takes the form a semi circle. We have included the parameter, m, in the modelling of our impedance as they have a depressed shaped.

$$Z_{\text{chem}} = \frac{RT}{2F^2}\frac{1}{aLc_{\text{o}}k_{\text{ex}}(1-(j\omega t_{\text{chem}})^m)} \tag{6.7}$$

$$t_{\text{chem}} = \frac{c_{\text{v}}(1-\epsilon)}{Aac_{\text{o}}k_{\text{ex}}} \tag{6.8}$$

Table 6.3: Experimentally based input parameters for fitting the impedance of Electrode A (stored for 2 months) at 600 °C in ambient air shown in Figure 6.12 to the *ALS-model* in the limiting case (II). This is expressed in equation 6.7 and corresponds to an electrode reaction that is controlled by surface exchange.

a	ϵ	L	$g(\epsilon_F)$	c_o	c_v	A
$cm^2\ cm^{-3}$	-	μm	$mol\ J^{-1}$	$mol\ cm^{-3}$	$mol\ cm^{-3}$	-
22000	0.3	25	$1.8 \cdot 10^{-5}$	0.091	0.00047	1.47

$$A = 1 + \frac{12}{g(\epsilon_F)RT}\frac{c_v}{c_{mc}} \tag{6.9}$$

where a is the surface area, ϵ is the porosity, L is the electrode thickness, A is the thermodynamic enhancement factor, $g(\epsilon_F)$ is the density of states at the Fermi level (see ref [80]) and c_o and c_v are the concentration of oxygen and oxygen vacancies in the oxygen sublattice. m has been included to correct for non-ideal capacitance and is the equivalent to γ in Equation 6.1. We have used the expressions 6.7 to 7.8 together with appropriate input parameters from thermograviometry, BET, XRD and SEM in order to fit the impedance spectra of Electrode A measured at 600 °C. The input parameters are listed in Table 7.1. Figure 6.12 shows the best linear least square fit to *ALS-model* under the limiting case (II) (see Equation 6.7) where the surface exchange coefficient, k_{ex}, and the exponent, m, were the only fitting parameter (m was found to be ≈ 0.75). At 600 °C the surface exchange coefficient was found to be $3 \cdot 10^{-7}$ cm s^{-1} with an activation energy of 1.2 eV. This is in the same order of magnitude as k_{ex} measured by de Souza *et. al.* [165] for $(La_{0.5}Sr_{0.5})CoO_{3-\delta}$ and $(La_{0.8}Sr_{0.2})CoO_{3-\delta}$ using oxygen isotope exchange/SIMS measurement. It disagrees however by several orders of magnitude when compared to measured data using conductivity relaxation by Søgaard *et. al.* [142] and van der Haar *et. al.* [129] More importantly the frequencies of the best fit to this model still deviates from measured data with a factor of about 100, which indicates that the impedance spectra cannot be satisfactorily fitted with Equation 6.7. This implies that Electrode A is not limited according to case (II) and that the whole electrode is not active for reduction. The fact that the impedance spectra has a semicircular shape, at least at low T, could instead indicate that the impedance of Electrode A is under influence of the first limiting case (I), described by the typical $(RQ)^\gamma$ circuit, where the reaction is limited to a region relatively close to the particle size and thus restricted to a region close to the interface between the electrode and the electrolyte.

R_2 of Electrode A would then, according to the limiting case (I) of the ASL-model, be limited by bulk diffusion. An electrode resistance limited by bulk diffusion is, however, expected to decrease with P_{O_2} as a lower P_{O_2} increases the concentration of oxygen vacancies necessary for oxide bulk diffusion to take place. [169] [164] Figure 6.5 shows however the opposite P_{O_2} dependence with R_2 increasing with decreasing P_{O_2}. The linear correlation $R2 \propto \delta^{-1} \cdot P_{O_2}^{-0.5}$, instead indicate that R_2 is dependent on the surface reaction rather than being associated with bulk diffusion. We thus arrive at the apparently contradictory

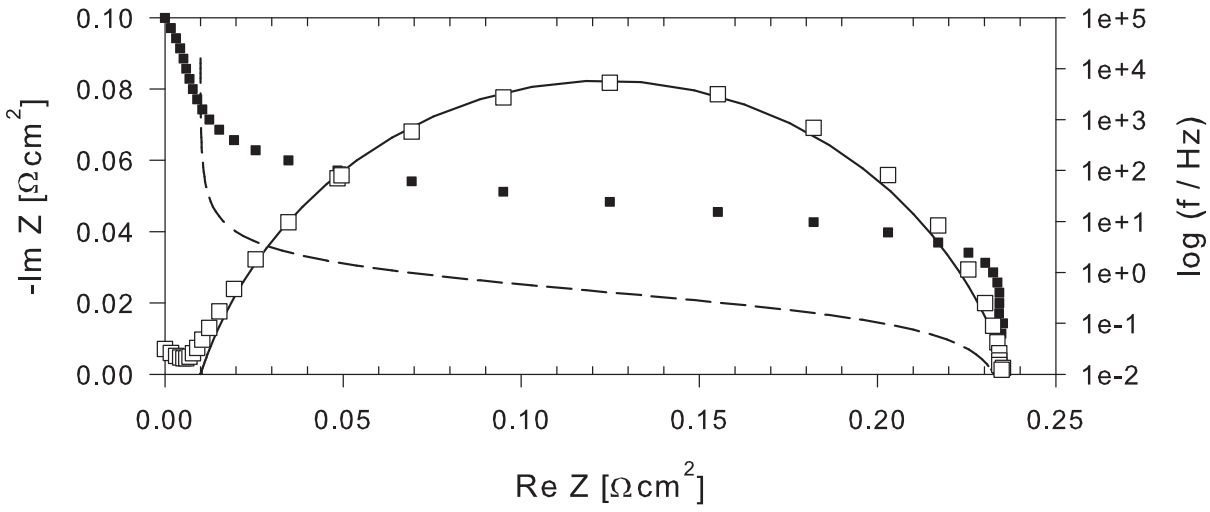

Figure 6.12: Measured impedance spectra (open square measured impedance; close squares=measured frequencies) of Electrode A (stored for 2 months) at 600 °C. The lines represent best fit to the Adler model [112] given a set of input parameters measured independently (see Table 7.1). The impedance spectra was fitted with the surface exchange coefficient, k_{ex} and the exponent, n=0.75).

conclusions that R_2 is dependent on the surface exchange reaction yet the reaction is still limited to an area close to that of the average particle size.

The vacancy diffusion coefficient, D_v, has been reported to be independent on P_{O_2}, whereas the surface exchange coefficient is known to decrease with P_{O_2}. [142], [111], [118] Thus decreasing P_{O_2} will increase l_δ and consequently C_{chem}, provided that diffusion occur via the bulk . Additionally a decrease in P_{O_2} will also increase the vacancy concentration, c_v and therefore also C_{chem} according to Equation 6.5. This could explain the increase in capacitance, C_2, with decreasing P_{O_2} seen in Figures 6.8 for both Electrode A and C. The reason why the capacitance, C_2, of Electrode C increases more dramatically with decreasing P_{O_2} than C_2 of Electrode A could possibly be explained with the above discussed hypothesis that Electrode A is only influenced by the surface exchange reaction whereas the exchange reaction of Electrode B/C is also to some extent dependent on diffusion (co-limited according to Figure 6.11). This will make C_2 of Electrode C dependent on both c_v and the *utilization length*, l_δ whereas Electrode A is only dependent on c_v.

The different trend of C_2 with respect to temperature reported for Electrode A and B/C in Figure 6.7 where C_2 was found to increase with decreasing temperature for Electrode A whereas it decreased with T for Electrodes B and C. Decreasing temperature will favour the surface exchange coefficient over the diffusion coefficient as it has lower activation energy.[165], [121], [112] This means that l_δ and thus also C_{chem} decreases with T in accordance with what was reported for Electrodes B and C. The trend that Electrode A

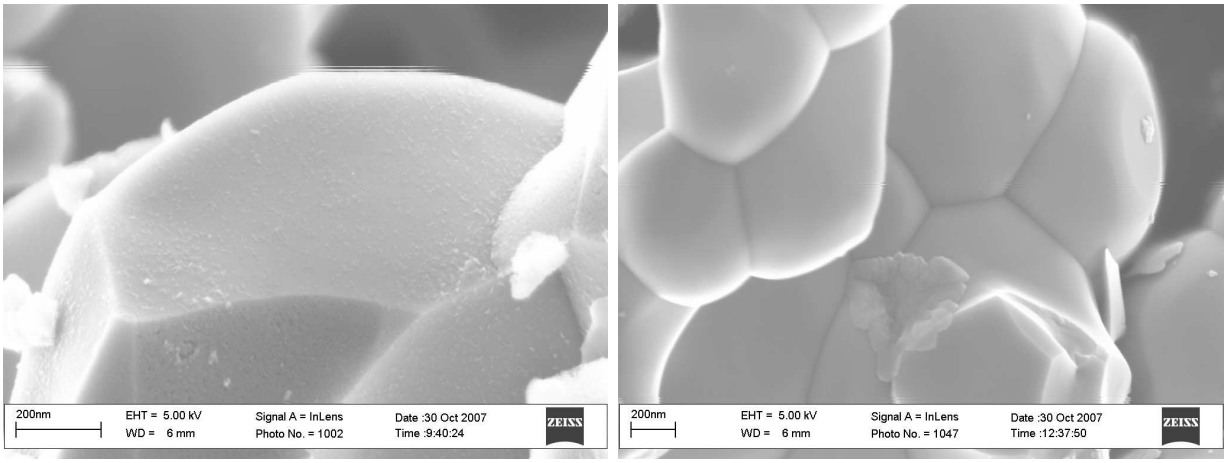

Figure 6.13: Scanning Electron Micrographs (SEM) of Electrode B powder stored in moisturised (left) and dry (right) air for 2 months. Note the small particles sitting on top of the surface of the powder stored in moisturised air.

increases with decreasing T might indicate that this impedance response is more associated with surface processes than with bulk diffusion.

The reason why aging the electrodes at room temperature reduces the polarisation resistance is not clear. One interesting aspect is the fact that the performance increased to a larger extent by storing Electrode B in moisturised air as compared to dry atmosphere. This indicates that water might have an influence on this process. Analysing powders stored in humidified conditions in SEM revealed small particles of a size less than 20 nm. The particle size is much smaller than the excitation volume of Energy Dispersive Spectroscopy (EDS) which disqualified elemental detection as a tool for more detailed analysis. The particles were found throughout the moisturised sample whereas similar particles could not be found on the surface of the powder that had been stored in dry conditions. It appears as though water might inflict changes in the surface morphology and chemistry. Further investigations will be undertaken in order to clarify this phenomena. The fact that the resistance again had increased after 18 months shows that time in moisturised air is not the only parameter of importance. It might indicate that some kind of reversibility because the properties of ambient air (T, P_{H_2O}, P_{CO_2}) may vary with time. The very slow reaction kinetics at room temperature makes it difficult to study this systematically.

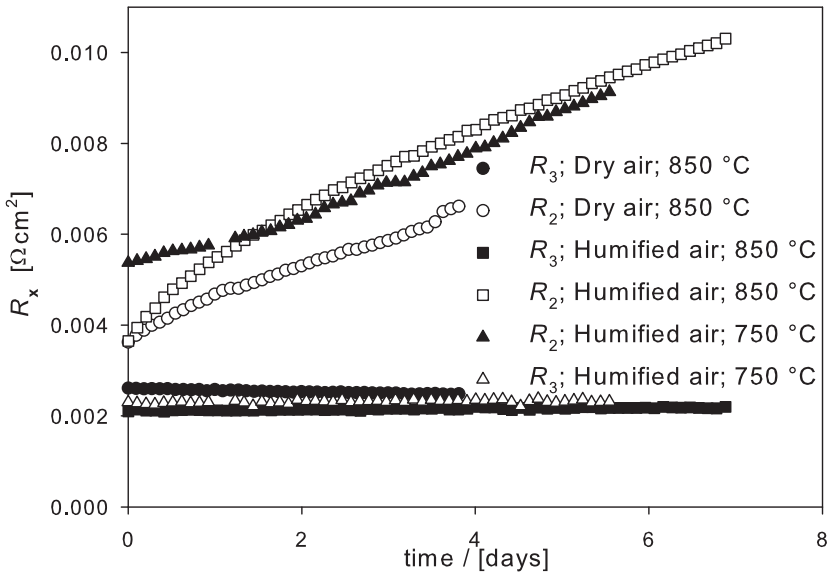

Figure 6.14: The increase in R_2 and R_3 with time at 850 °C in dry "synthetic" and moisturised air for Electrode A on a symmetric cell stored in ambient conditions for 12 months. Note that R_2 increases at a higher rate when measured in moisturised air, where as the R_3 appears to be independent on this treatment.

6.5 Degradation

6.5.1 Results

The increase in resistance with time for the different electrodes have been measured under different atmospheric conditions and after different storage times. Table 6.4 lists the degradation rates at 750 °C in both absolute numbers and relative to initial resistance. Figure 6.14 shows the increase in resistance of $Arc2$ and $Arc3$ of Electrode A at 750 °C and 850 °C, which have been stored for 12 months in ambient conditions. It clearly illustrates that degradation is exclusively associated with resistance, R_2, while R_3 remains stable over time. Figure 6.14 plots further the degradation of R_2 and R_3 at 850 °C in "synthetic" dry air and moisturized, "synthetic" air and illustrates a more rapid increase in the resistance, R_2, when measured in moisturised air. Note the remarkably low resistance of R_2 of only 5.5 mΩcm^2 at 750 °C.

Figure 6.15 plots the increase in polarisation resistance (R_P) and the serial resistance (R_S) with time at 750 °C for two symmetric cells with Electrode B and shows that R_P increases at a much higher rate than R_S. Deconvoluting R_P into its high and low frequency parts ($Arc1$ and $Arc2$) allows to discriminate between the two contributing processes to the overall resistance, R_P. This is also plotted in Figure 6.15 which shows that the increase of R_2 was found to be higher than for R_1.

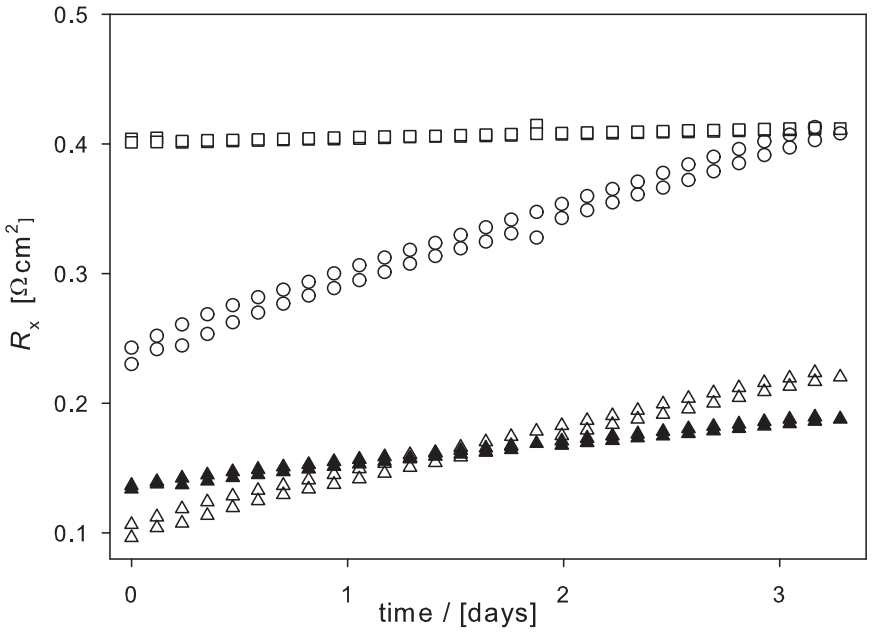

Figure 6.15: Degradation of R_P of Electrode B when deconvoluted into R_1 and R_2. Closed symbols represent R_2 and open symbols represent R_1.

The rates at which R_1 and R_2 degrades are found in Table 6.4 both in absolute values and relative to initial resistance for electrodes stored for different periods of time. Degradation of R_2 of Electrodes B and C stored for 2 weeks, increased at a rate that is approximately twice that of the degradation of R_1 when measured in mΩcm^{2}day^{-1}. Degradation of R_2 of the 2 weeks old Electrode B/C was also found higher than R_1 with a factor of 2 - 3 when measured relative to initial resistance. Storing these electrodes at room temperature and ambient air reduced the degradation rates substantially both in absolute and relative measures. The relative degradation rate of R_1 was reduced with a factor of 5 - 6 after being stored for an additional 4.5 months. The relative degradation rate of R_2 decreased with a factor of only 1.5 - 2 after being stored for 4.5 months, however, the absolute degradation rate of both Electrode B and C decreased with a factor of 14.

Figure 6.16 plots the change in capacitance, C_1 and C_2, during the degradation measurement reported in figure 6.15. C_1 is shown to decrease linearly whereas C_2 appears to remain stable over time.

A degradation measurement was carried out at 750 °C on Electrode D in order to test the effect of moisturised air on the degradation of the electrodes. The measurement setup was first was supplied with moisturised air for about 5 days followed by 5 days in a dry, compressed "synthetic" air mixture of 21 % O_2 and 79% N_2. The polarisation resistance, R_P, was measured continuously. Figure 6.17 plots the increase in resistance with time and shows that the degradation rate decreased from 41.5 to 21.4 mΩday^{-1} when dry air was switched on.

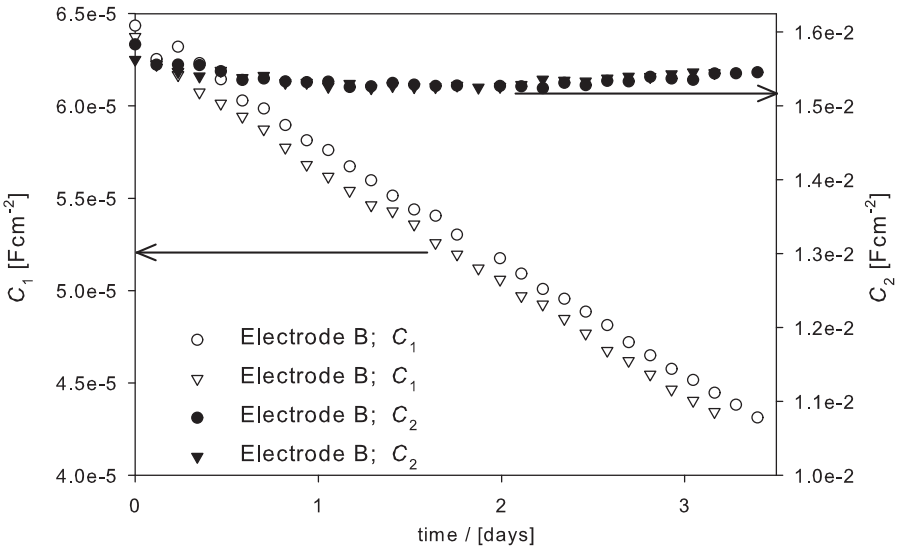

Figure 6.16: Change of capacitance with time at 750 °C of two symmetric cells with Electrode B. Closed symbols represent C_2 and open symbols represent C_1.

Table 6.4: Tabulated degradation rates measured at 750 °C and ambient or moisturised atmosphere.

Electrode	Storage [months]	Test atmosphere	RX	Initial R [mΩcm^2]	rate [mΩcm^{2}day^{-1}]	rel. rate [%day^{-1}]
A	14	ambient air	R_2	7.5	0.47	6.3
A	14	ambient air	R_3	2	0	
A	14	moisturized air	R_2	5.5	0.70	13
B	0.5	ambient air	R_1	135	17.6	12.3
B	0.5	ambient air	R_2	101	37.4	36.9
B	5	ambient air	R_1	32	0.78	2.6
B	5	ambient air	R_2	7	0.36	18.9
C	0.5	ambient air	R_1	117	21.8	18.7
C	0.5	ambient air	R_2	138	36.6	26.5
C	5	ambient air	R_1	42	2.2	4.1
C	5	ambient air	R_2	10	6.6	20
C	2	dry air	R_1	41	1.9	4.0
C	2	dry air	R_2	47	3.8	8.0
C	2	moisturized air	R_1	44	1.9	4.2
C	2	moisturized air	R_2	58	5.1	8.7

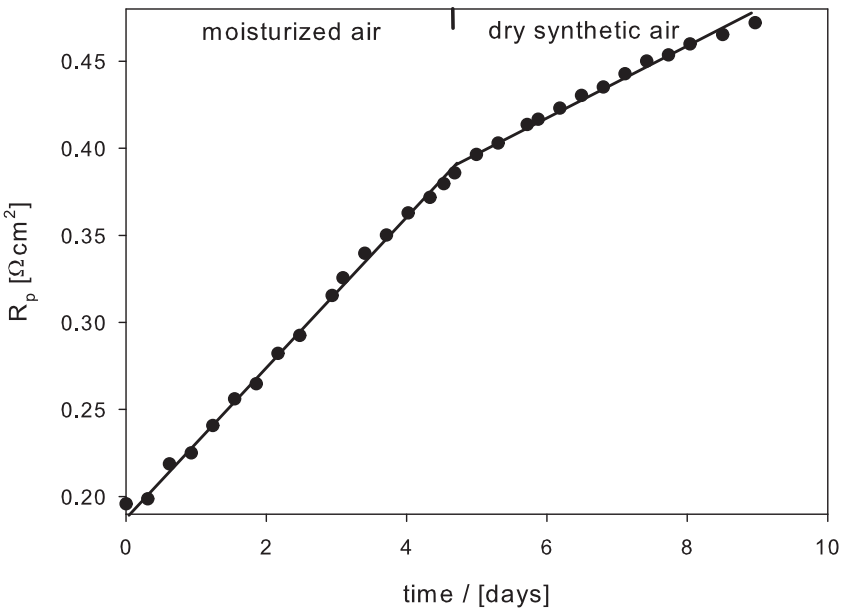

Figure 6.17: Polarization resistance, R_P, at 750 °C in moisturised and dry synthetic air of Electrode D. The degradation rate started decreasing when dry air was switched on.

Figure 6.18 shows the results of a degradation measurement on Electrode C in which the gas supply was, oppositely to the measurement reported in Figure 6.17, switched from a dry *synthetic* air mixture to a moisturized air. A surprising and sudden increase in R_2 is seen at the change of gas supply. This was followed by a higher degradation rate (5.1 $m\Omega cm^2 days^{-1}$) as compared to the measured rate in dry air (3.8 $m\Omega cm^2 days^{-1}$). The degradation of R_1 did not change its rate upon this sudden change in atmospheric condition.

6.5.2 Discussion

Results from the degradation measurements at 750 °C (see Table 6.4) showed that the major part of the degradation is associated with R_2, which we have attributed to the oxygen reduction reaction at the electrode surface. We have also found indications on a higher degradation of the electrode resistance when operated in moisturized air as compared to a synthetic "dry" mixture of 21 % O_2 and 79 % N_2. However, water is to some extent always present in air, even when considered "dry". The increased degradation measured in humidified air indicates that water might influence the degradation process. The importance of oxygen vacancies at the surface has been discussed earlier in this paper as well as in the literature. If the rate limiting step(s) of *Arc*2 depends on free surface vacancies one possible degradation mechanism is speculated to be a competing reaction by which water is adsorbed at surface vacancies to form strongly associated strontium hydroxides [170]

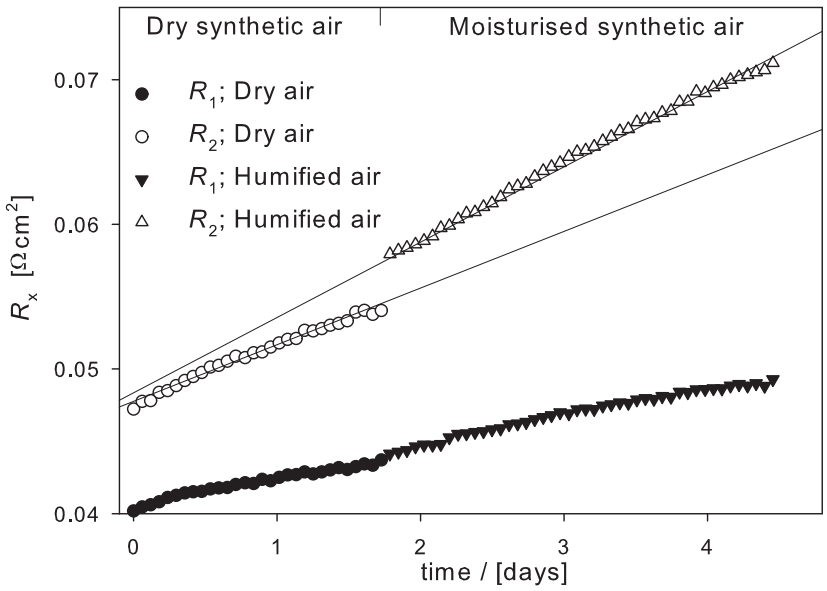

Figure 6.18: Degradation of Electrode C at 750 °C. Note that R_2 starts degrading at a higher rate when moisturised air is supplied whereas R_1 continue to increase at approximately the same rate.

according to the Reaction 6.10. These will inhibit the catalytic sites of the electrode surface and reduce the performance of the electrode with time. This could possibly explain the increased degradation in moisturised air but lacks substantial evidence. The hypothesis will be investigated in further experiments. There might also be several parallel degradation mechanisms acting to reduce the performance of $(La_{1-x}Sr_x)_sCo_{1-y}Ni_yO_{3-\delta}$ with time.

$$O_O^X + Sr'_{La,surf} + H_2O(g) \rightleftarrows [Sr(OH)_2]'_{La,surf} \tag{6.10}$$

A few studies have used thermodynamic modelling to support an association of strontium and oxygen vacancies at the surface of $(La_{1-x}Sr_x)_sCoO_{3-\delta}$. [45], [46], [47] These studies also concluded that strontium tends to segregate towards to surface, which potentially will change the surface chemistry. Segregation of strontium towards the surface has also been observed experimentally in $(La_{0.6}Sr_{0.4})_sCo_{0.2}Fe_{0.8}O_{3-\delta}$ using XPS.[53], [171] These papers do not discuss the rates at which these segregation processes occur. However, if they are acting on the same time scales as our degradation measurements one can speculate that a chemical change of that kind will affect the electro-catalytic properties. Substituting $LaCoO_3$ with strontium has been shown to dramatically decrease the polarisation resistance when used as an oxygen electrode.[94], [125] Strontium can therefore be considered crucial to the electrochemical performance of $(La_{1-x}Sr_x)_sCo_{1-y}Ni_yO_{3-\delta}$ and thus redistribution of strontium with time would be expected to also its efficiency.

6.6 Conclusions

Symmetric cells with porous $(La_{0.6}Sr_{0.4})_{0.99}CoO_{3-\delta}$, $(La_{0.6}Sr_{0.4})_{0.99}Co_{0.9}Ni_{0.1}O_{3-\delta}$ and $(La_{0.8}Sr_{0.2})_{0.99}Co_{0.8}Ni_{0.2}O_{3-\delta}$ as electrodes have been studied using EIS as function of temperature, P_{O_2} and storage time in ambient and moisturised condition. The electrodes have also been studied as function of time at SOFC operating temperatures. We have shown that it is possible to make porous electrodes of $(La_{0.6}Sr_{0.4})_{0.99}CoO_{3-\delta}$ with an electrode resistance of as low resistance as 5-10 mΩcm^2 at 750 °C and with a low activation energy of only 1.1 eV. A small impedance arc at frequencies of 1-10 Hz ($\sim$2 mΩcm^2) was attributed to concentration polarisation. Resistance and thermal behaviour of the electrochemical response of these electrodes were very difficult to reproduce. Even storing the electrodes at room temperature appears to change the electrochemical properties of the electrode. This change was found to be enhanced by a high atmospheric water content. Electrodes with powder of $(La_{0.6}Sr_{0.4})_{0.99}CoO_{3-\delta}$ calcined at 1150 °C instead of 1250 °C showed higher resistance and the appearance of a second, high frequency response (here referred to as $Arc1$), in the impedance spectra. Whether the different behaviour between the two electrodes (A and B) is related to the temperature treatment of the powder or the manufacturing temperature is not clear. Substituting 10 % cobalt with nickel in $(La_{0.6}Sr_{0.4})_{0.99}CoO_{3-\delta}$ did not inflict any major changes to the electrochemical behaviour. The major electrochemical response (here referred to as $Arc2$) showed a $R_2 \sim P_{O_2}^{-n}$ relation with n=0.35-0.42 for all electrodes. A linear correlation between the resistance of R_2 versus $\delta^{-1} \cdot P_{O_2}^{-0.5}$ indicated a reaction mechanism that is dependent on both an atomic oxygen species and an oxygen vacancy and that R_2 is dependent on the surface exchange reaction.

Degradation at operating conditions appears to be mainly associated with the $Arc2$ response, whereas the resistance of the high frequency response ($Arc1$) increased only slightly and concentration polarisation ($Arc3$) did not change at all over time. The degradation rates for all electrodes were found to be much lower after storing the cells at room temperature. Measurements in moisturised air indicated an enhanced degradation. A possible degradation mechanism that is based on the formation of strontium hydroxides at oxygen vacancies of electrode surface is presented.
sible degradation mechanism that is based on the formation of strontium hydroxides at oxygen vacancies of electrode surface is presented.

Chapter 7

Oxygen transport properties of dense and porous $(La_{0.8}Sr_{0.2})_{0.99}Co_{0.8}Ni_{0.2}O_{3-\delta}$

7.1 Abstract

We have determined k_{ex} and D_{chem} for $(La_{0.8}Sr_{0.2})_{0.99}Co_{0.8}Ni_{0.2}O_{3-\delta}$ by the use of electrical conductivity relaxation on a dense sample and by applying the *ALS-model* to measured AC impedance spectrum on a porous electrode. Extracting k_{ex} and D_{chem} from the methods resulted in comparable values. k_{ex} and D_{chem} also agreed well with literature values on $La_{0.8}Sr_{0.2}CoO_{3-\delta}$, indicating that nickel substitution does not change the oxygen transport properties. k_{ex} of the porous sample was further found to decrease with a five times higher rate than D_{chem} when measured using impedance over several days.

7.2 Introduction

Strontium substituted lanthanum cobaltite, $(La_{1-x}Sr_x)_sCoO_{3-\delta}$, has attracted broad attention in recent years due to scientifically interesting properties as well as technologically relevant potential as electro-catalyst for oxygen reduction.[125] This is related to good oxygen transport properties (oxygen surface exchange and oxide ion diffusion) which makes the material interesting for high temperature ceramic devices such as cathodes in solid oxide fuel cells (SOFCs) and ceramic membranes.

$(La_{0.6}Sr_{0.4})_{0.99}CoO_{3-\delta}$ has been reported as an excellent SOFC material with very low measured polarisation resistance when used as porous oxygen electrode. [3] One of the main reasons is believed to be the high concentration of vacancies in the oxygen sublat-

tice providing an oxide ion diffusion path as well as catalytically active sites for adsorption, dissociation and incorporation of oxygen.[83] These processes are often jointly referred to as the oxygen surface exchange. The composition $(La_{0.8}Sr_{0.2})_{0.99}Co_{0.8}Ni_{0.2}O_{3-\delta}$ has in one study been reported to give an even lower polarisation resistance as compared to $(La_{0.6}Sr_{0.4})_{0.99}CoO_{3-\delta}$. [22] This is surprising as the oxygen nonstoichiometry is substantially lower in $(La_{0.8}Sr_{0.2})_{0.99}Co_{0.8}Ni_{0.2}O_{3-\delta}$ as compared to $(La_{0.6}Sr_{0.4})_{0.99}CoO_{3-\delta}$ above 500 °C.[2] In another study on porous electrode of $(La_{1-x}Sr_x)_sCo_{1-y}Ni_yO_{3-\delta}$ it was found that the $(La_{0.8}Sr_{0.2})_{0.99}Co_{0.8}Ni_{0.2}O_{3-\delta}$ had a significantly lower electrochemical performance than $(La_{0.6}Sr_{0.4})_{0.99}CoO_{3-\delta}$.[2] It is therefore of interest to study the oxygen transport properties of this particular composition in order to clarify whether this discrepancy is related to intrinsic materials properties or an effect of secondary/impurity phases, microstructural differences etc. Moreover data on oxygen transport properties of $(La_{0.8}Sr_{0.2})_{0.99}Co_{0.8}Ni_{0.2}O_{3-\delta}$ are to the best of authors knowledge not available in the literature.

Adler *et. al.* [98] has derived a rigorous theoretical model that describes the electrochemical response of a porous electrode. The model couples the surface exchange reaction and oxide ion diffusion into an impedance expression that takes the form of a Gerischer impedance. In general Gerischer impedance arises in systems where a chemical and an electrochemical process are co-limited, in this case as a consequence of the oxygen surface exchange process being coupled to oxide ion diffusion.[105] Thus, despite that the overall reaction is governed by two processes only one response is obtained in the impedance spectrum. This makes contributions from oxygen surface exchange and oxide ion diffusion difficult to separate by the use of normal equivalent circuit models. The *ALS model* takes into account microstructural parameters (eg. porosity, tortuosity, surface area etc) as well as the oxygen nonstoichiometry parameter. It has been verified by comparing the transport properties extracted from fitting measured impedance spectrum to the model with independently measured transport parameters using relaxation or isotope exchange techniques. [98], [172]

In this study we report on oxygen transport properties measured on a dense polished sample of $(La_{0.8}Sr_{0.2})_{0.99}Co_{0.8}Ni_{0.2}O_{3-\delta}$ using the electrical conductivity relaxation technique (ECR). We will also derive the oxygen transport properties by applying the *ALS model* to measured impedance data on a porous electrode of $(La_{0.8}Sr_{0.2})_{0.99}Co_{0.8}Ni_{0.2}O_{3-\delta}$. The data are compared with each other and with recent results in the literature.

7.3 Experimental

A dense sintered bar of $(La_{0.8}Sr_{0.2})_{0.99}Co_{0.8}Ni_{0.2}O_{3-\delta}$ was fabricated as described in [2]. The dimensions where approximately $1.57\times1.76\times20$ mm^3. The surface of the bar was carefully polished using a 0.5 μm SiC cloth in order to gain as flat surface as possible. The relative density of the bar was measured to approximately 95 %. The conductivity relaxation measurement was conducted with a four point DC-technique. Sintered bars were wired with platinum wires and painted with platinum paste at both ends. Voltage probes were separated 0.5 cm apart in the middle of the sample. A current of about 0.5 A was passed through the sample and voltage drops of less than 10 mV were measured at each change of oxygen pres-

sure. The oxygen partial pressure in the gas surrounding the sample could be changed within the time frame of approximately 10 s, and the subsequent voltage transient was measured with a Keithley 2700 multimeter. Measurements were performed at temperatures ranging from 750-950 °C with 50 °C incremental steps starting at 750 °C. The P_{O_2} ranged from 1-0.005 atm with $P_{O_2,final}/P_{O_2,initial} \approx 2$, where $P_{O_2,initial}$ is the oxygen partial pressure prior to the transient and $P_{O_2,final}$ is the oxygen partial pressure is after the transient. The P_{O_2} was monitored using an external YSZ oxygen sensor set at 1000 °C. The data was acquisition set to every 3 seconds.

Powders of $(La_{0.8}Sr_{0.2})_{0.99}Co_{0.8}Ni_{0.2}O_{3-\delta}$ were synthesised and heat treated using the Glycine Nitrate combustion route (see refs, [130], [2]). Symmetric cells were fabricated according to the following procedure. A cathode slurry of 11 g perovskite powder, 15 g ethanol and 1 g polyvinylpyrrolidone (PVP) was prepared and ball-milled over night. The slurry was sprayed onto both sides of a 200 μm thick tape of $Ce_{0.9}Gd_{0.1}O_{1.95}$ (CGO) and sintered at 950 °C for 2 h in order to fabricate a symmetric cell with approximately 25 μm thick electrodes. The cells were cut to dimensions of 4×4 mm^2 and painted with platinum paste which served as current collector. Four identical cells were measured with Electrochemical Impedance Spectroscopy (EIS) under open circuit voltage (OCV) with a Solartron-1260 frequency response analyzer from 1Mhz - 0.01 Hz and with an amplitude of 75 mV. Measurements were conducted as function of T, P_{O_2} and time.

The specific surface area (SSA) was measured using BET-analysis (nitrogen adsorption/desoprtion measurements) in an Gemini 2360 V2.01. All samples were degassed at 300 °C for 24 hours before the BET analysis. SSA was calculated between 0.05-0.21 of relative N_2-pressures (p/p_0) of the adsorption isotherm. A Zeiss Supra 35 Scanning Electron Microscope (SEM) was used to study the microstructure of the symmetric cells and the polished surface of the dense conductivity bar.

7.4 Results

7.4.1 Electrical Conductivity Relaxation

Electrical conductivity relaxation (ECR) is based on a measurements of the change in conductivity of a dense "bar-shaped" sample upon an instant change in the surrounding oxygen partial pressure. A voltage drop is measured across a known distance in the middle of this sample and the conductivity can be calculated provided an accurately measured geometry. The conductivity of these types of perovskites depends on the charge carrier concentration which is related to the oxygen nonstoichiometry parameter, δ, via the electro-neutrality principle. Oxygen nonstoichiometry is a function of the oxygen partial pressure and thus a change in P_{O_2} of the surrounding atmosphere will also change the conductivity of the sample. The characteristic time scales for such a change in oxygen nonstoichiometry and ultimately the conductivity is related to the oxygen transport properties, the surface exchange coefficient, k_{ex}, and oxygen diffusion coefficient, D_{chem}. Methods have been derived using Fick's 2^{nd} law

of diffusion to extract these properties from the measured conductivity transient.[114] The Equations for fitting the conductivity transient are given in Equations 7.1-7.3.

$$\frac{\sigma_\infty - \sigma(t)}{\sigma_\infty - \sigma(t=0)} = \sum_{n=1}^{\infty} \frac{2L_x^2 exp\left(\frac{-\beta_{n,x}^2 D_{chem} t}{l_x^2}\right)}{\beta_{n,x}^2\left(\beta_{n,x}^2 + L_x^2 + L_x\right)} \sum_{n=1}^{\infty} \frac{2L_y^2 exp\left(\frac{-\beta_{n,y}^2 D_{chem} t}{l_y^2}\right)}{\beta_{n,y}^2\left(\beta_{n,y}^2 + L_y^2 + L_y\right)} \tag{7.1}$$

where $\sigma(\infty)$ is the conductivity after the relaxation has reach its new equilibrium. $\sigma(t)$ is the conductivity at time, t, and $\sigma(t=0)$ is the conductivity at the start of the relaxation. $\beta_{n,x,y}^2$ is the n'th positive root to the Equation:

$$\beta_{n,x,y}^2 tan\beta_{n,x,y}^2 = L_{x,y} \tag{7.2}$$

and where $L_{x,y}$ is the dimensionless number:

$$L_{x,y} = \frac{l_{x,y} k_{\mathrm{ex}}}{D_{\mathrm{chem}}} \tag{7.3}$$

The ECR method is based on several assumptions which are listed below:

1. A maintained local electro neutrality.
2. Proportionality between charge carrier concentration and conductivity.
3. A first order surface exchange reaction.
4. Sample dimensions fulfilling the criteria: $l_x \approx l_y << l_z$, where z is the direction of the current.
5. A constant D_{chem} between $P_{O_2,initial}$ and $P_{O_2,final}$.

These assumptions require that one perform a relatively small step change in $P_{\mathrm{O_2}}$ as also addressed by Wang et al.[118] who concluded that $P_{O_2,final}/P_{O_2,initial}$ must not exceed a factor of 20. Figure 7.1 shows two typical conductivity transients measured at 850 and 900 °C from 0.4 to 0.2 atm. The conductivity has been normalised as $(\sigma_\infty - \sigma_t)/(\sigma_\infty - \sigma_{t=0})$ to give values between 0 and 1. The solid lines represent the best least square fit to Equation 7.1, where k_{ex} and D_{chem} have been used as fitting parameters. The measured conductivity reached stable values after each transient. However, for $P_{O_2} < 0.025$ at 950 °C, long term transients were also observed. After the characteristic transient associated with oxygen stoichiometry was equilibrated, the conductivity decayed approximately linearly with time and the conductivity never reached a stable value before the next transient started.

The method of least square fit takes the sum of the squared deviation (SSD) between all fitted and measured data points for a given transient. The lowest sum of square deviation

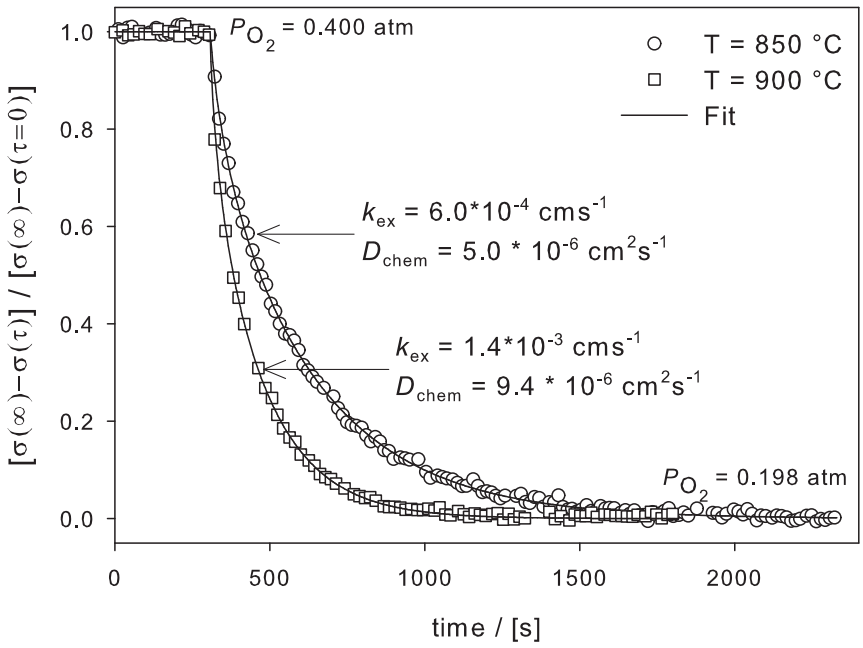

Figure 7.1: Illustration of two conductivity transients at 850 and 900 °C upon a change in P_{O_2} from 0.4 to 0.2 atm.

($SSD_{\min}$) represents the transient and the corresponding set of k_{ex} and D_{chem} that gives the lowest value of SSD and agrees best with measured data. This is achieved by systematically changing k_{ex} and D_{chem} and calculating the corresponding SSD. Fitting one transient response with two parameters (k_{ex} and D_{chem}) implicates an infinite number of solutions with the same SSD. Figure 7.2 shows a level curve of $SSD/SSD_{\min}$=2 for different parameters set of k_{ex} and D_{chem}. The relaxation is performed at 850 °C for P_{O_2} from 0.0094 to 0.0053 atm, which is the lowest measured P_{O_2} step. For all these pairs of k_{ex} and D_{chem}, which fulfill the criteria $SSD = 2 \times SSD_{min}$, D_{chem} deviates from D_{chem} at $SSD_{\min}$ with a factor that is 2-4 times higher than the corresponding factor for k_{ex}. This means that at this precise transient D_{chem} appears to have a slightly higher uncertainty than k_{ex}. The activation energy of these two parameters are, as will be shown, approximately the same so one should not expect this difference to change dramatically with T. k_{ex} increases with P_{O_2} whereas D_{chem} is relatively independent on P_{O_2} (see results further below). This increases the influence of diffusion to the overall equilibration and thus the difference in uncertainty of the two parameters will be even smaller for the transients measured at higher P_{O_2}s. For this particular sample (composition, geometry, microstructure and polishing) this method allows us to measure *both* k_{ex} and D_{chem} with relatively good precision.

Figure 7.3 shows k_{ex} extracted by fitting the measured conductivity transients to Equation 7.1. The data are presented as function of the final P_{O_2} for the five temperatures at which the conductivity relaxations were measured. The general trend with respect to P_{O_2} was found to be close to the power of 0.5 for all temperatures but 950 °C. Søgaard *et. al.* measured a similar P_{O_2} dependence for $(La_{0.6}Sr_{0.4})_{0.99}CoO_{3-\delta}$ using electrical conductivity relaxation.

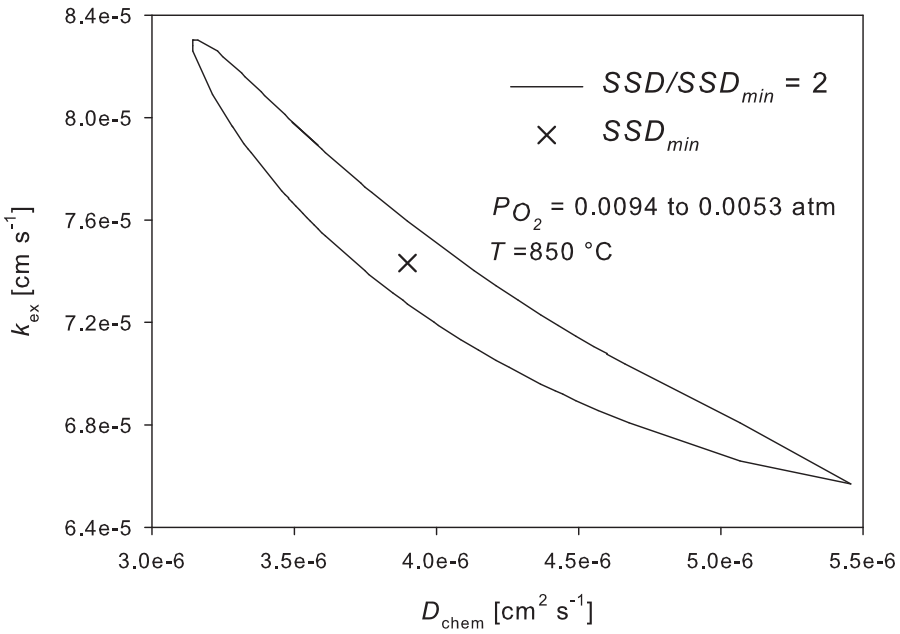

Figure 7.2: Map of the sum of square deviation (SSD) for sets of k_{ex} and D_{chem} and for the transient of $P_{\mathrm{O_2}}$ from 0.0094 to 0.0053 at 850 °C.

Also van der Haar *et. al.* found a similar $P_{\mathrm{O_2}}$ dependence for $La_{0.5}Sr_{0.5}CoO_{3-\delta}$. However, the same group also found that k_{ex} of $La_{0.8}Sr_{0.2}CoO_{3-\delta}$ was approximately independent on $P_{\mathrm{O_2}}$ within our measured T and $P_{\mathrm{O_2}}$ range.

It appears further that k_{ex} increases with temperature apart from 750 and 800 °C where it was found to be approximately the same. For each temperature an average $k_{\mathrm{ex,avg}}$ was calculated based on data from the entire measured $P_{\mathrm{O_2}}$ regime. An apparent activation energy of approximately 1.7±0.2 eV for (T = 800-950 °C and $0.005 < P_{\mathrm{O_2}} < 1$) was then estimated based on these $k_{\mathrm{ex,avg}}$. The extracted surface exchange coefficients are relatively close to what was measured on a dense bar of $(La_{0.6}Sr_{0.4})_{0.99}CoO_{3-\delta}$, manufactured using exactly the same procedure (10^{-3} - 10^{-4} cms^{-1} for T=700-800 and $P_{\mathrm{O_2}} \approx 0.2$). [142] The surface exchange data also agreed very well with what was reported by van der Haar *et. al.* for $La_{0.5}Sr_{0.5}CoO_{3-\delta}$ and $La_{0.8}Sr_{0.2}CoO_{3-\delta}$ at 750-850 °C (10^{-3} - $10^{-3.5}$ cms^{-1} for T=700-800 and $P_{\mathrm{O_2}} \approx 0.2$). This study found an activation energy of about 2 eV.[129] De Souza *et. al.* [165] used the oxygen isotope exchange/SIMS technique to measure the surface exchange rate, k_0, of $La_{0.8}Sr_{0.2}CoO_{3-\delta}$ and found it to be about 2-3 orders of magnitude lower than our reported values and with an activation energy of approximately 1.3 eV. k_0 is related to the surface exchange coefficient as $k_0=\gamma k_{\mathrm{ex}}$, where γ is the thermodynamic enhancement factor, defined in Equation 7.4. This factor is typically close to or above 100 for these types of mixed conductors. Thus, the result from this study is also in fair agreement with our data.

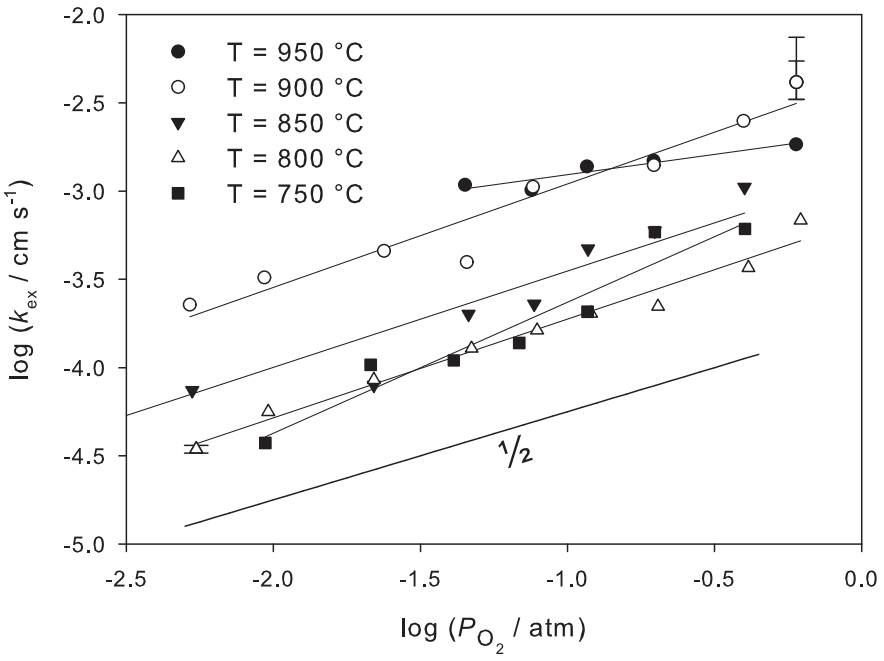

Figure 7.3: Surface exchange coefficients extracted from fitting Equation 7.1 to measured conductivity relaxations. P_{O_2} represent the final oxygen partial pressure.

$$\gamma = \frac{1}{2}\frac{\partial \ln P_{O_2}}{\partial \ln c_o} \tag{7.4}$$

Figure 7.4 shows D_{chem} extracted by fitting the measured conductivity transients to Equation 7.1. The data are presented as function of the final P_{O_2} for the five temperatures at which the conductivity relaxations were measured. From Figure 7.4 is clear that D_{chem} increases with temperature. A similar average chemical diffusion coefficient, $D_{\text{chem,avg}}$ for each T was determined. An apparent activation energy of 1.7±0.07 eV was calculated based on these $D_{\text{chem,avg}}$ for the entire P_{O_2} regime ($0.005 < P_{O_2} < 1$). It appears as though D_{chem} is relatively independent on P_{O_2} for all temperatures. This is in agreement with a number of studies (see eg. refs [118] [142]) on oxygen diffusion in related materials. Van der Haar *et. al.* also found D_{chem} to be independent on P_{O_2} for $La_{0.8}Sr_{0.2}CoO_{3-\delta}$.[129] The values of D_{chem} was measured to about 10^{-5}-10^{-6} cm^2 s^{-1} at 750-850 °C which is in close agreement with our measured coefficients. The activation energy, however, was found to be only about 1 eV. For compositions with high Sr content the study study of van der Haar *et. al.* that D_{chem} decreases with P_{O_2}. Søgaard *et. al.* [142] measured D_{chem} for $(La_{0.6}Sr_{0.4})_{0.99}CoO_{3-\delta}$ to about 10^{-4} - 10^{-5} cm^2 s^{-1}, independent on P_{O_2} for the same T regime. van der Haar *et. al.* found values of 10^{-5} cm^2 s^{-1} at T = 750-800 $P_{O_2} \approx 0.2$ for $La_{0.5}Sr_{0.5}CoO_{3-\delta}$. The values of D_{chem} measured by Søgaard and van der Haar for $(La_{1-x}Sr_x)_sCoO_{3-\delta}$ with 40-50 % Sr are thus close to one order of magnitude higher than our measured diffusion coefficients of $(La_{0.8}Sr_{0.2})_{0.99}Co_{0.8}Ni_{0.2}O_{3-\delta}$. De Souza *et. al.* measured the tracer diffusion coefficient, $D^\star$ to 10^{-7}-10^{-11} cm^2 s^{-1} at $T \approx$ 600-1000 °C for $La_{0.8}Sr_{0.2}CoO_{3-\delta}$. The activation energy was

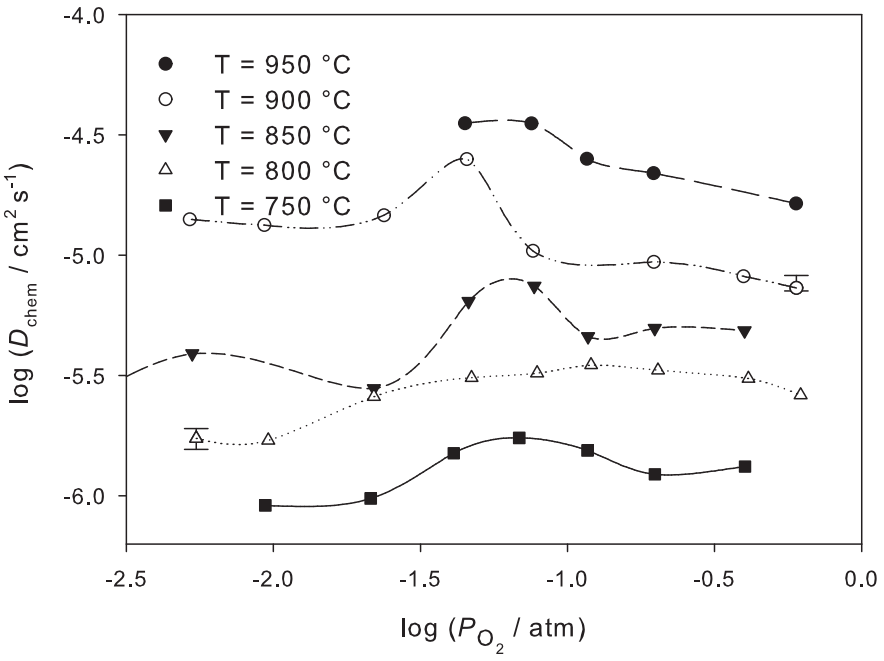

Figure 7.4: Chemical diffusion coefficients extracted from fitting Equation 7.1 to measured conductivity relaxations. P_{O_2} represent the final oxygen partial pressure.

found to be about 2 eV. Converted to D_{chem} via the thermodynamic enhancement factor, γ these are still lower by one order of magnitude compared our reported values.

7.4.2 AC Impedance Spectroscopy

Adler *et. al.* has derived a theoretical model, referred to as the *ALS model*, that couples the oxygen transport parameters into an impedance response. The model requires also microstructural and oxygen stoichiometric parameters. Knowing these parameters of a porous electrode it is possible to calculated a theoretical impedance response. Also given the microstructure and the oxygen stoichiometry one may extract the oxygen transport properties of the porous mixed conducting electrode from its impedance response. The model is expressed in Equations 7.5-7.7 and results in a Gerischer-type impedance. We will only present the equations of the model here and the reader is instead referred to the original paper [98] for a detailed theoretical background. Our measured impedance response resemble a Gerischer impedance with a 45° characteristic slope at high frequencies. The impedance spectrum was found to be slightly depressed, indicating a non ideal capacitive response. A depressed Gerischer-like impedance spectrum was also reported for the $(La_{1-x}Sr_x)_sCoO_{3-\delta}$ electrodes onto which the model was tested.[112] We have here included a third parameter, n, to account for the non-ideal *fractal* Gerischer. This concept has been discussed in a paper by

Table 7.1: Input parameters for the porous electrodes of $(La_{0.8}Sr_{0.2})_{0.99}Co_{0.8}Ni_{0.2}O_{3-\delta}$

a	τ	ϵ	$g(\epsilon_F)$	c_o	ρ	M
$[cm^2cm^{-3}]$	-	-	$[mol\ J^{-1}]$	$[mol\ cm^{-3}]$	$[g\ cm^{-3}]$	$[g\ mol^{-1}]$
$7.6{\cdot}10^4$	1.6	0.3	$1.68\ {\cdot}10^{-5}$	0.0886	6.94	235

Boukamp and coworker to which the reader is referred for further details. [104]

$$Z_{ger}(\omega) = \frac{R_{chem}}{\sqrt{1+(j\omega t_{chem})^n}} \tag{7.5}$$

where R_{chem} and t_{chem} are:

$$R_{chem} = \left(\frac{RT}{2F^2}\right)\sqrt{\frac{\tau}{(1-\epsilon)c_v D_v c_o k_o}} \tag{7.6}$$

$$t_{chem} = \frac{c_v(1-\epsilon)}{Aac_o k_o} \tag{7.7}$$

D_v and k_o are the vacancy diffusion coefficient and the surface rate cosntant. a, τ and ϵ are the surface area, tortuosity and porosity c_o and c_v are the concentration of oxygen and vacancies in the oxygen sublattice. A is the thermodynamic enhancement factor associated with oxygen vacancies, calculated according to Equation 7.8.[112] This is a different factor than γ, which is related to the oxide ions.

$$A = \frac{1}{2}\frac{\partial \ln P_{O_2}}{\partial \ln c_v} = 1 + \frac{12}{g(\epsilon_F)RT}\frac{c_v}{c_{mc}} \tag{7.8}$$

We have used different techniques to find as accurate input parameters as possible. Surface area was measured with BET. Porosity has been estimated from SEM-images. An SEM-image of the electrode is shown in Figure 7.5. Tortuosity was estimated from the empirical formula $\tau = 1 - 0.5\ln\epsilon$.[173] Density of states (g_{E_F}) and oxygen nonstoichiometry has been calculated from thermograviometric data using the itinerant electron model [80] with input data from [174]. Oxide concentration was calculated from theoretical density and molarity. The input parameters are listed in Table 7.1.

We have fitted the *ALS model* to the impedance of a porous electrode of $(La_{0.8}Sr_{0.2})_{0.99}Co_{0.8}Ni_{0.2}O_{3-\delta}$ measured under the various conditions described in the experimental section. Figure 7.6 shows a typical EIS spectrum measured at 700 °C under open circuit voltage and ambient air. The crosses represent best least square fit to the *ALS model*

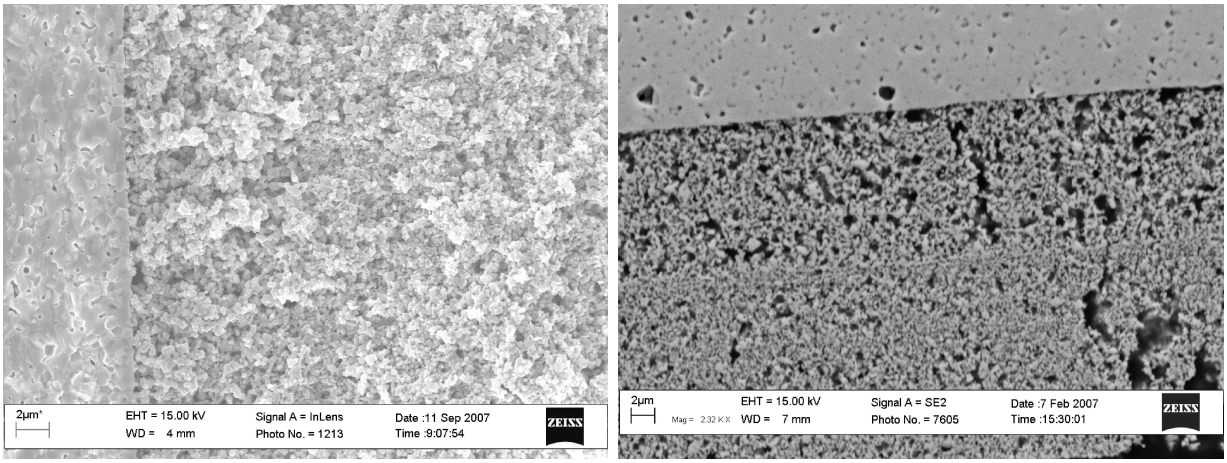

Figure 7.5: Left: SEM images of a fracture symmetric cell with $(La_{0.8}Sr_{0.2})_{0.99}Co_{0.8}Ni_{0.2}O_{3-\delta}$ as porous electrodes. **Right:** A cross section SEM images of a polished symmetric cell with $(La_{0.8}Sr_{0.2})_{0.99}Co_{0.8}Ni_{0.2}O_{3-\delta}$ as porous electrodes.

at each measured frequency. The model could be fitted nicely to all reported impedance spectrum measured as function of T, P_{O_2} and time using n, k_o, and D_v. The n values were found to range from 0.92-0.95 for most fits. Fitting the impedance spectrum with n=1 changed k_{ex} with $\approx 4\%$ and D_v with ≈ 0.1 %, which is well within the uncertainty limits of the input parameters and the model itself.

The results from fitting the impedance data to the *ALS model* are listed in Table 7.2. In order to compare the data with those extracted from the conductivity relaxations, D_{chem} was calculated according to Equation 7.9. k_o is the surface rate constant which expresses the surface exchange of atomic oxygen under equilibrium and can be converted to the surface exchange coefficient, k_{ex}, as $k_o=\gamma k_{ex}$. The oxygen transport properties are also plotted in Figures 7.8 and 7.9. The parameter, l_δ, expressed in Equation 7.10 is a thickness estimating the depth of the electrode within which the reaction is taking place, given the fitted set of parameters.[98] From Table 7.2 it is obvious that the estimated active thickness of the electrode, l_δ, is close to or slightly larger than its actual thickness.

$$D_{chem} = \frac{\gamma D_v c_v}{c_o} \tag{7.9}$$

$$l_\delta = \sqrt{\frac{c_v D_v (1-\epsilon)}{a c_o k_{ex}}} \tag{7.10}$$

Figure 7.8 shows that both k_{ex} and D_{chem} follows an Arrhenius-type temperature dependence apart from the lowest temperature (700 °C) at which both properties appears to deviate from linearity. The activation energy for both k_{ex} and D_{chem} were found to be about 1.1 eV and 1.35 eV for D_{chem} and k_{ex} respectively when calculated 750-950 °C. E_A of k_{ex} is higher than what was measured by van der Haar *et. al.* for $La_{0.8}Sr_{0.2}CoO_{3-\delta}$ but agreed very well with

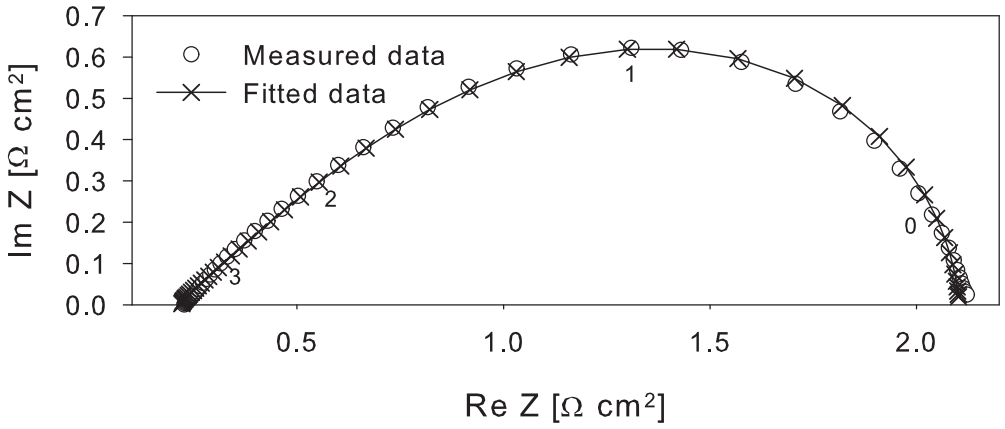

Figure 7.6: Nyqvist plot of the measured impedance of a porous $(La_{0.8}Sr_{0.2})_{0.99}Co_{0.8}Ni_{0.2}O_{3-\delta}$ electrode at 700 °C and ambient air.Crosses represent the best fit to the *ALS model* expressed in Equation 7.5 to 7.7.

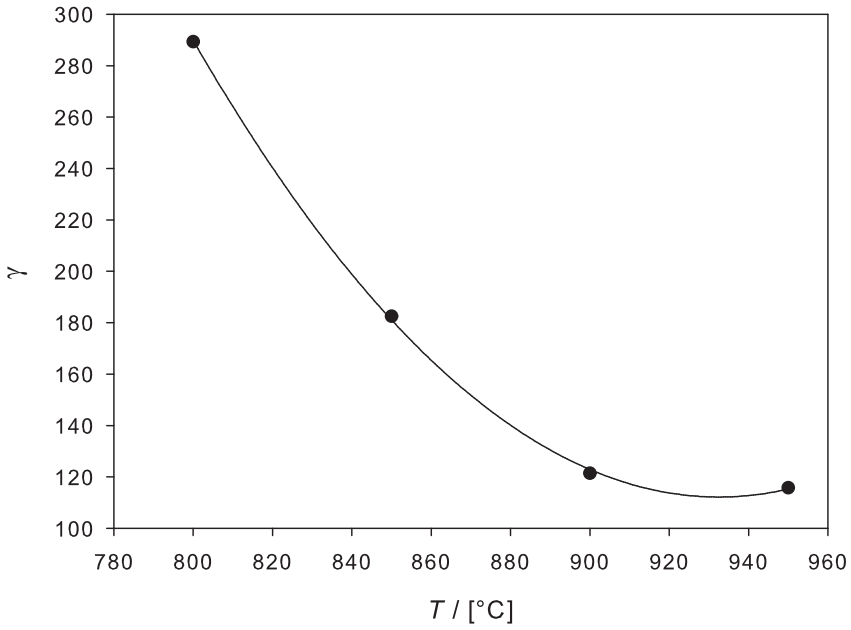

Figure 7.7: The thermodynamic enhancement factor, γ of $(La_{0.8}Sr_{0.2})_{0.99}Co_{0.8}Ni_{0.2}O_{3-\delta}$ calculated using Equation 7.4 at four temperatures.

Table 7.2: Calculated and fitted parameter of porous $(La_{0.8}Sr_{0.2})_{0.99}Co_{0.8}Ni_{0.2}O_{3-\delta}$

T	P_{O_2}	δ	k_0	k_{ex}	D_v	l_δ	A	D_{chem}	n
K	[atm]	-	[cm s^{-1}]	[cm^2 s^{-1}]	[cm^2 s^{-1}]	[μm]	-	[cm^2 s^{-1}]	-
1175	0.21	0.022	$3.1 \cdot 10^{-6}$	$3.5 \cdot 10^{-4}$	$5.3 \cdot 10^{-5}$	8.5	1.55	$4.4 \cdot 10^{-5}$	0.87
1123	0.21	0.014	$1.2 \cdot 10^{-6}$	$2.1 \cdot 10^{-4}$	$3.2 \cdot 10^{-5}$	8.4	1.36	$2.6 \cdot 10^{-5}$	0.92
1073	0.21	0.0082	$4.1 \cdot 10^{-7}$	$1.6 \cdot 10^{-4}$	$2.0 \cdot 10^{-5}$	8.6	1.22	$1.5 \cdot 10^{-5}$	0.95
1023	0.21	0.0039	$1.1 \cdot 10^{-7}$	$4.8 \cdot 10^{-5}$	$1.6 \cdot 10^{-5}$	10	1.11	$9.1 \cdot 10^{-6}$	0.95
973	0.21	0.0012	$1.7 \cdot 10^{-8}$	$1.1 \cdot 10^{-5}$	$2.9 \cdot 10^{-5}$	20	1.04	$7.8 \cdot 10^{-6}$	0.94
1025	0.08	0.0057	$3.8 \cdot 10^{-8}$	$1.7 \cdot 10^{-5}$	$2.6 \cdot 10^{-5}$	27	1.16	$2.1 \cdot 10^{-5}$	0.97
1025	0.14	0.0045	$7.2 \cdot 10^{-8}$	$3.1 \cdot 10^{-5}$	$2.0 \cdot 10^{-5}$	15	1.13	$1.3 \cdot 10^{-5}$	0.94
1025	0.21	0.0038	$9.3 \cdot 10^{-8}$	$4.1 \cdot 10^{-5}$	$1.9 \cdot 10^{-5}$	12	1.11	$1.0 \cdot 10^{-5}$	0.92
1025	0.30	0.0032	$1.1 \cdot 10^{-7}$	$4.8 \cdot 10^{-5}$	$1.9 \cdot 10^{-5}$	10	1.09	$9.0 \cdot 10^{-6}$	0.92
1025	0.48	0.0026	$1.2 \cdot 10^{-7}$	$5.3 \cdot 10^{-5}$	$2.2 \cdot 10^{-5}$	9.5	1.07	$8.4 \cdot 10^{-6}$	0.89

E_A of D_{chem}.[129]

Figure 7.9 plots k_{ex} and D_{chem} as function of P_{O_2} on a log-log scale and shows that neither of the two properties followed a true linear dependence with respect to P_{O_2}. The figure plots a decreasing k_{ex} with decreasing P_{O_2}, in accordance with literature. The P_{O_2} dependence is also relatively close to what was measured using the conductivity relaxation technique. D_{chem} was, oppositely to k_{ex}, shown to increase with decreasing P_{O_2}. This is contradictory to the literature in which D_{chem} is believed to be independent or, if the concentration of vacancies are high, decrease with decreasing P_{O_2}. k_{ex} extracted using the *ALS model* are about one order of magnitude lower than what was measured with electric conductivity relaxation, whereas D_{chem} where found to be slightly higher when measured on a porous sample as compared to a dense.

The impedance of the symmetric cells with $(La_{0.8}Sr_{0.2})_{0.99}Co_{0.8}Ni_{0.2}O_{3-\delta}$ as porous electrodes was also measured continuously over five days in order to study short term degradation trends. k_{ex} and D_{chem} were extracted using the *ALS model*. Figure 7.10 plots k_{ex} and D_{chem} relative to initial values as function of time ($k_{ex,init}$=$2.8 \cdot 10^{-5}$ cms^{-1} and $D_{chem,init}$=$8.7 \cdot 10^{-5}$ cm^2s^{-1}). The results show that k_{ex} decreased with a factor of 2 after only 5 days. It also shows that the relative decrease in k_{ex} is about 5 time higher than for D_{chem}.

Figure 7.11 shows an Arrhenius plot of the chemical capacitance, calculated as $C_{chem} = t_{chem}/R_{chem}$, and the resistance of the impedance response as function of time. The activation energy for R_{chem} was found to be 1.85 eV whereas the chemical capacitance was found to increase with T according to an "inverse" apparent Arrhenius-type dependence. Figure 7.12 plots the resistance and capacitance as function of P_{O_2} at 750 °C. R_{chem} proved relatively independent on P_{O_2} whereas C_{chem} appeared to increase with decreasing oxygen partial pressures.

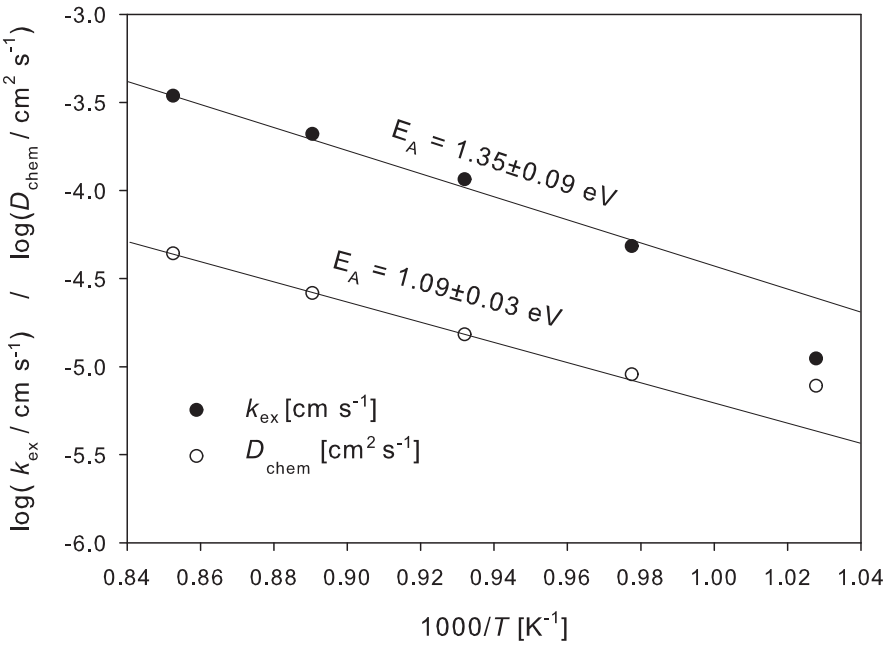

Figure 7.8: The surface exchange coefficient, k_{ex} and the oxygen diffusion coefficient, D_{chem}, as a function of temperature at ambient air pressure, extracted from fitting the Equation 7.5 to measured impedance data.

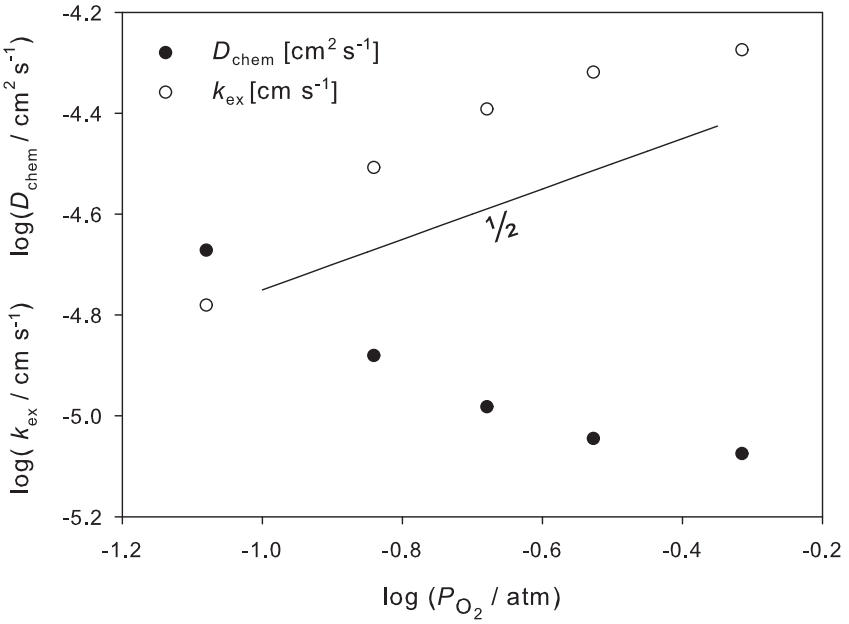

Figure 7.9: The surface exchange coefficient, k_{ex} and the oxygen diffusion coefficient, D_{chem}, as a function of $P_{\mathrm{O_2}}$ at 750 °C, extracted from fitting the Equation 7.5 to measured impedance data.

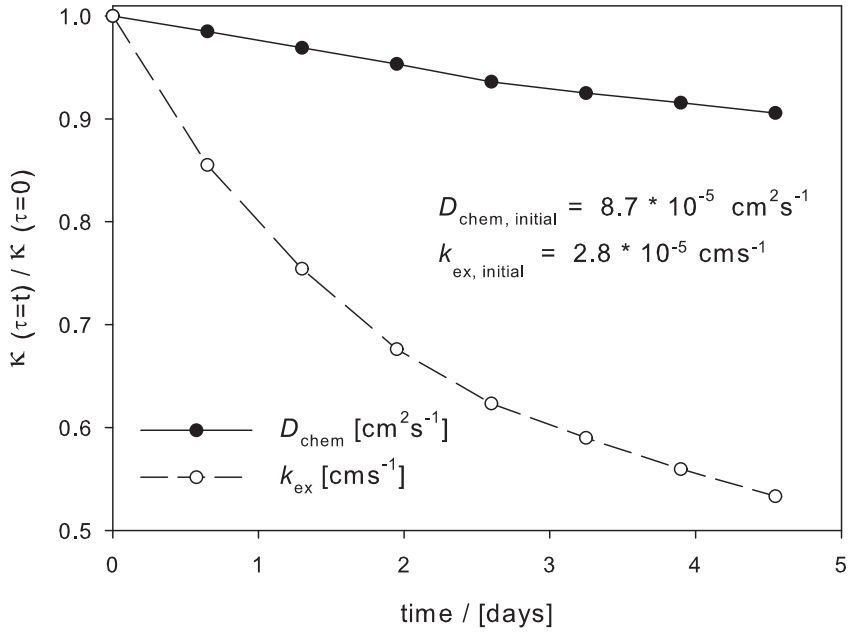

Figure 7.10: κ represent here both of k_{ex} and D_{chem}. The figure plots the surface exchange coefficient, k_{ex} and chemical diffusion coefficient, D_{chem}, divided with the initial values. Data has been extracted from fitting impedance data to Equation 7.5.

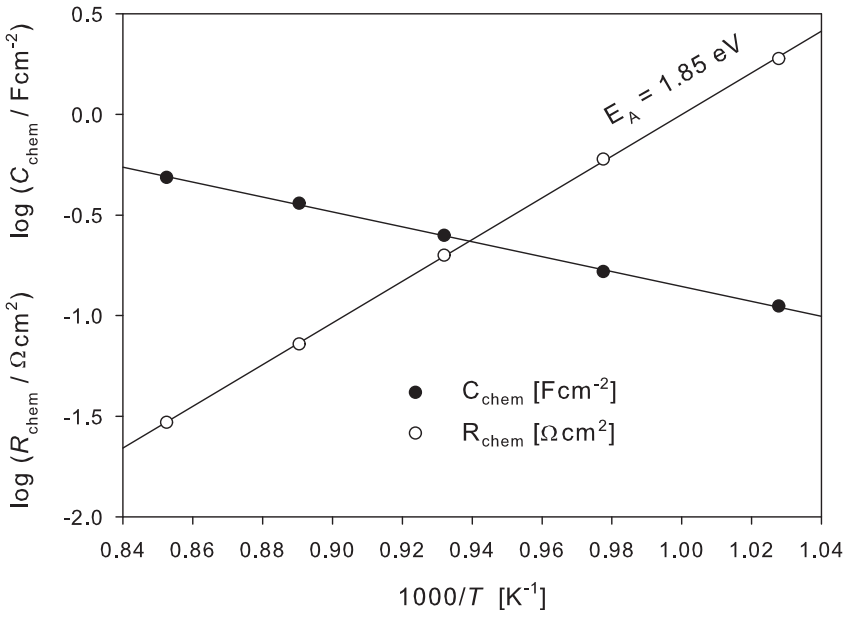

Figure 7.11: Resistance and capacitance of a porous $(La_{0.8}Sr_{0.2})_{0.99}Co_{0.8}Ni_{0.2}O_{3-\delta}$ electrodes as a function of temperature.

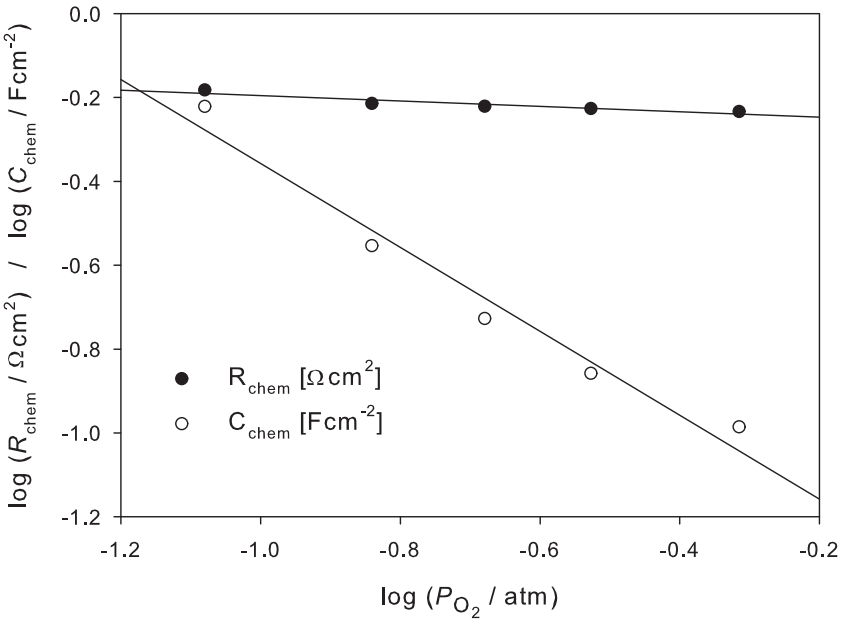

Figure 7.12: Resistance and capacitance of a porous $(La_{0.8}Sr_{0.2})_{0.99}Co_{0.8}Ni_{0.2}O_{3-\delta}$ electrodes as a function of P_{O_2} at 750 °C.

7.5 Discussion

The electrical conductivity was shown to relax to stable fully equilibrated values after each change in P_{O_2}. The long term transients observed at the highest temperature (950 °C) and below P_{O_2}=0.025 atm are likely not related to oxygen stoichiometric equilibrations. It is known that this perovskite is thermally unstable at high temperatures and reducing atmospheres. [9], [138] This indicates that the perovskite begins to breaks down under these conditions and that the long term transients are related to phase transition of the perovskite structure. Post-test Scanning Electron Micrographs - Energy Dispersive Spectroscopy (SEM-EDS) of the sample surface showed also evidence of SrO-phases on the surface, which were not seen prior to the measurements (see Figures 7.13).

The chemical diffusion coefficient, D_{chem}, when measured using the conductivity relaxation was shown to be relatively independent on P_{O_2}. Van der Haar *et. al.* [129] have also shown that D_{chem} is independent on P_{O_2} for $La_{0.8}Sr_{0.2}CoO_{3-\delta}$ at least within the range of 750-850 °C. This study reported further that D_{chem} decreases with P_{O_2} for $(La_{1-x}Sr_x)_sCoO_{3-\delta}$ with x=0.5 and 0.7. The authors argue that D_{chem} should be proportional to 3-$\delta \approx 3$ in oxides with noninteracting defects and thus relatively independent on P_{O_2} within our experimental range. Any deviation from this proportionality is believed to be related to vacancy ordering, which has been found to dramatically reduce the ionic conductivity.[87] This indicates that no vacancy ordering occurs in $(La_{0.8}Sr_{0.2})_{0.99}Co_{0.8}Ni_{0.2}O_{3-\delta}$ within the measured T and P_{O_2} range. D_{chem} was found to be about one order of magnitude lower when compared what was measured by Søgaard *et. al.*[142] on $(La_{0.6}Sr_{0.4})_{0.99}CoO_{3-\delta}$ and van der

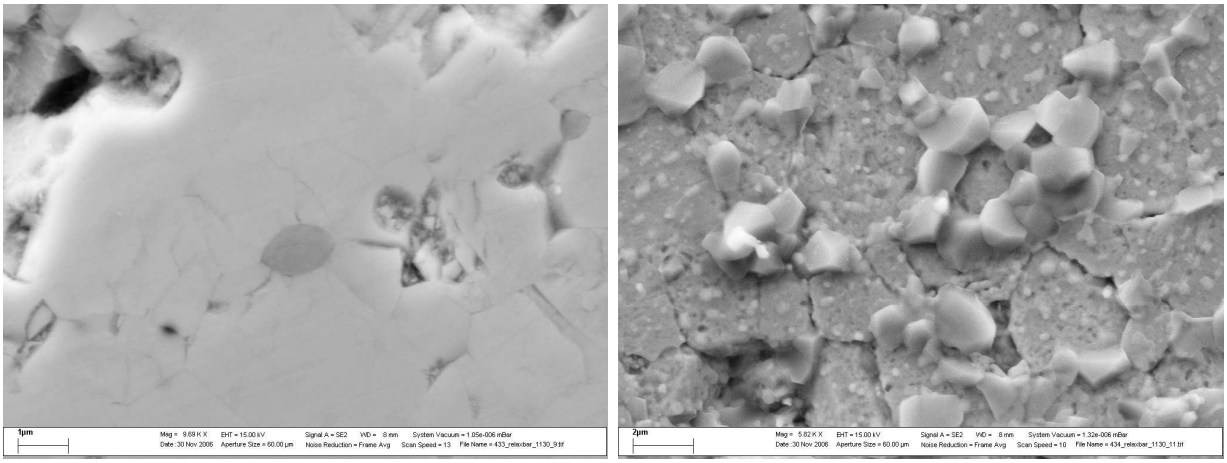

Figure 7.13: SEM images of the surface of the conductivity bar before (left) and after (right) the measurement. EDS-analysis showed clearly that the grains sitting on the surface after the measurement consist of pure SrO. The darker grain, incorporated in the bulk, that is seen in the micrograph to the left was shown to consist of pure NiO and are believed to be a consequence of A-site substoichiometry.

Haar *et. al.*.[129] on $La_{0.5}Sr_{0.5}CoO_{3-\delta}$. This is likely related to the higher concentration of vacancies in $(La_{0.6}Sr_{0.4})_{0.99}CoO_{3-\delta}$.

Values of both k_{ex} and D_{chem} for $(La_{0.8}Sr_{0.2})_{0.99}Co_{0.8}Ni_{0.2}O_{3-\delta}$ are in close agreement with what was reported in a study on $La_{0.8}Sr_{0.2}CoO_{3-\delta}$. This indicates that substituting cobalt with nickel does not change the oxygen transport properties dramatically. One should be careful, however, in the interpretation of data from two independent measurements on differently produced samples with possibly different surface structures and slightly different compositions. There is also a degree of uncertainty involved in the experimental procedure where two independent parameters are extracted from one set of data. The measurements are furthermore carried out within a limited P_{O_2} and T range due the low thermal stability of this composition.

using with appropriate microstructural and thermodynamic input data and with k_{ex}, D_{chem} and n as fitting parameters. The results plotted as function of temperature seen in Figure 7.8 show that both transport properties follow an apparent Arrhenius dependence with a similar activation energy of 1.35 and 1.1 eV for k_{ex} and D_{chem} respectively.

The measured impedance spectrum of the porous electrode consisting of $(La_{0.8}Sr_{0.2})_{0.99}Co_{0.8}Ni_{0.2}O_{3-\delta}$ could be fitted satisfactorily using the *ALS model*. However, the Arrhenius type dependence appeared to deviate from linearity at the lowest temperature (700 °C) for both k_{ex} and D_{chem}. Whether this is related to the transport properties themselves or to limitations of the model is not clear. It has been shown that $(La_{0.8}Sr_{0.2})_{0.99}Co_{0.8}Ni_{0.2}O_{3-\delta}$ is almost fully stoichiometric in ambient air at 750 °C (see Table 7.2). This could points towards that oxide ion diffusion is so low that the reaction will be restricted to the TPB and that the model is no longer valid. This limit of the model was also addressed by Adler *et. al.*.[112] In principle the model breaks down when the critical

length, defined as $L_c = D_V/k_{ex}$ is in the range of the particle size.

The thickness, l_δ, expressing the depth of the electrode within which the reaction is taking place is seen to increase with decreasing P_{O_2} (see Table 7.2). This is related to the fact k_{ex} decreases with P_{O_2} whereas D_{chem} increases with decreasing P_{O_2} as seen in Figure 7.9. This activates a larger surface area and thus a larger fraction of the electrode thickness according to Equation 7.10. The increase in chemical capacitance with reducing atmospheres plotted in Figure 7.12 is consistent with the trends of l_δ, expressing the fraction of the electrode thickness that is active. The absolute values of the capacitance are relatively high, close to 1 F cm^{-2}, which is much higher than the double layer capacitance typically about 10^{-4}-10^{-6} F cm^{-2} for SOFC cathodes. This supports that the bulk is being reduced and thus takes part in the electrode reaction resistance. Such a capacitance is often referred to as a chemical capacitance.[89] This also explains the increase in capacitance with T seen in Figure 7.11 as the the oxygen vacancy concentration increase with T, which allows a larger fraction of the bulk to take part in the oxidation/reduction.

Figure 7.10 shows that the surface exchange coefficient decreases with time at a much higher rate than the oxide ion diffusion. This reflects that the oxygen transport across surface is more susceptible to for instance chemical or structural changes than oxygen transport through the bulk. The reason for these degradation phenomena is difficult to conclude but it has been shown using computer modelling that SrO will tend to segregate towards the surface.[46] This was further shown experimentally using XPS on the surface of porous [171] and dense [53] $(La_{0.6}Sr_{0.4})_sCo_{0.2}Fe_{0.8}O_{3-\delta}$ electrodes. It was also detected in this study using SEM-EDS analysis (see Figure 7.13). The surface is in general more susceptible to impurities than the bulk. Impurity phases are inevitable in the synthesis and processing of the samples and these phases tend to segregate towards the surface. With a larger surface/bulk ratio in the porous sample, impurity phases can more easily reach the surface and thus porous samples are more susceptible to impurity phases. The electrolyte of the symmetric cells might further act as a potential source of impurities that may segregate to the electrode surface.

k_{ex} and D_{chem} extracted from the relaxation and impedance data respectively showed fair agreement. k_{ex} was found to be about one order of magnitude lower when extracted from impedance data as compared to the relaxation data whereas D_{chem} was found to be slightly higher when measured on a porous sample as compared to a dense. Whether this discrepancy has to do with input parameters being overestimated (such as the surface area) or a completely different surface morphology is difficult to say. It needs to be stressed, however, that the two samples are fundamentally different not only when it comes to microstructure (dense resp. porous) but also in the way they have been treated (e.g. processing and heat treatments). The bars used for conductivity measurements has been polished mechanically which might have exposed more catalytically active surfaces.

The fact that k_{ex} of $(La_{0.8}Sr_{0.2})_{0.99}Co_{0.8}Ni_{0.2}O_{3-\delta}$ agreed reasonably well with $(La_{0.6}Sr_{0.4})_{0.99}CoO_{3-\delta}$ whereas D_{chem} was about one order of magnitude lower is interesting when comparing the result of these two compositions when used as porous oxygen electrodes. We have earlier found that $(La_{0.6}Sr_{0.4})_{0.99}CoO_{3-\delta}$ has an area specific resistance that

was about one order of magnitude lower at 900 °C and about two orders of magnitude lower at 600 °C as compared to $(La_{0.8}Sr_{0.2})_{0.99}Co_{0.8}Ni_{0.2}O_{3-\delta}$.[2] This indicate the importance of oxide diffusion in these electrode. The fact that $(La_{0.8}Sr_{0.2})_{0.99}Co_{0.8}Ni_{0.2}O_{3-\delta}$ was found to have a slightly better performance in the study of Huang *et. al.* could possibly be explained by a microstructure that favour diffusion over the surface exchange reaction and that k_{ex} is rate determining the overall reaction in the electrodes of this study.

7.6 Conclusions

We have measured the oxygen transport properties, k_{ex} and D_{chem}, on a dense sample of $(La_{0.8}Sr_{0.2})_{0.99}Co_{0.8}Ni_{0.2}O_{3-\delta}$ using conductivity relaxation. We have also determined k_{ex} and D_{chem} from the impedance response of a porous electrode of $(La_{0.8}Sr_{0.2})_{0.99}Co_{0.8}Ni_{0.2}O_{3-\delta}$ using the *ALS model*. The results were in fair agreement for both properties. D_{chem} was found to be slightly higher when extracted using the *ALS model* whereas k_{ex} was found to be about one order of magnitude lower. The P_{O_2} dependence of k_{ex} extracted from the two methods agreed reasonably well, whereas D_{chem} measured using impedance spectroscopy was found to increase slightly with decreasing P_{O_2}. The calculated activation energies of both k_{ex} and D_{chem} were higher when extracted from relaxation data.

k_{ex} and D_{chem} measured using the conductivity relaxation technique was found to agree very well with what has been reported on $La_{0.8}Sr_{0.2}CoO_{3-\delta}$ which indicate that 20 % nickel substitution does not inflict any major changes in the oxygen transport properties. k_{ex} agreed also well with what has been measured for $(La_{0.6}Sr_{0.4})_{0.99}CoO_{3-\delta}$ whereas D_{chem} was found to be about one order of magnitude lower. Analysis of measured impedance during a short term degradation experiment using the *ALS model* showed that k_{ex} decreased five times faster than D_{chem}.

Chapter 8

Findings and Perspectives

This thesis has mainly focused on characterising the effect on structural and electrochemical properties when substituting cobalt with nickel in $(La_{1-x}Sr_x)_sCoO_{3-\delta}$. This is partly due to the literature on materials properties of the $(La_{1-x}Sr_x)_sCo_{1-y}Ni_yO_{3-\delta}$ materials system being scarce but also because the few existing papers have shown interesting indications when it comes to SOFC related properties. This chapter will try to put the scientific findings of this thesis into a SOFC perspective.

8.1 General discussion and conclusions

The total dopant (NiO/SrO) concentration was found to be about 50 % maximum when substituted into $LaCoO_3$, if the single phase perovskite is to be maintained. This limits the compositions possible to research and use in technological applications. It indicates further that the thermal stability might be reduced upon introduction of any of these two dopants, which is in agreement with literature. [82], [26], [9]

The results have shown indications that partial substitution of cobalt with nickel in $(La_{1-x}Sr_x)_sCoO_{3-\delta}$:

- increases the electron hole mobility.
- reduces thermal and chemical expansion coefficients.
- increases the oxygen nonstoichiometry factor at temperatures above ∼600 °C.

These findings indicate that partial substitution of nickel in $(La_{1-x}Sr_x)_sCoO_{3-\delta}$ could possibly enhance the electrochemical performance and technological compatibility of $(La_{1-x}Sr_x)_sCo_{1-y}Ni_yO_{3-\delta}$ when used as cathode in SOFC. The increased electron hole

mobility enhances the electronic conductivity, which is an important property for a material which is to be used as an electrode. The electronic conductivity mechanism of $(La_{1-x}Sr_x)_sCo_{1-y}Ni_yO_{3-\delta}$ was hypothesized to be of a dual nature where the *intrinsic charge* of intermediate and high spin cobalt was argued to follow a small polaron conduction and where the conductivity of the *p*-type charge (due to strontium substitution) was shown to be metallic-like. The reduced thermal and chemical expansion coefficients as an effect of nickel substitution lower the lattice expansion mismatch between the cathode and the rest of the cell and thus the risk of mechanical rupture during thermal cycling.

Moreover, the increase in oxygen vacancy concentration could possibly increase the oxide ion conductivity. A comparison of D_{chem} measured on $(La_{0.8}Sr_{0.2})_{0.99}Co_{0.8}Ni_{0.2}O_{3-\delta}$ with what is reported in the literature [129], [165] on $La_{0.8}Sr_{0.2}CoO_{3-\delta}$ could not established any pronounced increase in D_{chem}. However, it must be stressed that the uncertainty of relaxation experiments is rather large due to difference in sample preparation and measurement procedure, and that there might still be a difference of a factor of up to approx. 5. It has been argued in the literature that oxygen vacancies at the surface play a crucial role in the catalytic activity of oxygen reduction on mixed conducting oxides such as $(La_{1-x}Sr_x)_sCoO_{3-\delta}$. [83] This could point towards that nickel substitution in $(La_{1-x}Sr_x)_sCoO_{3-\delta}$ should increase the oxygen exchange coefficient as well as the electrochemical performance, i.e. the polarisation resistance, when used as an oxygen electrode. Our results on porous electrodes of $(La_{0.6}Sr_{0.4})_{0.99}CoO_{3-\delta}$ and $(La_{0.6}Sr_{0.4})_{0.99}Co_{0.9}Ni_{0.1}O_{3-\delta}$ showed, however, that there is no measurable difference within experimental uncertainty limits. Comparison between the measured surface exchange coefficient, k_{ex}, of $(La_{0.8}Sr_{0.2})_{0.99}Co_{0.8}Ni_{0.2}O_{3-\delta}$ with what is reported in the literature on $La_{0.8}Sr_{0.2}CoO_{3-\delta}$ [129], [165] did not revealed any pronounced difference either. Again the experimental error is rather large for these types of experiments and it might still be that nickel substitution enhances the surface exchange kinetics to a smaller degree. The major findings when it comes to electrochemical- and oxygen transport properties are summarised as:

- $(La_{1-x}Sr_x)_sCo_{1-y}Ni_yO_{3-\delta}$ has a very high electro-catalytic activity towards oxygen reduction/oxide ion oxidation. This activity increases strongly with strontium content.
- Nickel substitution into $(La_{0.6}Sr_{0.4})_{0.99}CoO_{3-\delta}$ and $La_{0.8}Sr_{0.2}CoO_{3-\delta}$ did not appear to dramatically change oxygen transport properties nor did alter the electrochemical activity.
- The activity of $(La_{1-x}Sr_x)_sCo_{1-y}Ni_yO_{3-\delta}$ is very susceptible to changes in manufacturing parameters such as sintering temperature.
- The activity is dependent on storage conditions and time.
- Short term degradation poses a durability problem.

A very low polarisation resistance of 7.5 $m\Omega cm^2$ at 750 °C was measured on a porous electrode of $(La_{0.6}Sr_{0.4})_{0.99}CoO_{3-\delta}$, however, it was very difficult to reproduce the electrochemical

behaviour of these electrodes. Even measurements on the same electrode when stored for a few months at room temperature resulted in very different electrochemical performance. Furthermore, electrochemical performance measured over an extended period of time showed a relatively rapid degradation. These features of $(La_{1-x}Sr_x)_sCo_{1-y}Ni_yO_{3-\delta}$ and related compounds needs to be studied further if these materials are to be used as cathode materials in SOFCs.

8.2 Future Outlook

We have found that $(La_{1-x}Sr_x)_sCo_{1-y}Ni_yO_{3-\delta}$ has a very high activity towards oxygen reduction, in accordance with previous literature. To integrate this material into an solid oxide fuel cell one needs, however, to better understand its problematic characteristics. It is also of great importance to study the degradation behaviour. For an electrode produced from $(La_{1-x}Sr_x)_sCo_{1-y}Ni_yO_{3-\delta}$ to be technologically relevant this requires more detailed work on several aspects.

- A detailed study on how the powder synthesis, thermal treatment and the electrode fabrication methods and processing parameters affect the electrode performance. Our results show that the electrode behaviour of porous electrodes of $(La_{1-x}Sr_x)_sCoO_{3-\delta}$ and related perovskites are susceptible to rather dramatic changes in manufacturing and storage conditions. This could give possibilities to further optimization of these electrodes.
- A study on the degradation under controlled conditions in order to reveal the degradation mechanisms. Degradation poses a big problem when it comes to commercialisation of SOFC, yet we know very little about degradation phenomena in $(La_{1-x}Sr_x)_sCoO_{3-\delta}$ and related perovskites.
- An electrochemical study on model electrodes of $(La_{1-x}Sr_x)_{0.99}Co_{1-y}Ni_yO_{3-\delta}$ with well known surface chemistry and structure. Apart from a series of studies by Fleig and coworkers [97], [96], [175] on lithographically produced micro-electrodes, literature is scarce on correlating surface chemistry and electro-catalytic activity despite all indications of the surface structure playing a crucial role. This could involve different surface techniques such as XPS, SIMS, LEED etc.
- Thermal stability of different compositions within $(La_{1-x}Sr_x)_sCo_{1-y}Ni_yO_{3-\delta}$ is an important property that has not been studied during this thesis. A study using CALPHAD/Thermocalc would be of great interest if these materials are to be used within the SOFC technology.

The electrode should also be optimised when it comes to microstructure. Important parameters appear to be particle necking and good adhesion to the electrolyte. In addition one needs

further to study how this electrode works when implemented in an operational SOFC when it comes to both electrochemical performance and chemical and mechanical compatibility.

APPENDIX

This appendix derives a general mathematical expression for the Gerischer Impedance as well as the case of electrochemical reduction oxygen coupled to an arbitrary diffusion process as described by Fick´s law. The mathematics has been taken as a whole from lectures given by T. Jacobsen at DTU, 2007 (course DTU-26910). [176] The appendix will also describe briefly the *ALS-model* [98] discussed explicitly in Chapters 6 and 7.

A - Gerischer Impedance

H. Gerischer derived early a mathematical impedance expression for the case of a chemical reaction coupled to an electrochemical as described by the reaction scheme below [177]:

$$A \overset{k}{\longleftrightarrow} Ox \overset{ne^{-1}}{\longleftrightarrow} Red$$

The AC impedance response for such a system in its most trivial form takes the following expression:

$$Z(\omega) = \frac{Z_0}{\sqrt{k + j\omega}} \tag{A-1}$$

where k is the rate constant for the chemical reaction. Z_0 is related to the warburg coefficient and can be used to calculated the diffusion coefficient or vice versa [178]:

$$Z_0 = \frac{RT}{n^2F^2A}\left(\frac{1}{D_O^{1/2}C_O^B} + \frac{1}{D_R^{1/2}C_R^B}\right) \tag{A-2}$$

One way to derive a Gerischer expression that is physically valid for an electrochemical system is to describe the scheme of reactions and processes with a transmission line. Transmission line is a concept first developed in electronics to describe impedance in long cable or at

low frequencies were the voltage of an AC-signal cannot be assumed constant along the conductor. This chapter will first derive the mathematics behind a general solution of a one dimensional, semi infinite "leaky" transmission line. [176] Secondly the solution to electrochemical reduction of oxygen on an electrode surface will be laid out.[176]

General solution

Consider the "leaky" transmission line illustrated in figure 8.1 (leaky referring to the parallel RC-circuits).

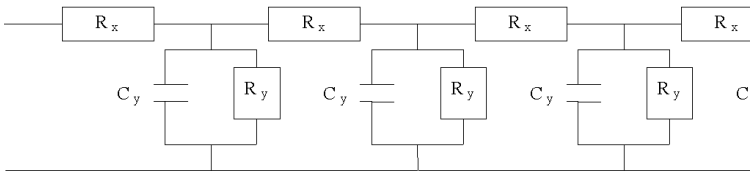

Figure 8.1: Illustration of a 1-D transmission line. The individual elements are infinitely small.

The current parallel to the line is a function of the distance x described the continuity equation:

$$\frac{\delta i_x}{\delta x} = -\frac{\eta(x)}{Z_y} \tag{A-3}$$

Derivation of ohms law ($i_x = -\frac{1}{R}\frac{\delta \eta}{\delta x}$) with respect to x gives:

$$\frac{\delta i_x}{\delta x} = -\frac{1}{R_x}\frac{\delta^2 \eta}{\delta x^2} \tag{A-4}$$

Combining Equation A-3 and A-4 yields the following differential equation for the voltage across the transmission line:

$$\frac{\delta^2 \eta}{\delta x^2} - \frac{R_x}{Z_y}\eta = 0 \tag{A-5}$$

which has the general solution:

$$\eta = Aexp\left[x\sqrt{\frac{R_x}{Z_y}}\right] Bexp\left[x\sqrt{\frac{R_x}{Z_y}}\right] \tag{A-6}$$

In order to solve Equation A-6 two boundary conditions are needed. The current at the start of the line (x=0) is normally one, which can be used in ohms law as:

$$i(x=0) = -\frac{1}{R_x}\frac{\delta\eta}{\delta x}|_{x=0} = A\frac{1}{\sqrt{R_x Z_y}}exp\left[x\sqrt{\frac{R_x}{Z_y}}\right] + B\frac{1}{\sqrt{R_x Z_y}}exp\left[-x\sqrt{\frac{R_x}{Z_y}}\right] \qquad \text{(A-7)}$$

The second boundary condition can be obtained by considering a short circuit of the transmission line at a certain penetration depth δ, where η will reduced to zero:

$$\eta(x=\delta) = Aexp\left[\delta\sqrt{\frac{R_x}{Z_y}}\right] + Bexp\left[-\delta\sqrt{\frac{R_x}{Z_y}}\right] = 0 \qquad \text{(A-8)}$$

In this case the impedance will be:

$$Z(shorted) = \frac{\eta}{i} = R_x\delta\frac{tanh[\psi_\delta]}{\psi_\delta} \qquad \text{(A-9)}$$

Another case is when the line instead is blocked to a certain depth, δ. The same current will then run through both $x = 0$ and $x = \delta$ and thus provide us with both boundary conditions:

$$i(x=\delta) = -\frac{1}{R_x}\frac{\delta\eta}{\delta x}|_{x=\delta} = A\frac{1}{\sqrt{R_x Z_y}}exp\left[\delta\sqrt{\frac{R_x}{Z_y}}\right] + B\frac{1}{\sqrt{R_x Z_y}}exp\left[-\delta\sqrt{\frac{R_x}{Z_y}}\right] \qquad \text{(A-10)}$$

The impedance will in this case results in a slightly different expression:

$$Z(blocked) = \frac{\eta}{i} = R_x\delta\frac{coth[\psi_\delta]}{\psi_\delta} \qquad \text{(A-11)}$$

where $\psi_\delta = \delta\sqrt{\frac{R_x}{Z_y}}$ is a measure of the transmission line´s length.

Electrochemical reduction of oxygen

The concept of transmission lines is also common in electrochemistry and can be used to describe oxygen reduction on an electrode. Assuming the following reactions scheme where the adsorption is rate limiting (not :

$$O_2(g) + 2\square \underset{k_-}{\overset{k_+}{\leftrightarrow}} 2O_{ads} \qquad (rds)$$

$$O_{ads} + 2e^- \overset{k_2}{\longleftrightarrow} O^{2-}$$

Assuming that surface coverage, $\Theta = (\Gamma/\Gamma_{max} << 1$ and pO_2 is constant the reaction rate can be expressed as:

$$v = k_2(k_- pO_2 - k_+\Theta^2 - k_{-1}pO_2) = k_2k_{-1}pO_2 - k_2k_+(\Theta_{eq} + \Delta\Theta)^2 \tag{A-12}$$

At equilibrium $k_+\Theta_{eq}^2 = k_- pO_2$. If we further assume that the concentration perturbation from equilibrium, $\Delta\Theta$ is small, the reaction rate can be simplified:

$$v = -2k_2k_+\Delta\Theta\Theta_{eq} + k_-(\Delta\Theta)^2 \approx -2k_2k_+\Delta\Theta\Theta_{eq} \tag{A-13}$$

If we now couple this chemical reaction with a surface diffusion process, expressed by Fick's 2nd law we obtain:

$$\frac{\partial\Delta\Gamma}{\partial t} = D\frac{\partial^2\Delta\Gamma}{\partial x^2} + v \tag{A-14}$$

where $\Delta\Gamma = \Gamma - \Gamma^{eq}$ is the deviation of the surface concentration from equilibrium. If we now make the substitution $\Theta = \Gamma/\Gamma_{max}$ we arrive at:

$$\frac{\partial\Delta\Gamma}{\partial t} = D\frac{\partial^2\Delta\Gamma}{\partial x^2} - 2k_2k_+\frac{\Gamma^{eq}}{\Gamma_{max}^2}\Delta\Gamma \tag{A-15}$$

The partial differential equation can be solved by Laplace transforming in time domain with the boundary condition that the perturbation of the surface concentration from equilibrium is zero at t=0. We then receive the following ordinary differential equation.

$$L\left(\frac{\partial\Delta\Gamma}{\partial t}\right) = s\Delta\overline{\Gamma(s)} - \Delta\Gamma(0) = s\overline{\Gamma(s)} = D\frac{\partial^2\Delta\overline{\Gamma}}{\partial x^2} - 2k_2k_+\frac{\Gamma^{eq}}{\Gamma_{max}^2}\Delta\overline{\Gamma} \tag{A-16}$$

which can be rewritten in analogy to equation A-4 as:

$$\frac{\partial^2\Delta\overline{\Gamma}}{\partial x^2} - \frac{1}{D}\left(\frac{2k_2k_+\Gamma^{eq}}{\Gamma_{max}^2} + s\right)\Delta\overline{\Gamma} = 0 \tag{A-17}$$

which resembles the differential equation describing the potential over a leaky transmission line with parallel coupled RC-circuits (see equation A-4). The solutions, A-8 and A-10, to this equation can be used provided the following parameters:

- $R_x = D^{-1}$
- $R_y = \frac{\Gamma_{max}}{2k_2k_+\Gamma_{eq}}$
- $C_y = 1$

Solving for the same boundary conditions as for the solutions in Equations A-9 and A-11.

$$\frac{\Delta\overline{\Gamma}}{\Delta\overline{i_O}} = \delta\frac{tanh[\psi_\delta]}{D\psi_\delta} = tanh[\psi_\delta]\sqrt{\frac{1}{D(2k_2k_+\Gamma_{eq} + i\omega)}} \tag{A-18}$$

$$\frac{\Delta\overline{\Gamma}}{\Delta\overline{i_O}} = \delta\frac{coth[\psi_\delta]}{D\psi_\delta} = coth[\psi_\delta]\sqrt{\frac{1}{D(2k_2k_+\Gamma_{eq} + i\omega)}} \tag{A-19}$$

If we now let ψ_δ increase both hyperbolic functions will rapidly go towards 1 and Equation A-18 and A-19 and take the simpler form:

$$Z = \sqrt{\frac{1}{D(2k_2k_+\Gamma_{eq} + i\omega)}} \tag{A-20}$$

Equation A-20 expresses the impedance in the form previously described by Gerischer (see Equation A-1) for a chemical-electrochemical reaction path and has the same form and dependance on diffusion and reactions coefficients. This case indicates that the electrochemical reaction does not need to be rate limiting and that a Gerischer-type expression also can be found for a chemical - electrochemical - chemical reaction path (adsorption and/or dissociation - reduction - diffusion).

B - The ALS model

Adler, Lane and Steele [98] have developed a model to predict the AC impedance response of a mixed ionic and electronically conducting electrode. As a starting point they specify that the overall reaction consists of three separate reactions, namely transfer of electrons across current collector/electrode interface, transfer of oxide ions across electrode/electrolyte interface and surface exchange of molecular oxygen across electrode/gas interface. In order to develop the model 8 starting points/assumptions are established:

1. The mixed conductor is treated as a dilute, ionic solvent. Electro neutrality reduces number of "charged" species to one (=the vacancy concentration).

2. Diffusion is treated as binary. Knudsen diffusion is considered in pores.

3. The electrolyte is treated ohmic with unity transference number. Current collector is treated with infinite conductivity.

4. Rate expressions for charge transfer reactions are treated as if being a single, activated rate limiting process.

5. Oxygen exchange reaction is treated as a heterogeneous catalytic reaction, independent on electronic state. Surface adsorption was not considered.

6. The porous electrode is treated as a superposition of the mixed conductor and the gas phase. This allows the electrode geometry, expressed with surface area, porosity, tortuosity to be treated statically.

7. The fermi level, E_F is treated as being uniform.

8. AC and DC responses can be linearised at zero bias (OCV).

Based on these definitions 6 equations (B-1-B-6) are derived. Equation B-1 expresses the vacancy concentration in the bulk. Equation B-2 expresses the oxygen mole at the gas/electrode interface as function of oxygen exchange reaction and diffusion. Equation B-3 describes gas diffusion in the pores. Equation B-4 expresses the rate constant, r, for the oxygen exchange reaction expressed in Equation B-3. Equations B-5 and Equation B-6 describes the interfacial charge transfer reactions at the mixed conductor/electrolyte interface and the mixed conductor/current collector interface respectively. See the appendix of the original paper [98] for the complete mathematical derivation of these expressions.

$$(1-\epsilon)\frac{\partial c_v^*}{\partial t} = \frac{(1-\epsilon)}{\tau} A D_v \frac{\partial^2 c_v^*}{\partial y^2} - ar \tag{B-1}$$

$$c\epsilon\frac{\partial x^*}{\partial t} = c\epsilon\frac{\chi_p}{\tau_p} D_{AB}\frac{\partial^2 x^*}{\partial y^2} - \frac{a(1-x\chi_p)}{2} r \tag{B-2}$$

$$\frac{\partial x_{bl}^*}{\partial t} = D_{AB}\frac{\partial x_{bl}^*}{y^2} \tag{B-3}$$

$$r = r_0(\alpha_f + \alpha_b)\left(A\frac{c_v^*}{c_v} + \frac{1}{2}\frac{x^*}{x}\right) \tag{B-4}$$

$$i = (1-\epsilon)\left(\frac{i_{01}(\alpha_{a1}+\alpha_{c1})}{RT}F + C_1\frac{\partial}{\partial t}\right)\left(\frac{\mu_v^{el*}}{2F}\|_{y=0} - \frac{ART}{2F} + \frac{c_v^*}{c_v}\|_{y=0} + \frac{\mu_e^{me*}}{F}\right) \tag{B-5}$$

$$i = \Phi \left(\frac{i_{02}(\alpha_{a2} + \alpha_{c2})F}{RT} + C_2 \frac{\partial}{\partial t} \right) \left(-\frac{1}{2}U - \frac{\mu_v^{mc*}}{F} \right) \tag{B-6}$$

c_v^* and x^* are the displacements of the vacancy concentration and oxygen mole fraction from zero the zero current condition. A is the thermodynamic enhancement factor, D is the diffusion coefficient for vacancies and and between O_2 and N_2. $\chi_p = D_2/(D_K + D_{AB})$ is a correction factor for Knudsen diffusion D_K, c is gas concentration, ϵ, a, τ, τ_p are the porosity, surface area, solid phase- and gas phase tortuosity respectively. where r_0 is the neutral flux density and α are mechanism constants of order unity. i is the area normalised current density, U is the oscillating cell potential ($U = U_0 e^{-j\omega t}$). μ_v^{el} and μ_e^{mc} are the displacements of the electric state from its value at i=0 of the electrolyte and mixed conductor. i_{01} and i_{02} are the exchange current densities, $\alpha_{a1,a2,c1,c2}$ are the anodic and cathodic transfer coefficients, C_1 and C_2 are the respective interface capacitances and Φ is the fraction of the electrode surface in contact with the current collector.

In order to solve these six partial differential equations equally many boundary conditions are sets up:

At the mixed conductor/electrolyte interface:

1. The current density in the mixed conductor must equal the current density in the electrolyte. (charge flow balance)
2. Molecular oxygen flux must equal zero. (non conversion steady state at OCV)

At the current collector/mixed conductor interface:

3. Flux of oxygen (molecular or ionic) in the mixed conductor must equal that in the boundary layer (gas diffusion layer outside the electrode)(mass flow balance).
4. Oxide ion flux in the mixed conductor must equals the O_2 exchange reaction rate at the surface. (internal mass flow balance)
5. The gas composition in the mixed conductor and the boundary layer is equal. (steady state)

In the gas phase:

6. Outside the boundary layer the gas composition is fixed. (steady state)

The linear equation system is solved for the periodic steady state solution when $t \to \infty$. For the full mathematical solution I will again refer to the appendix of the original paper [98]. The solutions are the impedance expressions of the three separate reactions described earlier in this appendix and the total impedance is obtained by summation (series coupling):

$$Z(\omega)_{total} = \frac{U(\omega,t)}{i(\omega,t)} = Z_{el} + Z_1 + Z_2 + Z_{chem} \tag{B-7}$$

where Z_{chem} is a composed expression of all non charge transfer processes including chemical reaction and solid state- and gas diffusion. Z_1 and Z_2 originates from the charge transfer processes at the mixed conductor/electrolyte- and the mixed conductor/current collector-interface:

$$\frac{1}{Z_1} = (1-\epsilon)\frac{i_{01}(\alpha_{a1}+\alpha_{c1})F}{2RT}\left(1 - \frac{j\omega C_1 RT}{i_{01}(\alpha_{a1}+\alpha_{c1})F}\right) \tag{B-8}$$

$$\frac{1}{Z_2} = (1-\epsilon)\frac{i_{02}(\alpha_{a1}+\alpha_{c1})F}{2RT}\left(1 - \frac{j\omega C_2 RT}{i_{01}(\alpha_{a2}+\alpha_{c2})F}\right) \tag{B-9}$$

$$Z_{chem} = R_{chem}\sqrt{\frac{1}{1+j\omega t_{chem}}} \tag{B-10}$$

where R_{chem} and t_{chem} are defined as:

$$R_{chem} = \left(\frac{RT}{2F^2}\right)\sqrt{\frac{\tau}{(1-\epsilon)c_v D_v r_0(\alpha_f+\alpha_b)}} \tag{B-11}$$

$$t_{chem} = \frac{c_v(1-\epsilon)}{Aar_0(\alpha_f+\alpha_b)} \tag{B-12}$$

R_{chem} is the resistance originating from non charge transfer processes (surface exchange and diffusion). The Equation B-10 has the same dependance on transport properties as Equation **??**, expressing the "simple" Gerischer impedance with a high frequency response characteristic of semi-infinite diffusion and a low frequency response typical that of simple RC-circuit.

The model also takes into account gas phase diffusion through a stagnant layer outside the electrode under which a gas diffusion impedance becomes.

$$Z_{gas} = \frac{R_{gas}}{1 - j\omega R_{gas} C_{gas}} \tag{B-13}$$

where the resistance is proportional to the oxygen mole fraction and diffusion coefficient as;

$$R_{gas} = \frac{1-x}{x}\frac{2L_{bl}RT}{16F^2 c D_{AB}} \tag{B-14}$$

The ideal gas assumption implies a reciprocal relationship to P_{O_2}, seen as $R_{gas} \propto 1/v = RT/P_{O_2}$. The capacitance can under both limits (oxygen transport or gas diffusion) be defined as:

$$C = \frac{2F^2(1-\epsilon)c_v L}{ART} \tag{B-15}$$

where $L = \delta$ if limited by surface exchange or/and solid oxide diffusion and the thickness of a stagnant layer outside the electrode in case of gas phase diffusion limitation.

Many papers [179], [89] have showed that, in mixed conducting SOFC-cathodes, interfacial charge transfer impedance, Z_1 and Z_2, are very small compared to chemical impedance, Z_{chem}, originating from the electrode/gas phase.

Bibliography

[1] P. Hjalmarsson, M. Mogensen, and Christensen C.H. Characterisation of the (La1-xSrx)0.99Co0.6+xNi0.4-xO3-delta SOFC cathode material. In P. Singh, Collins D, Yang G, Kumta P.N., Legzdins C.F., Sundaram S.K., and Manthiram A., editors, *Materials Science and Technology 2006: Materials and systems*, pages 201–212, 2006.

[2] P. Hjalmarsson, M. Sogaard, A. Hagen, and M. Mogensen. Structural properties and electrochemical performance of strontium- and nickel substituted lanthanum cobaltite. *Solid State Ionics*, 179:636, 2008.

[3] P. Hjalmarsson, M. Søgaard, and M. Mogensen. Electrochemical performance and degradation of (La0.6Sr0.4)0.99CoO3-delta as porous sofc-cathode. *Solid State Ionics*, 179:1422, 2008.

[4] Williams M.C. *Fuel Cell Hand Book 7th Ed.* National Energy Technology Center, 2004.

[5] R.M. Ormerod. Solid oxide fuel cells. *Chem.Soc.Rev.*, 32:17, 2003.

[6] A.B. Stambouli and E. Traversa. Solid oxide fuel cells (SOFCs): a review of an environmentally clean and efficient source of energy. *Renewable and Sustainable Energy Reviews*, 6:433, 2002.

[7] W.Z. Zhu and S.C. Deevi. A review on the status of anode materials for solid oxide fuel cells. *Materials Science and Engineering A*, 362:228, 2003.

[8] Y. Teraoka, H.M. Zhang, S. Furukawa, and N. Yamazoe. Oxygen permeation through perovskite-type oxides. *Chem.Lett.*, 1985:1743.

[9] Y. Teraoka, H.M. Zhang, and N. Yamazoe. Oxygen-sorptive properties of defect perovskite-type La1-xSrxCo1-yFeyO3-delta. *Chem.Lett.*, 1985:1367.

[10] H.M. Zhang, N. Yamazoe, and Y. Teraoka. Effects of b-site partial substitutions of perovskite-type La0.6Sr0.4CoO3 on oxygen desorption. *J.Mater.Sci.Lett.*, 8:995, 1989.

[11] T. Nakamura, M. Misono, and Y. Yoneda. - reduction-oxidation and catalytic properties of La¡sub¿1 - x¡/sub¿Sr¡sub¿x¡/sub¿coo¡sub¿3¡/sub¿. *J.Catal.*, - 83:151, 1983.

[12] L.W. Tai, M.M. NaSralLah, H.U. Anderson, D.M. Sparlin, and S.R. Sehlin. Structure and electrical-properties of La1-xSrxCo1-yFeyO3 .1. the system La0.8Sr0.2Co1-yFeyO3. *Solid State Ionics*, 76:259, 1995.

[13] S. Zongping and M.H. Sossina. A high-performance cathode for the next generation of solid-oxide fuel cells. *Nature (London)*, 431:170, 2004.

[14] Y. Teraoka, S. Furukawa, H.M. Zhang, and N. Yamazoe. Oxygen permeability of La1-xSrxCo1-yFeyO3 perovskite-type oxides. *Nippon Kagaku Kaishi*, 1988:1084.

[15] M. Hrovat, N. Katsarakis, K. Reichmann, S. Bernik, D. Kuscer, and J. Holc. Characterisation of LaNi1-xCoxO3 as a possible sofc cathode material. *Solid State Ionics*, 83:99, 1996.

[16] C.N.R. Rao, O. Parkash, and P. Ganguly. Electronic and magnetic-properties of LaNi1-xCoxO3, LaCo1-xFexO3 and LaNi1-xFexO3. *J.Solid State Chem.*, 15:186, 1975.

[17] C. Ftikos, S. Carter, and B.C.H. Steele. Mixed electronic/ionic conductivity of the solid-solution La(1-x)SrxCo(1-y)NiyO3-delta (x= 0.4, 0.5, 0.6 and y= 0.2, 0.4, 0.6). *J.Eur.Ceram.Soc.*, 12:79, 1993.

[18] Y. Teraoka, T. Nobunaga, K. Okamoto, N. Miura, and N. Yamazoe. Influence of constituent metal-cations in substituted LaCoO3 on mixed conductivity and oxygen permeability. *Solid State Ionics*, 48:207, 1991.

[19] H.J.M. Bouwmeester, H. Kruidhof, and A.J. Burggraaf. Importance of the surface exchange kinetics as rate-limiting step in oxygen permeation through mixed-conducting oxides. *Solid State Ionics*, 72:185, 1994.

[20] H. Nagamoto, I. Mochida, K. Kagotani, H. Inoue, and A. Negishi. Change of thermal-expansion coefficient and electrical-conductivity of LaCo1-xmxO3 (m = Fe, Ni). *J.Mater.Res.*, 8:3158, 1993.

[21] V.V. Kharton, A.V. Kovalevsky, V.N. Tikhonovich, E.N. Naumovich, and A.P. Viskup. Mixed electronic and ionic conductivity of LaCo(m)O3 (m = Ga, Cr, Fe or Ni) - ii. oxygen permeation through Cr- and Ni-substituted LaCoO3. *Solid State Ionics*, 110:53, 1998.

[22] K. Huang, H.Y. Lee, and J.B. Goodenough. Sr- and ni-doped LaCaO3 and LaFeO3 perovskites - new cathode materials for solid-oxide fuel cells. *J.Electrochem.Soc.*, 145:3220, 1998.

[23] L.G. Tejuca and J.L.G. Fierro. *Properties and applications of perovskite-type oxides*. Marcel Dekker Inc., 1993.

[24] A.N. Petrov, V.A. Cherepanov, and A.Y. Zuev. Thermodynamics, defect structure, and charge transfer in doped lanthanum cobaltites: an overview. *Journal of Solid State Electrochemistry*, 10:517, 2006.

[25] H.E. Hofer and W.F. Kock. Crystal-chemistry and thermal-behavior in the La(Cr, Ni)O3 perovskite system. *J.Electrochem.Soc.*, 140:2889, 1993.

[26] L.Y. Gavrilova, T.V. Aksenova, L.A. Bannykh, Y.V. Teslenko, and V.A. Cherepanov. Phase equilibria and crystal structure of complex oxides in the La-Sr-Co-Ni-O system. *J.Struct.Chem.*, 44:248, 2003.

[27] L.Y. Gavrilova, Y.V. Teslenko, L.A. Bannikch, T.V. Aksenova, and V.A. Cherepanov. The crystal structure and homogeneity range of the solid solutions in La-Sr-Co-Ni-O system. *J.Alloys Compd.*, 344:128, 2002.

[28] P.M. Raccah and J.B. Goodenou. First-order localized-electron collective-electron transition in LaCoO3. *Phys.Rev.*, 155:932, 1967.

[29] G. Maris, Y. Ren, V. Volotchaev, C. Zobel, T. Lorenz, and T.T.M. Palstra. Evidence for orbital ordering in LaCoO3. *Phys.Rev.B*, 67:224423, 2003.

[30] O. Haas, R.P.W.J. Struis, and J.M. McBreen. Synchrotron x-ray absorption of LaCoO3 perovskite. *J.Solid State Chem.*, 177:1000, 2004.

[31] S. Yamaguchi, Y. Okimoto, and Y. Tokura. Local lattice distortion during the spin-state transition in LaCoO3. *Phys.Rev.B*, 55:R8666, 1997.

[32] C. Zobel, M. Kriener, D. Bruns, J. Baier, M. Gruninger, T. Lorenz, P. Reutler, and A. Revcolevschi. Evidence for a low-spin to intermediate-spin state transition in LaCoO3. *Phys.Rev.B*, 66:020402, 2002.

[33] Y. Kobayashi, T. Mitsunaga, G. Fujinawa, T. Arii, M. Suetake, K. Asai, and J. Harada. Structural phase transition from rhombohedral to cubic in LaCoO3. *Journal of the Physical Society of Japan*, 69:3468, 2000.

[34] A. Mineshige, M. Inaba, T.S. Yao, Z. Ogumi, K. Kikuchi, and M. Kawase. Crystal structure and metal-insulator transition of La1-xSrxCoO3. *J.Solid State Chem.*, 121:423, 1996.

[35] J. Mastin, M.A. Einarsrud, and T. Grande. Structural and thermal properties of La1-xSrxCoO3-delta. *Chem.Mater.*, 18:6047, 2006.

[36] H. Obayashi and T. Kudo. Some crystallographic, electric and thermochemical properties of perovskite-type La1-xmxNiO3 (m-Ca, Sr and Ba). *Jpn.J.Appl.Phys.*, 14:330, 1975.

[37] T.C. Huang, W. Parrish, H. Toraya, P. Lacorre, and J.B. Torrance. High-temperature crystal-structures of orthorhombic and rhombohedral prNiO3. *Mater.Res.Bull.*, 25:1091, 1990.

[38] S. Rakshit and P.S. Gopalakrishnan. Oxygen nonstoichiometry and its effect on the structure of LaNiO3. *J.Solid State Chem.*, 110:28, 1994.

[39] R. Robert, L. Bocher, M. Trottmann, A. Reller, and A. Weidenkaff. Synthesis and high-temperature thermoelectric properties of Ni and Ti substituted LaCoO3. *J.Solid State Chem.*, 179:3893, 2006.

[40] I.C. Lekshmi, A. Gayen, and M.S. Hegde. Electrical transport properties of LaNi1-xmxO3 (m = Co, Mn) thin films fabricated by pulsed laser deposition. *Journal of Physics-Condensed Matter*, 17:6445, 2005.

[41] H. Nagamoto, I. Mochida, K. Kagotani, H. Inoue, and A. Negishi. Change of thermal-expansion coefficient and electrical-conductivity of LaCo1-xMxO3 (m = Fe, Ni). *J.Mater.Res.*, 8:3158, 1993.

[42] R.N. Singh, S.K. Tiwari, T. Sharma, P. Chartier, and J.F. Koenig. Investigation of oxygen evolution on LaNi1-xMxO3 (m = Fe, Co, Cu; 0 ¡ x ¡ 0.5) films of controlled roughness. *Journal of New Materials for Electrochemical Systems*, 2:65, 1999.

[43] J. Echigoya, S. Hiratsuka, and H. Suto. Solid-state reaction of La(Co1-xNix)O3 with 10-mol-percent Y2O3-ZrO2. *Mater.Trans., JIM*, 30:789, 1989.

[44] X.Y. Chen, J.S. Yu, and S.B. Adler. Thermal and chemical expansion of Sr-doped lanthanum cobalt oxide (La-1-xSrxCoO3-delta). *Chem.Mater.*, 17:4537, 2005.

[45] M.S.D. Read, M.S. Islam, G.W. Watson, F. King, and F.E. Hancock. Defect chemistry and surface properties of LaCoO3. *J.Mater.Chem.*, 10:2298, 2000.

[46] M.S. Islam. Computer modelling of defects and transport in perovskite oxides. *Solid State Ionics*, 154:75, 2002.

[47] S. Khan, R.J. Oldman, F. Cora, C.R.A. Catlow, S.A. French, and S.A. Axon. A computational modelling study of oxygen vacancies at LaCoO3 perovskite surfaces. *Phys.Chem.Chem.Phys.*, 8:5207, 2006.

[48] R.J.H. Voorhoeve, J.P. Remeika, and L.E. Trimble. Defect chemistry and catalysis in oxidation and reduction over perovskite-type oxides. *Annals of the New York Academy of Sciences*, 272:3, 1976.

[49] H. Arai, T. Yamada, K. Eguchi, and T. Seiyama. Catalytic combustion of methane over various perovskite-type oxides. *Applied Catalysis*, 26:265, 1986.

[50] J.P. Kemp, D.J. Beal, and P.A. Cox. Simple band model for La1-xSrxCoO3 - evidence from electron-spectroscopy. *J.Solid State Chem.*, 86:50, 1990.

[51] Y. Teraoka, N. Yamazoe, and T. Seiyama. surface states and catalytic properties of La1-xSrxCoO3. *Hyomenkagaka*, 3:153, 1998.

[52] I. Fullarton, J. Jacobs, H. van Benthem, J. Kilner, H. Brongersma, P. Scanlon, and B. Steele. Study of oxygen ion transport in acceptor doped samarium cobalt oxide. *Ionics*, 1:51, 1995.

[53] F.S. Baumann, J. Fleig, M. Konuma, U. Starke, H.U. Habermeier, and J. Maier. Strong performance improvement of La0.6Sr0.4CO0.8Fe0.2O3-delta sofc cathodes by electrochemical activation. *J.Electrochem.Soc.*, 152:A2074, 2005.

[54] D.D. Sarma, N. Shanthi, S.R. Barman, N. Hamada, H. Sawada, and K. Terakura. Band theory for ground-state properties and excitation spectra of perovskite LamO3 (m= Mn, Fe, Co, Ni). *Phys.Rev.Lett.*, 75:1126, 1995.

[55] M. Abbate, J.C. Fuggle, A. Fujimori, L.H. Tjeng, C.T. Chen, R. Potze, G.A. Sawatzky, H. Eisaki, and S. Uchida. Electronic structure and spin-state transition of LaCoO3. *Phys.Rev.B*, 47:16124, 1993.

[56] T. Arunarkavalli, G.U. Kulkarni, and C.N.R. Rao. Structural changes accompanying the spin-state transition in LaCoO3: A variable temperature Co-k-exafs study. *J.Solid State Chem.*, 107:299, 1993.

[57] M.A. Senaris-Rodriguez and J.B. Goodenough. LaCoO3 revisited. *J.Solid State Chem.*, 116:224, 1995.

[58] M.A. Senaris rodriguez and J.B. Goodenough. Magnetic and transport-properties of the system La1-xSrxCoO3-delta (0¡x¡to-0.50). *J.Solid State Chem.*, 118:323, 1995.

[59] T. Saitoh, T. Mizokawa, A. Fujimori, M. Abbate, Y. Takeda, and M. Takano. Electronic structure and temperature-induCed paramagnetism in LaCoO3. *Phys.Rev.B*, 55:4257, 1997.

[60] K. Asai, A. Yoneda, O. Yokokura, J.M. Tranquada, and G. Shirane. Two spin-state transitions in LaCoO3. *Journal of the Physical Society of Japan*, 67:290, 1998.

[61] R.H. Potze, G.A. Sawatzky, and M. Abbate. Possibility for an intermediate-spin ground-state in the charge-transfer material SrCoO3. *Phys.Rev.B*, 51:11501, 1995.

[62] P. Ravindran, P.A. Korzhavyi, H. Fjellvag, and A. Kjekshus. Electronic structure, phase stability, and magnetic properties of La1-xSrxCoO3 from first-principles full-potential calculations. *Phys.Rev.B*, 60:16423, 1999.

[63] M.A. Korotin, S.Y. Ezhov, I.V. Solovyev, V.I. Anisimov, D.I. Khomskii, and G.A. Sawatzky. Intermediate-spin state and properties of LaCoO3. *Phys.Rev.B*, 54:5309, 1996.

[64] M. Zhuang, W.Y. Zhang, and N.B. Ming. Competition of various spin states of LaCoO3. *Phys.Rev.B*, 57:10705, 1998.

[65] M. Takahashi and J. Igarashi. Excitation spectra of LaCoO3. *Phys.Rev.B*, 55:13557, 1997.

[66] P.G. Radaelli and S.W. Cheong. Structural phenomena associated with the spin-state transition in LaCoO3. *Phys.Rev.B*, 66:094408, 2002.

[67] R. Caciuffo, D. Rinaldi, G. Barucca, J. Mira, J. Rivas, M.A. Senaris-Rodriguez, P.G. Radaelli, D. Fiorani, and J.B. Goodenough. Structural details and magnetic order of La1-xSrxCoO3 (x 0.3). *Phys.Rev.B*, 59:1068, 1999.

[68] V.V. Sikolenko, A.P. Sazonov, V.V. Efimov, E.A. Efimova, V.V. Kriventsov, D.I. Kochubei, and U. Zimmermann. Phase separation in La1-xSrxCoO3 solid solutions with a perovskite structure. *Crystallography Reports*, 51:S67, 2006.

[69] D. Louca, J.L. Sarrao, J.D. Thompson, H. Roder, and G.H. Kwei. correlation of local jahn-teller distortions to the magnetic/conductive states of La1-xSrxCoO3. *Phys.Rev.B*, 60:10378, 1999.

[70] T. Saitoh, T. Mizokawa, A. Fujimori, M. Abbate, Y. Takeda, and M. Takano. Electronic structure and magnetic states in La1-xSrxCoO3 studied by photoemission and x-ray-absorption spectroscopy. *Phys.Rev.B*, 56:1290, 1997.

[71] D. Baskar and S.B. Adler. Electronic structure Studies of La1-xSrxCoO3-delta Using high temperature magnetization measurements. In K. Eguchi, Singhal S.C., H. Yokokawa, and J. Mizusaki, editors, *7*, pages 1279–1286, 2007.

[72] J.B. Goodenou and P.M. Raccah. Complex vs band formation in perovskite oxides. *J.Appl.Phys.*, 36:1031, 1965.

[73] J. Zaanen, G.A. Sawatzky, and J.W. Allen. Band-gaps and electronic-structure of transition-metal compounds. *Phys.Rev.Lett.*, 55:418, 1985.

[74] J.B. Torrance, P. Lacorre, C. Asavaroengchai, and R.M. Metzger. Why are some oxides metallic, while most are insulating? *Physica C*, 182:351, 1991.

[75] J.B. Torrance, P. Lacorre, A.I. Nazzal, E.J. Ansaldo, and C. Niedermayer. Systematic study of insulator-metal transitions in perovskites rNiO3 (r=pr,nd,sm,eu) due to closing of charge-transfer gap. *Phys.Rev.B*, 45:8209, 1992.

[76] J. Mizusaki, Y. Mima, S. Yamauchi, K. Fueki, and H. Tagawa. Nonstoichiometry of the perovskite-type oxides La1-xSrxCoO3-omega. *J.Solid State Chem.*, 80:102, 1989.

[77] A.N. Petrov, V.A. Cherepanov, O.F. Kononchuk, and L.Y. Gavrilova. Oxygen nonstoichiometry of La1-xSrxCoO3-delta(0¡x¡0.6). *J.Solid State Chem.*, 87:69, 1990.

[78] M.H.R. Lankhorst and H.J.M. Bouwmeester. Determination of oxygen nonstoichiometry and diffusivity in mixed conducting oxides by oxygen coulometric titration .2. oxygen nonstoichiometry and defect model for La0.8Sr0.2CoO3-delta. *J.Electrochem.Soc.*, 144:1268, 1997.

[79] M.H.R. Lankhorst, H.J.M. Bouwmeester, and H. Verweij. Thermodynamics and transport of ionic and electronic defects in crystalline oxides. *J.Am.Ceram.Soc.*, 80:2175, 1997.

[80] M.H.R. Lankhorst, H.J.M. Bouwmeester, and H. Verweij. High-temperature coulometric titration of La1-xSrxCoO3-delta: Evidence for the effect of electronic band structure on nonstoichiometry behavior. *J.Solid State Chem.*, 133:555, 1997.

[81] D.J. Sellmyer. *Electronic structure of metallic compounds and alloys: expermiental aspects*. Academic Press, 1978.

[82] A.N. Petrov, V.A. Cherepanov, A.Y. Zuyev, and V.M. Zhukovsky. Thermodynamic stability of ternary oxides in LnMo (Ln = La, Pr, Nd; m = Co, Ni, Cu) systems. *J.Solid State Chem.*, 77:1, 1988.

[83] S.B. Adler, X.Y. Chen, and J.R. Wilson. Mechanisms and rate Laws for oxygen exchange on mixed-conducting oxide surfaces. *J.Catal.*, 245:91, 2007.

[84] J. Kirchnerova and D.B. Hibbert. Vacancy ordering in La1-xSrxCoO3 prepared by calcination of freeze-dried powders of nitrates. *Mater.Res.Bull.*, 25:585, 1990.

[85] P.L. Gai and C.N.R. Rao. Cation ordering in Ln1-xSrxCoO3. *Mater.Res.Bull.*, 10:787, 1975.

[86] R.H.E. van Doorn and A.J. Burggraaf. Structural aspects of the ionic conductivity of La1-xSrxCoO3-delta. *Solid State Ionics*, 128:65, 2000.

[87] H. Kruidhof, H.J.M. Bouwmeester, R.H.E. Vondoorn, and A.J. Burggraaf. Influence of order-disorder transitions on oxygen permeability through selected nonstoichiometric perovskite-type oxides. *Solid State Ionics*, 63-5:816, 1993.

[88] D.B. Meadowcr. Low-cost oxygen electrode material. *Nature*, 226:847, 1970.

[89] S.B. Adler. Factors governing oxygen reduction in solid oxide fuel cell cathodes. *Chem.Rev.*, 104:4791, 2004.

[90] J. Fleig. On the current-voltage characteristics of charge transfer reactions at mixed conducting electrodes on solid electrolytes. *Phys.Chem.Chem.Phys.*, 7:2027, 2005.

[91] J. Fleig, R. Merkle, and J. Maier. The p(o-2) dependence of oxygen surface coverage and exchange current density of mixed conducting oxide electrodes: model considerations. *Phys.Chem.Chem.Phys.*, 9:2713, 2007.

[92] R. Merkle, J. Maier, and H.J.M. Bouwmeester. A linear free energy relationship for gas-solid interactions: correlation between surface rate constant and diffusion coefficient of oxygen tracer exchange for electron-rich perovskites. *Angew.Chem.Int.Ed.*, 43:5069, 2004.

[93] J.R. Wilson, M. Sase, T. Kawada, and S.B. Adler. Measurement of oxygen exchange kinetics on thin-film La0.6Sr0.4CoO3-delta using nonlinear electrochemical impedance spectroscopy. *Electrochemical and Solid State Letters*, 10:B81, 2007.

[94] Y. Takeda, R. Kanno, M. Noda, Y. Tomida, and O. Yamamoto. Cathodic polarization phenomena of perovskite oxide electrodes with stabilized zirconia. *J.Electrochem.Soc.*, 134:2656, 1987.

[95] V. Brichzin, J. Fleig, H.U. Habermeier, G. Cristiani, and J. Maier. The geometry dependence of the polarization resistance of Sr-doped LaMNO3 microelectrodes on yttria-stabilized zirconia. *Solid State Ionics*, 152:499, 2002.

[96] J. Fleig, F.S. Baumann, V. Brichzin, H.R. Kim, J. Jamnik, G. Cristiani, H.U. Habermeier, and J. Maier. Thin film microelectrodes in sofc electrode research. *Fuel Cells*, 6:284, 2006.

[97] F.S. Baumann, J. Fleig, H.U. Habermeier, and J. Maier. impedance spectroscopic study on well-defined (La,Sr)(co,fe)O3-delta model electrodes. *Solid State Ionics*, 177:1071, 2006.

[98] S.B. Adler, J.A. Lane, and B.C.H. Steele. Electrode kinetics of porous mixed-conducting oxygen electrodes. *J.Electrochem.Soc.*, 143:3554, 1996.

[99] R.H.E. van Doorn, H.J.M. Bouwmeester, and A.J. Burggraaf. Kinetic decomposition of La0.3Sr0.7CoO3-delta perovskite membranes during oxygen permeation. *Solid State Ionics*, 111:263, 1998.

[100] S.B. Adler. Limitations of charge-transfer models for mixed-conducting oxygen electrodes. *Solid State Ionics*, 135:603, 2000.

[101] J.H. Nam and D.H. Jeon. A comprehensive micro-scale model for transport and reaction in intermediate temperature solid oxide fuel cells. *Electrochim.Acta*, 51:3446, 2006.

[102] T. Kawada, K. Masuda, J. Suzuki, A. Kaimai, K. Kawamura, Y. Nigara, J. Mizusaki, H. Yugami, H. Arashi, N. Sakai, and H. Yokokawa. Oxygen isotope exchange with a dense La0.6Sr0.4CoO3-delta electrode on a Ce0.9Ca0.1O1.9 electrolyte. *Solid State Ionics*, 121:271, 1999.

[103] A. Ringuede and J. Fouletier. Oxygen reaction on strontium-doped lanthanum cobaltite dense electrodes at intermediate temperatures. *Solid State Ionics*, 139:167, 2001.

[104] B.A. Boukamp and H.J.M. Bouwmeester. Interpretation of the gerischer impedance in solid state ionics. *Solid State Ionics*, 157:29, 2003.

[105] B.A. Boukamp, M. Verbraeken, D.H.A. Blank, and P. Holtappels. Sofc-anodes, proof for a finite-length type gerischer impedance? *Solid State Ionics*, 177:2539, 2006.

[106] J. Jamnik and J. Maier. Generalised equivalent circuits for mass and charge transport: chemical capacitance and its implications. *Phys.Chem.Chem.Phys.*, 3:1668, 2001.

[107] J. Jamnik and J. Maier. Treatment of the impedance of mixed conductors - equivalent circuit model and explicit approximate solutions. *J.Electrochem.Soc.*, 146:4183, 1999.

[108] J. Mizusaki, J. Tabuchi, T. Matsuura, S. Yamauchi, and K. Fueki. Electrical-conductivity and seebeck coefficient of nonstoichiometric La1-xSrxCoO3-delta. *J.Electrochem.Soc.*, 136:2082, 1989.

[109] A.N. Petrov, O.F. Kononchuk, A.V. Andreev, V.A. Cherepanov, and P. Kofstad. Crystal-structure, electrical and magnetic-properties of La1-xSrxCoO3-y. *Solid State Ionics*, 80:189, 1995.

[110] A. Mineshige, M. Kobune, S. Fujii, Z. Ogumi, M. Inaba, T. Yao, and K. Kikuchi. Metal-insulator transition and crystal structure of La1-xSrxCoO3as functions of Sr-content, temperature, and oxygen partial pressure. *J.Solid State Chem.*, 142:374, 1999.

[111] W. Sitte, E. Bucher, and W. Preis. Nonstoichiometry and transport properties of strontium-substituted lanthanum cobaltites. *Solid State Ionics*, 154:517, 2002.

[112] S.B. Adler. Mechanism and kinetics of oxygen reduction on porous La1-xSrxCoO3-delta electrodes. *Solid State Ionics*, 111:125, 1998.

[113] C. Wagner. Equations for transport in solid oxides and sulfides of transition metals. *Prog.Solid State Chem.*, 10:3, 1975.

[114] I. Yasuda and T. Hikita. Precise determination of the chemical diffusion-coefficient of calcium-doped lanthanum chromites by means of electrical-conductivity relaxation. *J.Electrochem.Soc.*, 141:1268, 1994.

[115] T. Ishihara, H. Matsuda, and Y. Takita. Doped LaGaO3 perovskite type oxide as a new oxide ionic conductor. *Journal of the American Chemical Society*, 116:3801, 1994.

[116] W. Preis, E. Bucher, and W. Sitte. Oxygen exchange measurements on perovskites as cathode materials for solid oxide fuel cells. *J.Power Soures*, 106:116, 2002.

[117] R.H.E. vanDoorn, I.C. Fullarton, R.A. deSouza, J.A. Kilner, H.J.M. Bouwmeester, and A.J. Burggraaf. surface oxygen exchange of La0.3Sr0.7CoO3-delta. *Solid State Ionics*, 96:1, 1997.

[118] S. Wang, A. Verma, Y.L. Yang, A.J. Jacobson, and B. Abeles. The effect of the magnitude of the oxygen partial pressure change in electrical conductivity relaxation measurements: oxygen transport kinetics in La0.5Sr0.5CoO3-delta. *Solid State Ionics*, 140:125, 2001.

[119] C.H. Chen, H.J.M. Bouwmeester, R.H.E. vanDoorn, H. Kruidhof, and A.J. Burggraaf. Oxygen permeation of La0.3Sr0.7CoO3-delta. *Solid State Ionics*, 98:7, 1997.

[120] S. Carter, A. Selcuk, R.J. Chater, J. Kajda, J.A. Kilner, and B.C.H. Steele. Oxygen-transport in selected nonstoichiometric perovskite-structure oxides. *Solid State Ionics*, 53-6:597, 1992.

[121] R.A. De Souza and J.A. Kilner. Oxygen transport in La1-xSrxMn1-yCoyO3 +/-delta perovskites - part i. oxygen tracer diffusion. *Solid State Ionics*, 106:175, 1998.

[122] T. Ishigaki, S. Yamauchi, K. Kishio, J. Mizusaki, and K. Fueki. Diffusion of oxide ion vacancies in perovskite-type oxides. *J.Solid State Chem.*, 73:179, 1988.

[123] J.L. Routbort, R. Doshi, and M. Krumpelt. Oxygen tracer diffusion in La1-xSrxCoO3. *Solid State Ionics*, 90:21, 1996.

[124] H.Y. Tu, Y. Takeda, N. Imanishi, and O. Yamamoto. Ln(1-x)Sr(x)coo(3) (Ln=Sm, Dy) for the electrode of solid oxide fuel cells. *Solid State Ionics*, 100:283, 1997.

[125] O. Yamamoto, Y. Takeda, R. Kanno, and M. Noda. Perovskite-type oxides as oxygen electrodes for high temperature oxide fuel cells. *Solid State Ionics*, 22:241, 1987.

[126] M.A. Subramanian, G. Aravamudan, and G.V. Subba Rao. Oxide pyrochlores - a review. *Prog.Solid State Chem.*, 15:55, 1983.

[127] S.J. Skinner. Recent advances in perovskite-type materials for solid oxide fuel cell cathodes. *Int.J.Inorg.Mater.*, 3:113, 2001.

[128] R. Merkle and J. Maier. The significance of defect chemistry for the rate of gas-solid reactions: three examples. *Topics in Catalysis*, 38:141, 2006.

[129] L.M. van der Haar, M.W. den Otter, M. Morskate, H.J.M. Bouwmeester, and H. Verweij. Chemical diffusion and oxygen surface transfer of La1-xSrxCoO3-delta studied with electrical conductivity relaxation. *J.Electrochem.Soc.*, 149:J41, 2002.

[130] L.A. Chick, L.R. Pederson, G.D. Maupin, J.L. Bates, L.E. Thomas, and G.J. Exarhos. Glycine-nitrate combustion synthesis of oxide ceramic powders. *Mater.Lett.*, 10:6, 1990.

[131] A.K. Ladavos and P.J. Pomonis. Comparative-study of the solid-state and catalytic properties of La2-xSrxNiO4-lambda perovskites (x = 0.00-1.50) prepared by the nitrate and citrate methods. *J.Chem.Soc., Faraday Trans.*, 87:3291, 1991.

[132] S.P. Skaribas, P.J. Pomonis, and A.T. Sdoukos. Low-temperature synthesis of perovskite solids LaNiO3, LaCoO3, LaMnO3, via binuclear complexes of compartmental ligand n,n'-bis(3-carboxysalicylidene)ethylenediamine. *J.Mater.Chem.*, 1:781, 1991.

[133] Y. Teraoka, H. Kakebayashi, I. Moriguchi, and S. Kagawa. Hydroxy acid-aided synthesis of perovskite-type oxides of cobalt and manganese. *Chem.Lett.*, 1991:673.

[134] S. Verma, S.D. Pradhan, R. PaSricha, S.R. Sainkar, and P.A. Joy. A novel low-temperature synthesis of nanosized nizn ferrite. *J.Am.Ceram.Soc.*, 88:2597, 2005.

[135] H.M. Zhang, Y. Teraoka, and N. Yamazoe. Preparation of perovskite-type oxides with large surface-area by citrate process. *Chem.Lett.*, 1987:665.

[136] P.P. Chattopadhyay, I. Manna, S. Talapatra, and S.K. Pabi. A mathematical analysis of milling mechanics in a planetary ball mill. *Materials Chemistry and Physics*, 68:85, 2001.

[137] J. Alkebro, S. Begin-Colin, A. Mocellin, and R. Warren. Modeling high-energy ball milling in the alumina-yttria system. *J.Solid State Chem.*, 164:88, 2002.

[138] T.V. Aksenova, L.Y. Gavrilova, and V.A. Cherepanov. Phase equilibria at 1100 degrees c in air and crystal structure of solid solutions in the system LaCoO3-SrcoO2.5-SrNiO3-LaNiO3. *Inorg.Mater.*, 40:1336, 2004.

[139] Mukikagaku Henshuu Iinkai. Gihoodoo-shuppan, tokyo. 1981.

[140] K.Q. Huang, M. Feng, J.B. Goodenough, and C. Milliken. Electrode performance test on single ceramic fuel cells using as electrolyte Sr- and Mg-doped LaGaO3. *J.Electrochem.Soc.*, 144:3620, 1997.

[141] K.Q. Huang, M. Feng, J.B. Goodenough, and M. Schmerling. Characterization of Sr-doped LaMnO3 and LaCoO3 as cathode materials for a doped LagaO3 ceramic fuel cell. *J.Electrochem.Soc.*, 143:3630, 1996.

[142] M. Sogaard, P.V. Hendriksen, M. Mogensen, F.W. Poulsen, and E. Skou. Oxygen nonstoichiometry and transport properties of strontium substituted lanthanum cobaltite. *Solid State Ionics*, 177:3285, 2006.

[143] S.C. Grice, W.R. FLavell, A.G. Thomas, S. Warren, P.G. Marr, D.E. Jewitt, N. Khan, P.M. Dunwoody, and S.A. Jones. Electronic structure and reactivity of tm-doped La1-xSrxCoO3 (tm = ni, fe) catalysts. *Surf.Rev.Lett.*, 9:277, 2002.

[144] Y. Teraoka, M. Yoshimatsu, N. Yamazoe, and T. Seiyama. Oxygen-sorptive properties and defect structure of perovskite-type oxides. *Chem.Lett.*, 1984:893.

[145] K. Sreedhar, J.M. Honig, M. Darwin, M. MCelfresh, P.M. Shand, J. Xu, B.C. Crooker, and J. Spalek. Electronic-properties of the metallic perovskite LaNiO3 - correlated behavior of 3d electrons. *Phys.Rev.B*, 46:6382, 1992.

[146] J.G. Bednorz, K. Mller, and l. Perovskite-type oxides; the new approach to high-tc superconductivity. *Rev.Mod.Phys.*, 60:585, 1988.

[147] B. Lal, M.K. Raghunandan, M. Gupta, and R.N. Singh. Electrocatalytic properties of perovskite-type La1-xSrxCoO3 (0 ¡= x ¡= 0.4) obtained by a novel stearic acid sol-gel method for electrocatalysis of o-2 evolution in koh solutions. *Int.J.Hydrogen Energy*, 30:723, 2005.

[148] J. Mizusaki. Nonstoichiometry, diffusion, and electrical-properties of perovskite-type oxide electrode materials. *Solid State Ionics*, 52:79, 1992.

[149] P.M. Raccah and J.B. Goodenou. A localized-electron to collective-electron transition in system (La Sr)CO03. *J.Appl.Phys.*, 39:1209, 1968.

[150] N. Hamada. Electronic band structure of LaNiO3. *J.Phys.Chem.Solids*, 54:1157, 1993.

[151] A. Petrov, V. Cherepanov, T. Aksenova, and L. Gavrilova. The thermodynamic characteristics of point defects and the mechanism of charge transfer in lanthanum cobaltite doped with strontium and nickel. *Russian Journal of Physical Chemistry A, Focus on Chemistry*, 80:S134, 2006.

[152] A. Mineshige, J. Izutsu, M. Nakamura, K. Nigaki, M. Kobune, S. Fujii, M. Inaba, Z. Ogumi, and T. Yao. Electrical property, crystal structure and oxygen nonstoichiometry of La1-xSrxCO0.2Fe0.8O3-delta. *Electrochemistry*, 68:515, 2000.

[153] S.B. Adler. Chemical expansivity of electrochemical ceramics. *J.Am.Ceram.Soc.*, 84:2117, 2001.

[154] P.V. Hendriksen, Carter J.D., and M. Mogensen. expansion on reduction. In *4th*, pages 934–Singhal S.C. and Dokiya,M., 1995.

[155] P.H. Larsen, P.V. Hendriksen, and M. Mogensen. Dimensional stability and defect chemistry of doped lanthanum chromites. *Journal of Thermal Analysis*, 49:1263, 1997.

[156] R.D. Shannon. Revised effective ionic-radii and systematic studies of interatomic distances in halides and chalcogenides. *Acta Crystallogr., Sect.A*, 32:751, 1976.

[157] IUPAC. *Commission on Thermodynamics Oxygen International Thermodynamic Tables of the Fluid State 9*. Blackwell Scientific Oxford, 1987.

[158] Kittel C. *Introduction to Solid State Physics*. John Wiley & Sons Inc, 1996.

[159] C.N.R. Rao, M. Seikh, and C. Narayana. *Spin-state transition in LaCoO3 and related materials*. WILEY-VCH Verlag GmbH & Co, 2004.

[160] T.V. Aksenova, A.N. Petrov, V.A. Cherepanov, and L.Y. Gavrilova. The thermodynamic parameters of oxygen nonstoichiometry defects in lanthanum cobaltite doped with acceptor impurities (Sr and Ni). *Russian Journal of Physical Chemistry*, 80:1215, 2006.

[161] R. Männer, E. Ivers-Tiffee, and W. Wersing. Characterization of YSZ electrolyte materials with various yttria content. In F. Grosz, P. Zegers, Singhal S.C., and O. Yamamoto, editors, *1991*, pages 715–725.

[162] S. Primdahl and M. Mogensen. Gas diffusion impedance in characterization of solid oxide fuel cell anodes. *J.Electrochem.Soc.*, 146:2827, 1999.

[163] S. Primdahl and M. Mogensen. Gas conversion impedance: A test geometry effect in characterization of solid oxide fuel cell anodes. *J.Electrochem.Soc.*, 145:2431, 1998.

[164] H. Fukunaga, M. Koyama, N. Takahashi, C. Wen, and K. Yamada. Reaction model of dense sm0.5Sr0.5CoO3 as sofc cathode. *Solid State Ionics*, 132:279, 2000.

[165] R.A. De Souza and J.A. Kilner. Oxygen transport in La1-xSrxMn1-yCoyO3 +/-delta perovskites part ii. oxygen surface exchange. *Solid State Ionics*, 126:153, 1999.

[166] A. Mitterdorfer and L.J. Gauckler. Reaction kinetics of the pt, o-2(g)vertical bar c-zrO2 system: precursor-mediated adsorption. *Solid State Ionics*, 120:211, 1999.

[167] A. Mitterdorfer and L.J. Gauckler. La2zr2o7 formation and oxygen reduction kinetics of the La0.85Sr0.15MnyO3, o-2(g)vertical bar ysz system. *Solid State Ionics*, 111:185, 1998.

[168] T. Kawada, J. Suzuki, M. Sase, A. Kaimai, K. Yashiro, Y. Nigara, J. Mizusaki, K. Kawamura, and H. Yugami. Determination of oxygen vacancy concentration in a thin film of La0.6Sr0.4CoO3-delta by an electrochemical method. *J.Electrochem.Soc.*, 149:E252, 2002.

[169] J.A. Lane, S.B. Adler, Middleton P.H, and B.C.H. Steele. polarisation behaviour of mixed conducting perovskite cathode materials. In Singhal S.C. and M. Dokiya, editors, *PV 95-1*, volume 4, pages 584–588, 1995.

[170] F.A. Cotton and F.R.S. Wilkinson. *Advanced Inorganic Chemistry*. John Wiley & Sons, Inc., 1968.

[171] S.P. Simner, M.D. Anderson, M.H. Engelhard, and J.W. Stevenson. Degradation mechanisms of La-Sr-co-fe-O3sofc cathodes. *Electrochemical and Solid State Letters*, 9:A478, 2006.

[172] A. Esquirol, J. Kilner, and N. Brandon. Oxygen transport in La0.6Sr0.4CO0.2Fe0.8O3-delta/Ce0.8Ge0.2O2-x composite cathode for it-sofcs. *Solid State Ionics*, 175:63, 2004.

[173] M. Barrande, R. Bouchet, and R. Denoyel. Tortuosity of porous particles. *Analytical Chemistry*, 79:9115, 2007.

[174] P. Hjalmarsson, M. Sogaard, and M. Mogensen. Defect structure, electronic conductivity and expansion properties of (La1-xSrx)0.99Co1-yNiyO3-delta. *Solid State Ionics*, submitted:x, 2008.

[175] F.S. Baumann, J. Fleig, G. Cristiani, B. Stuhlhofer, H.U. Habermeier, and J. Maier. Quantitative comparison of mixed conducting sofc cathode materials by means of thin film model electrodes. *J.Electrochem.Soc.*, 154:B931, 2007.

[176] T. Jacobsen. *Lecture notes impedance spectroscopy course*. Torben Jacobsen, DTU, 2007.

[177] Gerischer H. –. *Z.Phys.Chem.*, 198:216, 1951.

[178] B.A. Boukamp. *Equivalent Circuit Users Manual*. Univ. Twente, Enschede, the Netherlands,, 1989.

[179] Y.L. Yang, C.L. Chen, S.Y. Chen, C.W. Chu, and A.J. Jacobson. impedance studies of oxygen exchange on dense thin film electrodes of La0.5Sr0.5CoO3-delta. *J.Electrochem.Soc.*, 147:4001, 2000.